The aerodynamics of a high-speed train running adjacent to windbreak walls

by

Syeda Anam Hashmi

A thesis submitted to the University of Birmingham for the degree of
DOCTOR OF PHILOSOPHY

School of Engineering

College of Engineering and Physical Sciences

University of Birmingham

July 2020

ABSTRACT

Crosswind stability of high-speed trains has been a prominent research topic for several decades, primarily motivated by the stability problems faced under strong crosswinds in order to make transport safer. In this study, the influence of different windbreak walls on train aerodynamic properties whilst subjected to crosswinds was assessed. Windbreak walls are built along the railway line, at sections where strong crosswinds are expected, to enhance the stability of trains and improving passenger comfort. The experimental campaign measured surface pressures on a stationary 1:25 model-scale of Class 390 Pendolino train under varying wind incidence angles with different windbreak walls inside a wind tunnel. The purpose of the stationary wind tunnel tests was to achieve valuable understanding of the aerodynamic flow that exists around a train surface due to the presence of different shapes of windbreak walls. In addition, these tests provided useful experimental data that acted as a benchmark for validating the numerical work carried out in this study. For the first time, the work considers transition regions in windbreak walls, where transition regions refer to the specific design implementations in terms of the geometry of a windbreak wall to tackle different topographies. This includes the changes in the distance of the windbreak wall from the railway track and the relative angles of different wall panels to each other. The numerical aspect of this study comprised of using Computational Fluid Dynamics to explore and map how a crosswind flow develops around a passenger train running adjacent to a windbreak wall, consisting of a transition region. Differences in pressure distribution on the train surface with and without different windbreak walls were evident. At a wind incidence angle of 90° for the stationary case, the tallest windbreak wall usually provided the most negative mean

pressure distribution on the surface of the model train due to the shielding effects; while the windbreak wall with a transition region consisting of a transition angle of 90° usually produced the lowest negative mean pressure distribution, comparatively. At a wind incidence angle of 30° for the stationary case, the results from windbreak walls with transition regions were relatively uniform indicating a smooth pressure distribution. Overall, the windbreak wall was able to significantly reduce the intensity of the pressures on the windward side of the train while also providing uniformity to the results on the leeward side of the train. This confirms the shielding effects provided by the windbreak wall to the train body from the oncoming crosswind flows. The transition region in a windbreak wall was observed to influence the flow in a significant manner. Different flow features were visible behind the transition region due to the non-uniformity of the transition region. Between the stationary and moving train cases, there were significant differences observed in the flow fields that develop around the trains with a windbreak wall.

ACKNOWLEDGEMENTS

TABLE OF CONTENTS

LIST OF FIGURES

xi

LIST OF TABLES

LIST OF PUBLICATIONS

Journal papers:

- **Hashmi, S.A.,** Hemida, H. and Soper, D. (2019). Wind tunnel testing on a train model subjected to crosswinds with different windbreak walls. Journal of Wind Engineering and Industrial Aerodynamics, 195.

  https://doi.org/10.1016/j.jweia.2019.104013

- Sun, Z., **Hashmi, S.A.,** Dai., H., Cheng, X., Zhang, T. and Chen, Z. (2020). Safety Comparisons of a High-Speed Train's Head and Tail Passing by a Windbreak Breach. Vehicle System Dynamics. International Journal of Vehicle Mechanics and Mobility.

  https://doi.org/10.1080/00423114.2020.1725067

- Vita, G., **Hashmi, S.A.,** Salvadori, S., Hemida, H. and Baniotopoulos, C. (2020). Role of Inflow Turbulence and Surrounding Buildings on Large Eddy Simulations of Urban Wind Energy. Energies, 13(19).

  https://doi.org/10.3390/en13195208

- Wang, M., **Hashmi, S.A.,** Sun, Z., Guo, D., Vita, G., Yang, G. and Hemida, H. (2021). Effect of surface roughness on aerodynamic characteristics of high-speed train subjected to crosswinds. Acta Mechanica Sinica.

- https://doi.org/10.1007/s10409-021-01099-7

- Chen, Z., **Hashmi., S.A.,** Liu, T., Sun, Z., Li, R., Hemida, H. and Hongkang, L. (2021). Sudden flow induced by the windbreak transition regions in a railway subject to crosswinds. Under review.

- **Hashmi, S.A.,** Soper, D., Hemida, H. (2021). Numerical investigation on a train model subjected to crosswinds with a transition region in a windbreak wall. In preparation.

- Chen, Z., **Hashmi., S.A.,** Liu, T., Hemida, H., Sun, Z. and Guo, Z. (2021). Impact of windbreak transition on the flow around a railway track with different angles of wind attack. In preparation.

Conference papers:

- **Hashmi, S.A.,** Hemida, H. and Soper, D. (2018). An experimental and numerical study on the effects of windbreak walls on the flow around trains subjected to crosswinds. Paper presented at The Fourth International Conference on Railway Technology, Sitges, Barcelona, Spain, 3-7 September, 2018.

- Chen, Z., **Hashmi., S.A.,** Liu, T. and Hemida, H. (2020). Effect of a train's cross-sectional shapes on its aerodynamic performance subjected to crosswinds at a windbreak transition. The 2020 World Congress on Advances in Civil, Environmental, & Materials Research (ACEM20), Seoul, Korea.

NOMENCLATURE

A	Area (m^2)
A_{ref}	Nominal side area (m^2)
C_Y	Non-dimensional side force coefficient
C_Z	Non-dimensional lift force coefficient
C_{M_X}	Non-dimensional rolling moment coefficient about the X-axis
$C_{M_{X,lee}}$	Non-dimensional rolling moment coefficient about the leeward rail
C_P	Non-dimensional pressure coefficient
d_w	Distance to the nearest wall
E_{BIAS}	Bias limit
E_{RND}	Random uncertainty
E_{TOTAL}	Total uncertainty
f	Frequency of the flow
F_X	Drag force (N)
F_Y	Side force (N)
F_z	Lift force (N)
F_1 and F_2	Shear Stress Transport blending functions
H_{ref}	Nominal height (m)
H	Height of the train (m)
I	Turbulence intensity
I_{uvw}	Overall turbulence intensity (%)
k	Turbulent kinetic energy

l	Characteristic length (m)
l_{IDDES}	IDDES length scale
L	Length of the train's leading car (m)
M_X	Aerodynamic rolling moment about the X-axis
M_Y	Aerodynamic pitching moment about the Y-axis
M_Z	Aerodynamic yawing moment about the Z-axis
P	Actual surface pressure on a train at any point (Pa)
P_k	Production term
P_o	Reference pressure (Pa)
Re	Reynolds number
S	Magnitude of the strain rate tensor
St	Strouhal number
t	time (s)
t^*	Non-dimensional time unit
U	Velocity (m/s)
u^*	Frictional velocity (m/s)
u_{wind}	Onset natural wind velocity (m/s)
u, v and w	Streamwise, lateral and vertical velocities (m/s)
V_{rel}	Relative velocity or the free stream velocity (m/s)
V_{train}	Train speed (m/s)
W	Width of the leading car (m)
y	Distance normal to the surface
y^+	Non-dimensional wall distance
z	Height above the ground (m)

z_o	Surface roughness length (m)

Greek Symbols

β	Onset natural wind angle (degrees)
δ	Boundary layer thickness (m)
ρ	Air density (kg/m^3)
σ	Standard deviation
μ	Dynamic viscosity
μ_t	Turbulent eddy viscosity
κ	Von Karman constant
v	Kinematic viscosity (m^2/s)
τ_w	Wall shear stress (N/m^2)
ψ	Yaw angle (degrees)
Ω	Magnitude of vorticity tensor
ω	Specific turbulent dissipation rate

Abbreviations

ABL	Atmospheric boundary layer
BSI	British Standards Institute
CAD	Computer Aided Design
CEN	European Committee for Standardization
CFD	Computational Fluid Dynamics
CFL	Courant-Friedrichs-Lewy
COT	Centre of Track
DES	Detached Eddy Simulation
DDES	Delayed Detached Eddy Simulation

DNS	Direct Numerical Simulation
GIS	Grid-induced Separation
HPC	High Performance Computing
HWP	Horizontal wind profile
IDDES	Instantaneous Delayed Detached Eddy Simulation
LES	Large-Eddy Simulation
LWS	Leeward side
MMR	Moving Model Rig
MSD	Modelled Stress Depletion
PIV	Particle Image Velocimetry
PSD	Power Spectral Density
RANS	Reynolds-averaged Navier-Stokes
RMS	Root Mean Square
RSSB	Rail Safety and Standards Board
SST	Shear Stress Transport
STBR	Single Track Ballast and Rail (Ground Scenario)
TFI	Turbulent Flow Instrumentation
TOR	Top of Rail
TRAIN rig	Transient Aerodynamic Investigation rig
TSI	Technical Specifications for Interoperability
UB	Underbody
VWP	Vertical Wind Profile
WMLES	Wall-modelled LES
WWS	Windward side

CHAPTER 1: Introduction

1.1 Research outline

This thesis presents an experimental and numerical investigation carried out to analyse the effect of a windbreak wall's geometrical design on the aerodynamics of a high-speed passenger train. Windbreak walls are usually built along the railway line, beside the tracks, where strong winds are expected in order to reduce the effect of crosswinds on the stability of trains while ensuring passenger comfort. The details and results of the experimental and numerical work form the main body of this doctoral thesis. Results from the experimental work performed at the University of Birmingham's wind tunnel facility have been published in the Journal of Wind Engineering and Industrial Aerodynamics. Preliminary versions of the numerical results in this thesis have been presented at several international research conferences, including the Fourth International Conference on Railway Technology in Barcelona, Spain. During the author's doctoral studies, the author also took part in several other research studies, related to train aerodynamics and wind engineering.

1.2 Research background

The high-speed rail industry is a growing sector in terms of passenger numbers, train speeds and the number of railway lines in the United Kingdom (RSSB, 2016; Department for Transport, 2017), and other countries including China, Japan, United States and many European countries (Fujii et al., 1999; Deeg et al., 2008). With clear indication that rail passenger numbers are likely to double in the upcoming years (RSSB, 2016), it is crucial

to develop high-speed and highly efficient trains, as well as the modern infrastructure required to be able to run such services. Optimisation of commercial rail vehicles involves designing high-speed trains to be as long and light-weight as possible (Diedrichs et al., 2003). This can however have knock on implications to the stability of these commercial rail vehicles to crosswind forces, a well-known problem for more than three decades now (Copley, 1987; Baker et al., 2004; Dorigatti et al., 2015). The effects of external aerodynamics on high-speed trains are usually pronounced under the interaction of strong crosswinds, creating a complex flow field around a train, leading to a series of steady and unsteady aerodynamic forces and moments. Such aerodynamic loads may induce significant changes in the vehicle dynamic behaviour, when compared to a no-crosswind condition (Gawthorpe, 1994; Diedrichs, 2006). As Copley (1987) pointed out, weight of the train is an important factor which counteracts the aerodynamic overturning forces. In addition, the width of the train wheel-base along with the vertical location of the centre of the gravity is crucial in determining how easily a train can overturn. Therefore, an obvious deterioration in the running performance of a train in terms of safety can be anticipated under high aerodynamic loads, caused mainly by high wind speeds. It is known that under crosswinds the yaw angle and resultant wind velocity, calculated using the wind and train speeds, are the important factors on vehicle dynamics. Consequently, Hemida and Krajnovic (2010) suggested that high-speed trains are potentially at a risk of derailing or overturning due to the impact of strong crosswinds. This statement was also supported by Browand et al. (2009) who suggested that design factors on the new generation of trains may lead to a huge impact on train stability, especially in light of the fact that drag and aerodynamic effects increase significantly with the square of speed (Browand et al., 2009; Baker, 2014a).

1.3 Research motivation

Dating back to the 19th century, there have been sporadic instances of strong winds blowing railway trains off tracks and causing accidents. The most notable of these accidents was in 1903 at Leven Viaduct in Cumbria, Britain (Gawthorpe, 1994). The accident involved an overturned passenger train due to crosswinds with gust speeds of up to 55 m/s (198 km/hr). Soon after, in 1925, another overturning accident took place on the Owencarrow Viaduct where strong winds of up to 54 m/s resulted in the derailment of train carriages. The roof of a carriage was completely destroyed by the accident, which resulted in four fatalities (Baker et al., 2019). A relatively recent accident occurred in 2002 near Uttendorf, Austria where a light commuter train was blown over by a 30 m/s (108 km/hr) wind gust, as shown in Figure 1.1.

Figure 1.1: A photograph of an overturned passenger train near Uttendorf, Austria in 2002 due to crosswinds with a gust speed of 30 m/s (Thomas, 2013).

Although the occurrence of wind-related accidents in the railway industry are rare, passenger safety cannot be compromised on. Therefore, it is important to understand the flow fields which develop around trains under crosswinds and thereafter, if necessary,

implement measures, such as speed control or adjustments to the surrounding infrastructure, to improve the safety and the stability of high-speed trains.

For a number of years, considerable attention has been paid to the issue of crosswinds affecting high-speed trains (Cooper, 1979; Matschke and Schulte-Werning, 1997; Fujii et al., 1999; Cheli et al., 2010; Hemida and Baker, 2010; Baker et al., 2011). These researchers have investigated the different factors which trigger vehicle instability under strong crosswinds. Tomasini et al. (2015) put forward the view that two approaches can be adopted to overcome the risks caused by crosswinds. One method is to impose strict regulations on the speed of the vehicles while the other method deals with installing wind barriers. Often referred to as wind fences or windbreak walls, these are usually built along the railway line, beside the tracks, where strong crosswinds are expected (Schulte-Werning et al., 2002; Bocciolone et al., 2008; Zhang et al., 2013; He et al. 2014) in order to reduce the effect of crosswinds on the stability of trains while ensuring passenger comfort.

Analysis of existing studies on the aerodynamics of windbreak walls has demonstrated that those with continuous geometries are more actively researched compared to discontinuous geometries. Installing windbreak walls is deemed effective if the wind barrier is built entirely parallel to the track. Whereas, in reality it is not possible to develop an entirely uniform and continuous windbreak structure due to possible complexities in the surrounding terrain such as cuttings, which cannot be avoided. The windbreak wall would therefore consist of a discontinuous structure with a series of transition regions. Transition regions refer to the specific design implementations on a windbreak wall to tackle different topographies and terrains that exist along the railway lines; essentially deviations in the structure from the generalised continuous form parallel to the railway

4

track. For instance, in China, the Lanzhou–Xinjiang high-speed railway line consists of a section which passes through a mountainous region where strong winds are expected. Due to these strong winds, a windbreak wall has been created. However, the mountainous region means that the railway line has to face several embankments and cuttings (Liu et al., 2018). This results in transition regions in the design of the windbreak wall, as illustrated in Figure 1.2. Such transition regions provide an additional sudden wind load on the train under crosswinds, which can further lead to a sudden deterioration in the aerodynamic performance of the train (Wu et al., 2015, 2017; Zhang, et al., 2019). Understanding the aerodynamic flow which exists around a train surface due to the presence of different kinds of windbreak walls, mainly ones with transition regions is important. Based on a detailed literature review, there are very few available studies that address this issue and are also backed by experimental validation.

Figure 1.2: Part of the of Lanzhou–Xinjiang railway line, comprising of a transition region in the windbreak wall (Chen et al., 2021).

1.4 Aims and objectives

The main aim of this research was to characterise the aerodynamic flow around a passenger train running along a windbreak wall subjected to crosswinds and investigate how transition regions in the windbreak wall affect the pressure distribution and magnitude of aerodynamic forces experienced by the train. To accomplish this aim, an experimental and numerical study was carried out on a 1:25 scale model of the Class 390

Pendolino train. A series of detailed research objectives were set to achieve this aim. These are:

1. Carry out a thorough literature review on the aerodynamics of passenger trains, mainly under crosswinds, and the effects of windbreak walls, in order to form a general understanding of the topic. In addition, to identify gaps in the current state of knowledge.

2. Develop a static scale model of a Class 390 Pendolino train with an appropriate Standard Track with Ballast and Rail (STBR) (as described in chapter 3) and different shapes of windbreak walls to operate at the University of Birmingham's wind tunnel facility for the experimental tests.

3. Develop a suitable test methodology and undertake wind tunnel experiments at different crosswind angles with and without different windbreak walls to measure surface pressures on the model train through the use of a Multi-Channel-Pressure-System.

4. Analyse the results obtained from the wind tunnel to investigate the flow fields that develop around the train and to aid in the selection of a case for the numerical simulations.

5. Develop CAD models which best represent the real geometry of the model-scale train, STBR and windbreak walls.

6. Based on the outcomes of objective 4, undertake a numerical study on a stationary Class 390 model-scale train subjected to crosswinds at a representative yaw angle with a windbreak wall consisting of a typical transition region. Validate the initial numerical results obtained through the experimental data achieved earlier.

7. Based on the outcomes of objectives 4 and 6, expand the numerical work to carry out simulations that assess the relative movement of the model train.

8. Discuss and quantify how a windbreak wall can improve the aerodynamic performance of a train under crosswinds while providing an interpretation on the aerodynamic flow around stationary and moving trains with and without windbreak walls.

1.5   Thesis structure

The structure of the thesis and content of the sections are organised as follows:

Chapter 2 presents a review of the relevant literature by first providing a detailed background on the aerodynamic flow around trains. This includes reviewing literature on the slipstreams around different regions of high-speed passenger trains without any crosswinds. Furthermore, the chapter presents a critical review on the methods of analysis currently undertaken by different researchers to investigate the aerodynamics of trains under crosswinds. The chapter then provides a review on the aerodynamic effects of windbreak walls and identifies the research gaps in the literature. Identification of the literature gap assists in defining the research aim of this novel study.

Chapter 3 describes the experimental and numerical methodologies adopted in this investigative research to determine the non-dimensional aerodynamic coefficients (pressure, force and rolling moment) of the model-scale Class 390 train under crosswinds with and without different shapes of windbreak walls. The methodologies adopted are in line with those currently prescribed in various railway standards (EC, 2008; RSSB, 2009; CEN, 2018). The chapter provides a description of the wind tunnel facility where the experimental work was performed while further providing details on the flow

characterisation inside the facility. The chapter then introduces the scaled model along with the motivation and development of the model design while elaborating onto the relevance of the chosen model in relation to this study. The experimental setup and the different test cases which were examined in this study were discussed along with the experimental procedure adopted. Next, the chapter discusses the numerical methodology adopted for all the numerical simulations by introducing the computational geometries, meshes, domain, boundary conditions and the numerical method used.

Chapter 4 provides a detailed discussion on the results of the mean non-dimensional surface pressure distribution and the aerodynamic load coefficients on the train for the different test cases assessed experimentally at the University of Birmingham's wind tunnel facility.

Chapter 5 provides and discusses the results obtained from the numerical simulations carried out on a stationary Class 390 model-scale train subjected to crosswinds at a yaw angle of 90° with a windbreak wall consisting of a transition region of 45° transition angle. The chapter provides the verification on the accuracies of the simulations carried out through a mesh sensitivity analysis along with the comparison of the numerical and the experimental results. An analysis on the streamline patterns developed from the time averaged velocity field is provided in this chapter along with the time-averaged surface pressure patterns. Further, analysis on the time-averaged velocity patterns and the flow properties is also provided.

Chapter 6 presents a discussion on the results obtained from the numerical simulations carried out on a moving Class 390 model-scale passenger train subjected to crosswinds with a windbreak wall consisting of a 45° angled transition region at a yaw angle of 15°. The chapter studies the influence of crosswinds across the specified transition region on

a moving passenger train by providing an in-depth analysis on the flow behaviour which exists around the windbreak wall and the subsequent effects of a moving train on the wind flow induced by a change in the windbreak wall geometry.

__Chapter 7__ presents a discussion on the comparisons of flow structures around the stationary and moving train and discusses whether the methodology for simulating stationary trains is adequate for moving trains or not, thus discussing the importance of considering the relative motion of the train and the windbreak wall.

__Chapter 8__ summarises the key findings of this research, provides the research novelties, and discusses recommendations for further works.

__Appendix A__ presents a full set of surface mean pressure coefficient distributions for the leading car of the Class 390 model-scale train analysed in this study for a single case, along with a discussion of the experimental uncertainty associated with the data obtained from the wind tunnel tests. An analysis of the total error is demonstrated for assessing the accuracy of results presented in this study.

CHAPTER 2: Literature review

Some of the sections in this chapter have been published in Hashmi et al. (2019).

2.1 Introduction

This chapter presents a review of the relevant literature by first providing a detailed background on the aerodynamic flow around a bluff body, before focusing on vehicles. Section 2.3 includes reviewing literature on the slipstreams around different regions of high-speed passenger trains without any crosswinds. Thereafter, the chapter reviews the effects of crosswinds, in section 2.4. Section 2.5 provides an understanding on the rail vehicle dynamics, explaining the different aerodynamic forces and moments acting on a typical rail vehicle. Section 2.6 lists the commonly used techniques for investigating train aerodynamics. The chapter then continues to present a critical review on the methods of analysis currently undertaken by different researchers to investigate the aerodynamics of trains under crosswinds, in section 2.7. Once the issue of crosswinds affecting the stability and safety of trains is realised, the chapter proceeds to provide a review on one of the possible solutions to this problem; the installation of windbreak walls, in section 2.8. Section 2.8 draws together knowledge from earlier studies focused on understanding the aerodynamic effects of windbreak walls. This assists in identifying the research gaps in the current literature while providing the foundations for this experimental and numerical study on a high-speed passenger train with different designs of windbreak walls.

2.2   The flow around a solid body

The existence of highly turbulent fluid flows in the vicinity of moving objects makes it crucial to investigate the cause of such turbulent flows. Turbulent flows are described as irregular and chaotic flows where each quantity of the flow behaves in a random manner with respect to time and space coordinates (Hinze, 1976). The following section presents the notion of how turbulent flows develop and interact around solid objects.

2.2.1   Wall turbulent shear flow

Hinze (1976) described the result of the presence of a solid boundary as the effect known as wall turbulence in the flow of a fluid. Figure 2.1 shows how the velocity of a flow develops from zero at a solid boundary to a maximum at height δ.
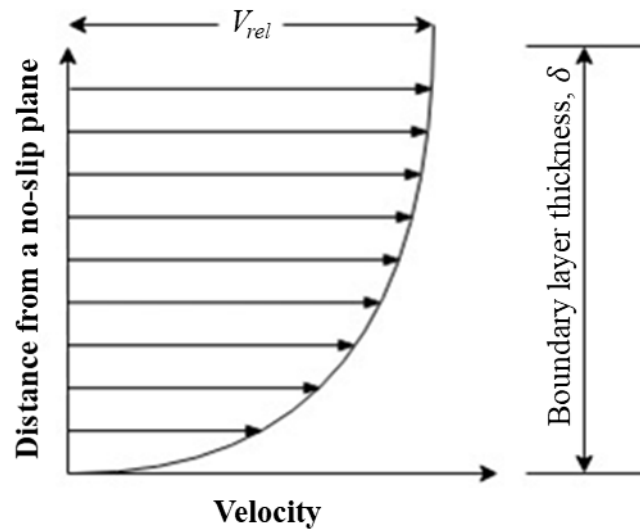
Figure 2.1: The variation of velocity with height for a typical boundary layer where the velocity in the boundary layer approaches the free stream velocity asymptotically (Adapted from Douglas et al., 2011).

A bluff body experiences much larger pressure drag components compared to skin friction drag; this is due to large flow separations which create drag due to a leading edge separation when placed in a flow medium (Cooper, 1993). Skin friction drag is a result of the viscous shearing between the solid body surface and the layer of fluid existing immediately above it. This is important for solid bodies that are long in the fluid flow direction as compared to their height. Andersson et al. (2009) stated that viscous forces and shear stresses influence the fluid molecules, which are present near the surface of a solid boundary. Friction at the surface of a solid body results in the fluid molecules being attached to the surface. This creates the no-slip condition and therefore the fluid velocity is zero at the wall surface but increases rapidly afterwards, reaching up to the free stream velocity. The fluid layers above the solid body surface are in constant motion and as a consequence, shearing takes place between the fluid layers. The wall shear stress can be expressed as the force per unit area applied by a solid boundary on a moving fluid in a direction on the local tangent plane. As mentioned above, this results in the velocity of the fluid increasing with height from the solid boundary, as shown in Figure 2.1. The resulting layer formed is known as the boundary layer (Douglas et al., 2011). The thickness of the boundary layer, δ, is defined as the distance required for the fluid velocity, u, to attain 99% of the free stream velocity, V_{rel}. The Reynolds number of the flow for such cases is given as,

$$Re = \frac{V_{rel}.l}{v} \qquad (2.1)$$

where V_{rel} is the free stream velocity, l is the characteristic length and v is the kinematic viscosity.

At lower Reynolds number, the viscous forces dominate over the inertial forces, thus, the boundary layer is laminar (layered) whereas at higher Reynolds number, it is turbulent (disordered). This indicates that at a particular distance from the leading edge at the same given velocity and viscosity, the flow will become turbulent.

For laminar boundary layers, the streamwise velocity tends to change uniformly with distance from the solid boundary while for the turbulent boundary layers, the flow velocity increases in a non-linear manner. The fluid flow is highly ordered in the laminar boundary layer and thus it is possible to identify streamlines along which a particle moves. A transition region lies between the laminar and turbulent regions. As the fluid approaches this transition zone, it tends to become more irregular. In turbulent flows, there exists a three-dimensional motion of particles and the streamlines do not remain parallel (Andersson et al., 2009). The three different regions of the boundary layer with different behaviours are shown in Figure 2.2 where the growing boundary layer can be noticed in the flow direction.
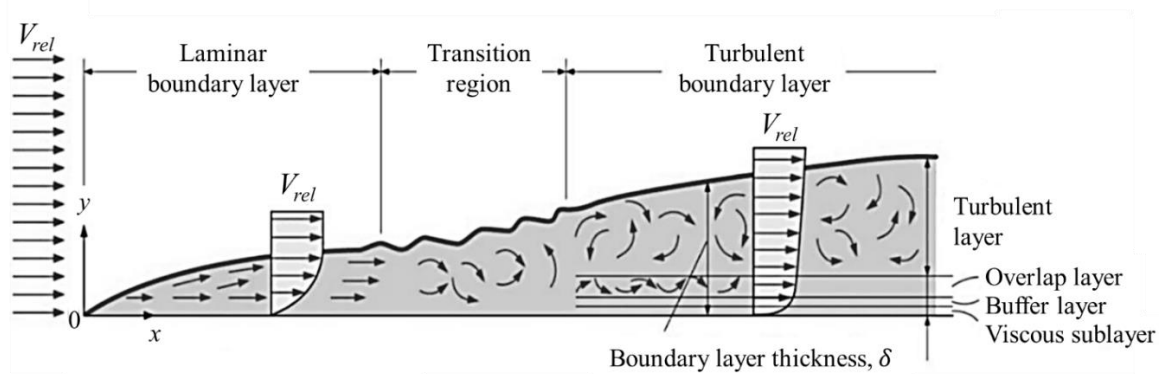
Figure 2.2: A boundary layer development with no-slip condition for flow over a thin flat plate, and the different flow regimes (Adapted from Cengel et al., 2008).

There is an overwhelming evidence for the notion that for long surfaces, the boundary layer is turbulent over most of the surface length (Andersson et al., 2009). A turbulent flow consists of two main regions, the inner and the outer regions (Cebeci and Smith,

1974). The inner region has a thickness of about 20% of the overall boundary layer thickness, δ. This region can be categorised into three sub-layers: a viscous sub-layer, a buffer region and a fully turbulent region. The viscous sub-layer is a very thin layer, which is present at the wall surface where mean velocities are zero and the flow is predominantly viscous. The buffer region consists of a partly viscous flow, which is also partly turbulent with some inertial effects that are in the order of the viscous effects. Lastly, the fully turbulent region exists where the fluctuations produce Reynold stresses that completely dominate over the viscous effects (Duncan et al., 1970). Turbulence frequencies with a wide spectrum are found in this region while the larger low frequency eddies exist farther away from the surface. The larger eddies extract energy from the mean flow and pass it on to smaller eddies. The smallest eddy dissipates the energy as heat and thus belongs to the dissipative scales. The dissipation phenomenon takes place due to the action of viscosity. Moreover, the eddy shear stress is maximum in this region whereas it is roughly constant near the surface (Duncan et al., 1970). For the turbulent boundary layer, Figure 2.3 below illustrates the velocity profiles for the sub-layers in the inner region by providing a plot of the non-dimensional parameters.
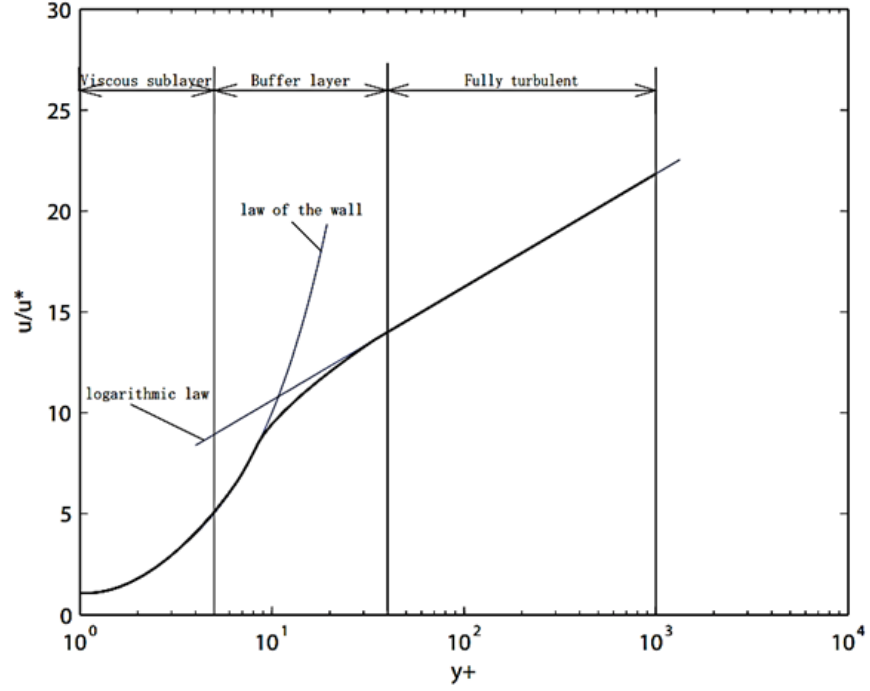
Figure 2.3: Velocity profiles in the different regions of a turbulent boundary layer
(Andersson et al., 2009).

The dimensionless length, y^+, used to define the characteristics of a turbulent flow in a boundary layer, is denoted as,

$$y^+ = \frac{yu^*}{v} \tag{2.2}$$

where y is the distance normal to the surface, u^* is the frictional velocity and is given as

$u^* = \sqrt{\frac{\tau_w}{p}}$ where τ_w is the wall shear stress and p is the density, while v is the kinematic

viscosity.

As shown in Figure 2.3, the velocity profile demonstrates a varied trend. In the viscous sub-layer, the viscous shear stresses are dominating, while there is no evidence of the eddying nature of the flow. Whereas for the fully turbulent layer, as the name suggests, the turbulent (Reynolds stresses) forces are dominating. In the buffer layer, the velocity

15

distribution is neither linear nor logarithmic with the existence of both, viscous and turbulent forces (Andersson et al., 2009).

The outer region represents about 80% of the boundary layer thickness, while the remaining belongs to the inner region. Upon reaching the free stream, the flow at any particular point becomes intermittently turbulent and thus, the shear stresses are relatively low in this region.

2.2.2 Flow around curved surfaces

The turbulent flow around a curved boundary is classified as a complex shear flow (Lakshminarayana, 1986). The streamline curvature not only introduces an extra strain rate but also causes velocity gradients to exist. The turbulent structure of the shear layers experiences large changes as boundary layer effects are additional to the streamline curvature effects. Moreover, a study carried out by Bradshaw (1969) can be used as an evidence to demonstrate that the flow around a body consisting of geometric curves, such as most aerodynamically considered transport vehicles, will be influenced by its shape. Curved streamlines of a mean flow may lead to energies being transferred between the mean flow and the turbulent motion. This would be comparable to the energy transfer by buoyancy forces in a stratified flow.

It has been observed that due to a body's curvature, different results are produced for the flow field along the concave inner face as compared to the flow field along the convex face (So and Mellor, 1973; Meroney and Bradshaw, 1975; Muck et al, 1985; Kim and Rhode, 2000). Furthermore, the results obtained from these extensive research studies also show that the wall shear stresses are larger on concave surfaces as compared to convex surfaces.

16

2.3 Train slipstreams

Slipstreams are created around a moving train as induced air gets dragged due to fluid viscosity and the formation of the boundary layer. These slipstreams usually start to begin ahead of the front of the train and continue along the entire length of the train while extending further in the wake of the flow (Soper, 2014). However, slipstream measurements might be taken at different locations depending upon the speed of the observed train and other research factors. Temple and Johnson (2003) elucidate that airflow is usually in the direction of train travel. However, there exist lateral and vertical components as well, which will be discussed later.

General public such as passengers standing at platforms are well aware of the notion of slipstream, often referred to as air turbulence, as train slipstream effects can be quite drastic. People standing at platforms experience strong wind gusts every time a train passes by. The strength of these slipstream gusts is mostly dependent upon the train speed, atmospheric wind speed and direction, and shape of the train (Pope, 2006). Nevertheless, around many parts of the world, there is an increasing trend of employing high-speed trains, which operate at speeds as high as 320 km/hr. Aerodynamic effects increase with an increase in train speed thus exerting significant forces on objects subjected to train slipstreams. Peak gusts may occur at several different points on a train. As Baker and Sterling (2009) explained, the highest peaks are found to be at the trackside where the flow is significantly affected by the unshielded wheel sets. Additionally, peak slipstream velocities can also arise at different positions along the train length. Train slipstreams are considered as highly turbulent and non-stationary flows, mainly influenced by pressure and velocity transients. The largest slipstream velocities for a freight train can be found in the boundary layer region whereas for passenger trains these are produced in the near

wake region (Baker and Sterling, 2009). This clearly shows how different train shapes affect the aerodynamic characteristics of the flows around trains. Along with experiencing fairly high drag, inadequate aerodynamic modification and sparse container loading of freight trains can encourage quick slipstream growth, producing large velocities at trackside. These are usually larger than those of high-speed passenger trains (Figura-Hardy, 2005; Sterling et al., 2008; Soper, 2014).

Several publications have appeared in recent years documenting the flows around passenger and freight trains. Some of these studies have been performed and carried out under the rail authorities in association with vehicle manufacturers, who help gather experimental and numerical data with the aim of quantifying flows (Baker et al., 2001; Temple and Johnson, 2003; Sterling et al., 2008; Soper, 2014). It is evident from such studies that dividing the flow fields into four different regions can be an easier way to investigate flows around trains. The four flow regions are:

- Upstream and nose region

- Boundary layer region

- Near wake region

- Far wake region

Each of these regions are discussed below with Figure 2.4 provided as a simplified sketch showing these regions, in order to form a better understanding of the fundamental nature of flow around trains.

```
Upstream                                              Near
and nose              Boundary layer                  wake        Far wake
  |←————→|←————————————————————————————————————————→|←——→|←——·········
     ▬▬      ▬▬      ▬▬      ▬▬      ▬▬

                        ←————
                   Direction of travel
```
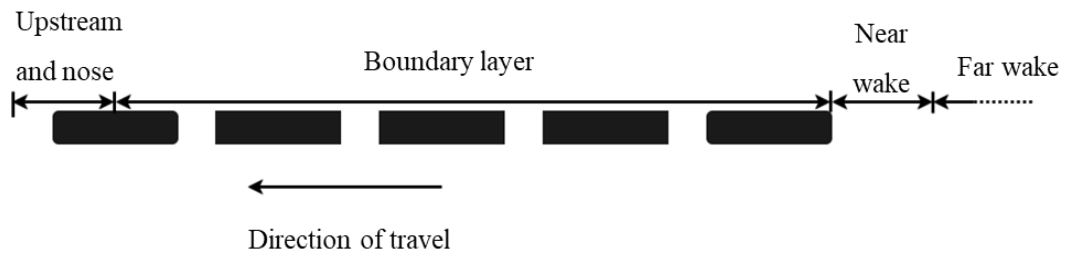
Figure 2.4: Schematic illustration of the different flow regions around a train (Adapted from Flynn, 2015).

2.3.1 Upstream and nose region

The nose region of the train extends from the upstream of the train to about 10 m behind the nose. It has been repeatedly reported in the literature that this region is usually characterised by a large velocity peak indicating an increased flow velocity in front of the vehicle. This leads to a localised velocity peak at the nose of the train. Baker et al. (2001) added that there are large flow accelerations specifically around the nose region of the train as compared to other regions.

In terms of pressure variations around the nose region, Baker et al. (2013a) compared pressure pulses from full-scale and Transient Aerodynamic Investigation (TRAIN) rig experiments around an observed train. The TRAIN rig is a purpose built facility for measuring the aerodynamics of scale moving model vehicles. The results obtained showed a static pressure fluctuation in the area around the nose of the train. A large positive peak was immediately followed by a negative peak in pressure. The magnitude of these peaks is dependent upon the flow separation at the nose of the train (Soper, 2014). Baker (2014a) stated that this is a common characteristic of most trains and similar results have been obtained through a number of different experiments (Soper et al., 2013). It was noted in Alam and Watkins (2007) that a minor interruption in the upstream region of the

airflow is capable of generating fluctuating pressure differences on the train thus causing the train containers to vibrate laterally.

Moreover, it has also been presented that there are large peaks in horizontal velocity around the nose of the train (Baker et al., 2013a; Soper et al., 2013; Baker, 2014a). These large peaks are caused due to obvious velocity variations in both x and y directions. Therefore, it can be assumed that the flow around the upstream region of the train is mainly inviscid and exists in a three dimensional form with low turbulence levels (Sanz-Andrés and Santiago-Prowald, 2002; Sanz-Andrés et al., 2003; Baker, 2014a).

2.3.2 Boundary layer region

Highly turbulent flow regions can be expected around the sides of trains. These can be expressed as turbulent gusts within the boundary layer. The development of boundary layers is usually observed along the nose and tail regions of the train i.e. along the majority of the train length. As Baker et al. (2013a) mentions, boundary layer thickness is a parameter that is dependent upon a number of factors such as the shape of the nose of the train, number of carriages in a train, the gap between each carriage and the surface roughness. However, it must be noted that for high-speed trains, a stabilised boundary layer reaches equilibrium along the first carriage and grows steadily from there onwards (Baker et al., 2001).

Previous experimental studies performed on the boundary layer region of different types of trains show that the flow around this region is recognised as three dimensional and the size of the boundary layer is comparable with the width, height and the length of the train (Sterling et al., 2008; Baker, 2014b; Soper, 2014). Also, there is a steady increase in the slipstream velocities followed by pressure and velocity transients (Flynn, 2015).

The results of an experimental work performed by Sterling et al. (2008) showed the boundary layer parameters and turbulence characteristics for an observed train. The data yielded by this study provided strong evidence on the increase of the displacement thickness, a parameter which is used in train slipstream analysis as an approximation of slipstream thickness, along the train length. However, the level of increase was seen to be different at full-scale testing and model testing. This might be due to some form of expected flow disturbance at the nose of the train in a full-scale test. Moreover, the results of this study suggested that the turbulence intensity is almost constant along the train.

A study by Baker et al. (2001) concluded that the main difference in the flow fields around the side of the train and along the roof of the train is the rapid growth of the boundary layer on the side of the train. Further CFD studies show that turbulence is often generated in areas with geometric discontinuities on the trains, such as bogies, inter-carriage spacing and body corners of the train (Hemida et al., 2014).

2.3.3 Wake region

As stated earlier, peak slipstream velocities occur in the near wake region of high-speed trains. Thus, in order to enhance the understanding of flow around trains, it is important to study flow structures of the wake- the near and far wake regions of a train.

The wake region comprises of a system with inclined trailing vortices, which occur due to the rolling up of the separated shear layers on the leeward side of a model train. These vortices then proceed to form on the roof and the bottom of the train while moving away from the vehicle as the vehicle elapses (Baker, 1991).

Depending upon the aerodynamic shape of a train, most complex flows with coherent flow structures occurs in the near wake region of the train. These flows appear in regions

with complete instability thus causing regular vortex shedding (Bearman and Obasaju, 1982; Lyn et al., 1995; Haque et al., 2014). The flow can take several forms and the pressure variations in this region show the opposite trend to the nose region- that is the pressure curve shows a negative peak followed by a positive peak. Also, the static pressure magnitudes of these peaks are less severe than the nose peaks.

According to Baker (2014), there lies little evidence of flow behaviour around blunt ended trains with an indication of large scale separation. However, for streamlined trains the flow behind the trains suggests the presence of a pair of unsteady longitudinal trailing vortices (Bearman, 1997). This is also verified in Baker (2010). As a result, high velocities can be expected in the train's wake region. Furthermore, it is discussed that the highest transient slipstream velocities are usually found in the tail region of the train before they decay into the wake (Baker et al., 2013a; Sterling et al., 2008). In addition, Baker (2010) stated that flow structures, which influence wake patterns are generally dependent upon the tail shape and the flow properties of the boundary layer. Therefore, some particular train designs can lead to a reduction in the intensity of vortices. Moreover, Sterling et al. (2008) explained that peak velocities are not present in the near wake region of a freight train. This flow mechanism is due to the absence of the trailing vortices, which are a result of the different geometry of freight containers not consisting of the rear sloped roofs.

The far wake region as shown in Figure 2.4, falls long after the train has elapsed. Although the flow in this region is still triggered by the train motion, Baker (2014a) showed that there is less pressure fluctuation and a gradual decrease in the flow velocities in this region. The gradual decay depicts the trend of the lateral spread of the wake.

2.4 Crosswinds

For several years, great effort has been devoted to the research on the effects of crosswinds on the flow around trains. These studies mainly concentrated on the inherent risks of rail vehicles' overturning and track instability (Gawthorpe, 1994; Sima et al., 2004; Alam and Watkins, 2007; Baker and Sterling, 2009; Hemida and Krajnovic, 2009). The pressure distribution and aerodynamic forces of rail vehicles running under crosswinds are dependent upon a number of different parameters, which are associated to the vehicle and the surrounding wind characteristics. These variables are listed as follows (Baker, 1991; Diedrichs, 2006):

- The reference area and height
- Vehicle's speed
- The air density and viscosity
- The wind speed and its standard deviation
- The wind angle relative to the vehicle's direction of travel
- Turbulence intensity and length scales

Hemida (2006) indicated that when trains travel at high-speeds in a crosswind, the effective crosswind component is very strong. To elaborate, the effective crosswind is the resultant of the train speed and the crosswind speed as shown in Figure 2.5a, where ψ is the yaw angle. This is discussed further in sections 2.4.1.2 and 2.4.1.3.

Figure 2.5: Vector diagram of wind and train velocities for (a) a moving train and (b) a stationary train, subjected to crosswinds.

The yaw angle is defined as the angle between the centreline of a train and the mean direction of the wind. The value of the yaw angle is dependent upon the train's travel speed (V_{train}), the crosswind speed (u_{wind}), and the wind direction (β). Typically, the value for such yaw angles is reported to be below 40° for relatively low speed side winds as compared to the speed of the train. However, larger resulting yaw angles might take place due to higher train and wind speeds (Hemida, 2006). Moreover, ground surface roughness can cause an instability and fluctuation in the vertical wind speed profile due to the development of boundary layers. However, train certifications often assume a constant vertical velocity profile (European Rail Agency, 2008).

Modern day trains are designed to be light in weight so that they can offer high acceleration while reducing energy requirements. Under strong crosswinds, a stagnant region with high pressure is formed on the streamwise side of the train. On the leeward side of the train, a low pressure region forms due to the recirculation of the wind flow. The impacting wind flows from the top of the train, over the roof, cause a region of low pressure on the upper side of the train. These pressure fluctuations are responsible for causing the trains to experience strong aerodynamic forces along with moments resulting from side and lift forces. Such circumstances can result in the derailment or overturning of high-speed trains (Hemida, 2006).

A train can potentially overturn under strong crosswind influence due to high wheel unloading. There have been several incidents in the recent years reporting the derailment of trains or overturning in some cases (Sima et al., 2004; Baker and Sterling, 2009). In addition to safety being a major critical issue for trains under crosswind influence, it must be noted that turbulent crosswinds can also cause comfort issues by providing passenger discomfort leading to a loss in ride quality. This is because high crosswinds can cause

24

specific vibration modes to be excited, which lead to strong lateral vibrations in the train thus causing the violent shaking of trains (Baker, 1991). Moreover, Cooper (1984) and Copley (1987) stated that although the danger of an occurrence of any catastrophic event based on the effects of crosswind impact is rare, there are chances that the frequent forces which hit the vehicle may lead to a temporary loss of control. While modern day trains are designed to provide comfort on a rough track with the provision of an adequate train suspension, it must be noted that the design of suspension systems is highly affected by an increase in the vehicle speed and resulting aerodynamic forces (Cooper, 1984).

A plausible solution to overcome such issues is to carefully adjust the train design. It is often claimed that the external vehicle shape has a huge influence on the vehicle performance. Therefore, to improve the vehicle stability as well as combat wind resistance, it is usually necessary to revise train designs. A key limitation of previous research studies is that these just concentrated on the vehicle's response to crosswinds and did not address the main issue which was to comprehend the flow fields that develop around trains under differing crosswind conditions. Understanding of flow mechanisms around a train along with the studies of impact of crosswinds on the train surfaces is extremely crucial. These need to be understood completely in both, the instantaneous and time-averaged flows.

Much research has been performed on the unsteady flows around trains primarily focusing on the measurement of some basic parameters (Copley, 1987; Chiu & Squire, 1992; Chiu, 1995; Hoppmann et al., 2002; Baker, 2003; Suzuki et al., 2003; Baker et al., 2004; Hemida and Krajnovic, 2010). These studies involved measuring parameters such as drag, lift and side force coefficients. Also, investigating the natural wind characteristics has been one of the main aims of such studies. Alternatively, other researchers made use

of numerical ways to analyse flow structures and investigate flow behaviour around trains (Diedrichs, 2003 and Khier et al., 2000).

2.4.1 Effects of crosswinds

The impact of crosswinds on trains may vary in incident levels, magnitude and duration. The effects of such crosswinds on rail vehicles are numerous. Not only do crosswinds cause a disturbance in the flow symmetry around trains (Khier et al., 2000), they also contribute an increase in the energy consumption of the vehicle while enhancing the slipstream effects on the leeward side of the vehicle. In addition, these crosswinds are strong enough to alter the aerodynamic lift of a pantograph. Furthermore, the crosswinds can cause an impairing effect on the infrastructure of the rail system causing a swaying motion of a catenary. Crosswinds can also affect rail systems by causing trees which are situated in the vicinity of the railway track to fall and block traffic (Diedrichs, 2003). Mean ambient winds are usually described by a standard logarithmic profile, which is discussed as follows.

2.4.1.1 Relative crosswind profile

In order to study the crosswind effects on train slipstreams, it is important to understand the characteristics of natural wind, which flows over a rail vehicle. Friction on the ground results in ambient wind speeds to be much slower as compared to wind speeds farther from the earth's surface. Near the ground, the ambient wind induced by local topography is highly turbulent and sheared.

An atmospheric boundary layer (ABL) is developed in the region closer to the earth's surface and can be approximated by a logarithmic velocity profile. This has been discussed earlier in section 2.2.1 and is shown in Figure 2.1. The logarithmic mean

velocity profile, which is a well-known solution of Prandtl, is defined as follows (Blackadar and Tennekes, 1968):

$$\overline{u_{wind}}(z) = \frac{u_*}{\kappa} ln\left(\frac{z}{z_o}\right) \tag{2.3}$$

where $\overline{u_{wind}}$ is the mean velocity profile representing the mean flow in the streamwise direction, u_* is the surface friction velocity, κ is the Von Karman constant, z is the height above the ground and z_o is the surface roughness length.

Turbulent fluctuations are dependent on time and position. The mean of such fluctuations is zero by the process of Reynolds decomposition (Reynolds, 1895). Turbulence can be defined by the turbulence intensity I, as the ratio of the standard deviation of the velocity fluctuations $\sigma(z)$, to the mean velocity $u(z)$ (Baker, 2014a),

$$I(z) = \frac{\sigma(z)}{\overline{u_{wind}}(z)} \tag{2.4}$$

Turbulence intensities depend upon surface topographies and diminish as height above a surface increases.

2.4.1.2 Crosswind relative to a moving vehicle

For a typical moving rail vehicle such as a high-speed train, the wind velocity relative to the train can be defined as the resultant of the onset wind velocity and the train speed, as demonstrated in Figure 2.5a, which illustrates a simplified vector diagram of a moving train in natural wind.

The resultant wind velocity relative to a train is given by:

$$V_{rel} = \sqrt{[\overline{u_{wind}}(h)sin\beta]^2 + [V_{train} + \overline{u_{wind}}(h)cos\beta]^2} \tag{2.5}$$

where $\overline{u_{wind}}(h)$ is the mean velocity at a reference height h, usually considered as 3m (Baker and Sterling, 2009; Dorigatti, 2013), V_{train} is the train speed and β is the natural wind angle.

The angle of the wind relative to the train is defined by the resultant yaw angle ψ as,

$$\psi = arctan\left(\frac{\overline{u_{wind}}(h)sin\beta}{V_{train} + \overline{u_{wind}}(h)cos\beta}\right) \tag{2.6}$$

Measurements for natural wind velocities around a train are carried out in the uninterrupted upstream flow region of the train. This is done to avoid the effect of train slipstreams.

As mentioned earlier, an ABL shows a logarithmic velocity profile near the ground. According to Equations (2.2) and (2.4), the resultant wind velocity, V_{rel}, can be considered as a skewed logarithmic profile. Also, it is important to study the wind characteristics just as observed by a moving train. This statement is based on an investigative study carried out by Baker (2010) on the effects of natural wind in regard to a moving train. In this work, a moving train was assessed over a flat ground with a surface roughness length, z_o, of 0.03m. Train speeds were varied while a logarithmic wind profile with a wind angle normal to the railway track was assumed. Crosswind speeds of 20 m/s were measured at 3m above the ground level. Baker (2010) then calculated the following parameters, V_{rel}, ψ and I. The results suggested that at lower train speeds, the velocity profile takes the form of a typical ABL. Also, the velocity profile shows a wide range of fluctuating velocity trend with high turbulence intensities along the train height. In contrast, it is apparent that with an increase in train speed, the velocity profile becomes uniform and flatter with a decrease in the effective turbulence intensity (Baker, 2014a).

Moreover, the research performed by Baker (2010) draws a limitation on the wind tunnel testing for freight trains indicating that testing should not be performed in wind tunnels consisting of lower turbulence intensities.

2.4.1.3 Crosswind relative to a static vehicle

In a static train representation, as demonstrated in Figure 2.5b, the vehicle is not moving and therefore the relative wind coincides with the onset wind. As a result, the effect of the yaw angle is determined by changing the relative orientation between the oncoming flow and the vehicle. This is due to the yaw angle being determined by the direction of the onset wind to the track.

2.5 Rail vehicle dynamics

2.5.1 Aerodynamic coefficients

Pressure differences can cause high-speed trains to experience aerodynamic forces and moments. Numerous studies have investigated the surface pressure distribution on a vehicle, such as train, in order to measure the forces acting on such a vehicle under crosswinds (Sanquer et al., 2004; Quinn et al., 2007; Dorigatti, 2013). The surface pressure distribution can be conveniently expressed in terms of the pressure coefficient, C_P as:

$$C_P = \frac{P - P_o}{0.5 \rho V_{rel}^2} \tag{2.7}$$

where P is the actual surface pressure at any point, P_o is the reference pressure, ρ is the air density and V_{rel} is the free stream velocity of the wind relative to the train.

To understand the aerodynamic behaviour of trains, the most important parameters are the pressure and velocity fields on and around trains. These parameters have components in the following directions:

- i: the direction of the velocity component
- X: the coordinate in the direction of travel, measured from the train nose
- Y: the lateral direction, measured from the centre of the track
- Z: the vertical direction, measured above ground level

Figure 2.6 shows the forces and corresponding moments in the X, Y and Z directions with respect to the direction of the crosswinds.
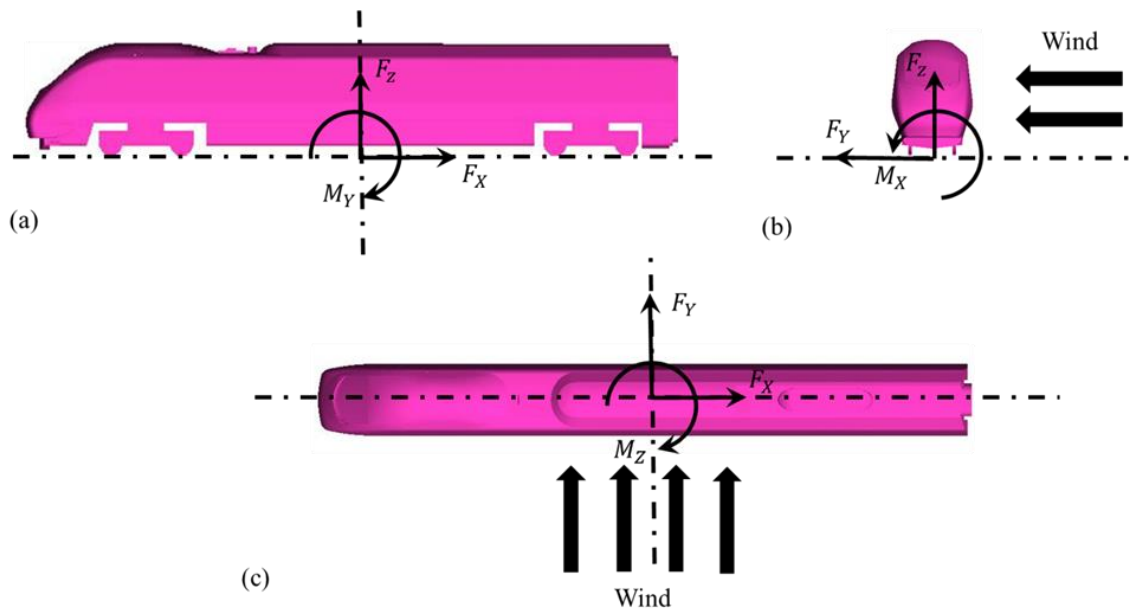
Figure 2.6: The different aerodynamic forces and moments acting on a typical rail vehicle under the influence of crosswinds.

As mentioned earlier, a high-speed train can experience strong aerodynamic forces due to crosswinds acting perpendicular to the lateral side of the train. The aerodynamic forces related to the directional components of a vehicles coordinate system are the drag force (F_X), the side force (F_Y) and the lift force (F_Z). The drag force resists the forward motion

of the train while the lift force causes the train to pitch upwards. The side force is a result of crosswinds, which acts perpendicular to the surface of the lateral side of a train. The combination of side and lift forces are considered to have a major influence on the overall stability of a train, potentially leading to overturning. It is therefore also important to consider the aerodynamic moments. About the X-axis is the rolling moment, M_X, while that about the Y-axis is the pitching moment, M_Y, and that about the Z-axis is known as the yawing moment, M_Z, as demonstrated in Figure 2.6.

These aerodynamic loads that act on a train in terms of the three forces (F_ξ) and three moments (M_ξ) can be defined with respect to the generic axis ξ of the Cartesian reference system (as shown in figure 2.6) adopted in this study as:

$$F_\xi = \frac{1}{2} C_\xi \rho A_{ref} V_{rel}^2 \qquad \text{(with } \xi = X, Y, Z) \qquad (2.8)$$

$$M_\xi = \frac{1}{2} C_{M_\xi} \rho A_{ref} H_{ref} V_{rel}^2 \qquad \text{(with } \xi = X, Y, Z) \qquad (2.9)$$

where A_{ref} and H_{ref} are the reference area and reference height of the train, while C_ξ and C_{M_ξ} denote the non-dimensional coefficients for each component of the forces and moments, respectively. Integration of the abovementioned C_P can help obtain these coefficients.

Baker (1991) added that these aerodynamic coefficients are the basis for providing useful information regarding the aerodynamics of a rail vehicle in crosswind conditions. The size of the aerodynamic forces and the resultant moments is dependent upon the Reynolds number and the shape of the train. Therefore, it is convenient to have a simplified approach for analysing trains with different shapes irrespective of their sizes.

2.6 Techniques of investigation

The evolving trends during the last two to three decades on lighter, more efficient and faster rail vehicles, have led to an increased interest in the aerodynamic studies of trains, particularly as a means of providing mitigation strategies to potential crosswind sensitivities. As noted in comprehensive texts such as Baker (1991), the understanding of the aerodynamic characteristics of the flows around trains was developed as early as 1980s by researchers such as Cooper (1984) and Copley (1987). Up till now, researchers aiming to investigate the aerodynamics of trains mainly running under crosswinds have made use of three major approaches. These techniques are: full-scale testing, physical modelling, and numerical modelling. Out of these three approaches, physical modelling on scaled models is the most widely used option as it is understood to offer the best compromise between time (and cost) effectiveness of the test methodology, practicality when compared to full-scale testing and the precision of the results obtained.

Full-scale tests are quite complex in sense that they require the availability of an actual, properly instrumented train, which can be tested. In addition, a test site availability is crucial for these tests. Full-scale tests are also inevitably subject to unmanageable environmental conditions (Baker et al., 2004; Quinn et al., 2007). Therefore, arrangements for a full-scale test can be fairly challenging. Since these tests are time-consuming as well as expensive (Baker et al., 2009), little full-scale work has been undertaken as compared to physical or numerical modelling (Matschke and Heine, 2002). Physical modelling involving model-scale experiments is known to provide a degree of approximation due to its intrinsic ability to entirely fulfil the Reynolds number similitude criteria (Gawthrope, 1994). The Reynolds number similitude theory offers the theoretical background which supports the ability of model-scale experiments to simulate a real

physical phenomenon correctly. For physical modelling, particular care is required for setting up the experiments and interpreting the results obtained. Nonetheless, physical modelling performed in conventional wind tunnels allows for simulating different incident flow characteristics along with the use of several measurement methods.

Numerical modelling involving the use of Computational Fluid Dynamics (CFD) to simulate numerical cases is perceived as particularly promising by the industry. A certain level of accuracy is ensured through these simulations, based on the associated computational costs. The use of CFD provides the researchers with the ability to extract vast amounts of useful data from a single simulation, which might be either difficult or practically impossible to obtain from model-scale physical tests. Furthermore, in CFD, it is also possible to simulate the correct relative motion between a train and the ground. However, it must be noted that results obtained from CFD simulations require validation from experimental results (EC, 2008; CEN, 2018) due to the technique being still under validation.

2.7 Review of previous investigations on train aerodynamics

As noted in section 2.6, the most widely used option for investigating train aerodynamics is physical modelling involving model-scale static experiments. Even so, researchers in the past have extensively made use of the three main techniques discussed in section 2.6, to investigate vehicle aerodynamics. The following sections provide a review of these three main techniques in relation to investigating train aerodynamics. Although the review briefly discusses each one of them, the application of CFD modelling to train aerodynamics is discussed in detail, consistent with the purposes of the present research

and the major use of numerical simulations in this thesis to investigate the effect of crosswinds.

2.7.1 Full-scale testing

In the investigation of train aerodynamics, full-scale tests are often used as they provide validation against results obtained from physical tests and numerical simulations. Full-scale tests are usually conducted on in-service trains in order to obtain realistic details of the actual moving train.

Full-scale tests have been conducted in the past on different types of trains operating in different countries, such as Spain, Germany, Japan and the UK to evaluate their responses to strong side winds (Matschke and Heine, 2002; Baker et al., 2013a; Baker et al., 2004; Suzuki and Hibino, 2016). One interesting finding presented by Baker et al. (2004) stated that the side force and lift force coefficients of a train tend to be higher in magnitude for trains that are positioned at an angled cant as compared to rail vehicles moving on the ground. Generally, this might be due to an increase in the effective side area and suggests that either the flow over the roof of the train is sensitive to inclination or the variations in the underbody flow conditions can result in such significances. Nevertheless, results for the rolling moment coefficient were found to be analogous to the side force coefficient results. This was as anticipated because the rolling moment around the lee rail is fundamentally determined by the side force. On the whole, the measurement results and analysis of these revealed that the data collected from such full-scale tests can be considered reliable. Obtained test results for turbulence intensity showed no discernible discrepancy with wind speeds. However, the data obtained for wind speeds lower than 5 m/s was very scattered. This might be due to the existence of convective effects in the

approaching flow, imperfections in the positioning of the vehicles or errors in the calibration process of the measuring devices. Overall, this shows that lower wind speeds may result in different aerodynamic results.

Wind tunnel testing was also performed as part of a couple of full-scale studies to determine the accuracy of the wind tunnel tests (Baker et al., 2013a; Suzuki and Hibino, 2016). The researchers found a reasonably good agreement between the full-scale and wind tunnel experimental results for the mean and peak aerodynamic forces and moments coefficients on trains. However, there were discrepancies in the lift force coefficient measurements which probably resulted from local roughness variations in close proximity to the wind tunnel models that cause significant variations in the vehicle's underbody flow. Also, the test results were limited to stationary vehicles only, which means that the effect of moving trains on the aerodynamic force and moment coefficients could not be determined.

Moreover, full-scale tests conducted in the past demonstrated that the flows around high-speed trains are dependent upon the shape of the nose and the tail of the train. The results obtained for trains with a pointed nose showed that the pointiness resulted in the formation of a thinner boundary layer along the lower side of the train while producing sharp increases in the slipstream velocities, in the near wake region of the flow (Baker et al., 2013a). This is probably due to the strong longitudinal velocity components, which result in the development of longitudinal vortices. On the contrary, trains with rounded noses showed a rapid generation of a boundary layer but with a reduced dynamic flow in the near wake region of the flow, which resulted in a negative velocity peak. Likewise, the influence of different train configurations, such as differences in the inter-carriage gaps and bogies, on the flow field that exists around trains has also been studied and the

results have shown that lateral flow variations where longitudinal flows exhibit reverse flows can influence results in terms of the slipstream velocities determined.

Generally, full-scale tests involve real time measurements with no requirements for any modelling assumptions and thus are complex and expensive. They can also be challenging due to site restrictions- promoting safety margins, ambient conditions and the availability of adequate instruments for measurement purposes (Deeg et al., 2008; Sterling et al., 2008; Flynn et al., 2014; Zhu et al., 2016). Also, the conditions of the full-scale tests such as wind speed and direction, turbulence intensity and length scales cannot be controlled. In addition, measurement campaigns in a full-scale test are limited to certain points only and thus the full-scale aerodynamic data acquired is not sufficient to elucidate the entire nature of the flow, which exists around trains. Furthermore, the results obtained may vary from train to train because of slight changes in train geometries and the differences in ambient conditions. Hence, it is proposed to ensemble average the experimental results in order to overcome the issue of fluctuating results (Baker, 2010). To do so, the time histories of pressure and velocity parameters are first determined for several trains. Each parameter is then non-dimensioned, followed by the averaging of results obtained (Baker et al., 2013a). Nevertheless, to conclude, full-scale tests results are still extremely important as they provide realistic data along with overcoming issues associated with reduced Reynolds number testing. These results are also required and are useful in order to provide validation against physical and numerical models.

2.7.2 Physical Modelling

Model-scale experiments are to a certain extent, an effective alternative to full-scale experiments. Model-scale testing is an experimental technique that has been widely used

by a number of researchers. This is because the conditions of model-scale tests can be easily controlled and these tests are simple and economical to carry out, thus are well-known to several researchers (Humphreys and Baker, 1992; Baker et al., 2001; Johnson and Dalley, 2002; Sterling et al., 2008; Gil et al., 2010; Bell et al., 2015; Yang et al., 2017). Model-scale testing can be carried out within two kinds of specifically built facilities. These are the Moving Model Rig (MMR) and the wind tunnel testing. In addition, model-scale experiments can be carried out either using static or moving models or even both (Dorigatti et al., 2015).

2.7.2.1 Moving Model Rig (MMR)

The MMRs are capable of investigating the transient aerodynamic behaviour of moving trains and this experimental technique involves the use of a moving model of a train, which is fired along a test track. This simulates ground conditions accurately but associates model complexity with it. The rigs comprise of a firing mechanism to project the train on the test track, an accelerator, a working region and a braking section. Along with providing highly accurate results as compared to wind tunnel testing, this method also offers precise measurement results for train slipstreams and pressure transients, in open air (Gil et al., 2010; Baker et al., 2013c; Soper, 2014; Yang et al., 2017).

Researchers investigating the flows around trains by carrying out experiments in a MMR have also attempted to study the effects of crosswinds (Baker et al., 2001; Sterling et al., 2008; Soper, 2014). In these tests, the MMRs were used to determine the transient aerodynamics of moving vehicles. Usually, a simple crosswind generator was used to simulate crosswind effects, while hot-film anemometers measured the velocity field around the model. Particle Image Velocimetry (PIV) and wavelength analysis

experiments were also carried out to study the flow structures around trains. Overall, results obtained from the MMRs have shown that the flow around a train can be described in five flow regions: the upstream, the nose, the boundary layer, the near wake and the far wake region, as discussed in section 2.3. Although meaningful results were obtained for velocity fields from these investigations, it was determined that there are severe three-dimensional effects and large flow accelerations in the nose region of the model train. The speed of the model was found to have no significant effects on the experimental results. A rapid boundary layer growth was observed on the sides of the vehicles examined, causing flow differences around the roof and the side of a tested vehicle. It was also revealed that the boundary layer reaches equilibrium along the first car, thereafter it grows steadily along the length of the train. In terms of the effects of the crosswinds, the crosswinds instigated in increasing the velocities of the wake and slipstream regions of the vehicle. A few researchers in the past (Pope, 1991; Humphreys and Baker, 1992 and Baker et al., 2001) have stated that using developed moving model rigs can be a successful approach for precisely simulating and reproducing the relative ground motion between the trains and the surroundings. According to Baker (2014b), the moving rig technique serves as a robust way for effectively determining aerodynamic loadings on a range of trackside structures along with the results possessing a good run to run repeatability. However, model-scale tests are not straightforward to carry out with limited runs allowed per day. Therefore, some of the model-scale tests conducted at MMRs might be considered to have a run-to-run variability.

A recent study by Dorigatti et al. (2015) explored the results achieved from a study based on the physical modelling of a 1/25th scale model of class 390 train. The study considered both, moving models and static models. In terms of the results, significant differences

were observed in the pressure distribution over the nose of the models, for the static and moving model experiments. However, for the remaining train length, similar results were obtained in terms of pressure distribution. Since the study involved the use of an Approximate Flat Ground (AFG) scenario, Dorigatti et al. (2015) suggested the need for further investigation on a more realistic case such as the Standard Track with Ballast and Rail (STBR).

In review of earlier studies, it can be evidenced that model-scale testing in the past has mainly focused on measuring slipstreams and transient aerodynamic pressure loadings with very few focusing on the effects of crosswinds, which suggests the need for further work in this field. Also, a key limitation of model-scale tests is that they are usually carried out indoors, hence the results obtained are not dependent on the surrounding atmospheric conditions such as low wind speeds (Flynn et al., 2014).

2.7.2.2 Wind tunnel testing

While investigating the effects of crosswinds on rail vehicles, wind tunnel tests have been used extensively and several publications have appeared in recent years documenting the methodology used for such tests (Mancini et al., 2001; Sockel, 2002; Alam and Watkins, 2007; Baker, 2014b).

The influence of Reynolds number on the fluid flow around an idealised model of a generic passenger train under strong crosswinds has been studied by some researchers (Copley, 1987 and Hemida, 2006; Bocciolone et al., 2008). For a range of Reynolds number (ranging from 10^5 to 10^6), it was determined that the aerodynamic coefficients of trains were not influenced by the Reynolds number at lower yaw angles. However, comparatively, a slight influence was observed at larger yaw angles. It was presented that

for very low Reynolds number, the flow regime around a train is in the laminar region. In such a case, the flow tends to attach itself to the surface of the train. Conversely, an increase in the flow's Reynolds number leads to the disjoining of the flow on the roof's windward edge of the train. This results in the separation of the flow from the face of the train along with causing the wake region to start shedding vortices, as shown below in Figure 2.7a. Moreover, as the Reynolds number increases further, the flow becomes fully turbulent in all regions i.e. in the wake and the separation region over the roof. However, at a particular Reynolds number, the flow tends to reattach itself to the face, thus forming a separation bubble. This is shown in Figure 2.7b. As Reynolds number increases further, the separation bubble gets supressed allowing the flow over the roof to be fully attached, as shown in Figure 2.7c. Upon the full attachment of flow to the roof, the aerodynamic coefficients of the train are independent of the Reynolds number (Hemida and Baker, 2010).
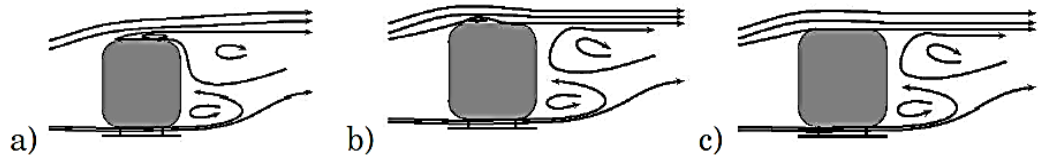
Figure 2.7: Effect of Reynolds number on the flow around trains subjected to crosswinds (Hemida, 2006).

In terms of freight trains, the effects of crosswinds on double-stacked container rail wagons were not well-known according to Alam and Watkins (2007). Therefore, they performed an experimental investigation to study the effects of Reynolds number on the aerodynamic coefficients of the train, which further assisted in evaluating rollover risks for various freight trains. Two $1/5^{th}$ scale models of two different types of double-stacked container wagons were subjected to varying wind speeds and yaw angles in order to

determine the effects of crosswinds. The experimental results revealed that the effect of Reynolds number is negligible for wind speeds over 40 km/h, which indicates that above this wind speed there are insignificant effects on the aerodynamic coefficients of the train. This finding led to the assumption that results for higher wind speeds can be approximated, as the non-dimensional parameters of forces and moments are independent of the Reynolds number. The results also portrayed highly turbulent airflows containing vortices in the leeward side of the model train. Although the flow around the models was consistently turbulent at a range of yaw angles, such as 0°, 45° and 90°, it was noted that the yaw angle of 90° had considerable effects on the flow characteristics. Similarly, it was also observed that a small disturbance in the upstream region of the airflow was able to generate fluctuating pressure transients on the model bearings, thus causing the carriages to vibrate. In terms of the side force, the study suggested that the side force coefficient tends to increase with an increase in the yaw angles up to 75° and after that remains constant. However, a slight variation in the side force coefficient was seen between the two models. This might be due to the additional height of one of the models as compared to the other, which results in an increased side area. Similarly, considering the rolling moment coefficient, the study showed an increase in the magnitude of the coefficient with an increase in the yaw angle, for both the models. However, the rolling moment coefficient for the model with an extra height was relatively smaller as compared to the other model. In terms of the lift force coefficient, both models showed comparable trends, demonstrating an increase in the magnitude of the coefficient with an increase in the yaw angle, up to 30° only. Thereafter, a reduction in the side force coefficient is predictable as with an increase in the yaw angle, the resultant airflow velocity starts to vertically hit the train surface in a downward direction, practically opposite to the lift force direction.

Although the experimental results of this study facilitated in drawing several logical conclusions, the main limitation of this research was that it was carried out in an isolation. In an attempt to further study the aerodynamic characteristics of trains subjected to crosswinds in wind a tunnel, researchers (Suzuki et al., 2003; Baker et al., 2013a) determined that the aerodynamic characteristics of the flow around trains are not only dependent upon the shape of the vehicle but also depend on the sort of infrastructure which exists in the vicinity of trains, such as bridges and embankments. These studies explained that the reason to adopt a uniform flow while neglecting the effect of a boundary layer was due to the fact that the simulated condition in a wind tunnel is more severe than the actual situation. As a result, the side force calculated in a wind tunnel test is much larger than one determined in a real case. Furthermore, results for the aerodynamic characteristics of vehicles on bridges showed that the side force coefficient tends to increase for vehicles with sharp edges. On the contrary, a rounded roof vehicle caused a decrease in the magnitude of the side force coefficient but an increase in the lift coefficient. This is due to a negative pressure area that establishes on the roof of the vehicles. Overall, the use of rounded roofs is recommended as a safer option against strong crosswinds as compared to the edgier roofs. This is because the vehicle is more prone to overturning under the influence of the side force compared to the lift force.

In terms of the results obtained for embankments under crosswinds, it was revealed that the natural wind that hits the embankment, bounces away with a change in its pitch and velocity. These changes were dependent upon the height of the embankment and the wind direction. In order to determine the effects of height of embankments, the height was changed in increments and it was found that the side force coefficient increases with height, being the largest at the greatest height. The rationale behind this trend is that wind

velocity tends to increase more, when around an embankment. Also, as the embankment gets higher, the exposed area above the boundary layer grows, due to its thin thickness. However, at lower heights of the embankment, the effects of boundary layer thickness on the side force coefficient were higher than that at increased heights. The study suggested the need for further research on comparing the results of this study with full-scale tests as it is important to understand the effects of the boundary layers and the aerodynamic characteristics of the natural wind around rail vehicles.

Baker et al. (2003; 2004) also performed extensive research studies on the measurements of the crosswind forces on trains in a wind tunnel to verify the results of the full-scale experiments. In terms of the wind characteristics, the wind tunnel tests had a turbulence intensity higher than that of the full-scale tests. It was then hypothesised that the boundary layer at the actual full-scale field test site was not in equilibrium, presumably due to the local topography of the coastal site. Even so, analysis of the results obtained for the mean and peak crosswind forces and moments showed that there was a realistically good agreement between the full-scale and wind tunnel experimental values. However, there were significant incongruities in the results obtained for the lift force coefficient. The most likely explanation of this discrepant result is the variations in the local roughness in the vicinity of the wind tunnel model, which might have caused such varied results in the underbody flow region of the vehicle. Overall, these results were considered conclusive as it is the rolling moment coefficients, which are of the most practical importance.

Overall, in addition to considering the findings of the abovementioned literature sources, a few key limitations of wind tunnel testing have been revealed. Generally, wind tunnel testing does not address those factors, which can affect the flow fields around trains. For instance, the model of train used in a study based on a wind tunnel experiment does not

move relative to its ground-plane thus the influence of the moving ground on the aerodynamic characteristics of the flow is not known. Whereas, in a real situation, when a train moves relative to its actual ground-plane, there is a growth of a complex sheared flow between the train and the ground. Moreover, the Reynolds number used is of the order of 10^5 for wind tunnel tests, whereas in reality, the Reynolds number for a train is two orders of magnitude, greater than this. The effects of a boundary layer are also disregarded in most wind tunnel studies, with experiments conducted in a flat velocity profile whereas in reality, rail vehicles may experience a range of velocity profiles. Similarly, the effects of long duration gusts and transients are also ignored in most wind tunnel tests. These limitations may mean that the results of a wind tunnel testing are under predicted at times.

2.7.3 Numerical modelling

Advances in computing power have made it easier to study vehicle aerodynamics. Mathematical description of fluid flows relating to motion of different fluids such as air and water, is extremely important in several disciplines concerning industry and academia. Although analytical description of fluid flows is important, it is very crucial to provide numerical solutions to obtain a good understanding of the flow behaviour (Persson, 2015).

CFD is one of most commonly used tools which is capable of providing a proficient way to numerically solve any governing equations related to fluid flow. In given computational domains, CFD has proven to provide numerical solutions to pressure and velocity components at any point with prescribed boundary conditions rather than just at sensor locations. In addition, the method used in CFD calculations is entirely based on

the physical law of Navier-Stokes equation. This makes CFD capable of simulating a number of different types of flows in a variety of applications (Wingstedt et al., 2013; Zhu et al., 2016).

However, simulating turbulent flows can become time-consuming due to the difficulty of solving Navier-Stokes equations related to such flows. Moreover, it is very costly to solve these equations because of the large turbulent scales which need to be considered (Flynn et al, 2014; Zhu et al., 2016). Hence, there are different simulation methods available to solve the flow (Pope, 2000). These are Direct Numerical Simulation (DNS), Reynolds-averaged Navier-Stokes (RANS) and Large-Eddy Simulation (LES).

Direct Numerical Simulation (DNS) is a method of CFD which helps evaluate flows at low Reynolds number along with resolving even the smallest turbulent scales and high frequencies. Such flows entail small time-steps to record their motion and thus are exceedingly computationally expensive (Gatski et al., 1996).

The varying velocity fields produced in a typical turbulent flow can be of both, small scale and high frequency. Therefore, simulating such flows can be computationally very expensive. Instead, another CFD method that could be implemented is the Reynolds Averaged Navier-Stokes (RANS) which is usually used for calculating the mean flow behaviour in complex turbulent flows by time-averaging the Navier-Stokes equations. This method results in a modified set of equations which are computationally less costly to solve. Moreover, this method also helps avoid the challenges of resolving turbulence directly. Averaging the governing equations involves Reynolds decomposition. At this stage, an instantaneous quantity decomposes into its fluctuating and time-averaged quantities. The instantaneous velocity can be substituted by the mean and fluctuating components in the governing equations. This is followed by averaging the terms present

in the resulting equations which results in providing the mean continuity and momentum equations. These equations are referred to as Reynolds-averaged Navier-Stokes equations (RANS). The revised equations attained characterise the mass and the conservation of momentum of the averaged motion. However, a major drawback of this method is the introduction of a turbulent stress tensor known as Reynolds stress tensor (Duncan et al., 1970; Cebeci and Smith, 1974; Pope, 2000). It is a crucial aspect of time-averaged simulations where the altered governing equations are unable to form a closed set, thus requiring further relations. The solution to this closure problem is to define the tensor in terms of its mean velocity. This modelling of the Reynolds stress tensor is known by the eddy-viscosity representation (Duncan et al., 1970; Hinze, 1976). Furthermore, Baker (2014) states that RANS is an ideal methodology for use in the study of more complex shapes such as the nose of the train or in the investigation of the leading cars of the train. Also, this technique is capable of effectively dealing with distorted flows and limited separation regions. Therefore, it could also be used to study the effects of crosswinds at lower yaw angles (Diedrichs, 2003).

Whilst turbulence modelling techniques such as DNS and RANS can help in overcoming turbulent flow issues, an alternative approach is to use Large Eddy Simulation (LES). This approach has gained an increasing amount of popularity due to improvements in computational power which makes this method even more accessible (Tabor and Baba-Ahmadi, 2010). Persson (2015) points out that LES is frequently used today due to its capability of simulating spatially developing flows. To do so, specifying (formulating) inlet conditions is extremely important while performing LES as the fluid turbulence behaviour under study is mostly dependent on the inlet behaviour (Tabor and Baba-Ahmadi, 2010) and thus makes LES an attractive methodology (Castro et al., 2011) which

is capable of resolving large turbulent eddies (Persson, 2015). Methods such as LES decompose the flow structures into larger and smaller scales. They resolve the larger turbulent scales while model the smaller scales using the eddy-viscosity model known as a sub-grid model.

Furthermore, a hybrid technique known as the Detached Eddy Simulation (DES) was proposed in 1997 as a numerically feasible and plausibly accurate approach for predicting massively separated flows. In this DES approach, RANS models are employed in the near wall regions where the flow is attached to the surface, while the LES approach is adopted in the regions where the flow is detached from the surface, i.e. far away from the wall. Usually, the LES region is linked with the core turbulent region where large turbulence scales play a fundamental part. In this region, the DES approach makes use of the LES subgrid models while the respective RANS models are used in the near-wall region (Baker et al., 2019). In order to address the limitations of the original formulation of the basic DES concept, several modifications to the basic DES concept have been proposed. Delayed Detached Eddy Simulation (DDES) was the first enhancement that addressed issues faced by researchers in the original DES concept. DDES model prevented the switch from RANS to LES mode within attached boundary layers solely due to the details of the mesh design. This was achieved by the alteration of the DES length scale to integrate a flow-dependent shielding function which maintained the RANS length scale in the attached boundary layer flow regions. Quite recently, another incarnation of the DES formulation was presented through the Improved Delayed Detached Eddy Simulation (IDDES) variant. Two major enhancements are incorporated to the original DES concept in the IDDES model, which features various blending and shielding

functions that allow using the model for both, the DDES and Wall Modelled LES (WMLES) modes (Gritskevich et al., 2012).

2.7.3.1 The application of CFD to train aerodynamics

The main aim of applying CFD to rail vehicle study is to evaluate the set of aerodynamic loads which are appropriate for the determination of the mechanical stability of a rail vehicle. Generally, the aerodynamic loads required are the side and the lift forces. The moments as stated earlier are roll, pitch and yaw. CFD is capable of predicting the velocity and pressure fields of a flow around a rail vehicle while allowing for different configurations to be taken into consideration (CEN, 2010). Also, CFD can provide a vast amount of data results with just a single simulation. Realistically, this is not possible with a model-scale experiment.

Numerical and experimental investigative studies on the flow fields around bluff bodies such as trains reveal that generally, such flows are highly unsteady and exist in a three-dimensional form (Bearman, 1997; Mittal and Moin, 1997; Kravchenko and Moin, 2000; Constantinuescu and Squires, 2003; Krajnovic´ and Davidson, 2004; Singh and Mittal, 2005; Hemida and Krajnovic, 2010; Hemida et al., 2012).

Furthermore, the flow around a rail vehicle possesses the following characteristics (CEN, 2010);

- Three-dimensionality

- High Reynolds number

- Turbulence

- Deceleration and acceleration

- Curved boundaries

- Separation

- Possible reattachment

- Recirculation

- Swirling

Some of the early numerical investigations carried out on the aerodynamics of trains included the work of Copley (1987), Chiu (1991; 1995), Chiu and Squire (1992), Gaylard (1993) and Masbernat et al. (1993). However, it must be understood that numerical modelling cannot offer an exact representation of the actual crosswind conditions, a train is subjected to. This is due to various simplifications and assumptions, which are applied during the numerical investigations.

Copley (1987) numerically measured the aerodynamic forces and moments on an idealised wind tunnel model of a train, in steady crosswinds. The results of his computational method were compared to the results obtained from the experimental measurements for a range of yaw angle incidences from 25° to 35°. The comparison showed a lack of agreement and thus, Copley further extended their computational work to a realistic geometry by using a much larger yaw angle range of 15° to 70°. The new comparison showed that until the yaw angle of 50°, the reliability of the results was quite comparable to the earlier case. However, over the yaw angle of 50°, the computational results showed significant deviation from the experimental results. According to Cooper (1979; 1984), for trains travelling under crosswinds, the strong forces experienced by a train usually occur around the yaw angle of 50°. This notion could be used as an explanation for the varying test results. Moreover, Copley also found out that the structure of the wake remains almost constant at yaw angles below 50°. Since the calculation method adopted was based on predicting the aerodynamic characteristics of an Advanced

Passenger Train this approach may not be practical in all situations, such as the simulation of freight trains. Further limitations of this work include the inconsideration of other possible factors, which affect the flow fields around a real train. Further work was proposed by Copley, which would consider the new vortex calculations in order to accurately predict the flow fields around trains.

Khier et al. (2000) aimed to provide a better understanding on the aerodynamic behaviour of the flows around trains, particularly under side wind conditions along with demonstrating the power of current computational techniques. The study considered a simplified high-speed three-dimensional train geometry, which reproduced the essential characteristics of the flow structure around typical trains. A simple method based on an algorithmic technique was employed to numerically solve the three-dimensional, Reynolds-Averaged Navier-Stokes (RANS) equations for the flow around trains. Due to the unavailability of high-powered computational resources, the study considered the flow fields around simplified train geometries only as these can be easily and reliably computed with available computational resources. However, the simplification of the limited train length was based on Cooper's (1979) study, which showed that flow structures are roughly constant downstream a certain distance from the nose of the train. In addition, further simplifications to the model geometry included the omission of surface and underside details along with inter-carriage gaps and wheel sets. Moreover, the ground was assumed as a smooth, moving surface, which means the roughness factor in between a real train and the ground was neglected. The time-averaged RANS equations were combined with the eddy viscosity hypothesis in order to compute the flow fields while the flow domain was resolved using a block-structured grid.

The results illustrated the dependence of the flow structures, aerodynamic coefficients of forces and moments and velocities on the incident yaw angles. Qualitatively, it was shown that side winds result in the disruption of the flow symmetry around trains while causing an increase in the additional aerodynamic forces and moments. These then impair the overall rollover threshold of a train. Since computations were performed on a range of yaw angles from 0° to 90°, the results showed the generation of two distinct flow structures upon variations in the angle of incidence. For smaller yaw angles, the vortices were observed to emerge from the leeward face of the nose, which were then rapidly convected by the flow, away from the train. For moderate angles of incidence, no significant fluctuations were observed in the flow structure. However, as the yaw angle exceeded 80°, a changed flow pattern was noticed where the flow separation was influenced by both, the upper and lower leeward sides. Whereas, no detachment of the flow was noticed at the windward edges. In terms of the pressure distribution, it is explained that the flow undergoes unexpected acceleration and deceleration stages upon approaching the train at an angle of incidence. This results in the generation of non-symmetric pressure fields in the vicinity of the train, creating lateral force and rolling moment along with leading to a rise in the magnitude of other components of forces and moments. Thus, it can be concluded that the pressure distribution of the flow over a surface is highly dependent on the angle of incidence. Overall, along with validating Cooper's (1979) assumption of the flow structure staying almost constant downstream a certain distance from the nose, this study confirmed the findings revealed in several other research works as well.

Furthermore, Diedrichs (2003) addressed the crosswind stability for a German high-speed train (ICE 2) by evaluating the relationship between the aerodynamic characteristics of

the flow around a train and yaw angle, for yaw angles in the range of 12° to 40°. The work used RANS in CFD, as a validation tool. The computational results were compared with the results achieved from the wind tunnel tests of an ICE 2 and the Swedish high-speed train. While numerically investigating the sensitivity of various factors in CFD, Diedrichs (2003) mentioned that the continuous advancement in the computational resources has eased the process of computational modelling by producing highly accurate results as compared to before. However, despite such upgrades, three-dimensional fluid flow calculations are confined to a number of engineering assumptions. For instance, in this work, it was assumed that the air flow around the train is stationary, incompressible, isothermal and turbulent in all domains.

The results of the study showed that under crosswind conditions, the inclination of a canted track results in an increase in the roll moments on the leeward side of the vehicle with higher roll moment achieved at the subsequent coach as compared to the lead coach. Although minimal differences were observed in the results of roll moments for different geometries, the side force was lower and the lift force was higher for the configuration without a rail-bed. Moreover, in comparison with the second coach, the lead coach was found to have a greater overturning moment. This explains the reason behind considering the lead vehicle as a critical vehicle. There were some difficulties faced while modelling the lee vortex and obtaining a constrained stagnant pressure on the windward side. To avoid such challenges, it is suggested to use a higher order bounded scheme, which could be combined with a non-linear, eddy-viscosity turbulence model. Furthermore, this recommendation is also emphasized for the second coach due to bigger challenges faced while predicting the aerodynamic loads of the second coach. In terms of the comparison with both the wind tunnel tests, a fairly good agreement was found for the side forces.

However, the lift force is expected to be higher in the calculation method probably due to the blockage effects of the rails employed in the computational modelling. Nevertheless, the overestimation means that the calculations are to a certain extent, conventional. Also, this study provided by Diedrichs (2003) can be considered suitable for qualitatively comparing different train shapes under crosswind conditions.

While modelling and investigating train aerodynamics, RANS methodology used by Diedrichs (2003) can show potential difficulties in some regions around the train. At a particular distance from the nose of the train, the boundary layer thickness is very large and in the wake region of the train, there are large scale separations, which is also the case for high yaw angle in crosswind conditions. In such circumstances, unsteady flow LES technique is essential to use as it can adequately simulate the unsteady flow fields (Hemida and Krajnovic, 2010). Also, Golovanevskiy et al. (2012) used RANS methods to evaluate the force coefficients on a model-scale freight train under crosswinds at varying yaw angles. There was a poor comparison found between the numerical and experimental data results. This could possibly be due to choosing a poor turbulence model, which was unable to realistically simulate the increased effective viscosities in the flow around a bluff-body such as a freight train.

The study by Hemida and Krajnovic (2010) provides an important insight into the flow structures on the train surfaces by exploring both, the instantaneous and time-averaged flows. A time-dependent technique, Large Eddy Simulation (LES), is introduced in this work, as a reliable method to achieve instantaneous information about the flows around simplified trains (Hemida et al., 2005). As Diedrichs (2003) expresses that time scales are usually neglected as simplifications to numerical modelling, Hemida and Krajnovic (2010) report that with LES, it is possible to accurately predict the time-dependent flows

around a train model. Moreover, LES is also capable of resolving complex flow structures, which develop in the wake region of the trains and are mainly controlled by large turbulent structures. A simplified model, provided in Chiu and Squire (1992), was used to investigate the influence of yaw angles and the shape of the nose on the corresponding flow structures. LES results yielded showed similarity in the flow structures for trains with a long and short nose with the exception of differences in the leeward side- close to the nose and on the face of the roof side. The flow was identified as axial from the nose tip onwards to the entire length of the train body. This was due to the disappearance of small vortices that had appeared at the short nose train, in the leeward flow. Consequently, the flow on the face of the roof stayed attached along the surface. A good agreement was found for the comparison of surface pressure distribution between the time-averaged and experimental results. However, slight complexities were found in the underbody flows, which had a localised influence on the pressure distribution and thus the aerodynamic coefficients. This could be possibly due to the differences in boundary layer thickness of the LES flow and the experimental flow. Moreover, although the attachment of the flow on the roof side resulted in supressing the strength of lift force, strong side force forces still stayed prominent because of unsteadiness in the shear layers. Overall, the shape of the nose was verified to have a significant influence on the time-averaged and instantaneous flows. In regard to the influence of different yaw angles on the aerodynamics of trains, LES showed at a large yaw angle, the crosswind flow is mostly unsteady with showing constant vortex shedding. In contrast, at a lower yaw angle, the crosswind flow was observed to change from a steady slender body form to an unsteady flow with vortex shedding taking place along the distance from the nose of the train. Such results have also been found in several previous studies, which are also

54

mentioned in this review. Furthermore, the upper vortices in the wake flow were found to be much stronger than the lower vortices and it is the lower vortices mostly, which result in the vortex shedding in the wake region of the train. This study presented by Hemida and Krajnovic (2010) is not only well-grounded but is also constructive in understanding the flows around trains at high Reynolds number. The findings of this work along with a very similar study by Hemida and Krajnovic (2009) can be used to further investigate the possible solutions to prevent the unwanted influences of crosswinds.

Apart from passenger trains, freight trains are also widely used in many countries such as North America, China and Australia (Alam and Watkins, 2007; Liu et al., 2014). With an increase in the loading capacity, concerns arise regarding the associated aerodynamic consequences of double-stacked freight trains. A high loading capacity implies a significant increase in the draft and lift forces of a freight train under crosswinds, which may result in critical aerodynamic issues (Alam and Watkins, 2007). In light of such issues, Hemida and Baker (2010) used LES to investigate the transient flow and the flow characteristics around one of the wagons of a freight train. The study also evaluated the overall aerodynamic response of a freight wagon when subjected to crosswind. In this research, a single-stacked container wagon was selected for scrutiny as it was presumed that freight trains comprise of similar wagons and thus the flow around each wagon will be identical. With crosswind at a 90° yaw angle, a Reynolds number of 300,000 was chosen. The study reported results for both; stationary and moving wagon model under crosswinds. The LES results indicated the existence of a complicated and rapid flow around the freight wagon with a low surface pressure on the roof of the container, which was not observed in previous publications. Moreover, the flow separated at the streamwise edges of the container causing a wide-reaching flow on the roof of the

container. Furthermore, no influence of the moving ground was found on the windward side pressure with minute differences noticed in the surface pressure of the downstream and top faces. Nevertheless, comparatively the ground motion did have a significant impact on the underbody flow structures and surface pressure. Overall, the results yielded from this study are quite meaningful as they provide a clear understanding on the flow structures on and around the surface of a model train in both; the instantaneous and the time-averaged flow. However, the study lacked verification as the results were not validated against results obtained from physical experiments.

Hemida and Baker (2010) also claimed that defining a model, which can precisely reproduce the Reynolds stresses in the wake region of a real train is very difficult. In addition to previous studies (Bearman, 1997; Singh and Mittal, 2005; Nishino et al., 2008) along with Hemida and Baker (2010), it is shown that two major instabilities begin to arise in the wake region of the flow as the flow inclines towards becoming fully turbulent. These instabilities are known as the large-scale shedding and the high frequency mode and are strong enough to cause major changes in the vortex shedding along with changing the structure of the near wake region. Large-scale shedding is marked by the progressive wave motion of the flow with alternative fluctuations, which are caused due to the shear forces existing between the recirculation zone and the exterior fluid. The periodic shedding of the vortices in the wake region of the flow behind a bluff body can be determined by the alternate fluctuations. High frequency mode is usually referred to as the spiral mode and is related to the small scale shear layer Kelvin-Helmholtz instability on the boundary of the recirculation zone. As mentioned earlier, this high frequency mode is an instability, which is responsible for causing a number of hindrances to the flow as listed by Constantinuescu and Squires (2003). This mode leads to the distortion of large

vortex assemblies, shedding of vortex tubes inside the detached shear layers, production of small scales and consequently the transition to fully turbulent region in the wake (Hemida and Krajnovic, 2009).

Numerical studies such as Osth and Krajnovic (2014) and Liu et al. (2014) show close resemblance to Hemida and Baker (2010). These studies also employed LES to evaluate the flow characteristics around a freight wagon. However, these studies did not consider the effects of crosswind and thus cannot be considered relevant. Moreover, taking into consideration other computational approaches, Detached Eddy Simulations (DES) has also been used to simulate airflows around ground vehicles under crosswinds (Spalart et al., 1997; Favre et al., 2010; Hemida and Krajnovic, 2009). DES is often employed for studies concerning train aerodynamics as it has proved successful in reducing computational costs as compared to the LES technique and is also able to provide much better time-averaged results than RANS models (Flynn et al., 2014; Morden et al., 2015; Baker et al., 2019).

Further, Delayed Detached Eddy Simulation (DDES) was used successfully by Muld et al. (2012) to evaluate the characteristics of the flow in the wake region of a model-scale high-speed train. The results of this study were in good agreement with the experimental results although the implications of the results are questionable. This is due to the Reynolds number of the case being 60,000, which is 24% of the minimum Reynolds number recommended in CEN (2013). Therefore, Flynn et al. (2014) used DDES to investigate the highly turbulent nature of slipstreams generated by a model-scale, Class 66 locomotive. With an appropriate Reynolds number of 300,000, the results compared well with the physical experiments. Although several computational (CFD) approaches have been mentioned before in literature, Morden et al. (2015) pointed out the limited

research on the comparison of different approaches. Therefore, Morden et al. investigated the consistency of the wind tunnel methodology with the CFD technique by comparing surface pressures in train aerodynamics. The comparison results concluded that the DDES approach was quite capable of replicating the wind tunnel results. Some recent work provides a deeper understanding on the numerical investigation of the slipstreams around high-speed trains through LES (Hemida et al., 2014), DES (Zhu et al., 2016) and Improved Delayed Detached Eddy Simulation (IDDES) (Huang et al. 2016).

A delay factor is used in the Delayed Detached Eddy Simulation (DDES) model for improving the robustness and usability of the DES model in order to differentiate between RANS and LES regions, where meshes with refinement, specially close to the walls, would lead to an increase in the ambiguous determination of different turbulent areas. In an IDDES model, the DDES concept is taken further by the incorporation of a wall distance based RANS-LES differentiation. To elaborate, in such a case, the RANS model will be used for much smaller regions, close to the wall. Consequently, this would allow for some wall-modelled LES (WMLES) abilities to be introduced into the DES model.

In the study of train aerodynamics for engineering applications, IDDES simulations have been successfully used (Li et al., 2019; Chen et al., 2019; Niu et al., 2017b; Xia et al., 2017a and 2017b; Wang et al., 2019). Precisely, IDDES is a hybrid RANS-LES model which helps achieve an instantaneous and an accurate time-averaged view of the flow around a model-scale passenger train. It offers a more flexible and convenient scale-resolving simulation model for flows with higher Reynolds number as well. The classic DES approach is usually considered as promising; however, it has some drawbacks associated with its use. DES is sensitive to the mesh quality. Therefore, in cases where there exists a relatively thick boundary layer and small separation regions, DES may

result in modelled stress depletion (MSD) as well as grid-induced separation (GIS) if the wall-parallel grid spacing is not larger than the thickness of the boundary layer to make RANS valid or adequately small to activate pure LES (Huang et al., 2016). On the contrary, IDDES combines the advantages of the wall-modelled LES (WMLES) and the DDES models along with its inbuilt methods which avoid the issue of grid induced separation. Additionally, due to the model's design, it is possible to perform LES simulation of the wall boundary layers at increased Reynolds number as compared to the traditional LES model. Also, the WMLES model is developed to reduce the Reynolds number dependency (Shur et al., 2008).

The governing equations of the SST-IDDES model are (Menter et al., 2003; Gritskevich et al., 2012):

$$\frac{\partial \rho k}{\partial t} + \nabla \cdot (\rho \vec{U} k) = \nabla \cdot [(\mu + \sigma_k \mu_t) \nabla k] + P_k - \rho \sqrt{k^3} / l_{IDDES}$$

$$\frac{\partial \rho \omega}{\partial t} + \nabla \cdot (\rho \vec{U} \omega) = \nabla \cdot [(\mu + \sigma_\omega \mu_t) \nabla \omega] + 2(1 - F_1) \rho \sigma_{\omega 2} \frac{\nabla k \cdot \nabla \omega}{\omega} + \alpha \frac{\rho}{\mu_t} P_k - \beta \rho \omega^2$$

$$\mu_t = \rho \frac{\alpha_1 \cdot k}{\max(\alpha_1 \cdot \omega, F_2 \cdot S)} \qquad (2.10)$$

In Equation (2.10), ρ is the fluid density, k is the turbulent kinetic energy, t is the time, U is the velocity, μ is the dynamic viscosity, μ_t is the turbulence eddy viscosity, P_k is the production term, l_{IDDES} is the IDDES length scale, ω is the specific turbulent dissipation rate, F_1 and F_2 are the SST blending functions, S is the magnitude of the strain rate tensor and σ_k, σ_ω, $\sigma_{\omega 2}$, α, β and a_1 are the base model coefficients.

In Equation (3.1), F_1 and F_2 read as follows:

59

$$F_1 = \tanh(\arg_1^4)$$

$$\arg_1 = \min\left(\max\left(\frac{\sqrt{k}}{C_\mu \omega d_w}, \frac{500\nu}{d_w^2 \omega} \right), \frac{4\rho\sigma_{\omega 2} k}{CD_{k\omega} d_w^2} \right)$$

$$CD_{k\omega} = \max\left(2\rho\sigma_{\omega 2} \frac{\nabla k \cdot \nabla \omega}{\omega}, 10^{-10} \right) \tag{2.11}$$

$$F_2 = \tanh(\arg_2^2)$$

$$\arg_2 = \max\left(\frac{2\sqrt{k}}{C_\mu \omega d_w}, \frac{500\nu}{d_w^2 \omega} \right)$$

In Equation (2.11), d_w is the distance to the nearest wall, ν is the kinematic viscosity of the fluid and C_μ is the model coefficient for turbulent viscosity.

In Equation (2.10), the production term is given as:

$$P_k = \min(\mu_t S^2, 10 \cdot C_\mu \rho k \omega) \tag{2.12}$$

where a production limiter is used in the SST model to prevent the build-up of turbulence in stagnation regions.

In Equation (2.10), the IDDES length scale is given as:

$$l_{IDDES} = \tilde{f}_d \cdot (1 + f_e) \cdot l_{RANS} + (1 - \tilde{f}_d) \cdot l_{LES}$$

$$l_{LES} = C_{DES} \Delta$$

$$l_{RANS} = \frac{\sqrt{k}}{C_\mu \omega} \tag{2.13}$$

$$C_{DES} = C_{DES1} \cdot F_1 + C_{DES2} \cdot (1 - F_1)$$

In Equation (2.13), $\tilde{f}_d$ is the empiric blending function, f_e is the elevating function, C_{DES} is the DES model coefficients and Δ, the LES length-scale, is defined as:

$$\Delta = \min\left\{ C_w \max\left[d_w, h_{max} \right], h_{max} \right\} \tag{2.14}$$

In Equation (2.14), h_{max} is the maximum edge length of the cell and C_w is a fundamental empirical constant.

The empiric blending function, $\tilde{f}_d$, in Equation (2.13) is computed using the following equations:

$$\tilde{f}_d = \max\left\{(1-f_{dt}),f_b\right\}$$
$$f_{dt} = 1-\tanh\left[(C_{dt1}\cdot r_{dt})^{C_{dt2}}\right]$$
$$r_{dt} = \frac{v_t}{\kappa^2 d_w^2 \sqrt{0.5(S^2+\Omega^2)}} \tag{2.15}$$
$$f_b = \min\left\{2\exp(-9\alpha^2),1.0\right\}$$
$$\alpha = 0.25-d_w/h_{max}$$

In Equation (2.15), r_{dt} is the turbulent analogue of r_d, which is a marker of the wall region, v_t is the turbulent viscosity and Ω is the magnitude of vorticity tensor. Detailed formulations for functions f_{dt} and f_b can be found in Shur et al. (2008).

In the original model formulation, f_e in Equation (2.13) is given as:

$$f_e = f_{e2}\cdot \max\left((f_{e1}-1.0),0.0\right)$$
$$f_{e1} = \begin{cases} 2\cdot\exp(-11.09\cdot\alpha^2), & \alpha \geq 0 \\ 2\cdot\exp(-9.0\cdot\alpha^2), & \alpha < 0 \end{cases}$$
$$f_{e2} = 1.0-\max\left(f_t,f_l\right)$$
$$f_t = \tanh\left((C_t^2\cdot r_{dt})^3\right) \tag{2.16}$$
$$f_l = \tanh\left((C_l^2\cdot r_{dl})^{10}\right)$$
$$r_{dl} = \frac{v}{\kappa^2 d_w^2 \sqrt{0.5(S^2+\Omega^2)}}$$

Finally, the values for all the model constants given in Equations (2.10-2.16) are:

$C_\mu = 0.09$, $\kappa = 0.41$, $a_1 = 0.31$
$C_{DES1} = 0.78$, $C_{DES2} = 0.61$, $C_{d1} = 20$, $C_{d2} = 3$
$\alpha_1 = 5/9$, $\beta_1 = 0.075$, $\sigma_{k1} = 0.85$, $\sigma_{\omega1} = 0.5$
$\alpha_2 = 0.44$, $\beta_2 = 0.0828$, $\sigma_{k2} = 1$, $\sigma_{\omega2} = 0.856$
$C_w = 0.15$, $C_{dt1} = 20$, $C_{dt2} = 3$, $C_l = 5.0$, $C_t = 1.87$

Generally, CFD modelling has been more widely used in the study of train aerodynamics. CFD is often employed in industry as it is capable of successfully simulating the complex flow around stationary and moving trains. The analysis performed by this technique is often much higher in resolution as compared to experimental data. However, there are some major challenges associated with the use of this technique specifically with regard to trains. Although CFD can completely exclude the effects of external factors such as ambient winds while proving detailed results, it is not easy to handle. This suggests the need for specialised techniques and expertise (Baker, 2010) to simulate large length to height ratios of high-speed trains. Moreover, the CFD technique requires validation against physical experiments to verify the results of numerical investigations (Flynn et al., 2014; Zhu et al., 2016). Moreover, an appropriate selection of an accurate combination of computational mesh, computational method and turbulence modelling is another main challenge of CFD (CEN, 2010). Although this could get a little complex, Franke et al. (2010) confirms that if normal CFD routine is practised, that is in terms of mesh size, resolution and convergence, then valuable results can be achieved.

Overall, several researchers in the past have attempted to simulate aerodynamic characteristics of moving trains using either experimental or numerical simulations (Krajnovic et al., 2012; Dorigatti et al., 2015; Premoli et al., 2016; Niu et al., 2018; Liu et al., 2018; Deng et al., 2019; Yang et al., 2019). Their results contributed significantly to the literature, however, most CFD studies present in the literature lack accurate validation data from wind tunnel tests or similar. Thus, it is important to explore both, experimentally and numerically, the aerodynamic performance of trains subjected to crosswinds when conducting any investigation.

2.8 Windbreak walls

In the last few years, considerable attention has been paid to the issue of crosswinds affecting high-speed trains (Cooper, 1979; Matschke and Schulte-Werning, 1997; Matschke et al., 2000; Fujii et al., 1999; Cheli et al., 2010; Hemida and Baker, 2010; Baker et al., 2011). Tomasini et al. (2015) put forward the view that two approaches can be adopted to overcome the risks caused by crosswinds. The former is through subjecting the speed of the vehicles to strict regulations while the latter deals with installing or constructing wind barriers. Over the past, a few researchers have tried to study the influence of wind barriers on trains and railways (Schulte-Werning et al., 2002; Bocciolone et al., 2008; Zhang et al., 2013; He et al. 2014; Zhao et al., 2015; Guo et al., 2015). Although these studies either referred to wind protection measures as wind barriers, windbreak walls or windbreak fences, the sole purpose of such studies was to determine the effects of wind barriers on the overall aerodynamic performance of trains. Research conducted within the TRANSAERO project (Schulte-Werning et al., 2002) involved performing experimental studies to report an initial analysis of the influence of windbreaks. The study considered the influence of strong crosswinds with different types of wind barriers for both static and moving models and further attempted to address the reduction of the aerodynamic forces and wind loads on rail vehicles through wind barriers. Similar experimental analyses have also been carried out by Bocciolone et al. (2008) in a wind tunnel to evaluate the characteristics of solid and porous kinds of wind barriers. Generally, wind barriers have been examined through the use of four techniques; full-scale and field tests (Richardson and Richards, 1995); wind tunnel tests (Chu et al., 2013; Tomasini et al., 2015); numerical modelling and analytical methods (Kiya et al., 1980). Quite recently, few researchers have investigated the aerodynamic performance of

wind barriers and their corresponding influence on trains through CFD studies (Barcala and Meseguer, 2007; Bi et al., 2011; Li et al., 2012; Zhao et al., 2015; Guo et al., 2015). However, the simulations performed in these studies lacked experimental validation.

Wind barriers are usually built or installed along the railway line, beside the tracks in order to reduce the effect of side winds on trains. Such windbreaks can be customised according to the side wind speed, wind pressure and the surrounding topological conditions. One very common example of a windbreak is the use of windbreak walls. CEN (2010) provides a description of windbreak walls as vertical surfaces with null porosity. However, there might be walls with different porosities and different configurations built along the railway line. Moreover, since crosswinds may risk the overall stability of a train, a wind protection along the railway line can either maximally or completely prevent the crosswind effect. This would also ensure passenger comfort and stability of the train. A wind barrier reduces the magnitude of the aerodynamic rolling moment coefficient acting on the train (Zhang et al., 2013).

Zhao et al. (2015) presented the effects of a noise barrier on the aerodynamic performance of a high-speed rail vehicle in crosswinds. The study develops the claim that a noise barrier not only prevents the propagation of noise, induced by a high-speed train, but also acts as windbreak wall, protecting trains under crosswind influence. The study numerically modelled a three-dimensional model of a Chinese CRH train to investigate the effects of a noise barrier on the overall aerodynamic behaviour of the model train. The study simulates a crosswind condition, where the train is running on an embankment. The analysis involves comparing the flow fields around a model train with and without a noise barrier. The influence of the height of the noise barrier on the aerodynamic performance of the train is also investigated. The simulation results demonstrated that the existence of

a noise barrier had significant effects on the flow structure around trains, which resulted in affecting the overall performance of the high-speed train. It was shown that the noise barrier was able to hinder the path of wind from directly impacting the train. In addition, vortices were generated on both the windward and leeward sides of the train. However, the formation of negative pressure areas on the windward side may induce a resultant lateral force on the train, which acts in an opposite direction to the wind. This can result in the overturning of the train. The results concluded that in a crosswind situation, the overall aerodynamic performance of a high-speed train is better with a noise barrier compared to without a noise barrier. In terms of the height of the noise barrier, an optimized height was suggested. Thereafter, an increased height could result in an adverse trend causing a deterioration in the aerodynamic performance of the train. The findings are of direct practical relevance; however the research was limited to the aerodynamic performance of a high-speed train running on an embankment. This study does not consider several other important parameters such as the different terrains including complex ground types, which may exist in the vicinity of the noise barrier. In addition, the effects of wind at transition regions, which may exist on the noise barrier, were not investigated. This was also the case for a few other studies, which dealt with the influence of a wind protection but were confined to either embankments or bridges (Guo et al., 2015; He et al., 2014).

A recent example of physical modelling on windbreaks for high-speed railway lines is provided by Tomasini et al. (2015). On the basis of the current evidence, which states that creating long barriers in length and achieving high Reynolds number is quite problematic in wind tunnel testing, Tomaisini et al. (2015) carried out two experimental campaigns to overcome such issues. The purpose of their investigation was to compare the different

types of windbreaks by performing a sensitivity study as a function of different parameters. A series of tests were performed in a wind tunnel to analyse the characteristics of different windbreaks and their corresponding effects on train wind loads. Stage 1 of the tests was performed at a series of high Reynolds number (ranging between 1.3×10^5 and 6.6×10^5), comparable to Reynolds number of a full-scale train, to avoid scaling effects and employed long wind barriers (3 m long model-scale and 45 m in full-scale) to reduce boundary effects, which are pronounced with short length barriers. If the wind barrier is short in length as compared to the infrastructure around it, the oncoming flow will be able to attack the train from the leading edges, thus reducing the sheltering effects of the wind barrier. The work used a stationary model of the ETR500 train. While this contrasts the real-life situation, where there is a relative movement between the train and the windbreak walls, the results are considered meaningful. This is because using a stationary train model makes it possible to simulate the actual yaw angle faced by the train and the windbreak. In addition, these results yield important information with regards to the sheltering and shielding effects provided by the windbreaks. Once the importance of windbreaks is identified in terms of their protective effects, these results can be useful in the future to understand the effects of windbreaks when there is relative motion between the train and the windbreak, as explored in this study. Based on previous research studies (Bocciolone et al., 2008; Barcala and Meseguer, 2007; Cheli et al., 2010; Li et al., 2012), the study assumed that significant aerodynamic forces are present around the leading coach of the train. Therefore, the model of the train used consisted of one and a half coach. The experimental results from the study provided measured force, moment and pressure coefficients for the different tests. The first set of tests were conducted in the high-speed test section of the facility. The dependency of the force coefficients to the

Reynolds number was evaluated with the wind barriers. To analyse the results, the work carried out by Tomasini et al. (2015) was compared with the study performed by Cheli et al. (2011a) which mainly looked at the sensitivity of the Reynolds number of the same vehicle model without any barrier. Figure 2.8a, c and e, show the lateral force, vertical force and the rolling moment coefficients, respectively, for the scenario without any barriers at different Reynolds number obtained in Cheli et al. (2011a). Whereas Figure 2.8b, d and f, show the same vehicle's lateral force, vertical force and rolling moment coefficients, respectively, for the scenario with a wind barrier at different Reynolds number obtained by Tomasini et al. (2015). It must be noted that for the latter, the tests were carried out for yaw angles higher than 30°, as for lower yaw angles than 30° the finite length of the infrastructure model with barriers alters the flow of wind interacting with the vehicle in regard to the real case, where the infrastructure has a pseudo-infinite length. Analysis of the results revealed that the existence of a wind barrier significantly decreases the dependency of all aerodynamic coefficients to the Reynolds number, as demonstrated in Figure 2.8. Specifically, the sensitivity of the side force and rolling moment coefficients was observed to disappear while the lift force coefficient reduced considerably.
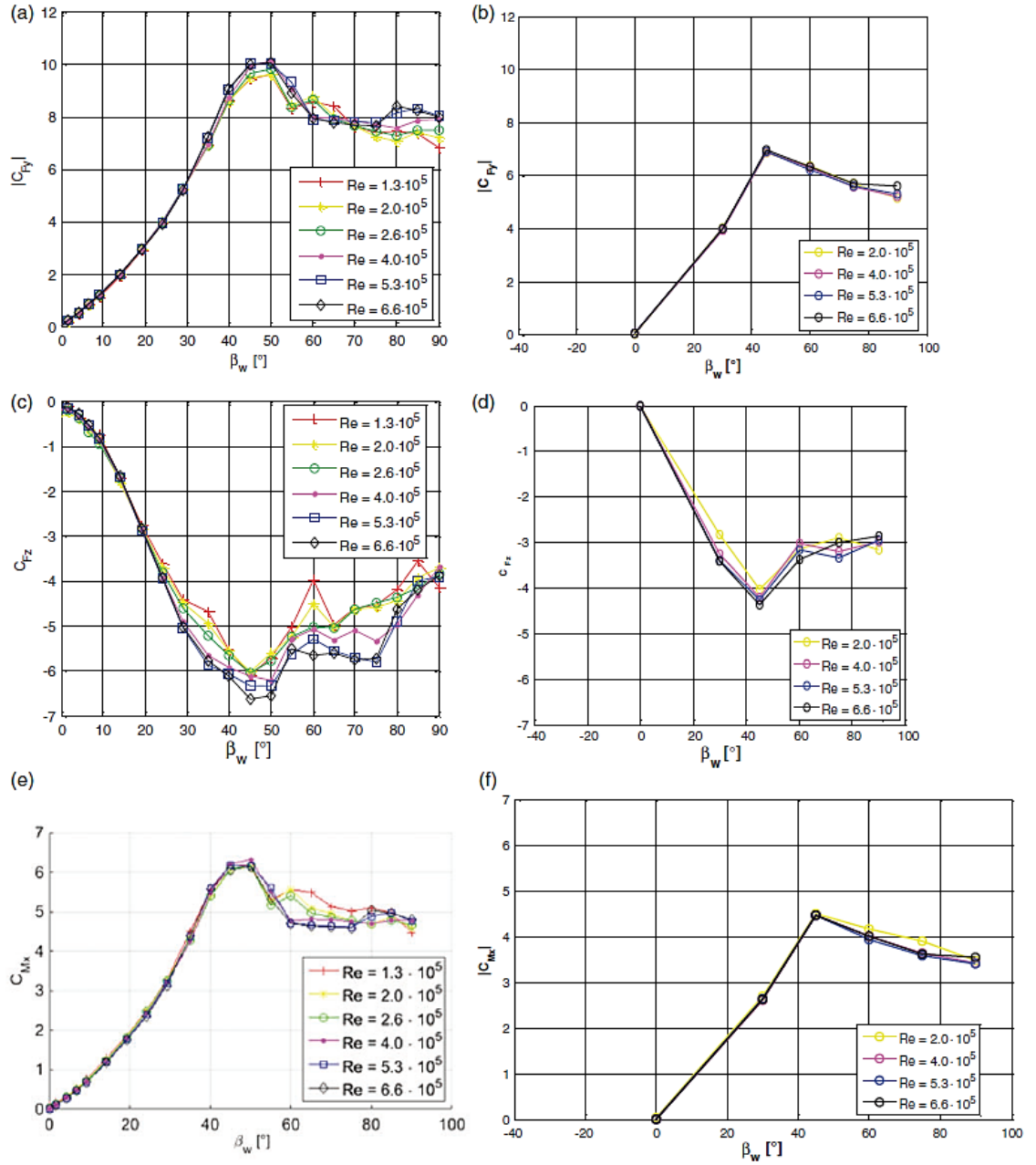
Figure 2.8: Aerodynamic coefficients for a stationary ETR500 train model as a function of wind angle for different Reynolds numbers (a, c and e) with no wind barrier and (b, d and f) with a wind barrier (Tomaisini et al., 2015).

The second set of tests were performed in the low-speed section of the test facility with longer wind barriers. Seven different wind barriers were tested to identify the most appropriate choice for effectively reducing the overturning risk related to crosswinds. In view of the pressure distribution, the results showed that the existence of a wind barrier

led to a reduction in the pressure on the windward side of the train along with modifying the wake region behind the train. Furthermore, it was observed that at low wind angles, the wind barriers inclined the flow parallel to the train. This reduced the negative pressure area in the wake of the train, thus enhancing the area where the train behaves as a slender body. The results of this study also concluded that the distance between the wind barrier and the track is another important parameter. Overall, the results of this study can be considered conclusive to a certain extent, given that the assumptions are further evaluated for their validity. The results can be used as a guide for designing wind barriers. Further work can be carried out to simulate the relative motion between the train and the wind barrier through physical or numerical modelling.

Despite the several benefits of wind protections, a few research studies have stated the drawbacks associated with the use of wind barriers. As mentioned by Zhao et al. (2015), wind barriers can create a large number of vortices when interacting with train aerodynamic flows and crosswind creating potential issues for the stability of the train. Wind barriers can agitate the wind flow thus causing increased turbulence effects, which lead to complexities in the flow fields around the trains (Zhang et al., 2013; Guo et al., 2015; Zhao et al., 2015).

There are several publications available in the literature such as the works of Zhang et al. (2013; 2017), which have studied the aerodynamic properties of wind barriers on a train bridge model to calculate dynamic response. These studies, which are considered notable as they provide a first step towards understanding an aerodynamic issue that is not well understood, were performed on stationary models to obtain the three-component coefficients for the vehicle. The achieved data is still valuable for a complicated engineering problem that is yet to be explored further. Avila-Sanchez et al. (2014; 2016)

also presented an interesting research where the shelter effectiveness of a set of windbreaks placed over a railway twin-track embankment is experimentally analysed. A set of wind tunnel tests were undertaken and results corresponding to pressure tap measurements over a section of a typical high-speed train were presented. All of these studies along with the studies of Cheli et al. (2010), He et al. (2014) and Tomasini et al. (2015) did not take into account the relative movement of the train unit compared to the walls, but the results presented were considered remarkable and ones which would benefit the readers.

Even though windbreak walls have been under considerable attention, few publications discuss in precise detail the effects of wind barriers in particular. Most studies, such as Avila-Sanchez et al. (2016), considered only the effects of windbreaks on a bridge system while some other CFD related studies lacked proper experimental validation through full-scale or model-scale tests (Bi et al., 2011; Li et al., 2012; Guo et al., 2015). It is therefore important to explore both, experimentally and numerically the aerodynamic performance of trains subjected to crosswinds with different types of windbreak walls in order to propose the best possible design of a windbreak wall.

Furthermore, an important problem which has not been addressed yet is the random geometrical change in the structure of windbreak walls. The abovementioned technique of installing windbreak walls is deemed effective if the wind barrier is built entirely parallel to the track. Whereas, in reality it is not possible to develop an entirely uniform and continuous windbreak structure due to possible complexities in the surrounding terrain such as cuttings, which cannot be avoided. The windbreak wall would therefore consist of a discontinuous structure with a series of transition regions. Transition regions

refer to the specific design implementations in terms of the geometry of the windbreak wall to tackle different topographies and terrains that exist along the railway lines.

For instance, in China, the Lanzhou–Xinjiang railway line consists of a section which passes through a mountainous region where strong winds are expected. A recent study by Chen et al. (2020) presented a case study of the Lanzhou Xinjiang high-speed railway where the terrain around the railway line was studied. It was revealed in their study that at times, railway lines pass through constantly changing terrain types. The mountainous regions mean that the railway line has to face several embankments and cuttings (Liu et al., 2018). This can generate transition regions between two terrain types. Such transition regions provide an additional sudden wind load on the train under crosswinds, which can further lead to a sudden deterioration in the aerodynamic performance of the train (Wu et al., 2015, 2017; Zhang, et al., 2019). This results in possible transition regions in the design of the windbreak wall created, as explained in Figure 2.9. The change in the distance between the windbreak wall and the railway track, known as the transition region, can result in the formation of vortices around the train body which may hit the train surfaces leading to stability issues for the train while causing a loss in ride quality and increased passenger discomfort.
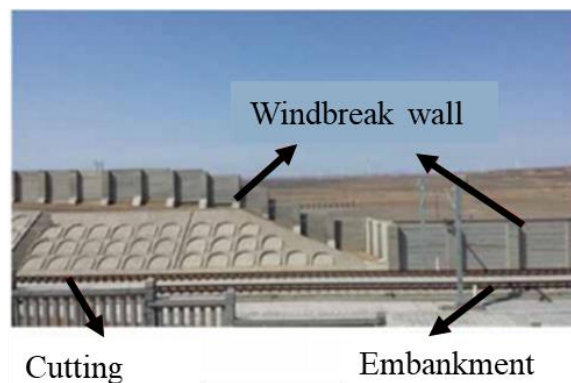
Figure 2.9: Part of the of Lanzhou–Xinjiang railway line, comprising of a rectangular transition region in the windbreak wall (adapted from Liu et al., 2018).

2.8.1 Summary of windbreak research

Analysis of existing studies on the aerodynamics of windbreak walls has demonstrated that those with continuous geometries are more actively researched compared to discontinuous geometries; even though it is not possible to develop an entirely uniform and continuous windbreak structure due to various unavoidable terrains and cuttings. Therefore, the literature review indicates the need of a focused study on understanding the aerodynamic flow, which exists around a train surface due to the presence of different kinds of windbreak walls, mainly ones with transition regions. Up till now, the aerodynamic flow around continuous geometries of windbreak walls has received limited analysis. However, based on the literature reviewed in this study, it appears that a fluid flow is sensitive to its surrounding environment. As a result, it is suspected that a fluid may behave and interact differently with different geometries of windbreak walls. Therefore, it is expected that varying angles of transition regions in windbreak walls can influence the flow around a model-scale passenger train. By conducting an experimental and numerical investigation on windbreak walls, it will be possible to assess the influence of different designs on the flow around a high-speed passenger train subjected to crosswinds. Therefore, in this research, An experimental investigation will be carried out to understand the effect of transition regions on a stationary train model, using techniques similar to those presented in previous research. These results will be used to validate the numerical work as well. However, it must be noted that experimental results are limited as they only provide insights on the surface pressure and aerodynamic force coefficients of the train. Thus, in order to obtain a further understanding on the aerodynamic flow which exists around the surface of a train with the presence of a particular kind of windbreak wall, it is important to perform numerical simulations. The research will

continue investigating the effects of crosswinds with a specific shape of a windbreak wall by performing numerical simulations that can exhibit numerous flow features which may not be evident through experimental results. Thereafter, the numerical work can be expanded to consider the relative movement between the train and the windbreak wall.

CHAPTER 3: Experimental and numerical methodologies

The majority of sections in this chapter have been published in Hashmi et al. (2019).

3.1 Introduction

Chapter 3 provides an explanation on the experimental and numerical methodologies adopted in this investigative research to determine the non-dimensional aerodynamic coefficients of the model-scale Class 390 train under crosswinds with and without different shapes of windbreak walls. Section 3.2 aims to provide a description of the wind tunnel facility where the experimental work was performed while further providing details on the instrumentation used in section 3.3.1 and the flow characterisation inside the facility in section 3.2.2. Section 3.3 introduces the scaled model along with the motivation and development of the model design while elaborating on the suitability of the chosen model in relation to this study. Section 3.4 illustrates the experimental setup and the describes the different test cases which were examined in this study. The experimental procedure is listed in section 3.5. Section 3.6 presents the aerodynamic load experimental processing methodology. Furthermore, the numerical methodology used in this research is described from section 3.7 onwards, which discusses the numerical details including the geometries, computational domain, boundary conditions, numerical method and computational mesh used in this study.

3.2 The UoB wind tunnel facility

The University of Birmingham's (UoB) wind tunnel is an open-circuit wind tunnel facility which was constructed in 2012 with the purpose of simulating velocity and

turbulence profiles. The wind tunnel consists of a 10 m long working test section and has a 2 m by 2 m square cross-section. The facility is powered by a total of 49 axial fans which are arranged in 7 rows of 7 units each. The maximum wind speed achievable at the test section is 7.2 ± 0.2 m/s. Figure 3.1 shows the front and rear view of the current wind tunnel. To provide a uniform wind speed with minimal turbulence, wind from the fans flows through a honeycomb screen, which acts as a flow straightener, before entering the wind tunnel test section.

(a)   (b)
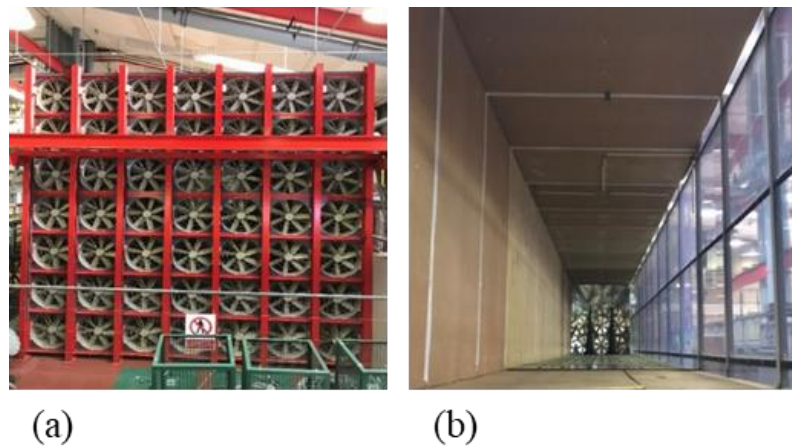
Figure 3.1: (a) Rear view and (b) Front view of the UoB wind tunnel.

3.2.1 Instrumentation

3.2.1.1 Cobra Probes

The wind tunnel facility makes use of 2 kHz Series 100 Cobra probes (TFI, 2011), which can measure 3D velocities of the flow and the static pressure. These multi-hole (4-hole) cobra probes, which are shown in Figure 3.2, are mounted to clamp stands, positioned at the designated measuring points, and are capable of providing the three components of time-varying (fluctuating) and time-averaged (mean) velocity in real-time (TFI, 2011).

Based on the probe's ability to measure flows with a frequency response of up to 2 kHz, these probes are considered to be an ideal instrument for measuring turbulent flows. In this study, a sampling frequency of 1 kHz was used, which was shown to be sufficient in the preliminary tests to achieve the required flow information, while meeting manufacturer guidelines (TFI, 2011).

In terms of the performance of the cobra probes, they come with an accuracy of ± 0.3 m/s and $\pm 1.0°$ for velocity and flow direction respectively, and the probes are about ± 5 Pa accurate for the differential static pressure (TFI, 2011). In addition, the manufacturer declares that these cobra probes can provide relatively accurate results even for turbulent intensities greater than 30%. Even though these cobra probes were delivered fully calibrated, the probes were statically calibrated to take accurate flow measurements.

Although the manufacturer of the cobra probe mentions that three types of calibration can be performed: static, frequency response and head calibrations, the only calibration needed by the user is a static calibration check to be performed periodically. For the other two calibration types, these are only needed if the probe is physically damaged or any of the ports become blocked, in such a case the probe must be returned to the supplier. In the process of static calibration, the voltage-to-pressure scaling factors of the pressure transducers are determined. To do so, the user is needed to apply a range of accurately known pressures to the reference pressure port, located at the tail end of the cobra probe. A device capable of supplying a stable pressure must be connected to both the reference pressure transducer and the probe's reference pressure port, where the applied pressure should be displayed. Next, at the reference pressure port of the cobra probe, a range of pressures is applied. The user needs to manually register the magnitude of each pressure being applied, where the software samples the voltage at that particular pressure. The

software then calculates the voltage-to-pressure scaling ratios using a number of pressure points and a least squares fit (TFI, 2011).

Figure 3.2: Series 100 Cobra probe (a) dimensional view (b) head view (Adapted from TFI, 2011).

Pressures measured by the probes are relative to the pressure applied at the reference pressure port. Therefore, it is important to vent the reference port at a location out of the flow stream in order to make sure no flow induced pressure variations affect the reference pressure. Thus, it was ensured in this study that the reference pressure port was vented outside the wind tunnel. The probes were positioned and aligned at the beginning of measurement sessions while, prior to each measurement, the probes were 'zeroed' using the TFI control software.

3.2.1.2 Multi-Channel-Pressure-System

The pressure distribution on the surface of the model train is measured using a 64-channel, Multi-Channel-Pressure-System manufactured by Solutions for Research Ltd. Figure 3.3 shows the 8-channel modules of the Multi-Channel-Pressure-System. The device is made up of two main components; the pressure modules and an interface unit. Each channel in the dynamic pressure modules contains a separate pressure transducer for the measurement of pressure. The interface unit assists in the connection of the modules and comprises of a data acquisition system. The device is very useful as it allows for

simultaneous pressure measurements. The system was supplied fully calibrated with calibrations being very stable over long periods of time. Similar to the cobra probe's reference port, each dynamic pressure module of the pressure measurement system was connected to a reference pressure port which was used to provide a common reference pressure for the transducers. The reference port was vented outside the wind tunnel section in order to ensure the flow induced pressure variations did not influence the reference pressure. The static pressure measured at the transducer is the difference between the measured surface pressure at the pressure tap of the test model and the reference pressure. Pressure differences were measured by the pressure transducers as electrical signals. Solutions for Research Ltd provided a relevant software which was used in this work to convert the digital signal back to pressure difference with the aid of a previously generated calibration file. Further, collected surface pressure time series were saved to a file for post-processing.

Figure 3.3: An image of the 8-channel modules of the Multi-Channel-Pressure-System used in this study.

3.2.2 Crosswind characterisation of the wind tunnel

Characterising flows inside a wind tunnel is very important as it helps gain a better understanding of the crosswind simulations by providing an in-depth flow history in terms of the mean wind speeds and turbulence intensities of the flow. Therefore, this study first investigated the flow in the wind tunnel by taking measurements at horizontal and vertical points. Horizontal Wind Profiles (HWP) were measured at different heights from the ground and comprised of a total of 150 spanwise measuring positions. Vertical Wind Profiles (VWP) were measured from the floor of the wind tunnel to a height of 1.5 m and comprised of a total of 100 measuring positions. These measurements were made at a distance of 6 m from the fans, which was the position of experimental setup. This position was considered ideal for performing the tests based on the development of flow and the requirements for achieving a uniform flow regime. The wind speed was measured at a height of 1.5 m at different locations from the fan. The probe measuring the wind speed reached a steady value of 7.2 m/s ± 0.2 m/s at a distance of 6 m from the fan. At closer distances to the fans, the wind speed was found to be unsteady, with a larger standard deviation beyond that required to achieve a steady flow scenario. This may be due to flow irregularities being present at distances closer to the fans due to contraction effects at the inlet of the wind tunnel. A greater distance than 6 m would also not satisfy the flow requirements as the incident wind speed would be too low.

Figure 3.4a shows the HWP of the mean streamwise velocity while Figure 3.4b shows the lateral and vertical mean velocities, at a height of 350 mm from the floor of the wind tunnel. Figure 3.4c illustrates the overall spanwise turbulence intensities at the same height. Overall, according to Figure 3.4, a limited spanwise uniformity is observable. Also, it can be noted that the fans on the left-hand side (negative spanwise coordinate)

are slightly more efficient and probably perform better as compared to the right-hand side fans. This could explain the slightly stronger mean streamwise velocity component on the negative span (left-hand side). In addition, in any wind tunnel, lateral homogenous conditions are expected in a fraction of the spanwise wind tunnel size. Thus, a boundary layer and inhomogeneity can be anticipated. Although the wind profile is not completely uniform across the test section, for the requirements of this study relatively stable velocity values are obtained across the central portion of the wind tunnel at the position where the train body is situated. Since the wind profile varies negligibly, it is expected that the wall boundary layer on the wind tunnel sides does not impact the results significantly.

Moreover, although the wind tunnel makes use of a honeycomb screen, which acts as a flow straightener, the air flow inside the wind tunnel is still expected to be three-dimensional, as the flow straightener can only minimise but not eliminate the lateral velocity components. Therefore, while non-zero lateral velocity components of the wind are anticipated, the magnitude of these is very low, as observed in Figure 3.4b. CEN (2016) states, the horizontal component of the mean wind (u) is used for analysis as this represents the prominent part of wind fluctuations and projects the instantaneous wind vector in the mean wind direction. Furthermore, the cobra probe measures the three components of velocity within a 45° range of the front face of the probe. This can have a direct impact on the measured data. For instance, if the recorded data quality is less than 100%, this can then introduce a bias in the calculated velocity vector, i.e. as the data quality decreases, the potential bias increases. As a result, in this study, only those positions which had a data quality of 100% were accepted for further analysis in order to minimise the bias in the time-averaged velocities. To do so, the cobra probes were positioned carefully, and extra care was taken to reduce any human errors.
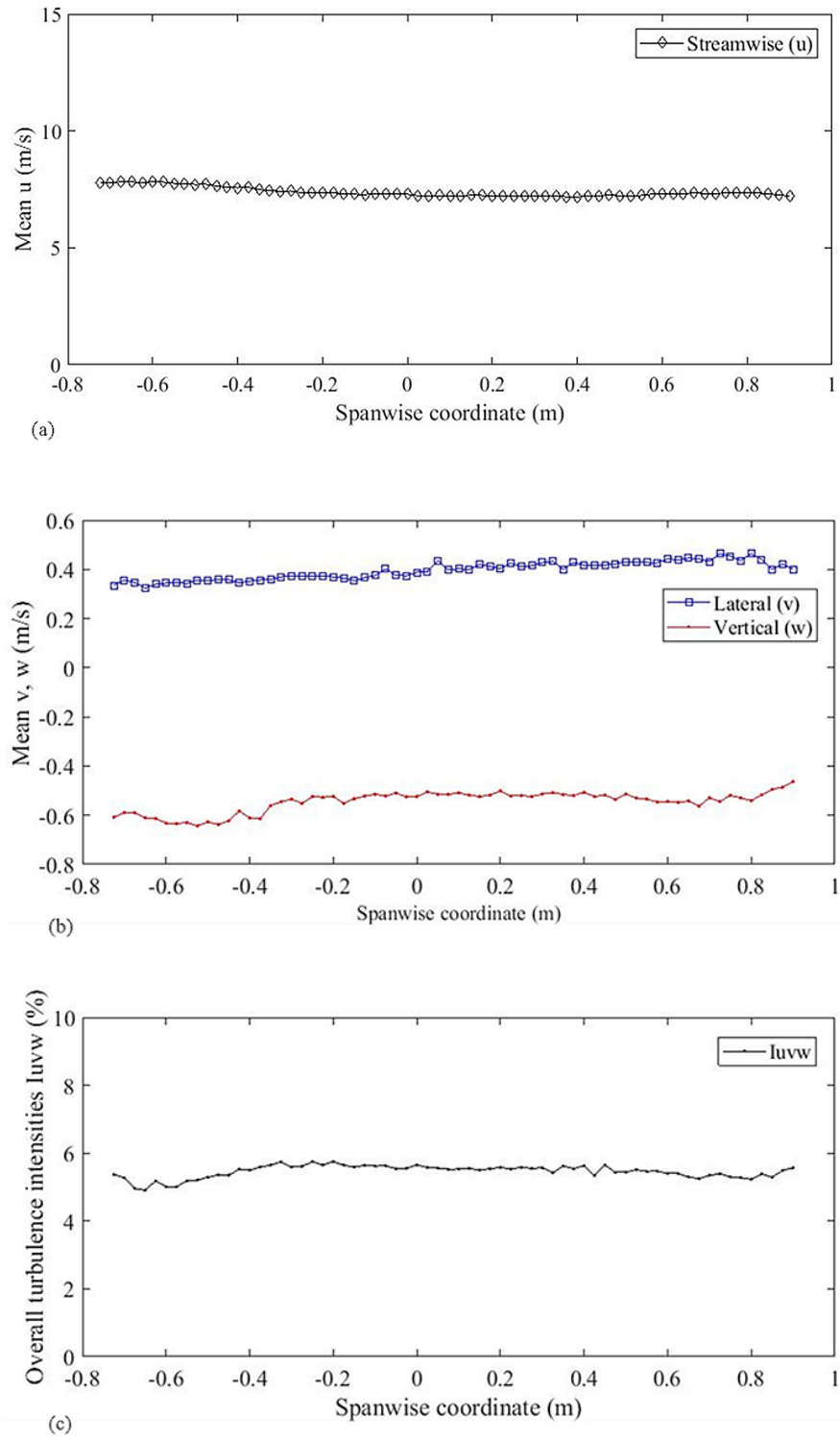
Figure 3.4: Horizontal mean Wind Profile: (a) Streamwise velocity (b) Lateral and Vertical velocity (c) Overall spanwise turbulence intensities at a height of 350 mm from the wind tunnel floor.

It was also observed by a number of HWP tests performed at different heights from the ground that there are much more differences in the vertical and lateral mean velocities at lower heights as compared to higher heights. This is due to the turbulence intensity being higher near the ground. Thus, by analysing the HWP and VWP at different heights and positions, it was determined that the most feasible section for carrying out the experimental tests was at a height of 350 mm from the floor of the wind tunnel. At this height or higher, the mean wind velocities were found to vary negligibly. Also, a height of 350 mm for placing the splitter plate was chosen for its convenience in terms of modelling and instrumentation purposes. For illustrative purposes, Figure 3.5 shows the setup of the raised splitter plate along with the experimental models inside the wind tunnel at a yaw angle of 90°.

Figure 3.5: Setup of the splitter plate and other experimental models inside the wind tunnel at a yaw angle of 90°.

Figure 3.6 shows the VWP of the streamwise mean wind velocity and the overall turbulence intensity in correspondence to the height of the model train. As evident, there is a boundary layer growth near the floor of the wind tunnel with an increase in the streamwise mean wind velocity with height. A splitter plate assists in reducing the

boundary layer thickness along with the unwanted turbulence and boundary layer effects which would be experienced by the model on the wind tunnel floor. Therefore, it deemed appropriate in this study to place the test models on a splitter plate. Further details on the splitter plate are discussed in section 3.4.

The measurement of the vertical velocity profile over the splitter plate allows for determining the impact of the presence of a wooden splitter plate, its upwind edge and the blockage under the plate. However, upon measurement of both profiles, as illustrated in Figure 3.6, it was visible that the presence of a splitter plate does not modify the wind speed profile significantly, especially in the section where the train model was placed.
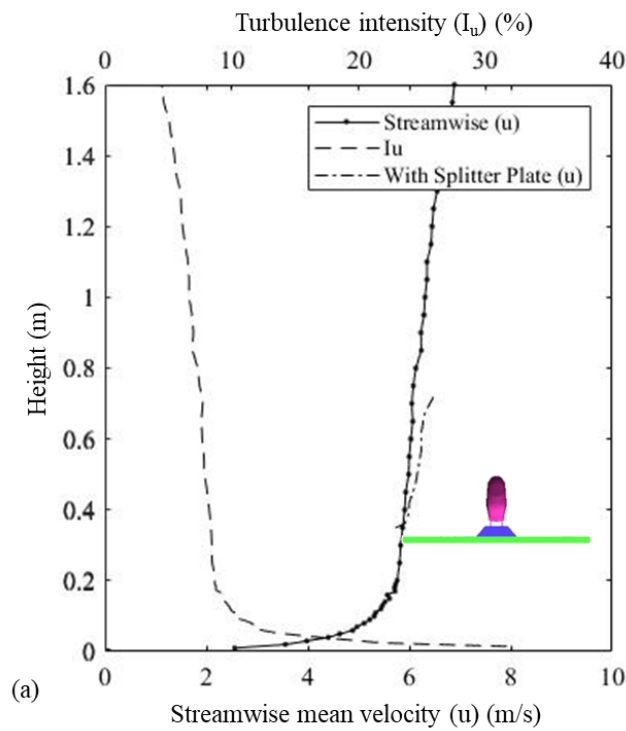
Figure 3.6: Vertical mean Wind Profile: Velocity and streamwise turbulence intensity profiles of the wind tunnel measured at the centre of the position where the experimental models were placed.

Further VWP measurements near the roof of the wind tunnel showed an irregular trend in the upper area of the wind tunnel. This signifies that the roof of the wind tunnel

effectively acts as another boundary layer and thus might be possibly introducing larger irregularities and a resulting higher level of turbulence in the corresponding flow, circulating through the top part. However, this is not a cause of concern as the model used in this study is located much below the section where irregularities begin.

Furthermore, Table 3.1 provides the spanwise averages of the mean velocities (streamwise [u], vertical [v] and lateral [w]) and the associated turbulence intensities at a height of 350 mm from the floor of the wind tunnel, essentially where the train model was placed. A wind speed of 7.2 m/s is considered to be representative of the wind conditions close to the rail network in Great Britain, based on data presented in Gallagher et al. (2018), which assessed a wide range of locations across the Great Britain railway network in terms of their wind speeds over a period of almost two years. Also, as noted in the literature review presented in chapter 2, Baker et al. (2004) found that at wind speeds lower than 5 m/s, the turbulence intensity data obtained was scattered (Baker et al., 2004), even though the initial conditions were different for Baker et al. (2004) work, thus confirming the claim.

Table 3.1: Spanwise averages of mean wind velocity and turbulence intensities along the horizontal at a height of 350 mm from the floor of the wind tunnel.

Mean wind velocity (m/s)			Turbulence intensity (%)			
u	v	w	I_u	I_v	I_w	I_{uvw}
7.2	0.4	-0.5	6.2	5.2	4.9	5.5

3.3   Scale model

A 1:25 model of the Class 390 Pendolino train is adopted as the test vehicle in this study, as the model was readily available based on the work conducted by Dorigatti et al. (2015).

Dorigatti et al. (2015) examined the simplest case possible by adopting a conventional flat ground scenario with no ballast shoulder or windbreaks. Based on the study by Baker et al. (2009), in the process of standardising wind tunnel tests, a reference scenario known as STBR (Single Track and Ballast Rail) has been proposed as the only ground scenario which should be considered (CEN, 2013) as this is a more realistic and critical scenario. A STBR is a ground configuration which has a single track only instead of double tracks and must consist of properly simulated ballast profile (track bed) along with rails suggested in CEN (2013). Thus, a STBR was chosen as a ground scenario in this study. Furthermore, wind tunnel experiments on a stationary model are carried out as these are the types of experiments which are currently prescribed in the railway standards (EC, 2008; RSSB, 2009; CEN, 2018) and have also been performed in a variety of investigations (Baker and Brockie, 1991; Cheli et al., 2010; Dorigatti et al., 2015; Avila-Sanchez et al., 2016). In terms of the choice of the wind incidence angle, a yaw angle of 30° is chosen because this value is considered at the top of the realistic range for high-speed trains (Cheli et al., 2011b) and is well within the boundaries of the low yaw angle range which ranges from 0° to 50° (Dorigatti et al., 2015). The yaw angle of 90° represents the highest transversal wind case (Cheli et al., 2010), is recommended in CEN (2018) standards and as Baker (2014) states higher yaw angles (above 60 degrees) are relevant for stationary trains. These wind incidence angles of 30° and 90° were used for the first set of experiments to form a general understanding on the use of windbreak walls with different designs. Based on the outcomes of the first set of experiments, the objectives of this study were further developed to perform a second set of experiments. For the second set of experiments, four specific experimental cases were chosen and were investigated under a varying wind incidence angle from 20° to 90° with an increment of

10°. This was done to comprehend the sensitivity of the results to varying wind incidence angles and for understanding the worst wind incidence angle to the track and the train for the Class 390 train model, specifically at a particular case.

Figure 3.7a shows an image of the scale model which was used in this study and Figure 3.7b shows the full-scale Class 390 train. The scale model used in this study is a full reproduction of the leading car and partial trailing car of the full-scale train. This research entailed measurements only on the leading car of the train for investigation, primarily because of the limitations of the wind tunnel size and also several researchers (Barcala and Meseguer, 2007; Bocciolone et al., 2008; Cheli et al., 2010; Dorigatti et al., 2015) in the past have focused their studies on the leading coach of the train only based on the assumption that significant aerodynamic forces are present around this region. The partial trailing car which was a half-car is only included in this study to provide a realistic flow around the train, based on the CEN (2018) standards.

(a)   (b)
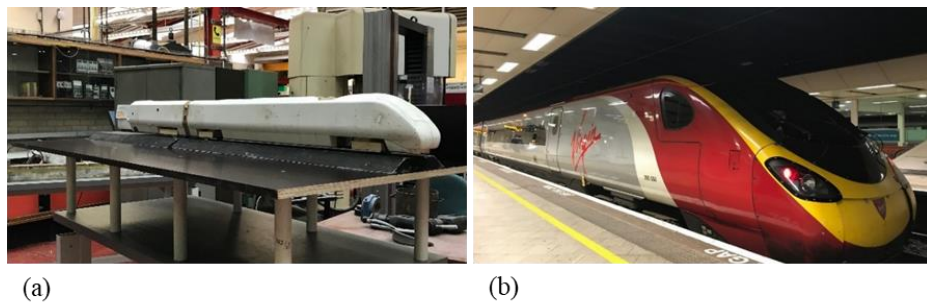
Figure 3.7: Image of the (a) 1:25 scale model of Class 390 Pendolino train used in this study (b) full-scale of the Class 390 Pendolino train.

3.3.1 Pressure taps

Pressure taps are created by drilling a small hole in the model surface. Each pressure tap is fashioned by the insertion of cylindrical stainless-steel tubes with an inner diameter of 1.5 mm and an outer diameter of 2 mm. Each tube is 12 mm long and is connected to the

holes on the internal walls of the model by gluing them in place using an epoxy structural adhesive.

PVC tubings were used to connect the pressure taps to channels of the Multi-Channel-Pressure-System. A total number of 162 pressure taps are used in the experiments. All of these pressure taps are fitted on the model's leading car and are arranged in a series of 14 loops (A-N), as shown in Figure 3.8. Table 3.2 provides the distance of each loop (X) from the nose of the train, normalised to the total length of the first car (L), which was 1000 mm. In order to ensure consistency of the data received from different experimental runs, one pressure tap was considered as the reference pressure tap. This tap was constantly monitored in each experiment by keeping it connected to one of the channels of the Multi-Channel-Pressure-System. Since the Multi-Channel-Pressure-System consists of only 64 channels, each experiment was carried out three times.
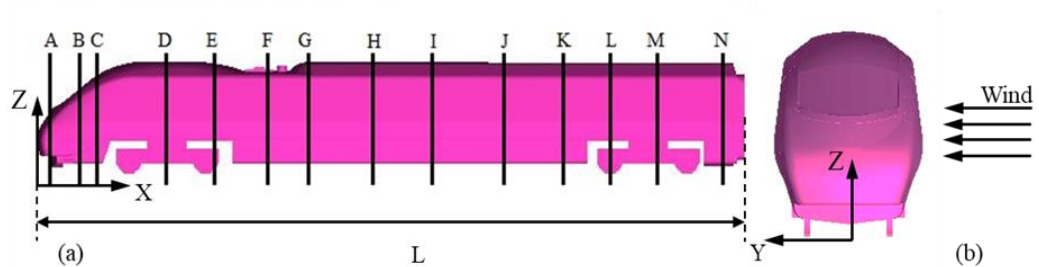
Figure 3.8: (a) Position of the loops consisting of pressure taps along the vehicle and (b) Coordinate system with reference to onset wind.

Table 3.2: Longitudinal position of each loop (X) with respect to the overall length of the model (L).

Loop	A	B	C	D	E	F	G
X/L	0.018	0.055	0.085	0.185	0.250	0.325	0.390
Loop	H	I	J	K	L	M	N
X/L	0.480	0.560	0.665	0.750	0.810	0.890	0.970

3.4 Experimental setup

The train model was placed on top of the STBR which was mounted centrally on a splitter plate. Figure 3.9 shows the overall dimensions of the train, STBR and the splitter plate. The overall length of the model train is 1500 mm while the width is 110 mm and the height is 156 mm. The splitter plate is a wooden plate with a 20 mm thickness, positioned at a 300 mm height from the floor of the wind tunnel.
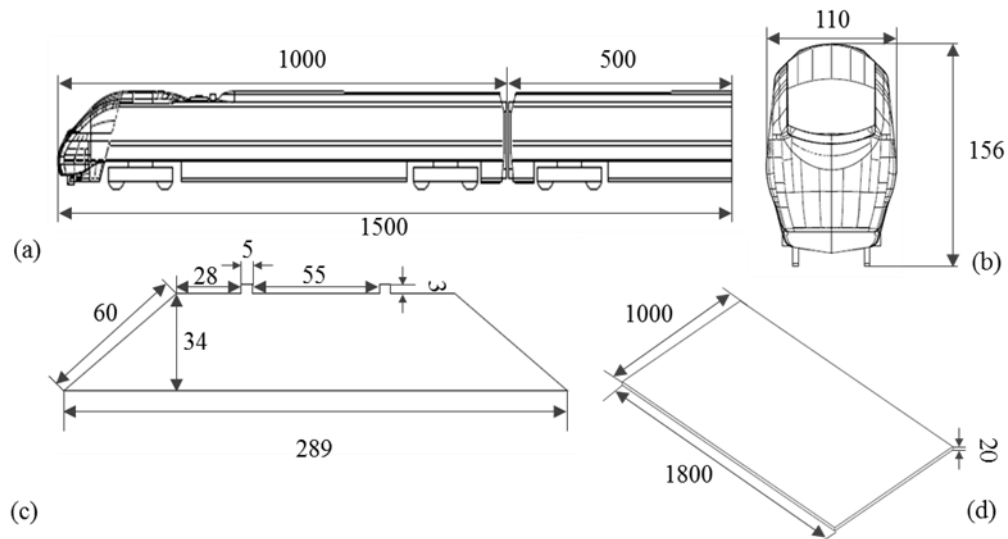
Figure 3.9: Overall dimensions in mm of (a and b) the Class 390 Pendolino scale model (c) the STBR used in this study and (d) the splitter plate.

3.4.1 Test cases

A number of experiments were carried out for different cases at two different wind incidence angles: 30° and 90°. These cases are illustrated in Figure 3.10 and are listed below:

(a) Track without any windbreak wall
(b) Track with windbreak wall 1 (Height of 160 mm)

(c) Track with windbreak wall 2 (Height of 190 mm. Same as the train height)

(d) Track with windbreak wall 3 (Height of 260 mm)

(e) Track with windbreak wall 4 (Height of 210 mm with a 45° transition angle)

(f) Track with windbreak wall 5 (Height of 210 mm with a 90° transition angle)

It must be noted that the distance between the leeward side of the windbreak wall and the centre of the track (COT) was 1.54H, where H is defined as the height of the train. For walls with transition regions, the distance between the COT and the leeward sides of the transition regions of windbreak walls 4 and 5, was 0.95H and 0.91H, respectively. Furthermore, although the main aim of this research was to investigate the effect of different types of windbreak walls on the flow which forms around the train, it was important to first obtain data for a case without any walls and just the model train. Therefore test case (a) will be used as a benchmark case and will show the intensity of the change in the results when compared to the cases with windbreak walls. With regards to the windbreak walls, the main reason for choosing three different heights for the continuous windbreak wall was to express these heights with respect to the train height along with the track. Hence, windbreak wall 1 was meant to be shorter than the train height, windbreak wall 2 was same as the train height and windbreak wall 3 was designed to be much taller than train height. All these heights were chosen to assess the sheltering effects of the windbreak walls on the train. It must be noted that for the test case (c) listed above, the height of the windbreak wall is 190 mm in order to to match the height of the train and the STBR as the train model is placed on the STBR and the splitter plate.

Moreover, several initial tests were also carried out where the researcher of this study carried out a number of different experiments on the continuous windbreak walls with heights of 160 mm, 190 mm (same as train height), 210 mm (not shown in this thesis) and 260 mm. Analysis of the results revealed that similar results (within experimental

uncertainty limits) were achieved for windbreak walls with heights of 190 mm and 210 mm. However, for the windbreak walls with transition regions, a slightly higher height of 210 mm was chosen to provide a greater shielding effect, if any. In addition, the transition regions were chosen in accordance with the appropriateness of the physical angle. A transition region of 90° appears to be the "normal" shape as it is the most appropriate physical angle and is also the maximum possible angle. Since 45° transition angle would account for a mid-way between the no transition region (0° transition angle) and maximum transition region (90° transition region), it was also considered in this study. Obviously, due to resource constraints, not every transitional angle can be examined. Also, the experimental results obtained with the use of wall 4 will be used to validate the numerical work carried out in this study.
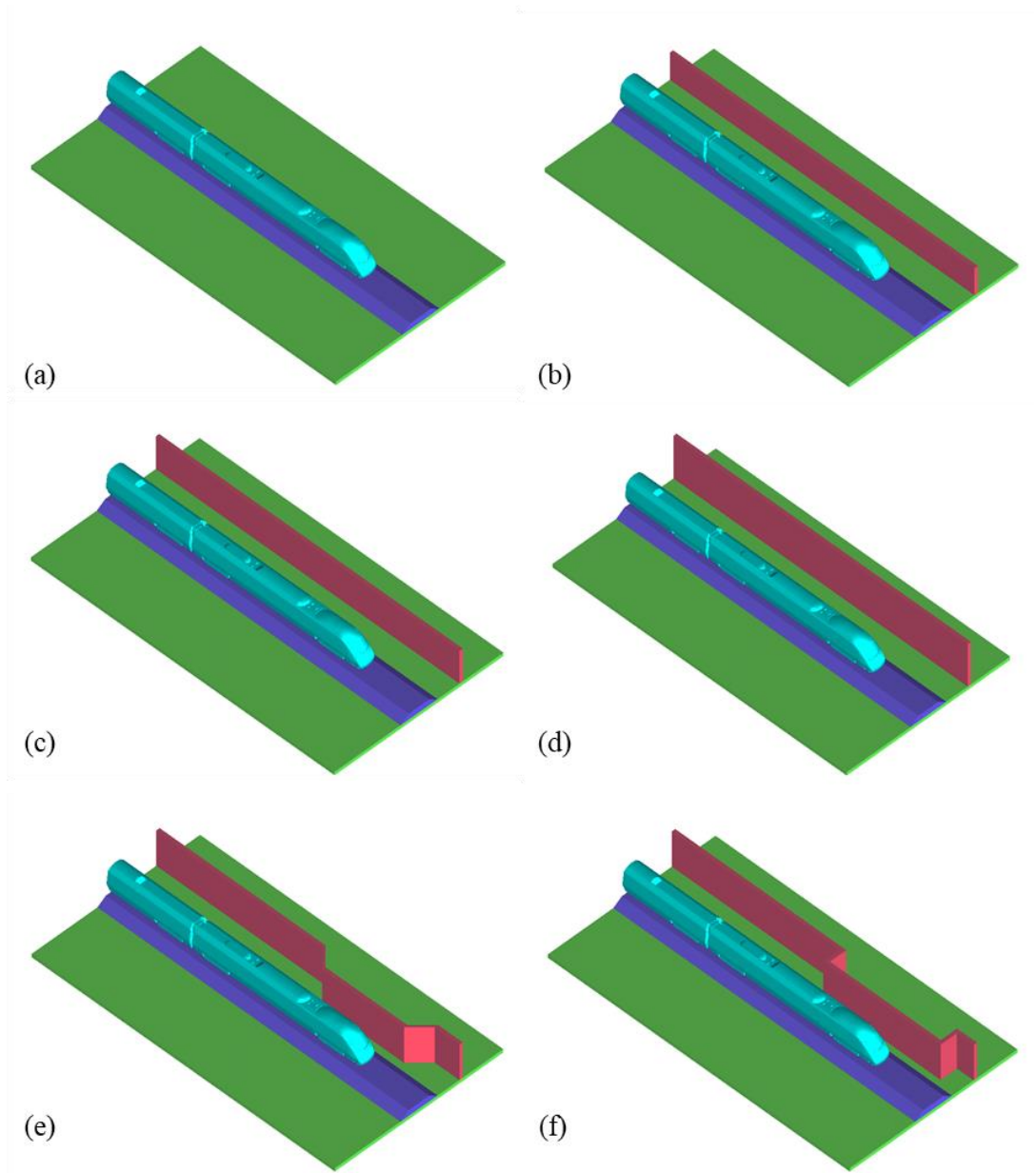
Figure 3.10: An illustration of the isometric views of different cases, which were examined in this study.

While the first set of experiments were performed to provide data on a few different types of cases which could help form a general understanding on the different windbreak walls analyses, these results may be limited in terms of the wind incident angles. Therefore, following on, another set of experiments were carried out with the purpose of investigating the effect of changing the wind incidence angle on the cases examined. To

elaborate, in these experiments, windbreak walls 4 and 5 (i.e. the walls with transition regions) were mainly examined and explored in depth in addition to two more cases. The reason behind choosing windbreak walls 4 and 5 mainly for these second set of experiments was merely based on the aim of this study, which is to form a deep understanding on the aerodynamic flow around a passenger train placed along a windbreak wall subjected to crosswinds and investigate how transition regions in the windbreak wall affect the pressure distribution and magnitude of aerodynamic forces experienced by the train. As discussed in chapter 1, constructing continuous windbreak walls is not possible due to possible complexities in the surrounding terrain such as cuttings, which cannot be avoided. Hence, additional experimental work on the discontinuous structures of windbreaks is essential.

The terms WWS and LWS denote Windward Side and Leeward Side, respectively. It must also be noted that each case was performed at varying wind incidence angles, ranging from 20° to 90°, with an increment of 10°. These cases are listed below:

    (g) Track without any windbreak wall

    (h) Track with windbreak wall 4 (Height of 210 mm with a 45° transition angle) in the WWS

    (i) Track with windbreak wall 5 (Height of 210 mm with a 90° transition angle) in the WWS

    (j) Track with windbreak wall 2 (Height of 190 mm) on the LWS only

A further test was performed to understand the effect of with wind barriers on both sides at two different wind incidence angles, 30° and 90° for:

    (k) Track with windbreak wall 4 (Height of 210 mm with a 45° transition angle) in the WWS and windbreak wall 2 (Height of 190 mm) in the LWS

Figure 3.11 shows the model set-ups at yaw angles of 90° for different cases where Figure 3.11a shows the case with continuous windbreak wall 2, Figure 3.11b shows the case with windbreak wall 4 consisting of a transition region of 45° and Figure 3.11c shows the case with windbreak wall 5 consisting of a transition region of 90°. In light of the flow characterisation, for a yaw angle of 90°, the model was placed slightly on the left hand side in order to prevent any constraining effects of the wind tunnel side walls on the nose of the train along with an enhanced spanwise uniformity to the onset wind. Also, according to railway standards (CEN, 2018), a minimum distance of 8000 mm with respect to full-scale geometry is required from the nose of the train to the start of the track. Thus, in this study at 1:25 scale, a distance of 300 mm was maintained.

According to CEN (2018) standards, the blockage ratio is defined at a yaw angle of 30°. In this study, the blockage represented by the train model, STBR and the splitter plate is approximately 6%, based on a length averaged cross-sectional area of the splitter plate at a 30° yawed configuration. It is worth mentioning that the lower bound for the blockage ratio was 6% while the upper bound for the tallest windbreak wall case was 10%. The UoB's wind tunnel used in this study requires no blockage correction, based on EN 14067-6, section 5.3.4.7 of CEN (2018). As CEN (2018) states, in closed test sections, the coefficients are overestimated, thus it is conservative not to apply any blockage corrections. Nevertheless, the blockage ratio, defined at a yaw angle of 30°, is recommended to be less than 15%, which was also the case in this study, where the blockage ratio was much lower than 15%.

The Mach number is calculated as 0.03 while the ratio of the total length of the train model to the width of the tunnel is 0.75. These factors in addition to the design of the STBR agree well with the CEN (2018) standards. The Reynolds number based on the

reference velocity of the wind relative to the train of 7.2 m/s and train height, was ~1×10^5. It is acknowledged that the Reynolds number of the flow was lower than 2.5×10^5, specified by CEN (2018), and the turbulence intensity of the flow was 5.5%, which was higher than 2.5%, specified by CEN (2018). This is one of the limitations of this study which was experienced due to the potential constraints of the wind tunnel facility. It is also recognised that the Reynolds numbers of the experiments presented in this study are lower than the corresponding full-scale values. However, previous work done by Sterling et al. (2010) within similar Reynolds number ranges has shown that such modelling can achieve appropriate results provided they are interpreted with care.
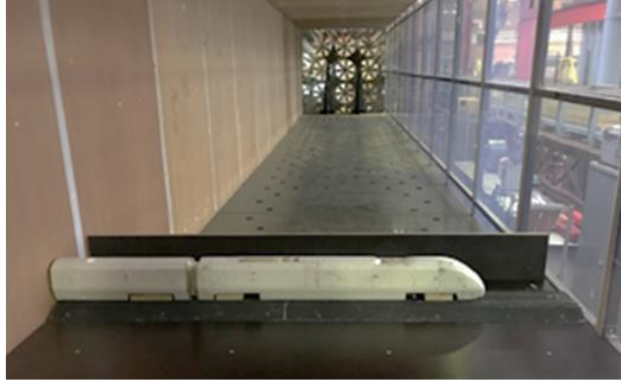
(a)

(b)

(c)

Figure 3.11: The experimental set-up of the models inside the wind tunnel at a yaw angle of 90° with a (a) continuous windbreak wall 2, (b) windbreak wall consisting of a transition region of 45°, (c) windbreak wall consisting of a transition region of 90°.

3.5   Experimental procedures

Following on the crosswind characterisation of the wind tunnel as discussed in section 3.2.2, in addition to the cobra probes, a TFI traversing system was used for undertaking the measurements. The reference pressure tubing was vented far away from the wind tunnel facility. Each wind profile measurement involved the Cobra probe to be zeroed prior to the activation of the fans. This was done to ensure that the measurements carried out were made with respect to a still air situation. The probe needs to be zeroed regularly to eliminate the offset voltages from the pressure transducers as offsets can change with variations in temperature and the rotation of the probe.

Ambient conditions including temperature, atmospheric pressure and relative humidity were all monitored using a digital barometer and all measurements recorded were input in the software manually, prior to each run, in order to set the working fluid characteristics in the sampling control settings. This is important as these parameters are needed to produce the relevant output data. Next, the wind tunnel fans were activated and allowed to power on their full running capacity. To achieve the full operational mode, a start-up time of around 60 seconds was maintained. Following this, the measurements were carried out and data was recorded at a sampling time of 30 seconds for each measuring point. This sampling time was chosen based on convergence tests conducted, where running averages were measured with increasing sampling durations from 10 seconds to 60 seconds. From the convergence tests, it was revealed that a sampling duration of 30 seconds was long enough to determine the time average of the quantities measured with an uncertainty below 1%. The total number of samples collected were 30,000 resulting in a data output rate of 1 kHz. As noted earlier, this sampling frequency was shown to be sufficient in the preliminary tests while meeting manufacturer guidelines (TFI, 2011).

96

Once the flow characterisation was achieved and a reasonable position for carrying out the experiments was chosen, as discussed in section 3.2.2, the next step involved introducing the test models inside the wind tunnel facility. The train model was placed on top of the STBR which was mounted centrally on a splitter plate, which was further supported using PVC frame legs. The train model was equipped with pressure taps which were then connected to the channels of the Multi-Channel-Pressure-System through PVC tubings. To ensure consistency of the data received from different experimental runs, one pressure tap was considered as the reference pressure tap. Multiple runs are needed to improve data quality as one of the reasons for experimental measurement uncertainty is due to the operator errors. Therefore, repeatability refers to the degree to which repeated measurements under unchanged boundary conditions demonstrate same outcomes.

The Multi-Channel-Pressure-System was then connected to a University-owned desktop computer, located outside the wind tunnel facility with the use of a long communication cable. Following on, the fans were activated with the use of wind tunnel circuitry and the relevant software. Similar to the flow characterisation steps, in order to achieve the full operational mode, a start-up time of around 60 seconds was provided before any data was recorded. With the aid of the Multi-Channel-Pressure-System and the data acquisition system, the surface pressure distribution was sampled. Each test case was repeated twice for a greater accuracy in the results. Upon completion, the wind tunnel fans were deactivated, and the automatically collected and stored data was downloaded and backed up. Finally, all secure connections were detached, and the models were removed from the wind tunnel facility.

3.6 Aerodynamic load experiment processing methodology

Under the action of crosswinds, a vehicle experiences several flow patterns around its body. As a result, a pressure distribution forms around a body leading to a series of aerodynamic loads to develop. These aerodynamic loads, which act on a train, can be classified as aerodynamic forces and moments. This section aims to provide a description of the methodology adopted to calculate the overall mean aerodynamic load coefficients for the side (lateral), $\overline{C_Y}$, and lift (vertical), $\overline{C_Z}$, forces along with the rolling moments about the X-axis and leeward rail, $\overline{C_{M_X}}$ and $\overline{C_{M_{X,lee}}}$, respectively, for different test cases. Generally, these coefficients are considered as the main components of the aerodynamic loads and are usually examined for cases involving the investigation of train stability under crosswinds (Baker et al., 2004; Sanquer et al.,2004; Baker et al., 2009; RSSB, 2009; Cheli et al., 2011b; Dorigatti et al., 2015; Gallagher et al., 2018).

In this study, the overall mean aerodynamic load coefficients were calculated using a methodology based on the measurement of surface pressure distribution over the train surface. This approach has been successfully used in several earlier studies as well (Sanquer et al.,2004; Dorigatti et al., 2015; Gallagher et al., 2018) and basically, involves the discrete integration of the mean pressure coefficient distribution over the train surface. This is achieved by converting the model surface into a simplified geometry composed of discreet rectangular surfaces. While each discretised surface is centred on a pressure tap, the edges of the surfaces extend all the way to the midpoint between two neighbouring pressure taps or the model edges for outer end taps. This discretisation of the model surface area into a number of smaller areas around each pressure tap assumes that the pressure measured at each individual pressure tap is constant and uniformly distributed across the corresponding surface. This methodology, in fact, is an excellent approach when the surfaces associated to each pressure tap are small, especially where the pressure gradient is high. Similarly, the Class 390 model used in this study was

discretised into longitudinal stripes consisting of one loops of taps each. Forces on each surface were then calculated using the mean pressure coefficients.

The mean overall load coefficients per unit length for the entire vehicle can be defined as (Dorigatti et al., 2015):

$$\overline{C_Y} = \sum_j \left[\sum_i \frac{\overline{C_{p_{i,j}}} A_{i,j} (\mathbf{n}_{i,j} \cdot \mathbf{y})}{A_{ref} L_j} \right] L_j$$

(3.1)

$$\overline{C_Z} = \sum_j \left[\sum_i \frac{\overline{C_{p_{i,j}}} A_{i,j} (\mathbf{n}_{i,j} \cdot \mathbf{z})}{A_{ref} L_j} \right] L_j$$

(3.2)

$$\overline{C_{MX}} = \sum_j \left[\sum_i \frac{\overline{C_{p_{i,j}}} A_{i,j}}{A_{ref} L_j H_{ref}} \frac{\|\mathbf{d}_{i,j} \times \mathbf{n}_{i,j}\|}{\mathbf{x}} \right] L_j$$

(3.3)

$$\overline{C_{MX,lee}} = \sum_j \left[\sum_i \frac{\overline{C_{p_{i,j}}} A_{i,j}}{A_{ref} L_j H_{ref}} \frac{\|\tilde{\mathbf{d}}_{i,j} \times \mathbf{n}_{i,j}\|}{\mathbf{x}} \right] L_j$$

(3.4)

Where, based on the model discretisation, i is the index for an individual pressure tap on each loop, j is the index for the loops (or stripe) consisting of pressure taps and corresponds to the stripes of the discretised train geometry, $\overline{C_{p_{i,j}}}$ and $A_{i,j}$ represent the mean pressure coefficient value and the discretised area of each rectangular surface, respectively, A_{ref} is the nominal side area of the Class 390 leading car (78.66 m² at full-scale), H_{ref} is the nominal height of the Class 390 leading car (3.159 m at full-scale) and L_j is the length of each longitudinal stripe on the discretised model. Furthermore, considering a 2D simplification for an individual loop (at a known X/L), $\mathbf{n}_i$ is the normal

unit vector relative to each surface, associated to each pressure tap, i, $\mathbf{d}_i$ is the vector directed from the longitudinal axis (X) to the midpoint (pressure tap) of each surface and $\tilde{\mathbf{d}}_i$ is the corresponding of $\mathbf{d}_i$ but beginning from the leeward rail. Finally, $\mathbf{x}$, $\mathbf{y}$ and $\mathbf{z}$ are the unit vectors related to the X, Y and Z axes.

3.7 Numerical methodology

Computational Fluid Dynamics (CFD) is commonly used for investigating the effects of crosswinds on a model train. This present research also aims to make use of CFD as a tool to numerically solve the flow around the Class 390 model-scale train with and without windbreak walls under crosswinds.

Outcomes of the experimental work can help act as a benchmark for performing numerical simulations to better understand the flow structures in order to form an enhanced understanding of the flow behaviour around trains with windbreak walls. In this study, results of the experimental work are limited to surface pressure and aerodynamic force coefficients of the train. To obtain a further understanding on the aerodynamic flow which exists around the surface of a train with the presence of a particular kind of windbreak wall, it is important to perform numerical simulations.

Numerical simulations will be able to exhibit numerous flow features which may not be evident through experimental results while the experimental results will be used to validate the initial numerical simulations. In addition, the flow around a high-speed train consists of several small structures due to the instabilities in the shear layers (Hemida and Krajnovic, 2010). The numerical simulations will help in studying the time-dependent behaviour of the flow structures and the resulting impact on the surface pressure of the train along with the aerodynamic coefficients. In addition, numerical simulations will be

able to easily assess the relative movement of the train with different windbreak walls along with providing further details of the flow around transition regions in windbreak walls.

Numerical investigation requires CFD to solve a set of governing equations of fluid dynamics for important and desired variables related to the flow such as pressure and velocity. A set of boundary conditions are to be defined along with a prescribed computational domain. However, although CFD simulations are quite accurate, they must not be completely relied upon for real life situations as they are prone to errors based on numerical approximations, fluid behaviour assumptions, boundary conditions and human errors. In order to ascertain the accuracy of the results of numerical simulations, standard practice in academia and industry calls for the need to perform validation against physical experiments. Therefore, this research also adopts a similar approach of performing wind tunnel experiments along with CFD simulations in order to provide accurate results.

The following sections provide the numerical methodology adopted in this thesis for performing the CFD simulations on the stationary cases, comparable to the wind tunnel experiments, and on a moving case. The CFD simulations are performed to understand the external aerodynamic flow around the stationary and moving $1/25^{th}$ Class 390 pendolino train. This would allow for a comparison to be made between the experimental and numerical results in terms of the coefficients for surface pressure while also providing further information on the moving train results.

3.7.1 Geometry

In the study of CFD, it is extremely important to first understand the physics of the case being analysed along with comprehending the geometry of the model being used in the

study. To do so, a well-designed and well-developed CAD model is produced prior to performing any numerical work. However, it might be practically impossible to produce an exact replication of the full-scale model and often irrelevant details may be added. Therefore, careful adjustments should be made prior to any finite element modelling on the CAD model and any unnecessary details may be simplified for ease in meshing and simulations.

As experimental work performed at The University of Birmingham's wind-tunnel facility is used to validate the numerical simulations in this research, exact dimensions of the train model, the STBR and the windbreak wall used in the experiments are used for the CAD model. The geometry of the train model is shown in Figure 3.9. This is done to ensure a quality validation of the numerical simulations.

The origin in the current study is in line with the front face of the train, at the centre of track (COT) and at the top of rail (TOR). Hence, all given distances in this thesis are relative to the origin, unless otherwise stated.

As seen in Figure 3.8 and Figure 3.10, the numerical model has a good degree of similarity with the experimental model used in this study, shown in Figure 3.7, which had an excellent similarity with the real full-scale model. In terms of the numerical CAD model, any simplifications present were made to allow for a higher quality mesh. It is worth mentioning that similar to the wind tunnel experiments, the model used in the numerical investigation consisted of a leading vehicle and a partial trailing car. As mentioned earlier, CEN (2018) also states that the inclusion of the partial trailing car leads to a realistic flow in the vicinity of the leading vehicle as this allows for the mitigation of the influence of the wake flow, close to the leading car. Nevertheless, the adopted CAD model includes a

spoiler in the nose region, electricity equipment on the roof, a set of simplified bogies with wheels and an inter-car gap between the leading vehicle and the partial trailing car. For the moving train analysis, instead of a leading vehicle and a partial trailing car, a 1/25th three car model of the Class 390 train was used, as demonstrated in Figure 3.12. The geometry was simply created by the mirror effect in CAD modelling and hence the dimensions are consistent with Figure 3.9. In terms of the windbreak wall used for the moving train analysis, the windbreak wall had a height of 210 mm with a 45° transition angle. The rationale behind choosing this design for the moving train analysis is discussed in detail in chapter 6, section 6.1. The only difference in this windbreak wall and the wall utilised for the stationary analysis was in the length of this windbreak wall. The splitter plate, the tracks and the windbreak wall were all doubled in length. However, the distance between the train and the windbreak wall was same as in the stationary analysis. Figure 3.14 provides an illustration of the moving train case with the windbreak wall.

Figure 3.12: Train geometry used for moving train analysis.

3.7.2   Computational domain and boundary conditions

In terms of the computational domains, two domains were created; one for the stationary analysis and one for the moving analysis. Figure 3.13 presents the model geometries inside the computational domain used for the stationary analysis, where H refers to the characteristic height of the train model, 0.156 m. Although comparisons are made to the wind tunnel measurements, the computational domain is not exactly the same in size as compared to the wind tunnel. It is not necessary to keep the same dimensions as long as the domain boundaries do not interfere with the flow around the train in a physically

103

incorrect way. As CEN (2018) states, "the computational domain shall extend in the streamwise direction relative to the vehicle of interest: at least 8 characteristic heights upstream and 16 characteristic heights downstream." Similarly, in the numerical aspect of this study, the computational domain extends 29H in the streamwise direction. The width and height of the wind tunnel is 12.8H and 8H, respectively. The model centreline position is kept at a distance of 8H from the inlet and 21H from the outlet of the wind tunnel. Hemida and Krajnovic (2009) also used similar dimensions for their study and confirmed that these dimensions were considered sufficient in several other numerical studies concerning flows around similar bodies. The computational settings are similar to that of the stationary experiment. The scaled models were mounted statically and subjected to a relative wind at a 90° yaw angle, as shown in Figure 3.13.

Figure 3.13: Computational domain for stationary analysis (where H= height of the train model = 0.156 m).

Applying boundary conditions to a computational domain is one of the most important steps in a CFD simulation. This is because the boundary conditions to be applied must be realistic and practical in order to obtain an accurate numerical solution. For instance, applying a slip boundary condition to a flat plate, over which a fluid flows, would be unreasonable. This is because such a boundary condition would impose no growth of a boundary layer on the surface of the plate, which is contrary to a real-life case. Thus,

boundary conditions must be carefully applied without compromising the accuracy of the numerical solutions.

In terms of the boundary conditions applied to the computational domain for the stationary case in this study, as shown in Figure 3.13, a no-slip boundary condition is applied to the train surfaces, STBR, the splitter plate and the windbreak wall. A slip-wall boundary condition was set at the domain sides, floor and the roof. As noted in figure 3.4 and figure 3.5, the wind profile is not uniform, however, relatively stable values are obtained across the central portion of the wind tunnel and at the position where the test models are situated. Since the wind profile varies negligibly at the points of interest, it is expected that the wall boundary layer on the wind tunnel sides, roof and the floor does not impact the results significantly. A no-slip condition implies that for flows regarding viscous fluids, the fluid will have a zero-velocity relative to the solid boundary (wall). In simpler terms, a no-slip boundary condition assumes the velocity to be zero at walls. At the outlet boundary, a zero-pressure condition is prescribed. For the inlet boundary, a constant velocity condition was applied. This was based on the experimental wind tunnel characterisation, which showed an average velocity of 7.2 m/s at the point of interest. It is acknowledged from the experimental work demonstrated in Figure 3.4 and Figure 3.6 that the wind profiles are not actually uniform but are observed to vary negligibly, hence, a uniform constant velocity condition is assumed.

For the moving train analysis, a sliding mesh technique was utilised, which allows for the relative motion between the train, tracks and the windbreak wall. To do so, two domains were created: stationary domain and moving domain. The stationary domain is treated as the computational domain while the moving domain is the sliding domain, as demonstrated in Figure 3.14. The moving domain including the train body slides along

the stationary domain in the longitudinal direction with a speed of 55.83 m/s, which is the maximum operating speed of the Class 390 Pendolino train in Britain. The inlet of the stationary domain provides wind at a constant speed of 15 m/s. Therefore, based on the crosswind speed and the train speed, the corresponding yaw angle is 15° with a relative velocity of 57.8 m/s. A 15° yaw angle was chosen as it belongs in the low yaw angle range. Usually, higher yaw angles are relevant for stationary or slow-moving trains only (Baker, 2014a). In addition, this yaw angle creates an opportunity to further validate the numerical results obtained in this study.

It must be noted that a velocity inlet boundary has commonly been utilised for simulating oncoming flow in several earlier works (Hemida and Krajnovic, 2009; Wang et al., 2014; Garcia et al., 2015; Morden et al., 2015; Niu et al., 2017a).
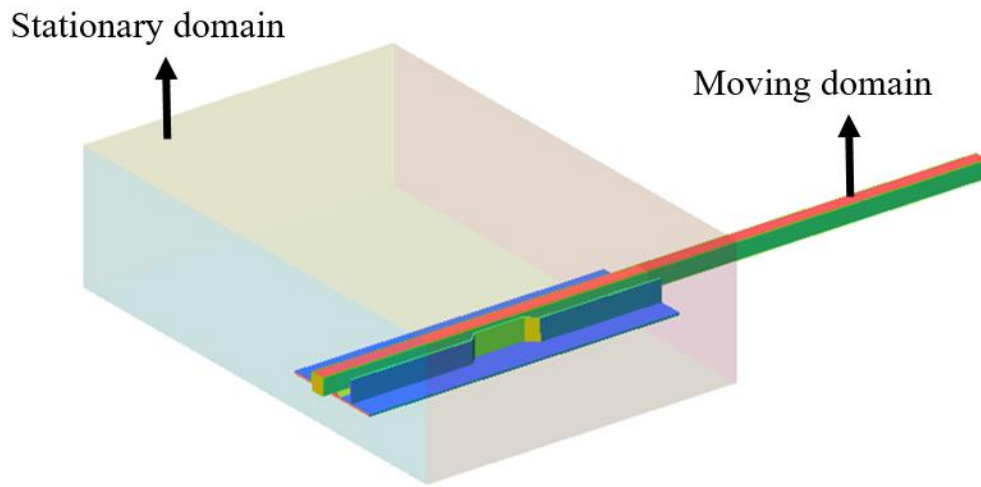
Figure 3.14: Computational (stationary) domain and sliding (moving) domain for moving train analysis.

The distance between the train and the windbreak wall was kept same as the stationary case, and thus the only difference between this case and the stationary case was in the size of the train, the design of the windbreak wall and the movement of the train. In terms of the boundary conditions, a constant velocity of 55.83 m/s was applied at the inlet of

the stationary domain while a zero-pressure condition was prescribed at the outlet. A no-slip boundary condition is applied to the train surfaces, STBR, the splitter plate, the windbreak wall and the floor of the wind tunnel. A slip-wall boundary condition was set at the domain sides and the roof. The boundary condition between the stationary domain and the moving domain is the interface boundary condition, which helps exchange data between the two meshes.

3.7.3 Numerical method

The current study uses the open-source software, OpenFOAM version 5.0 (Openfoam, 2018) for performing numerical simulations on the stationary case and the commercial finite volume solver ANSYS Fluent version 18.2 (Ansys, 2017) to carry out numerical simulations on the moving train case. It must be noted that widely distributed codes such as those used for OpenFOAM and ANSYS are considered to be accurate and reliable because of being scrutinised and enhanced by a large group of diverse developers all determined to make sure that the code performs well. A number of researchers have also made comparisons of the two well-known CFD software, OpenFOAM and ANSYS (Fluent) for simulating same cases and have concluded that these software have comparable predictive powers (Welahettige and Vaagsaether, 2016; Ariza et al., 2018). In addition, researchers have verified that these codes use same constant values and initial values for the turbulence models used. Therefore, if the creation of the geometry, generation of the mesh, definition of boundary conditions and the use of turbulence models is kept consistent when using the two different CFD software, the obtained solutions can be expected to be similar with demonstrating analogous flow patterns and flow fields.

The Improved Delayed Detached Eddy Simulation (IDDES) investigation based on the turbulence model SST (Shear Stress Transport) k-ω is used in this study to explore the flow properties as well as flow behaviour around the train surface. The flow is considered as incompressible as the Mach number of the flow around the train is lower than 0.3. Earlier numerical works on passenger train aerodynamics have shown that SST k-ω approach offers the best prediction of surface pressure, amongst the available RANS models (Morden et al., 2015; Premoli et al., 2016). Researchers have also determined that a DES approach is able to successfully replicate the results from a wind tunnel experiment, obviously within the margins of uncertainty (Diedrichs, 2010; Morden et al., 2015). Hence, the study adopted the SST k-ω and DES methods for the numerical simulations of the flow around the train, subjected to crosswinds.

Based on the reasoning provided in chapter 2, section 2.6.3.1, the IDDES model was chosen in this work to numerically investigate the effects of windbreak walls on the aerodynamic performance of a high-speed passenger train. In this study, for the stationary simulation performed in OpenFOAM, a second order backward implicit scheme was used to discretise the temporal terms for all IDDES simulations. A second order central-differencing scheme was used to discretise the diffusive and sub-grid fluxes. A second order blended LUST (Linear-Upwind Stabilised Transport) scheme was used to discretise the convective term. In this scheme, the blending factor optimises the balance between stability and accuracy (OpenFOAM, 2018). For the pressure-velocity decoupling in RANS simulations, the widely used Semi-Implicit Method for Pressure-Linked equations (SIMPLE) was selected while the Pressure Interpolated Splitting of Operators (PISO) algorithm was used for the DES simulations. For the moving train simulation conducted using ANSYS Fluent, to solve the momentum equations and the k-ω equations, a bounded

central differencing scheme and a second order upwind scheme were used, respectively. For the time integral, a second-order implicit scheme was implemented. Overall, these numerical schemes and functions are commonly chosen for train aerodynamic studies as researchers have determined their importance and relevance to achieve both stable and accurate numerical solutions (Flynn et al., 2014; Li et al., 2018; Niu et al., 2018; He et al., 2019).

For both, stationary and moving simulations, the time step was set as $\Delta t = 1.0 \times 10^{-4}$ s, which ensured corresponding Courant-Friedrichs-Lewy (CFL) numbers around the model and in the majority of the computational domain were less than 1. The cases were also run initially for a few seconds to fully develop the flow field. Although the associated computational costs are high with such small time steps, these are compensated by the resolution of the high frequency / small-scale structures in the flow. Further, at each time step, the solutions to the discretised equations were considered to converge when the absolute value for the residuals was 10^{-8}, for both the momentum and continuity equations. Also, at each time, non-orthogonal correctors were used. For both simulations, once the flow was fully developed in the computational domain, the time-averaging of pressure and velocity took place, and this was ensured through the monitoring of aerodynamic coefficients. All simulations were initialised with the use of a steady state RANS solver before switching to DES. The simulations were then allowed to run for a few seconds during which the flow field was time averaged. Fully developed turbulent flow was obtained after a non-dimensional time, $t^* = \frac{tV_{rel}}{H} = 75$, where t is the simulation time, V_{rel} is the free stream velocity and H is the height of the train. The time-averaging was carried out for the time needed for the flow to travel the entire domain 8 times, giving an equivalent full-scale time of 20s ensuring that the lower frequency

motions had occurred for several periods. For the moving simulations, an unsteady calculation method with a dual-time step format was used for time discretisation and as mentioned before, the physical time step was set as $\Delta t = 1.0 \times 10^{-4}$ s. Once the flow was developed completely inside the stationary domain, the train was allowed to enter the domain and the different forces and moments on the moving train were monitored against time. The IDDES numerical simulations were run on the University of Birmingham's BlueBEAR facility, which allows for high performance computing (HPC). The computations were run in parallel using 200 cores for three weeks.

3.7.4 Computational mesh

This work used Numeca International's product, HEXPRESS™/Hybrid version 6.2 (NUMECA International, 2017) as a 3D mesh generation tool for generating unstructured hexahedral meshes. Amongst the several different meshing utilities available, HEXPRESS/Hybrid is used in this present work due to its ability of meshing large and complex geometries in a fast and easy manner. In addition, the use of this utility for meshing allows for the generation of isotropic and hexahedral dominant meshes. Due to the complexity of the geometry, the meshes did contain cells of tetrahedral, pyramids and prism types which are all applicable for use in ANSYS Fluent. The meshes used in this study were in the range of 8-20 million cells and the quality of these meshes was validated with the use of mesh metrics feature. It was ensured that the maximum skewness of each cell was maintained below 4 while the maximum non-orthogonality was less than 60, where corrections were made in the solver for the non-orthogonality. Also, the aspect ratio was maintained as less than 5. As noted by previous researchers (Flynn, 2015), maintaining these quantities allows for verifying the quality of the meshes in accordance

with those recommended by modelling guides of different solvers such as ANSYS Fluent and OpenFOAM.

Figure 3.15 shows the surface mesh on the first car of the complex geometry of the Class 390 pendolino train. Although a few simplifications are made to the CAD model if necessary in order to generate a high quality mesh, the under body area of the vehicle is carefully considered due to the larger boundary layer growth expected in that region (Sterling et al., 2008; Baker et al., 2013b) and due to its known importance on the flow field around a train (Baker, 2010). Additionally, different refinement techniques were applied to different regions in the mesh in order to capture any sensitive and turbulent regions which may develop near the surface of the train with the aim of increasing the accuracy of the simulations results to be achieved. This was done using multiple refinement boxes of different sizes based on the height of the train. These refinement boxes were created to ensure that the mesh around the train and the windbreak wall is sufficiently fine and the computational resources are used for the most interesting regions where the interaction of the flow and the train occurs. Another point of refinement zone was the underbody of the train in order to adequately resolve the highly turbulent flow which exists beneath the train. The overall number of cells in the meshes generated were controlled through a combination of altering the number of divisions that occurred within each refinement region, the surface refinement level and the cell size of the base mesh. Figure 3.16 shows the top view mesh resolution in a cut-plane around the first and partial second car of the Class 390 Pendolino train used in this study. Figure 3.17 shows the side view mesh resolution in a cut-plane around the first car of the Class 390 Pendolino train used in this study. The boundary layer shown in Figure 3.17 is an important element of the turbulent flow and therefore, its representation or resolution is essential to enhance

the accuracy and reliability of the numerical simulations. Also, in order to correctly represent the velocity gradients near the wall, prism layer cells were applied at the train surface. The first cell size was maintained as 1.1 mm. The mesh quality near the train model is extra-fine, followed by fine mesh and coarse mesh. Additionally, as Roache (1998) discussed, results arising from at least two different mesh densities should also be compared for confirming the mesh independence. Therefore, for the determination of mesh independence on the simulation results for the stationary analysis, two meshes were created in this study: 8 million and 18 million cells, respectively. In terms of wall modelling strategies, the viscous sublayer was resolved for the stationary simulation. Therefore, for the mesh created, the expansion ratio was 1.2 and this sizing resulted in an average of non-dimensional near wall spacing, $y+$, of about 1 over the train surface. This ensures that the mesh created is able to adequately resolve gradients in the sublayer. Figure 3.18 illustrates the mesh resolution for the stationary simulation around the first car of the Class 390 train in terms of $y+$. Furthermore, for the moving simulation, wall functions were used to solve the near wall flow. This resulted in an average value of $y+$ of 50, over the majority of the train's surface.
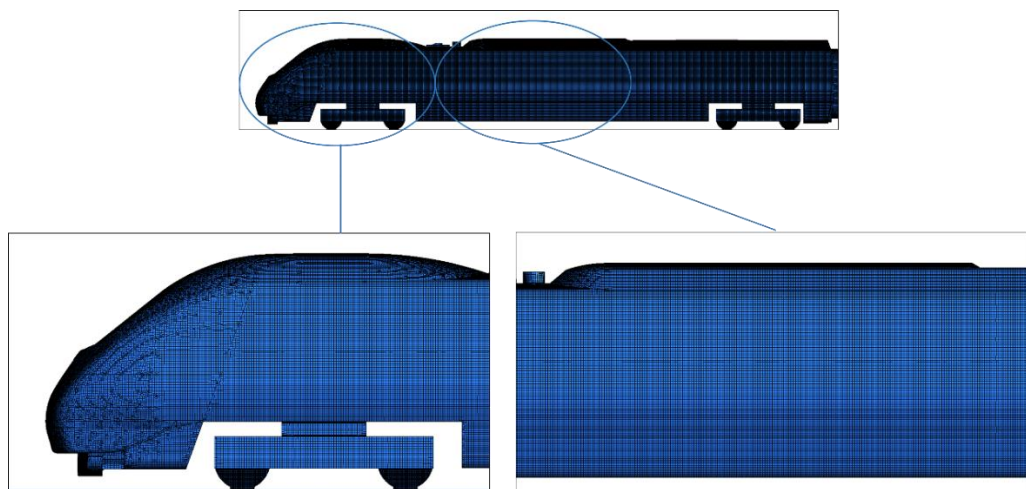
Figure 3.15: Surface mesh on the first car of the Class 390 train, for the stationary analysis.
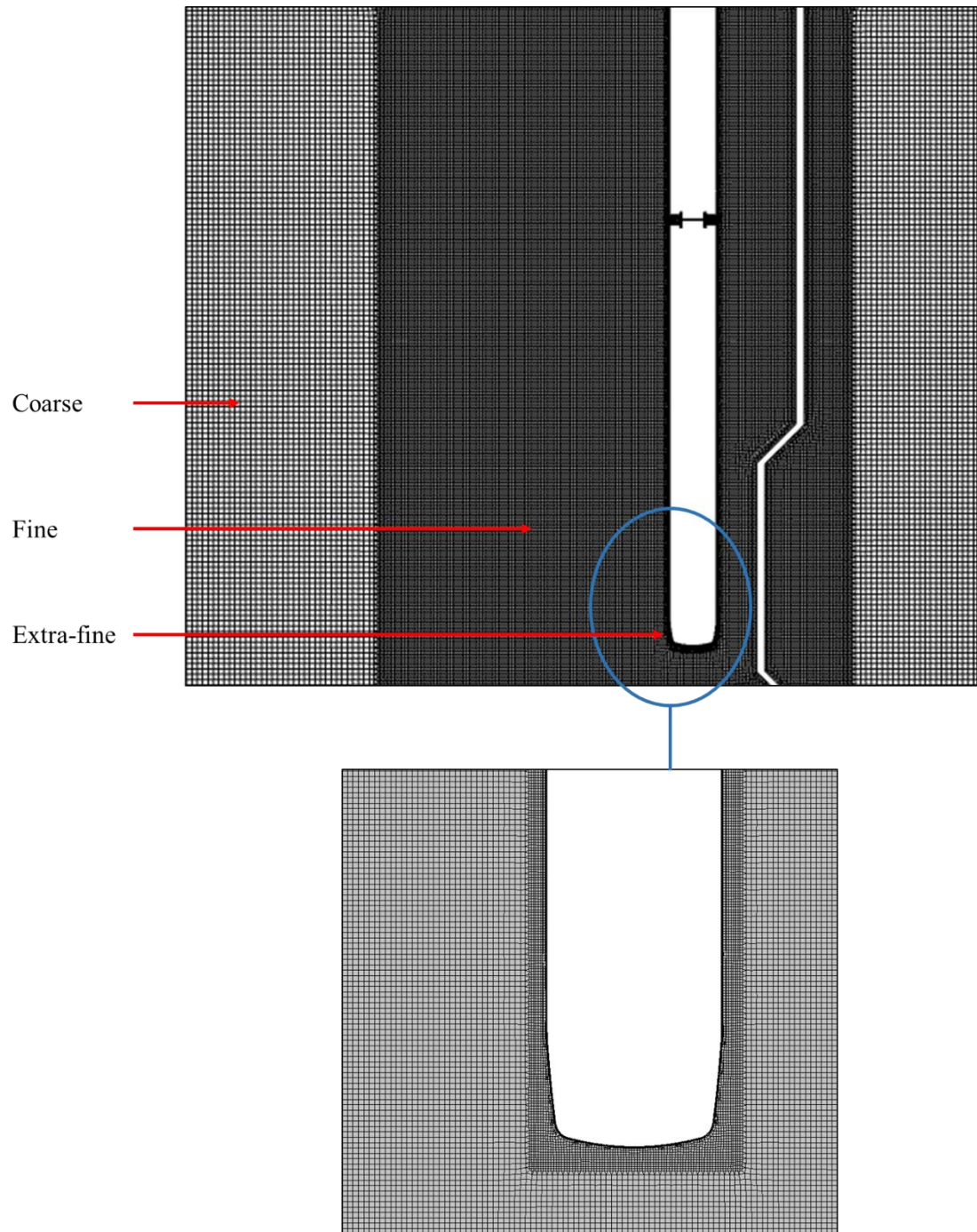
Figure 3.16: Top view: mesh resolution around the Class 390 train on a cut-plane, for
the stationary analysis.
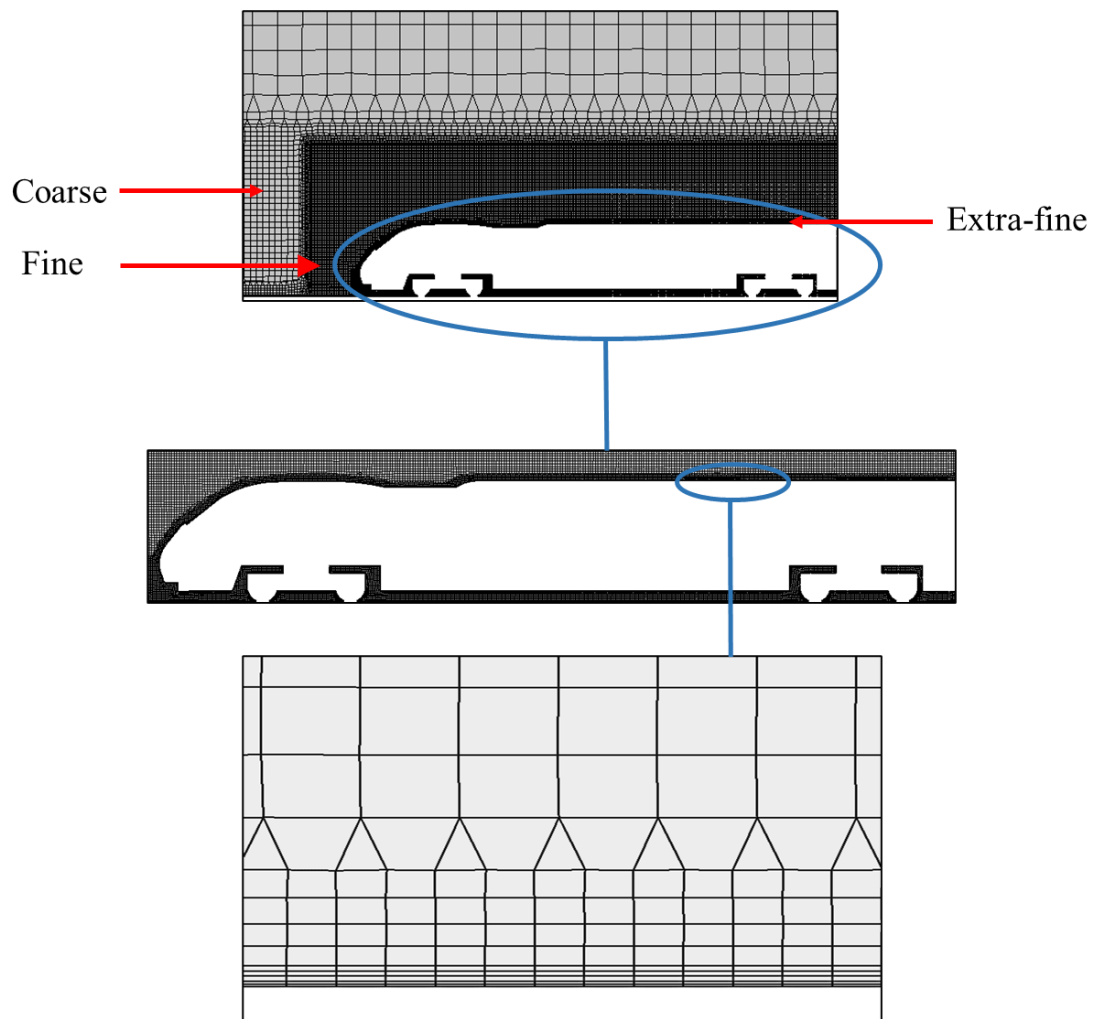
Figure 3.17: Side view: mesh resolution around the Class 390 train on a cut plane, for the stationary analysis.
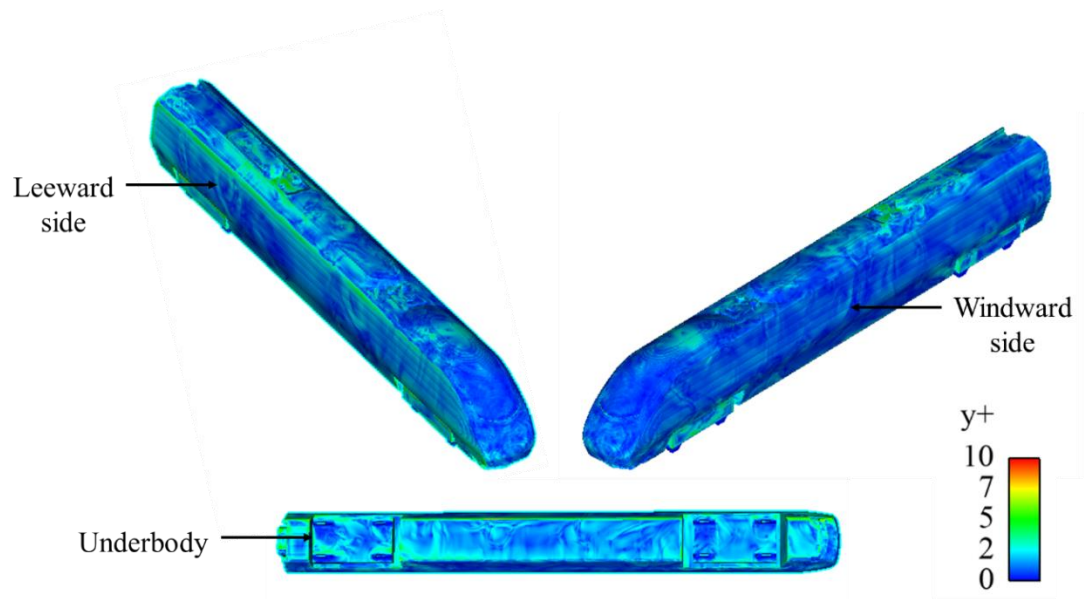
Figure 3.18: Representation of mesh resolution around the first car of the Class 390

train in terms of y^+, for the stationary analysis.

CHAPTER 4: Results of wind tunnel testing on a passenger train model subjected to crosswinds with different windbreak walls

The majority of sections in this chapter have been published in Hashmi et al. (2019).

4.1 Introduction

The main motivation of this chapter was to obtain an understanding of the aerodynamic flow which exists around a train surface in the presence of different kinds of windbreak walls. This chapter provides an insight into potential future research opportunities where the ultimate aim of this chapter would be to further analyse safety and stability of a typical high-speed passenger train. While it is acknowledged that, in reality, there is a relative movement between the train and the windbreak walls, the aim of the current chapter was to provide valuable experimental data. This data can be used as validation data for numerical simulations to better understand the flow structures in order to form an enhanced understanding of the flow behaviour around trains with windbreak walls.

This chapter provides a detailed discussion on the results of the mean non-dimensional surface pressure distribution and the aerodynamic load coefficients on the train for the different test cases assessed experimentally at the University of Birmingham's wind tunnel. Presenting results as their mean values is consistent with CEN (2016) standards, as well as other work performed in the field of railway aerodynamics (Dorigatti et al., 2015; Tomasini et al., 2015).

Section 4.2 provides and discusses the pressure distribution results obtained over the train surface for experimental cases (a – f), discussed in chapter 3, section 3.4.1, at wind

incidence angles of 30° and 90° in terms of a non-dimensional pressure coefficient C_P.

Section 4.3 provides an analysis on the overall mean aerodynamic load coefficients for

the side (lateral), $\overline{C_Y}$, and lift (vertical), $\overline{C_Z}$, forces along with the rolling moments about

the X-axis and leeward rail, $\overline{C_{MX}}$ and $\overline{C_{MX,lee}}$, respectively, for different test cases at wind

incidence angles of 30° and 90°. Section 4.4 provides and discusses the pressure

distribution results obtained over the train surface for the experimental cases (g – j),

discussed in chapter 3, section 3.4.1, in terms of a non-dimensional pressure coefficient,

C_P. This assists in understanding the effect of varying wind incidence angles on the mean

pressure coefficients. Finally, section 4.5 discusses the main outcomes of the

experimental research, while providing recommendations for further developments to this

investigation.

4.2 Mean pressure coefficients

This section provides and discusses the pressure distribution results obtained over the

train surface for experimental cases (a – f), discussed in chapter 3, section 3.4.1, at wind

incidence angles of 30° and 90° in terms of a non-dimensional pressure coefficient, C_P:

$$C_P = \frac{P - P_o}{0.5\rho V_{rel}^2}$$

(4.1)

where P is the actual surface pressure at a particular pressure tap, P_o is the reference

pressure, ρ is the air density and V_{rel} is the free stream velocity of the wind relative to the

train. In terms of normalising the data for achieving an accurate C_P value for each pressure

tap, the reference pressure of a known location, outside the wind tunnel section, was

considered. This was done to ensure the location is not affected by the onset wind

conditions. For the reference velocity, this was measured at the position of the test models

without the presence of the models, prior to the any experimental work. In addition, the mean non-dimensional pressure coefficient, $\overline{C_P}$, provided for each tap was calculated based on the time-average values of the actual surface pressure at a particular pressure tap.

As discussed earlier and demonstrated in Figure 3.8, loops A-N were arranged in a progressive manner from the nose to the tail of the leading car of the model with a total of 162 pressure taps positioned on the first car only. Figure 4.1 shows the four circumferential sections where the pressure distribution was measured at each segment. It must be noted that the location of pressure taps for each loop differed in sectional placements due to the changing cross section of the train shape. Therefore, the best method of representing data was in a polar coordinate form. The results can be divided into four different sections; where WWS and LWS refer to the windward and leeward side of the model train respectively, roof denotes the roof and UB denotes the underbody region of the model. Due to the design of the model, which shows continuous changes in its symmetry, the range of the polar angle varied for each region at different longitudinal positions of the loops i.e. at different distances from the nose of the train, as evident in Figure 4.1. The orientation of angle θ is chosen such that it aligns with the axis located at the approximate centre of the train. Also, $\theta = 0°$ is on the horizontal axis, which is close to the attachment line of the onset wind. $\theta = 90°$ represent the middle of the roof, $\theta = 180°$ is right in the centre of the wake and $\theta = 270°$ marks the centre of the underbody of the train. In addition, this method of representing data has been adopted by a number of researchers in the past (Copley, 1987; Hemida and Krajnovic, 2010; Li et al., 2018).
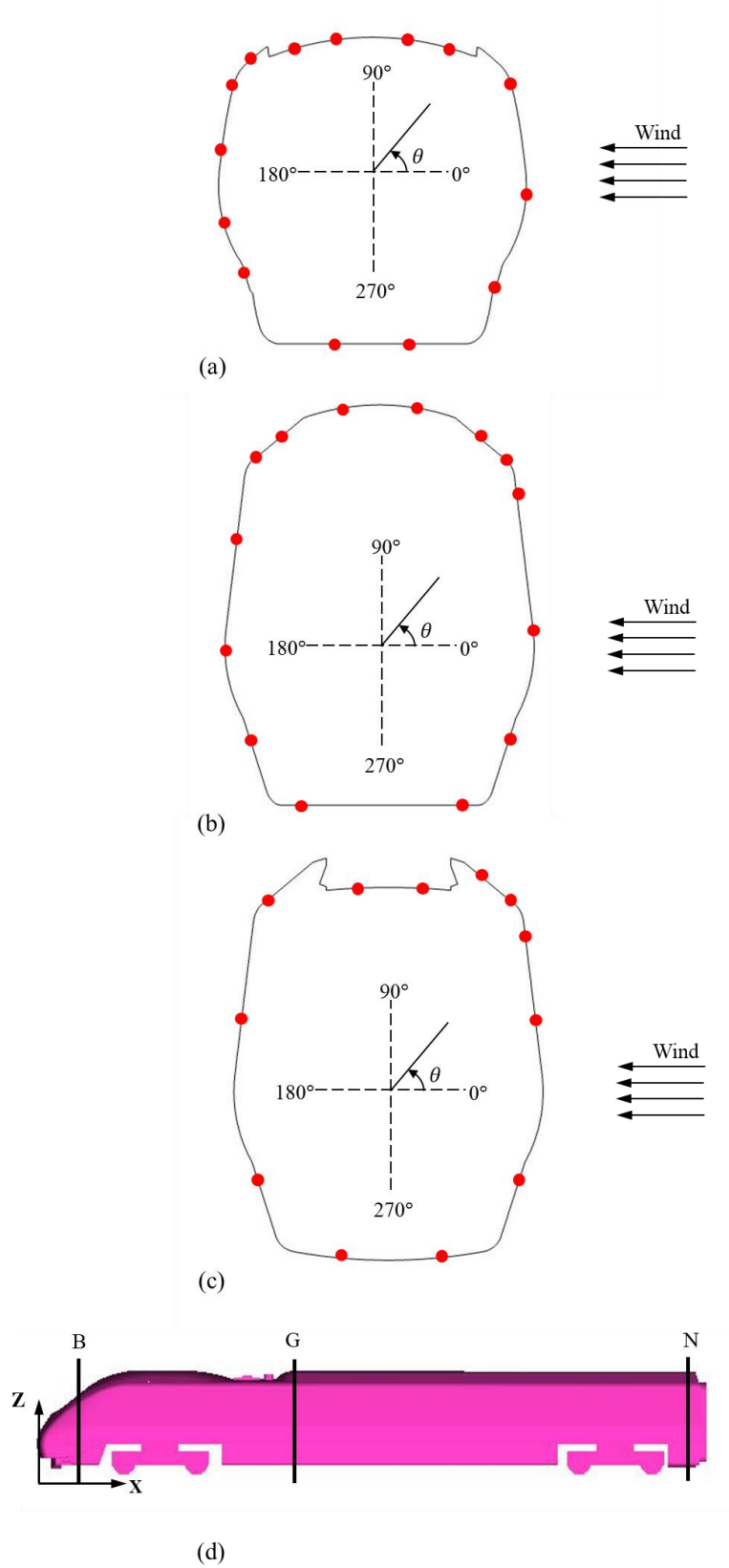
Figure 4.1: (a) (b) (c) The orientation of angle θ with respect to onset wind at Loops B, G and N, respectively and (d) the position of Loops B, G and N along the vehicle.

In terms of the results obtained, different patterns of pressure distribution are evident over the surface of the train. Firstly, it is worth mentioning that the leading car of the Class 390 train has a streamlined design. Therefore, the cross-section of the frontal region of the train, characterised as the nose of the train, presents a significant increase in the cross-sectional area down the train length (from Loops A-C). For simplicity, results on loops B, G and N are illustrated even though measurements were made at 14 loops located at different distances from the nose of the train. Appendix A presents the full set of surface mean pressure coefficient distribution for the leading car of the Class 390 model-scale train analysed in this study for the configuration without any windbreak walls at a yaw angle of 90°. As can be noted by Figures A.1 – A.4, in Appendix A, loops located near each other follow similar trendlines. Hence, only three loops are chosen to represent the nose, central and tail regions of the leading car, respectively. Nevertheless, this results section discusses the trend over the entire length of the train.

4.2.1   Results at a yaw angle of 90°

This section aims to discuss the test results obtained at a yaw angle of 90° for the experimental cases (a – f), mentioned in section 3.4.1.

4.2.1.1   Case (a): Track without any windbreak wall

Figure 4.2 shows the mean surface pressure distribution at pressure taps around loops B, G and N for the case without any windbreak wall at a yaw angle of 90°. In this case, at and near the nose of the train (loops A-B), the highest pressure values (up to $\overline{C_P} = 0.67$) are observed on the WWS of the model, compared to other regions. This is as expected due to the wind directly impinging on the surface of the vehicle at the WWS thus indicating a region of stagnation at the windward face of the train. As expected, this is the

case for all the loops which show positive $\overline{C_P}$ values at the WWS except for a few pressure taps on certain loops, which are under the impact of flow separation due to possible corner and edges with different surface orientations.

Based on the results presented in Figure 4.2, upon transition from the WWS to the roof of the model, a sharp decrease in the positive pressure values can be observed signifying a large suction at this point. This suggests that the windward edge on the roof of the train has a significant impact on the flow resulting in a negative gradient of pressure, thus indicating flow separation at this point. For similar flows, based on the train height and free-stream velocity, the flow is expected to separate from the windward corners of the roof (Copley, 1987; Baker and Sterling, 2009), which was also the case in this study. Consequently, the flow tends to show weak suctions over the roof of the model while the wake downstream of the model seems to show a little effect on the overall pressure distribution on the LWS. This analysis is based on the magnitude of the $\overline{C_P}$, which appears to be uniform on the leeward face, as the flow progresses.

At further distances from the nose of the train, similar trends in the pressure distribution can be seen as compared to the loops on the nose such as loop B. Positive pressure peaks (upto $\overline{C_P}$ =1) are evident on the WWS of the model. Regions of negative pressure are observed on the roof and LWS of the model with a strong suction peak obtained in all cases on the windward edge of the roof, as mentioned before. Also, it seems that the flow stabilises from the middle of the roof to the leeward side of the train, as shown by constant pressure values, possibly indicating the reattachment of flow after separation. In terms of the underbody region of the model, slight differences can be seen in the overall results obtained for the flow in this region. These are perhaps not surprising based on the practical limitations and difficulties noted in the experimental set-up. Since the pressure

measurement system in this work was not on board and was based externally, the pressure tubes were sourced from the bottom of the model. This might have provided a blockage effect on the flow thus creating the variations in the flow in this small region. The $\overline{C_P}$ in this region tends to vary with showing both positive and negative $\overline{C_P}$ values. Reasons for positive $\overline{C_P}$ in this region could be based on the induction of stagnation area occurring at the upstream WWS, which might influence this region.

Finally, according to the results obtained, it can be observed that close to the nose of the train, the pressure varies significantly from one tap to another and also from one loop to the other. This is as anticipated due to the cross-section of the nose of the train, and thus shows the importance and influence of the shape of the nose in any crosswind stability case. However, at distances further down the train, the results tend to become more uniform. Near the roof of the train, the results show significant changes. Nevertheless, each loop and in fact each measuring point has its own characteristic due to its position and the surrounding influence on the entire train body. Over the middle of the roof, the flow showed uniform results at the tail of the train while the results at the leeward side showed that near the nose of the train, there was a lower $\overline{C_P}$ distribution as compared to a farther distance (near the tail), where the $\overline{C_P}$ magnitude decreased and the results provided lower negative values (up to $\overline{C_P}$ = -0.5 on the LWS), comparatively. This indicates the strong characteristics of suction near the nose of the train in the leeward side of the model and suggests that a fully developed wake might be present which is probably dominated by large vortices forming on the leeward side at much farther distances from the nose. The results and trends presented for this case are very similar to the results obtained by several researchers in the past (Copley, 1987; Chiu and Squire, 1992; Baker and Sterling, 2009; Baker, 2010).
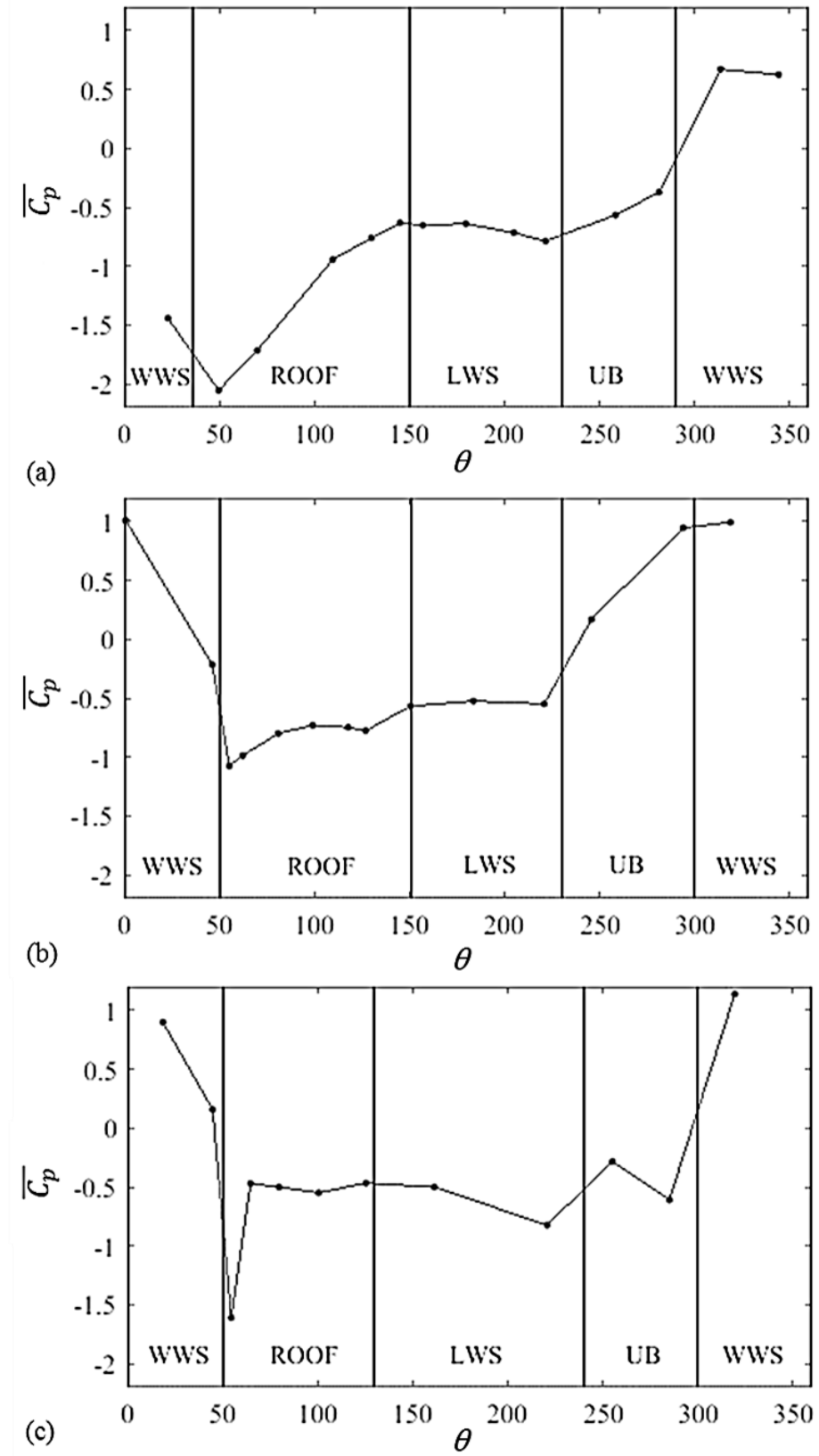
Figure 4.2: Surface mean pressure coefficient distribution at (a) loop B, (b) loop G and (c) loop N for the configuration without any windbreak walls at a yaw angle of 90°.

123

4.2.1.2 All windbreak wall cases (b-f)

This section presents and discusses the results obtained for cases examining different windbreak walls at a yaw angle of 90°. In order to provide a closer look at the results obtained with different types of windbreak walls, Figure 4.3 shows a comparison of the different types of windbreak walls examined at three loops, B, G and N.

For loops located near the nose of the train such as loop B, the results for the three continuous walls (walls 1, 2 and 3) showed that as the height of the windbreak wall increased (from 160 mm to 260 mm), the $\overline{C_P}$ distribution decreased, possibly due to the increased shielding effect as the flow is expected to deflect from the top of the windbreak wall, away from the windward side, causing suction effects. However, the trend depicted over the entire circumference of the loop was similar for all three continuous wall types. Relatively uniform values for $\overline{C_P}$ are present over the windward side and roof of the model. This statement is supported by the experimental uncertainty calculations presented in Appendix A, which discusses the relative influence of the bias limit and random uncertainty in relation to the total uncertainty. The total uncertainty estimations reveal that the total error values (of about ±0.17) in general were relatively constant for all pressure taps throughout different test configurations. It was observed that the random uncertainty input was much less than the bias limit. This was due to the low reference wind speed in the wind tunnel that was one of the limitations of this study. In spite of this limitation, the uncertainty estimations suggest there was a good agreement between the maximum and minimum values of each individual run as the bias limits for all the loops of the train remained relatively constant for each test configuration.

Similarly, for loop B, the results at the windward side of the model showed uniform values of pressure from one tap to another with wall 1. Again, wall 3 resulted in the lowest pressure (i.e. with most negative $\overline{C_P}$ values) along with wall 2 for the WWS and most of the roof region. The pressure results were similar for walls 2 and 3; approximately similar values were obtained for the pressure taps on the WWS of the model. This is also supported by the experimental uncertainty calculations presented in Appendix A. The total uncertainty estimations revealed that the total error values were relatively constant for all the pressure taps on the WWS of the model for both the test configurations (i.e. for walls 2 and 3). It is likely that these results occur due to the fact that these pressure taps were all protected from the oncoming crosswind due to the wall and thus a shielding effect of the windbreak wall was induced. However, it must be noted that instead of achieving a zero $\overline{C_P}$, a negative $\overline{C_P}$ was obtained as there is a suction effect generated due to the possible flow deflection by the windbreak wall. It is likely that this deflection causes the growth of vortices in the distance between the windbreak wall and the train body. Whereas for wall 1, it can be seen that slight variations in the pressure distribution were apparent on the WWS because of the shorter height of the wall and the crosswind flow separating from the top edge of this wall and directly impacting on the train surface.

In terms of the leeward side, the results showed slightly different trends. As shown in Figure 4.3a, for loop B, wall 1, which was much shorter in height exhibited the largest change in the results in comparison to the other walls examined. These results may also be affected by the nose region of the train.

Along the longitudinal length of the train, at positions slightly farther from the nose of the train, at loop G, wall 1 resulted in results demonstrating strong suction ($\overline{C_P}$ = -0.94) mostly, which then escalated to an increase in pressure (up to $\overline{C_P}$ = -0.48) as compared to

the results obtained with most of the other walls, as the flow progressed on the leeside. At similar positions (i.e. farther from the nose of the train) it was observed that wall 3, which was the tallest, provided quite uniform results over the windward side of the model. It was also noticed that wall 3 showed the most negative $\overline{C_P}$ values in the results comparatively. This can be based on the increased height of this wall.

In terms of the effect of wall 1 on the pressure distribution results, the shorter height of the wall meant that some of the pressure taps on the roof were exposed to the onset wind and were not provided with any shielding effect of the wall. Thus, the results linked with this wall were noticed to show a sudden increase in pressure values as the flow progressed from the WWS to the roof, specifically near the rear end of the train, as shown by Figure 4.3c. A suction peak can also be found at the windward edge of the roof at loop N. However, along the rest of the surface of the roof and all the way to the LWS of the model, the $\overline{C_P}$ values transitioned from a low value ($\overline{C_P}$ = -0.94) to a much higher value ($\overline{C_P}$ = -0.48). One of the key findings from the results revealed that the frontal loops, which were situated near the nose of the train showed less negative $\overline{C_P}$ results on the WWS compared to the leeward side, which was masked by either similar values or more negative $\overline{C_P}$ values. Whereas, at much further distances from the nose of the train, it was observed that the LWS showed $\overline{C_P}$ values that were less negative when compared to the WWS for all different wall cases.

Another interesting finding from the results is based on loop N. Compared to other loops, the circumferential pressure distribution on this loop showed a significant drop (of about 50% percentage difference) in the $\overline{C_P}$ value at the windward edge of the roof, as mentioned earlier. Another suction peak was noticed near the bottom edge of the LWS. These could be based on the fact that loop N was located right at the end of the first car

and thus the results could have been influenced by the inter-carriage gap which was next to this loop. The random change in the geometry of the model might have led to the possible flow vortex being separated at this point thus the strong suction. Close to the rear end of the train, mostly over the leeward side onwards, wall 3 was again observed to show a pressure distribution with pressure results that were most negative, mainly due to the abovementioned reason that this wall was the tallest thus was able to provide the greatest shielding effect. Overall, one interesting trend which was observed again was that near the nose of the train, the $\overline{C_P}$ values were mostly more negative compared to near the tail of the train, where the $\overline{C_P}$ showed values that were less negative. It is also worth mentioning that the results for the wall 2 (which was 190 mm tall) were very similar, within the experimental uncertainty, to the results of a continuous wall with a height of 210 mm. In this study, the results for wall 2 are presented as they represent the interesting case of whether a windbreak wall of same height as the train is sufficient to provide complete shielding effects to the train or not.

For walls 4 and 5, consisting of transition regions, at the nose of the train, it is apparent that wall 5 with a 90° transition region resulted in a less negative pressure distribution as compared to wall 4 with a 45° transition region, despite the fact that there is still a suction effect induced by both the walls. This is demonstrated in Figure 4.3a which shows that wall 5 provided the lowest negative pressure results on all the pressure taps located at the windward and roof side and for most of the leeward side while showing clear difference as compared to the results obtained with other walls near the nose of the train.

A significant pressure peak is observed in all cases at the transition from the middle of the roof to the leeward side with wall 5 presenting the weakest suction peak ($\overline{C_P}$ = -0.79). However, along the longitudinal length of the train, at positions slightly farther from the

127

nose of the train, such as at loop G, as shown in Figure 4.3b, it can be observed that wall 4 with a transition region of 45° showed a pressure distribution with the lowest negative values over most of the roof of the train. Additionally, wall 4 usually presented lowest negative pressure values (which can also be referred to as the lowest suction values) as compared to wall 5 in some of the regions, as shown in Figure 4.3b and Figure 4.3c. One reason for this could also be due to the design of the transition which meant that the distance between the model and wall decreased comparatively, as shown in Figure 3.10e and Figure 3.10f. These experimental uncertainty estimations demonstrated that the magnitude of the total error remained consistent for these tests, with good agreement seen at the same pressure taps for different test configurations.

To further elaborate the effect of the sharp transition regions in walls 4 and 5 on the flow around the train, loops near the transition region such as loop G were examined carefully as these were mainly the loops which were under the influence of these regions. As compared to all other loops, the usual trend involved wall 5 showing a pressure distribution with lowest negative $\overline{C_P}$ values at the entire circumference of the loops A-D, in comparison to wall 4. Whereas, at loop G, where a sharp transition was present in both the walls, a slight difference in the trend can be observed. At this point, wall 4 with a 45° transition region showed that the obtained $\overline{C_P}$ values were less negative as compared to wall 5 that showed $\overline{C_P}$ values which were slightly more negative, over the roof. At loop E (X/L =0.250), the influence of wall 5 on the flow resulted in a weak suction peak at the middle of the roof of a considerable different magnitude as compared to the results obtained on other pressure taps. This might be an indication of the surface pressure approaching the reference pressure at this particular point, which was clearly under the influence of the sharp transitions in the walls.

Overall, it is clearly apparent that the addition of any type of windbreak wall results in a significant difference in the surface pressure as compared to a case with no walls. It can be stated that the addition of any windbreak wall provides more uniform pressure results between adjacent taps with almost comparable magnitudes as compared to a no wall case where the mean surface pressure varies rapidly when transiting from one region to another. A windbreak wall significantly reduces the intensity of pressures on the windward side of the train while providing some uniformity to the results on the leeward side of the train. These findings clearly make sense as the train is somewhat shielded from the on-coming crosswind flows by the windbreak structures.
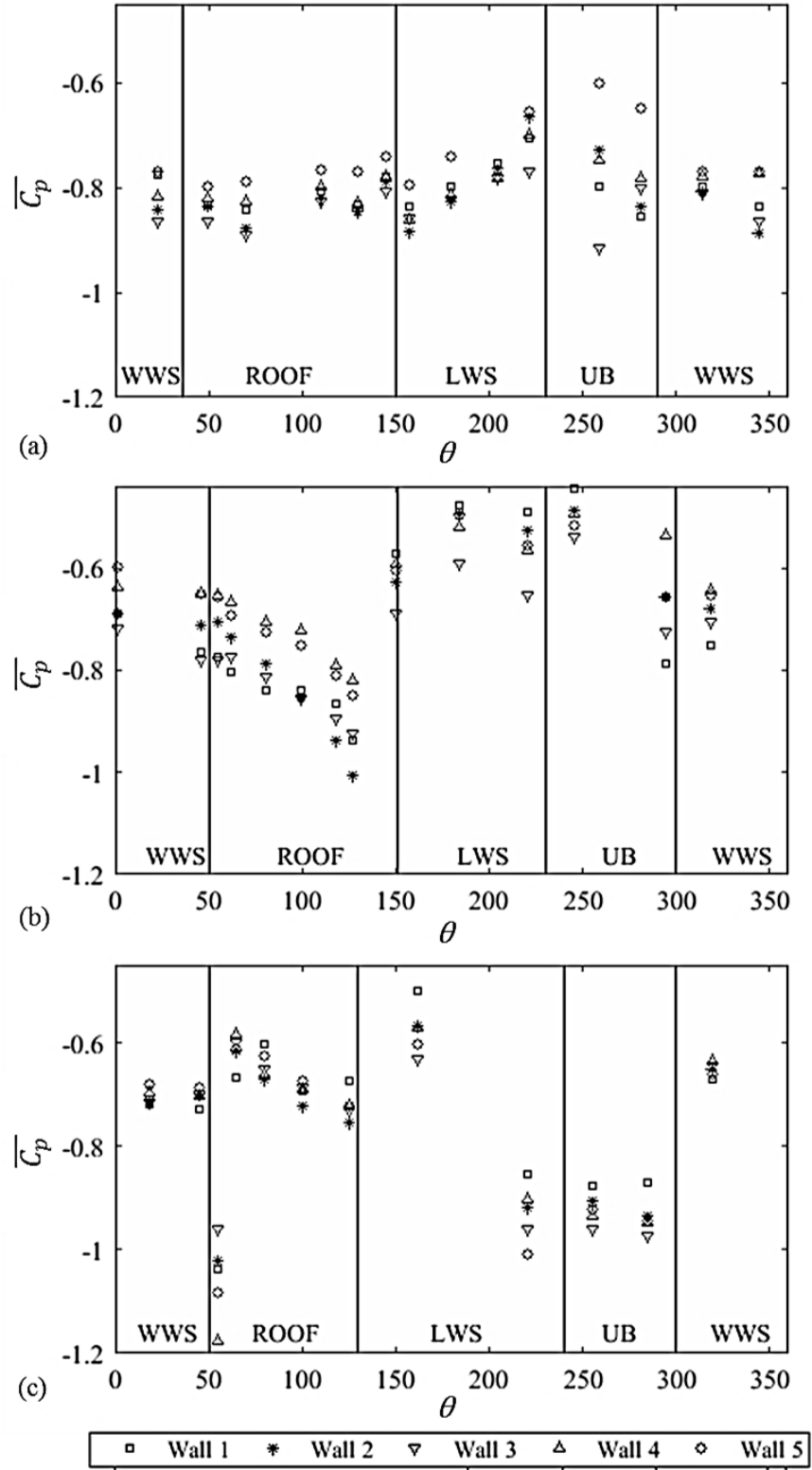
Figure 4.3: Comparison of mean surface pressure coefficient distribution at (a) loop B, (b) loop G and (c) loop N for different windbreak wall cases at a yaw angle of 90°.

4.2.2 Results at a yaw angle of 30°

4.2.2.1 Case (a): Track without any windbreak wall

For a no wall case, different flow patterns for the mean surface pressure distribution were identified along the longitudinal length of the train, as shown in Figure 4.4. The nose of the train, which embraced loops A, B and C was characterised by positive values of $\overline{C_P}$ for the WWS and the windward portion of the roof. This was the case at each different loop of the train, thus indicating a stagnation region created due to the wind being directly impinged on the surface of the model. As the circumferential pressure distribution results show, on each loop, the positive magnitude of $\overline{C_P}$ appeared to increase initially at the WWS and then this positive magnitude continued to decrease continuously. Around the roof, the results for the $\overline{C_P}$ show a negative gradient as the flow transits from the WWS to the LWS, possibly due to delayed separation caused by the presence of vortices on the roof of the train surface. The transition from a stagnation region to a suction region is obvious from the results. The leeward side of the train was characterised by a region of suction which included the roof of the model as well as the entire leeward side near the nose of the train. The only exception in the results was on loop A, where the magnitude of $\overline{C_P}$ remained positive over the roof as well. This could be due to the reduced cross-sectional area of this loop. Based on these results, a maximum suction peak is observed at the leeward edge of the roof for loops close to the nose of the train, such as loop B, as shown in Figure 4.4a. This indicates that there might be one or more vortices attached to the train surface which then progressively roll away from the train surface resulting in $\overline{C_P}$ values that tend to become less negative. This finding was also reported by Hemida and Karjnovic (2009) and Dorigatti et al. (2015). However, moving away from the nose of

the train, at loops such as loops G and N, as shown by Figure 4.4b and Figure 4.4c, a suction peak is found to appear at the windward edge of the roof. This was also the case for a yaw angle of 90°, suggesting a flow separation point at the windward edge of the roof. This echoes previous studies such as Copley (1987) and Baker and Sterling (2009). The flow separates from the windward edge of the roof and does not reattach. Since all adjacent loops seem to show similar results at this point, it can be stated that perhaps this vortex is rolling up on the roof. It continues to drift progressively from the edge to the centreline of the roof in some cases (Loop M) before completely detaching away from the train. Moreover, near the rear end of the train, such as at loop N, a weaker suction peak is found at the bottom side of the leeward face. This suction peak might be related to a vortex which emanates from the leeward edge of the LWS. Overall, the results and trends presented for this case are very similar to the results obtained by several researchers in the past (Copley, 1987; Hemida and Karjnovic, 2009; Dorigatti et al., 2015).

Finally, it is worth mentioning that in contrast to the results obtained for a yaw angle of 90°, the magnitudes of the results for a no wall case at a yaw angle of 30° were somewhere near the magnitudes of different wall cases. This was not the case for the former investigation involving a yaw angle of 90°, where the wind was hitting the surface of the train perpendicularly and thus the addition of walls implied that all or at least most of the train surface was covered by the direct impingement of the wind. Nevertheless, a significant difference was still apparent further down the train length and has been discussed in this section and section 4.2.2.2.
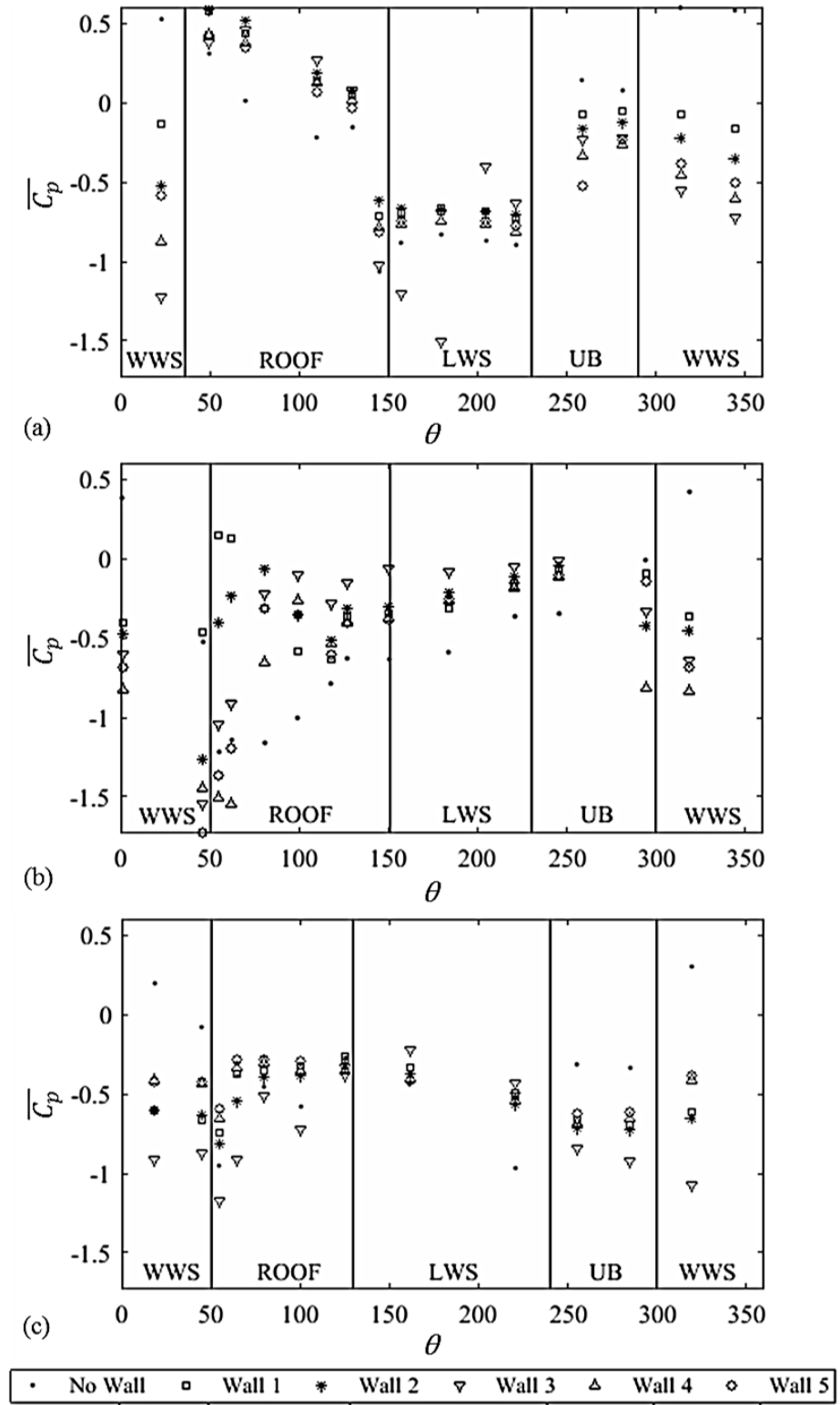
Figure 4.4: Comparison of the mean surface pressure coefficient distribution at (a) loop
B, (b) loop G and (c) loop N for all cases examined at a yaw angle of 30°.

4.2.2.2 All windbreak wall cases (b-f)

The different types of windbreak walls showed a significant difference in the trend of the results as compared to a no wall case, as evident in Figure 4.4. Firstly, for all walls, a similar trend was observed for the circumferential pressure distribution with the exception being wall 1, which showed positive pressures at the WWS/roof interface of loop G, most likely due to the shorter height of the wall. For a no wall case, the WWS showed a stagnation region characterised by positive $\overline{C_P}$ values; whereas, the addition of walls led to a region of suction on the WWS, as anticipated from the 90° results presented in section 3.1.2. Comparatively, at the nose, the tallest wall, wall 3, showed $\overline{C_P}$ values that were most negative while the least negative $\overline{C_P}$ distribution was shown by the shortest wall, wall 1, on the WWS. Following on, the circumferential pressure distribution showed that on the nose of the train, the walls led to a less negative value of $\overline{C_P}$ for each case for the roof region. This indicates that the walls were able to provide a shielding effect to the WWS of the model but in case of the roof, the wind was able to directly impinge and create stagnation regions thus producing large positive pressure values. The $\overline{C_P}$ values then dropped significantly as the flow transits from the roof to the LWS, producing regions of suction in the LWS. For the shorter height wall, wall 1, a similar trend was seen near the nose of the train with a positive $\overline{C_P}$ peak occurring at the windward edge of the roof, while suction peaks were observed at the leeward edge of the roof and at the bottom of the leeward face (loop B). Away from the nose of the train, at loops G and N, as depicted by Figure 4.4b, a suction peak was observed at the windward edge of the roof; however this was not the case for loops located at and near the nose of the train. A similar trend was also noticed at a yaw angle of 90°. Walls 2 and 3 showed somewhat similar results in comparison to each other with wall 3 showing the lowest pressure distribution

(i.e. with most negative $\overline{C_P}$ values). This statement is supported by the experimental uncertainty estimations, which revealed that the magnitude of the total error remained consistent for these two test configurations and there was a good agreement between the minimum and maximum values of each individual run. One interesting finding was that the LWS of the model depicted a smooth pressure distribution near the nose of the train with the use of wall 2, which was not the case for the tallest wall (wall 3). In terms of transition regions in walls 4 and 5, near the nose of the train, wall 5 presented $\overline{C_P}$ values that were less negative as compared to the values obtained for wall 4 over the WWS. However, in the same region as the flow progressed around the surface of the train, wall 5 presented the most negative $\overline{C_P}$ values compared to wall 4. In order to determine the effect of the sharp transitions on the exact location where these were situated, the respective loops which were under the influence of the sharp transitions, such as loop G, were carefully examined; results on Loop G are presented in Figure 4.4b. At the WWS, wall 4 showed the most negative $\overline{C_P}$ distribution not only compared to wall 5 but to all other walls. An interesting phenomenon revealed at yaw angle of 30° was that walls 4 and 5, with transition regions, led to more uniform results where $\overline{C_P}$ was seen to approach zero. It is assumed that these uniform results with small variations indicate the smooth pressure distribution around the train signifying the complete detachment of any vortical structures from the train body, especially at the LWS of the model.

4.3 Overall aerodynamic load coefficients

Section 4.2 discussed the pressure results on the train surface for different cases by expressing the surface pressure distribution as a non-dimensional mean pressure coefficient, $\overline{C_P}$. This section aims to provide an analysis on the overall mean aerodynamic

load coefficients for the side (lateral), $\overline{C_Y}$, and lift (vertical), $\overline{C_z}$, forces along with the rolling moments about the X-axis and leeward rail, $\overline{C_{M_X}}$ and $\overline{C_{M_{X,lee}}}$, respectively, for different test cases. In this section, the overall mean aerodynamic load coefficients were calculated using the methodology discussed in section 3.6, chapter 3. Figure 4.5 and Table 4.1 show the calculated values for the overall mean aerodynamic load coefficients per unit length of the vehicle for the different test cases at 90° and 30° yaw angles.
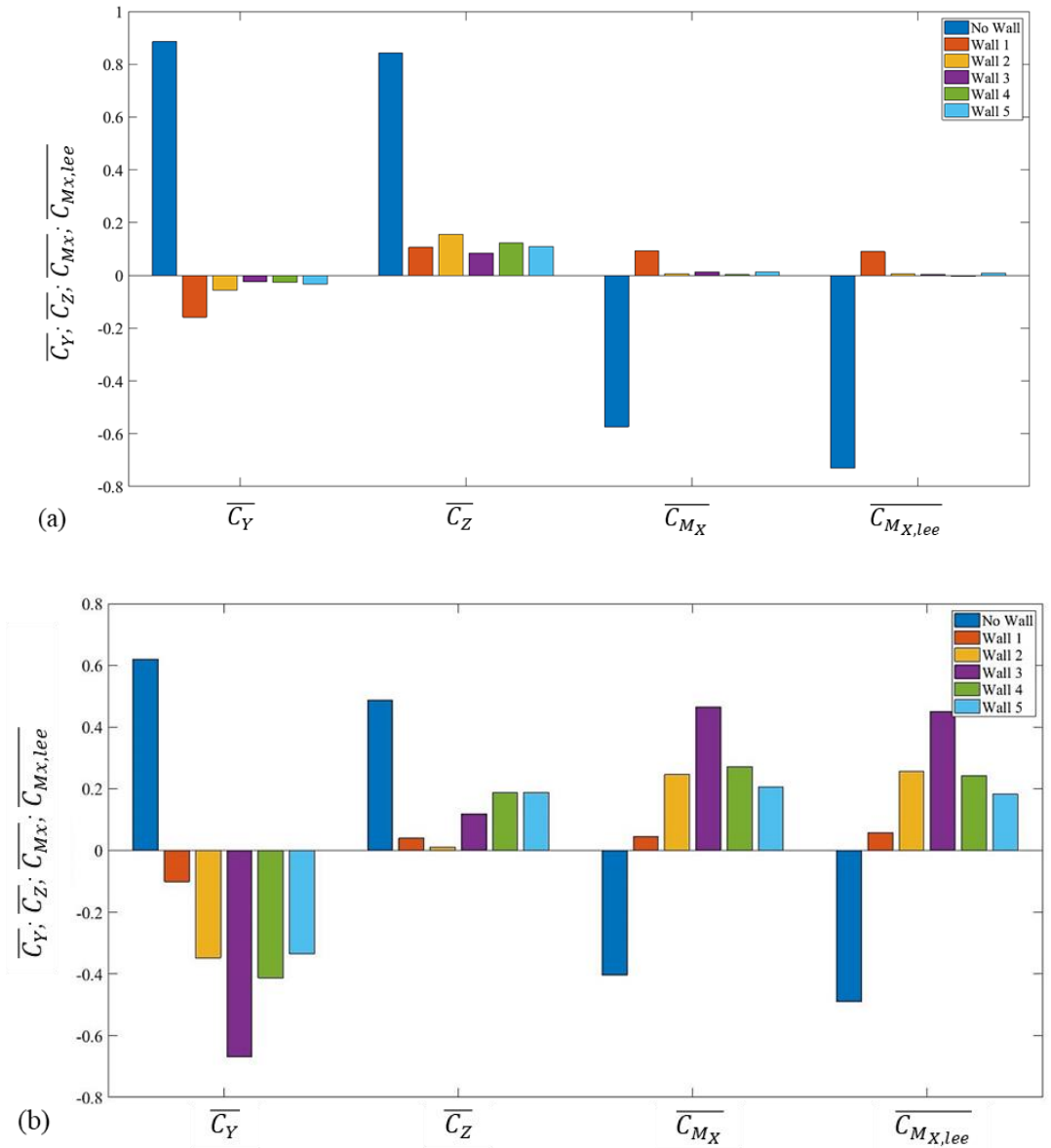
Figure 4.5: Overall mean aerodynamic load coefficients for different test cases at a yaw angle of (a) 90° (b) 30°.

Table 4.1: Overall mean aerodynamic load coefficients for different test cases.

Cases	Yaw angle of 30°				Yaw angle of 90°			
	$\overline{C_Y}$	$\overline{C_Z}$	$\overline{C_{M_x}}$	$\overline{C_{M_{X,lee}}}$	$\overline{C_Y}$	$\overline{C_Z}$	$\overline{C_{M_x}}$	$\overline{C_{M_{X,lee}}}$
No Wall	0.620	0.487	-0.404	-0.490	0.886	0.844	-0.573	-0.730
Wall 1	-0.101	0.040	0.045	0.058	-0.158	0.106	0.094	0.090
Wall 2	-0.348	0.011	0.246	0.257	-0.057	0.156	0.006	0.006
Wall 3	-0.669	0.118	0.465	0.451	-0.024	0.085	0.014	0.004
Wall 4	-0.413	0.187	0.271	0.243	-0.026	0.122	0.003	-0.004
Wall 5	-0.335	0.188	0.206	0.183	-0.033	0.110	0.012	0.008

In terms of the results, side forces are a measure of the difference in pressure between the WWS and LWS. As noted earlier, WWS experiences positive pressures, contrary to LWS which experiences negative pressure. These two effects conjoin together to form an overall side force. Therefore, positive values of $\overline{C_Y}$ indicate that the side force is directed from the WWS to the LWS while positive $\overline{C_Z}$ values refer to the lift force being directed upwards. Likewise, for rolling moments, $\overline{C_{M_X}}$ and $\overline{C_{M_{X,lee}}}$, based on the reference system shown in Figure 3.8b, about the centre of track (COT) and leeward rail, respectively, negative values refer to overall moments which tend to overturn the vehicle towards the WWS. It is worth mentioning that some of the aerodynamic coefficients have changed signs but retained a similar magnitude to a certain extent, such as wall 1 in Figure 4.5a and wall 3 in Figure 4.5b. Since these coefficients are derived from vector components, a negative value can occur due to the direction in which the force or velocity acts. This means that the windbreak wall in such scenarios may lead to the rolling over of the train in the opposite direction to the crosswinds. It is presumed that this could mainly be due

to the formation and recirculation of vortices at different sides of the train, induced due to the geometry of the windbreak wall.

4.3.1   Results at a yaw angle of 90°

4.3.1.1   Case (a): Track without any windbreak wall

For the case with no wall, since the crosswinds were able to impact the train surface directly, high positive values for $\overline{C_Y}$ and $\overline{C_Z}$ were noticed, as illustrated in Figure 4.5a. This validates the point that the action of wind forces in terms of their magnitude can clearly lead to the overturning or derailment of a vehicle. At a yaw angle of 90°, the magnitudes of the side force coefficient and the lift force coefficient were 0.89 and 0.84, respectively. Whereas, at a yaw angle of 30°, the magnitudes of the side force coefficient and the lift force coefficient were 0.62 and 0.49, respectively. This is again as expected, signifying the increased overturning probability when the crosswind blows perpendicularly to the vehicle. However, while this is true for stationary vehicles, in the moving case, the maximum yaw angle usually faced by most trains is 15° (Gallagher et al., 2018). This is also in agreement with earlier studies, which show that the aerodynamic force coefficients tend to increase in magnitude with an increase in the yaw angle (Baker et al., 2009). Furthermore, at a yaw angle of 90°, the rolling moment about the leeward had a larger negative value compared to the rolling moment about the X-axis. This is an important finding as Baker et al. (2009) mentions that usually for rail vehicles, the rolling moment about the leeward rail is required for overturning risk calculations. This result is due to the fact that the vertical force, which is directed upwards contributes to the lee-rail rolling moment while it does not contribute to the rolling moment about the X-axis.

Figure 4.6 presents the results for the mean load coefficients per unit length for different test cases at a yaw angle of 90° with respect to the longitudinal position of each loop normalised on the vehicle length (i.e. *X/L*). The presented results show only eight of the loops along the length of the train body as other loops were equipped with only a few pressure taps.

Firstly, based on Figure 4.6a, it can be observed that the entire train model is characterised by positive values of $\overline{C_Y}$ per unit length except on loop A. This shows that a lateral net force exists in the direction of wind and thus indicates the stagnation and suction pressure regions which are present on the WWS and LWS of the train. The side force coefficients seem to increase on the nose of the train and then decrease along the length of the train body with the exception being on loops D and N. Also, a higher and positive side force coefficient at loop N probably indicates the effects of space behind the leading car and in front of the second car.

Positive values of the lift force coefficients are observed on the entire train body, as shown by Figure 4.6b. The lift force coefficients also follow the same trend as side force coefficients around the nose region of the train. However, at positions further from the nose, the lift force coefficients tend to decrease with the exception being at loop H. Since the lift force coefficient at each loop is evaluated based on the balance between the pressures on the roof and the UB region, it can be noticed that the UB region of loop H has a higher pressure as compared to the roof thus the high value.

In terms of the rolling moments, as illustrated in Figure 4.6c and Figure 4.6d, it is worth mentioning that the side force contributes to an overall overturning moment, which then leads to negative $\overline{C_{M_X}}$ values. Therefore, both $\overline{C_{M_X}}$ and $\overline{C_{M_X,lee}}$ values follow a similar trend as the side force coefficient along the length of the train body. Overall, it can be

stated that the side force contribution to the rolling moments is dominant as compared to the lift force on any loop of the train. Nevertheless, the positive lift force coefficients are also able to increase the negative magnitudes of both $\overline{C_{M_X}}$ and $\overline{C_{M_{X,lee}}}$ per unit length at any loop thus increase the overturning moment of the vehicle.

Figure 4.6: (a) Mean side force coefficient per unit length (b) mean lift force coefficient per unit length (c) X-axis mean rolling moment coefficient per unit length (d) Leeward rail mean rolling moment coefficient per unit length at a yaw angle of 90°.

4.3.1.2 All windbreak wall cases (b-f)

A comparison between the no wall and with wall cases shows clearly that the overall $\overline{C_Y}$ values for most loops of the train changed from positive to negative with the addition of any wall, as illustrated in Figure 4.5a. This was as expected and shows the huge impact

140

of windbreak walls. The shielding effect of windbreak walls results in negative and in some cases negligible overall $\overline{C_Y}$ values. An unusual trend seems to appear at loop D for all cases at a yaw angle of 90°. Positive values of the side force coefficients per unit length are observed in all cases. As Dorigatti et al. (2015) described, such a situation is an indication of the lateral net force which exists in the direction of wind. Based on the respective stagnation and suction regions of this loop, it is clearly evident that an intense low-pressure peak exists on the LWS of the loop, which might reflect the presence of vortices in this region and hence the positive $\overline{C_Y}$ results. Overall, the negative side force coefficient values for the different windbreak walls at other loops decrease in magnitude with an increase in wall height. The lift force coefficients at an individual loop can be noticed to decrease in magnitude with an increasing wall height. Also, it appears that the transitional walls show results similar to wall 3, the tallest wall.

A comparison on the results with and without transitional windbreak walls on loops E and H shows that there are not major differences in the results. However, wall 5 with a transition region of 90° seems to have slightly lower magnitudes of rolling moments around the transition regions.

4.3.2   Results at a yaw angle of 30°

4.3.2.1   Case (a): Track without any windbreak wall

For the case with no wall at both yaw angles, since the crosswinds were able to impact the train surface directly, high positive values for $\overline{C_Y}$ and $\overline{C_Z}$ were noticed, as shown in Figure 4.5. Furthermore, at a yaw angle of 30°, shown in Figure 4.5b, the rolling moment about the leeward had a larger negative value compared to the rolling moment about the X-axis. This trend was also observed for the yaw angle of 90° and also in similar

investigations carried out earlier (Dorigatti et al., 2015) As mentioned earlier, this result is due to the fact that also the vertical force, which is directed upwards, contributes to the lee-rail rolling moment while it does not contribute to the rolling moment about the X-axis.

Figure 4.7 presents the results for the mean load coefficients per unit length for different test cases at a yaw angle of 30° with respect to the longitudinal position of each loop normalised on the vehicle length (i.e. *X/L*). The presented results show only eight of the loops along the length of the train body as other loops were equipped with only a few pressure taps. Based on the results, it can be observed that the entire train model is characterised by positive values of $\overline{C_Y}$ per unit length. This shows that a lateral net force exists in the direction of wind and thus indicates the stagnation and suction pressure regions which are present on the WWS and LWS of the train.

As shown by Figure 4.7a, the side force coefficients seem to increase on the nose of the train with maximum values being reached at loops B and C. This is expected as the results agree with the study presented by Dorigatti et al. (2015) and the reason for this is the existence of low-pressure, suction peaks which exist in the LWS sections. Slightly lower side force coefficients at some positions of the train sections indicate the absence of low-pressure peaks in the LWS of the train and the reduced intensities of pressure fields on the WWS and LWS. Also, a higher and positive side force coefficient at loop N probably indicates the effects of space behind the leading car and in front of the second car. Positive values of the lift force coefficients are observed on the entire train body as portrayed by Figure 4.7b. The lift force coefficients also follow the same trend as the side force coefficients around the nose region of the train. In addition, positive values of $\overline{C_Z}$ are also characterised by the suction on the upper face of the train being more intense than the UB

region. Lower $\overline{C_Z}$ values along the length of the train coincide with the low-pressure peaks found on the roof.

In terms of the rolling moments shown in Figure 4.7c and Figure 4.7d, the side force contributes to an overall overturning moment and negative $\overline{C_{M_X}}$ and $\overline{C_{M_{X,lee}}}$ values occur which follow a similar trend as the side force coefficient along the length of the train body. Once again, the side force contribution to the rolling moments can be seen to be dominant as compared to the lift force on any loop of the train.
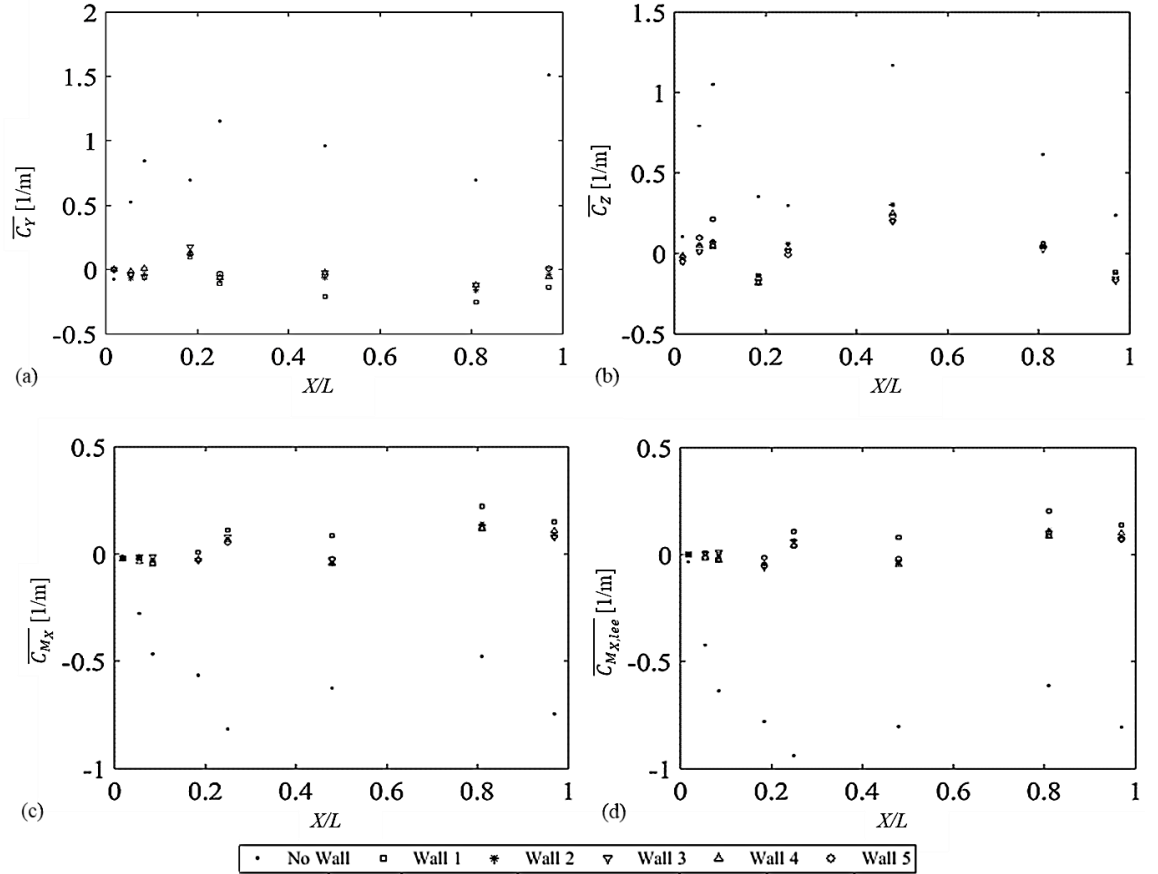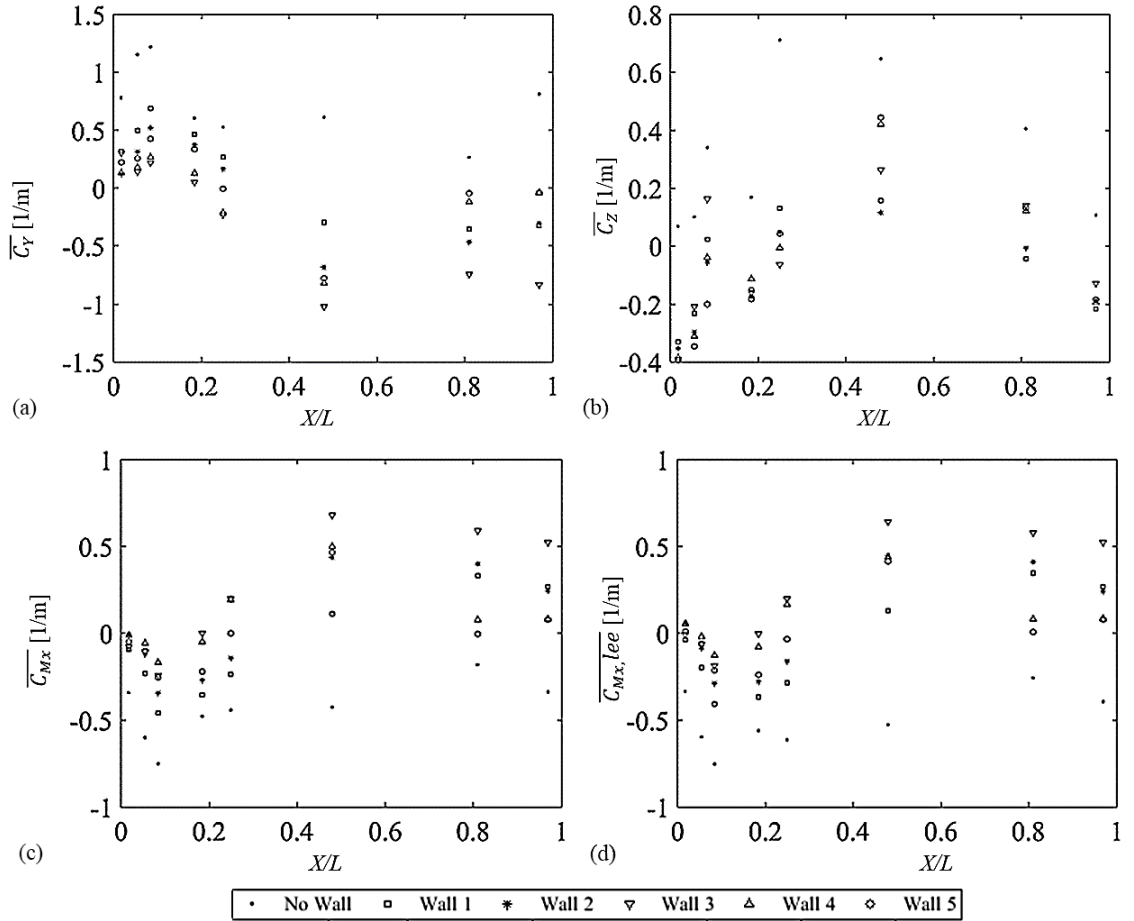

Figure 4.7: (a) Mean side force coefficient per unit length (b) mean lift force coefficient per unit length (c) X-axis mean rolling moment coefficient per unit length (d) Leeward rail mean rolling moment coefficient per unit length at a yaw angle of 30°.

4.3.2.2 All windbreak wall cases (b-f)

For all the wall cases, a comparison shows that the nose region and sections slightly father from the nose region are characterised by positive side force coefficient values. This was most likely due to the limitations faced in the wind tunnel at a wind incidence angle of 30° where constructing very long windbreak walls was practically challenging. This meant that some onset wind was able to attack the train surface, potentially the nose region. However, from the central part to the tail of the train, negative side force coefficients are evident. The shielding effect of windbreak walls is apparent as the magnitude of the overall $\overline{C_Y}$ values decreases with an increase in the height of the walls, as shown in Figure 4.7b. However, it is obvious that the results for the side force coefficient along with the resulting rolling moment coefficient tend to become sensitive to the overall increase in height of the windbreak wall. To elaborate, with windbreak wall 3, $\overline{C_Y}$ becomes increasingly negative at this wind incidence angle. This would mean that this particular configuration would be worse in terms of safety than the case without any windbreak wall. This is because the train would be at a higher risk of overturning in the opposite direction with respect to wind. Although such a situation is probable, it appears that the main reason for such a result could be based on the practical limitations of the experimental work at the wind incidence angle of 30°, as discussed earlier. Also, opposite to higher wind incidence angles, it is clear that at lower wind incidence angles, while the windbreak wall height has a sheltering effect on the WWS of the train, a possible vortex is generated due to an increased windbreak wall height (i.e. wall 3) and the interaction the train has with the flow, which causes a low pressure region. This then produces a strong suction in the LWS that can result in the overturning of the train in the windward direction. This result is confirmed by Figure 4.4a, which shows the increased negative $\overline{C_P}$

at the nose of the train. Further from the nose of the train, this is not the case due to the setup of the geometry. The lift force coefficients for the different wall cases follow the same trend as the case without a wall, however with much lower magnitudes, comparatively. Negative lift force coefficients at the nose of the train indicate a force directed downwards. This is mainly due to the intense stagnation over the roof of the nose of the train and low pressures in the UB regions. Thereafter, positive lift force coefficients are visible over some loops indicating the reduced magnitude and extensions of the stagnation regions on the roof. Moving on towards the rear of the train, the $\overline{C_Y}$ values per unit length tend to reduce due to the existence of low-pressure peaks on the roof side of the train. Since the overturning moments are dependent mainly on the side force, the roll moments are mostly characterised by negative values for the nose region of the train. However, these roll moments then become positive near the rear of the train. In terms of the effects of the transition regions on loops E and H, the result show that wall 5 with a transition region of 90° leads to much lower overturning moments hence signifying the stability this wall provides to the overall train body. In fact, detailed analysis on the results show that the lowest roll moments at loop E were obtained from the use of wall 5. This was also the case for the yaw angle of 90°. Therefore, based on these findings it appears that wall 5 with a transition region of 90° can provide better stability to the train body when compared to other designs of windbreak walls discussed in this study.

4.4 Effect of varying wind incidence angles on the mean pressure coefficients coefficients

Similar to section 4.2, this section provides and discusses the pressure distribution results obtained over the train surface for the experimental cases (g – j) in terms of a non-

dimensional pressure coefficient, C_P. For simplicity, results on only certain important loops are illustrated. Nevertheless, this section discusses the trend and results over the entire length of the train.

4.4.1 Case (g): Track without any windbreak wall

Figure 4.8 shows the $\overline{C_P}$ distribution at loop B and loop G of the train at varying wind incidence angles for the case without any windbreak wall, respectively. With reference to Loop B, it is apparent that at lower wind incidence angles (i.e. at 20° and 30°), the overall pressure results are much higher (i.e. more positive and less negative) as compared to the other wind angles on the WWS. This is because loop B is located at the nose of the train and thus at low wind incidence angles there is a direct impact of oncoming wind on the nose of the train. For wind incidence angles between 0° and 40°-50°, the aerodynamic behaviour of the first car of the train body is comparable to that of a slender body. It is expected that a series of vortices would form on the roof and on the bottom edge of the leeward side. These vortices are known to roll up progressing from the nose of the train to the tail while gradually detaching themselves from the surface of the vehicle. On the other hand, at wind incidence angles of 60°-90°, the aerodynamic behaviour of the first car of the train body is comparable to that of a smooth-edged bluff body. At these angles, a large wake is expected to occur, possibly by the onset of vortex shedding. Also, the resulting surface pressure at these wind angles is in the mid-range of the lowest and highest pressure results achieved at those particular tappings. At the windward edge of the roof, a drop in surface pressure is observed where lower surface pressure results (i.e. with more negative $\overline{C_P}$ values) are yielded at higher wind incidence angles as compared to the lower wind incidence angles. This phenomenon stays valid over the roof. As the

flow progresses over the train surface, the flow tends to show weaker suctions over the roof of the model. These trends have been discussed earlier as well in section 4.2.1.1. Hence, to be more specific in terms of the different wind incidence angles in the LWS, the wind incidence angle of 50° seems to result in the most negative yet varying pressure distribution while higher wind incidence angles such as 60° to 90° lead to a uniform pressure distribution in the wake of the train.

Further away from the nose of the train, over the WWS and the roof of the train, the trend in the surface pressure distribution is same, however, the magnitude of the pressure values is different. Particularly in the WWS of the train, similar to Loop B, the wind incidence angle of 20° results in lower pressure results as compared to other increasing wind incidence angles. However, over the roof and the LWS of the train, the wind incidence angle of 20° results in the highest pressure distribution (i.e. with highest positive $\overline{C_P}$ values or lowest negative $\overline{C_P}$ values) comparatively. Dissimilar to Loop B, it appears that near the midpoint of the train and at distances farther from the nose of the train, the pressure distribution is similar in terms of the trends it adopts regardless of the wind incidence angles, with obvious differences in terms of the magnitude of the pressure values.

Towards the rear of the first car of the train, it is apparent that from 20° to 50° of wind incidence angle, the pressure results follow a similar trend in the WWS with the lowest pressure results being yielded at the lowest wind incidence angle. As the wind incidence angle increases, the highest wind incidence angle results in the highest surface pressure distribution (i.e. either with highest positive $\overline{C_P}$ values or lowest negative $\overline{C_P}$ values, comparatively). This is as expected due to the increased possibility of the direct impingement of wind on the train surface at increased wind incidence angles, thus

147

resulting in stagnation regions. Over the windward edge of the roof, a sharp decrease in pressure is observable where strong suctions are likely to represent the possible detachment of flow vortices. As the flow progresses, uniform pressure distribution is obtained at the LWS with the lower wind incidence angles resulting in pressure results that are less negative, comparatively. Finally, as Dorigatti (2013) discussed, it is worth mentioning that the wind incidence angles from 40° - 50° and 60° - 70° are considered to be a transition interval, where unstable flow conditions can be expected.

Figure 4.8: Surface mean pressure coefficient distribution at (a) loop B and (b) loop G for varying wind incidence angles without the presence of any windbreak walls.

4.4.2 Case (h): Track with windbreak wall 4 (Height of 210 mm with a 45° transition angle) in the WWS

Figure 4.9 shows the $\overline{C_P}$ distribution at loop B and loop G of the train for varying wind incidence angles with the windbreak wall 4 (i.e. the windbreak wall with the transition region of 45°) in the WWS of the train, respectively. The results near the nose of the train show a fairly interesting trend where it is apparent that at higher wind incidence angles (i.e. at wind incidence angles from 50° to 90°), the shielding effect of windbreak walls was able to play a role, hence resulting in much uniform pressure distribution as compared to the lower wind incidence angles. In addition, even though the windbreak wall was designed in order to barricade the oncoming flow, it appears that at a wind incidence angle of 20° and to some extent at wind incidence angles of 30° and 40° as well, a strong suction point existed at the windward edge of the roof. This was not the case for higher wind incidence angles. Also, over the roof of the train, lower wind incidence angles resulted in higher pressure results (i.e. with more positive $\overline{C_P}$ values or less negative $\overline{C_P}$ values) as compared to the uniform resulting effects of the windbreak wall at higher wind incidence angles. Nevertheless, in terms of the leeward side, it was observed that the wind incidence angles do not have a major effect on the pressure distribution with somewhat uniform results achieved at higher wind incidence angles. However, compared to other wind incidence angles, the wind incidence angle of 60° results in much lower surface pressure results (i.e. with $\overline{C_P}$ values that are more negative) mostly, specially over the roof and the LWS of the train. It could be interpreted from these results that apart from a wind incidence angle of 20°, which seems to be one of the most severe cases, the shielding effects of the windbreak wall 4 are apparent.

Away from the nose of the train, near the midpoint, the results show that all wind incidence angles lead to a fairly uniform pressure distribution with the lowest pressure results observed at lower wind incidence angles. An interesting trend is evident at the windward edge of the roof where it can be observed that at higher wind incidence angles (i.e. from 50° to 90°), a uniform constant pressure distribution is obtained. However, for lower wind incidence angles at the same point, there is a sharp increase in the surface pressure. This signifies the possible reattachment of flow in this region at lower wind incidence angles (i.e. 20° to 40°) where it is also apparent that the windbreak wall was not able to provide a complete shielding effect. The effect of the wind incidence angles is also apparent in the LWS of the train.

At the rear of the train, it appears that at higher wind incidence angles, there is a decrease in the resulting $\overline{C_P}$ values. This was the case over the entire circumference of loops located at the end of the first car such as loop M. A strong suction peak exists at the windward edge of the roof. While these results are not shown in Figure 4.9 due to repetition, they are discussed in detail in section 4.2.1.2 and shown in Figure 4.3c.

Figure 4.9: Surface mean pressure coefficient distribution at (a) loop B and (b) loop G for varying wind incidence angles with the windbreak wall 4 in the WWS.

4.4.3   Case (i): Track with windbreak wall 5 (Height of 210 mm with a 90° transition angle) in the WWS

Figure 4.10 shows the $\overline{C_P}$ distribution at loop B and loop G of the train for varying wind incidence angles with the windbreak wall 5 (i.e. the windbreak wall with the transition region of 90°) in the WWS of the train, respectively.

Compared to the results obtained with the windbreak wall 4, slightly different results were obtained with the use of windbreak wall 5. At the nose of the train, while a suction point exists at the windward edge of the roof at lower wind incidence angles, similar to with

the use of windbreak wall 4 along with an increase in pressure over the roof, a suction peak no longer exists in the LWS of the train. However, one interesting finding is apparent at a wind incidence angle of 60°. If the two windbreak walls with transition regions (i.e. walls 4 and 5) are compared, it is clearly visible that while a uniform surface pressure distribution is achieved with the use of windbreak wall with a transition region of 45°, this is not the case with the windbreak wall with a transition region of 90°. With the latter, a varying flow field is apparent indicating some disturbances in the flow, specifically at this wind incidence angle. At such a wind incidence angle, it seems that a windbreak wall with a transition region of 45° is a better option. Also, any positive pressure values with the use of a windbreak wall indicate that the wind flow was able to directly impinge and create stagnation regions. A physical interpretation of this trend could be that while the oncoming flow was able to separate from the top edge of the windbreak wall, it possibly reattached at the leeward edge of the roof. For higher wind incidence angles, i.e. 70° to 90°, the surface pressure distribution is fairly similar and uniform over the entire circumference of the train. This is as expected due to the complete shielding effect of the windbreak wall.

At the midpoint of the train, as seen in Figure 4.10b, due to the difference in the geometries of windbreak walls 4 and 5 (i.e. the difference in the shapes of the transition regions), there exists some dissimilarities in the pressure results. To elaborate, in terms of the WWS of the train, at lower wind incidence angles (i.e. 20° to 40°), it is visible that the windbreak wall 5 results in higher surface pressure values (i.e. with $\overline{C_P}$ values that are less negative) as compared to the results obtained with the use of windbreak wall 4. Another interesting point is the windward edge of the roof where the use of windbreak wall 4 results in a sharp increase in pressure but the use of windbreak wall 5 has no

resulting significant impact on the surface pressure. Once again, at lower incidence angles the flow of the LWS of the train shows some differences when compared for cases with windbreak walls 4 and 5, respectively. Following on, at higher incidence angles, i.e. from 50° to 90°, not only do the results show a uniform pressure distribution over the entire train surface, the results for windbreak walls 4 and 5 are quite similar in terms of the trends and to a certain extent in magnitude. It is worth mentioning that the results of these experimental cases (g – j) are similar to the ones mentioned in section 4.2.1.2 for cases (a – f).

Towards the rear of the train, it is clear that the trend is very similar for both cases (h) and (i). This is mainly because the results at this section are at a farther distance from the actual position of the transition region. Nevertheless, some differences exist in these two cases at the same loop at some wind incidence angles. This shows that the wind incidence angle along with the shape of the transition region may have an impact on the train even at positions much further away from the point, which was directly under the impact of the transition region.
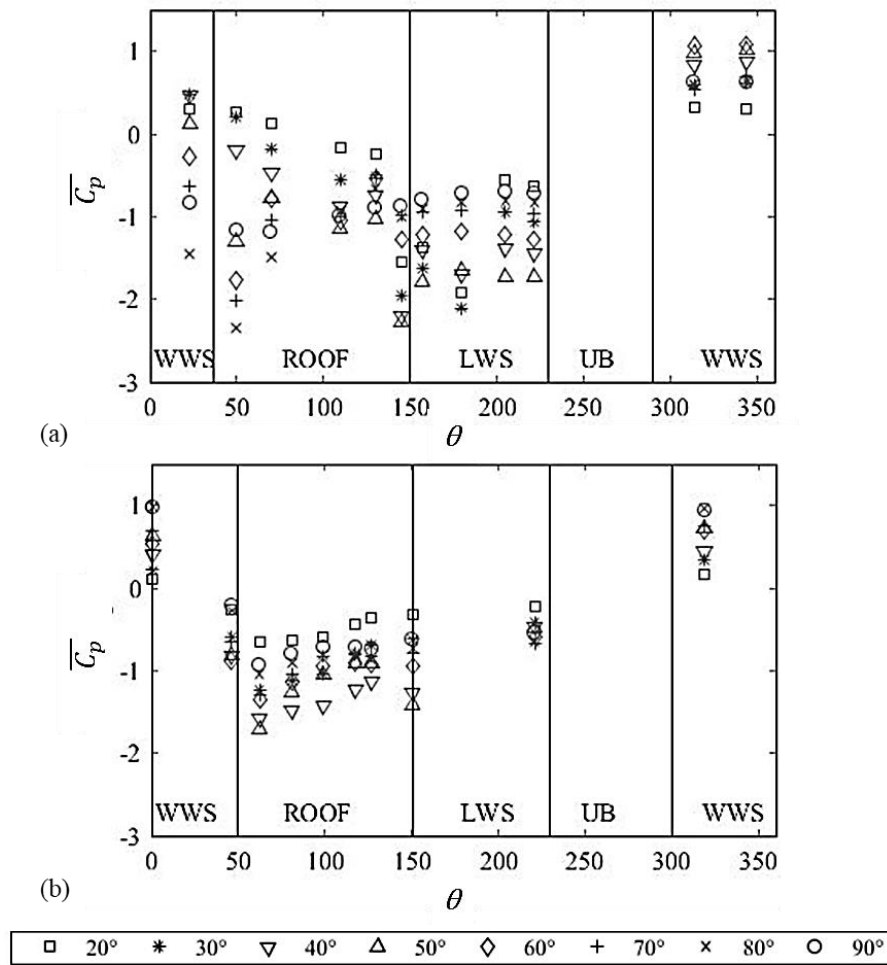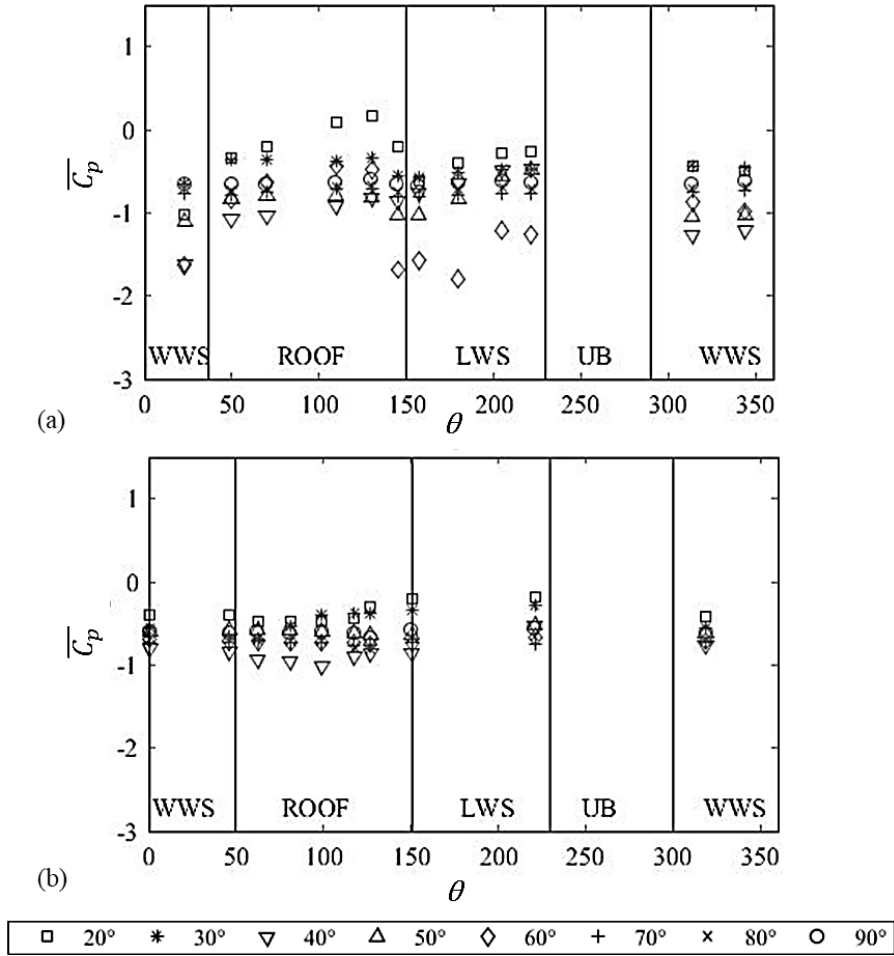
Figure 4.10: Surface mean pressure coefficient distribution at (a) loop B and (b) loop G for varying wind incidence angles with the windbreak wall 5 in the WWS.

4.4.4 Case (j): Track with windbreak wall 2 (Height of 190 mm) in the LWS

Figure 4.11 shows the surface mean pressure coefficient distribution at loop B for varying wind incidence angles with the windbreak wall 2 (i.e. the continuous windbreak wall with the same height as the train height) in the LWS of the train. This experimental case allowed for modelling the windbreak wall behind the train (i.e. downwind). In order to understand the impact of a windbreak wall behind the train, the results of this case were compared with the results presented in Figure 4.8 of case (g) where no windbreak wall was used. Overall, as expected, no differences were observed in the WWS. For wind

incidence angles from 20° - 50°, the trend of the surface pressure distribution was similar for the two cases. Also, not significant differences in the magnitude of the pressure distribution were observed at all wind incidence angles over the roof of the train. This statement is supported by the experimental uncertainty estimations, which revealed that the magnitude of the total error remained consistent for each test configuration while there was a good agreement between the minimum and maximum values of each individual run. Moreover, in the wake of the flow, from 60° to 80° of wind incidence angle, while the case with no windbreak wall resulted in uniform pressure, the addition of a windbreak wall behind the train resulted in a lower but non-uniform surface pressure distribution.

At slightly further distances from the nose and at lower incidence angles, the results of the surface pressure distribution are similar to the case without the presence of any windbreak wall. However, although the trend is similar, the magnitude of the surface pressure distribution is different with the wall 2 in the LWS always resulting in higher pressures (i.e. with lowest negative $\overline{C_P}$ values), specifically in the LWS. Slight differences arise from a wind incidence angle of 60°, where the comparison between the two cases tend to show similar results over the circumference of the loops. Also, the wall in the LWS continues to yield pressure results that are less negative, comparatively.

Further on, towards the rear of the train for lower wind incidence angles, while the pattern of the surface pressure distribution is similar to the case without the presence of any windbreak wall, it is observed that the windbreak wall on the LWS of the train does lead to a reduction in the haphazard pressure distribution over the train's circumference. Although the fluctuations exist in terms of the flow as it transits from one pressure to the other, these are less severe, comparatively. Moreover, at slightly higher wind incidence angles (i.e. 50° and 60°), an irregular trend is observed over the roof of the train. This can

155

be based on the nature of the wind incidence angle, which allows for lower pressure values with the use of a windbreak wall in the LWS. However, as the wind incidence angle increases further (i.e. 70° to 90°), both the trend and the magnitude of the surface pressure results are very similar to the case without any windbreak wall in the LWS.
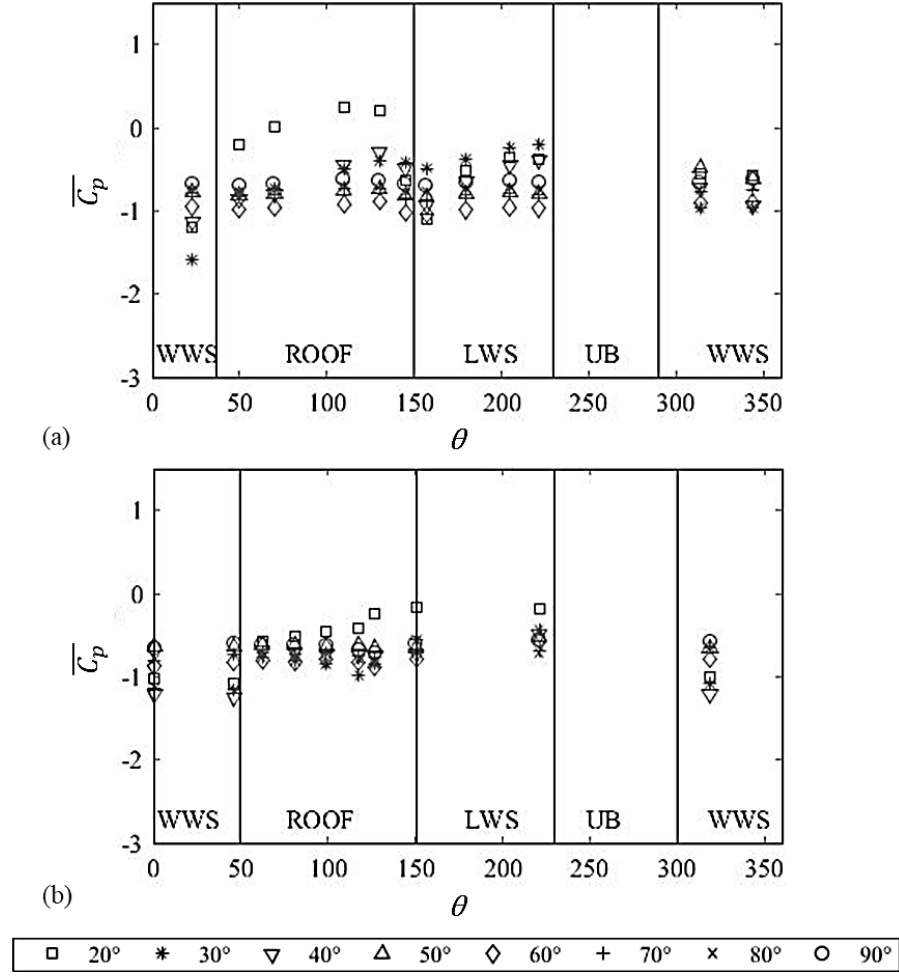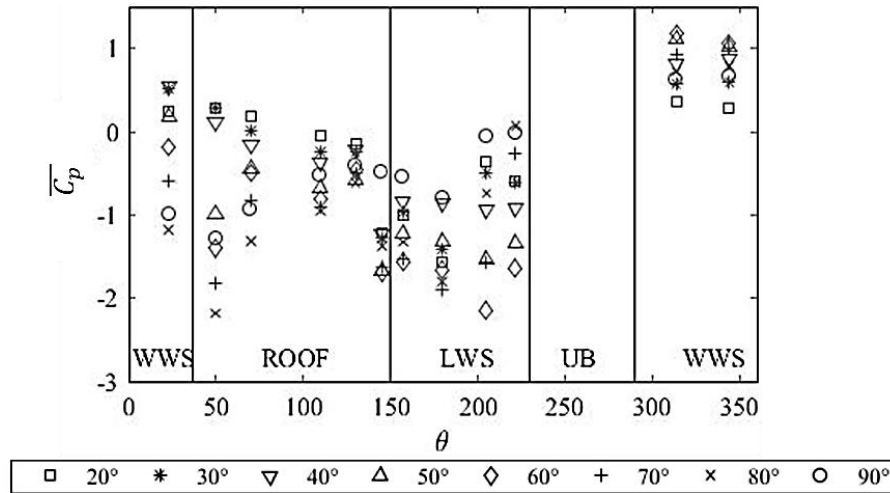

Figure 4.11: Surface mean pressure coefficient distribution at loop B for varying wind incidence angles with the windbreak wall 2 in the LWS.

4.4.5 Case (k): Track with windbreak wall 4 (Height of 210 mm with a 45° transition angle) in the WWS and windbreak wall 2 (Height of 190 mm) in the LWS

Figure 4.12 shows the comparison of surface mean pressure coefficient distribution at loop B for wind incidence angles of 30° and 90° for cases (e), (f) and (k), where 2 walls represent case (k). The purpose of such a test was to test the effect of two barriers on the overall flow. Hence, this experimental case allowed for modelling windbreak walls both, upwind and downwind the train. The comparison showed that the results for case (k) follow the same trend as case (e).

For the wind incidence angle of 30°, the results for case (k) agree with the results for case (e) in the WWS, as expected, with no major differences. The only differences observed

were on the roof of the train where the use of two walls resulted in an increased $\overline{C_P}$ distribution. However, over the rest of the LWS of the train, the results for case (k) agree well with the results for case (e).

For the wind incidence angle of 90°, overall, slightly higher $\overline{C_P}$ results (i.e. with lowest negative $\overline{C_P}$ values) were obtained with the use of two windbreak walls, but the trend was same as mentioned above. Also, this can be stated based on the estimates of the total uncertainties obtained for these cases which demonstrated that the total error remained consistent throughout these tests. Away from the nose of the train, further down the body, the results did not show any significant differences.
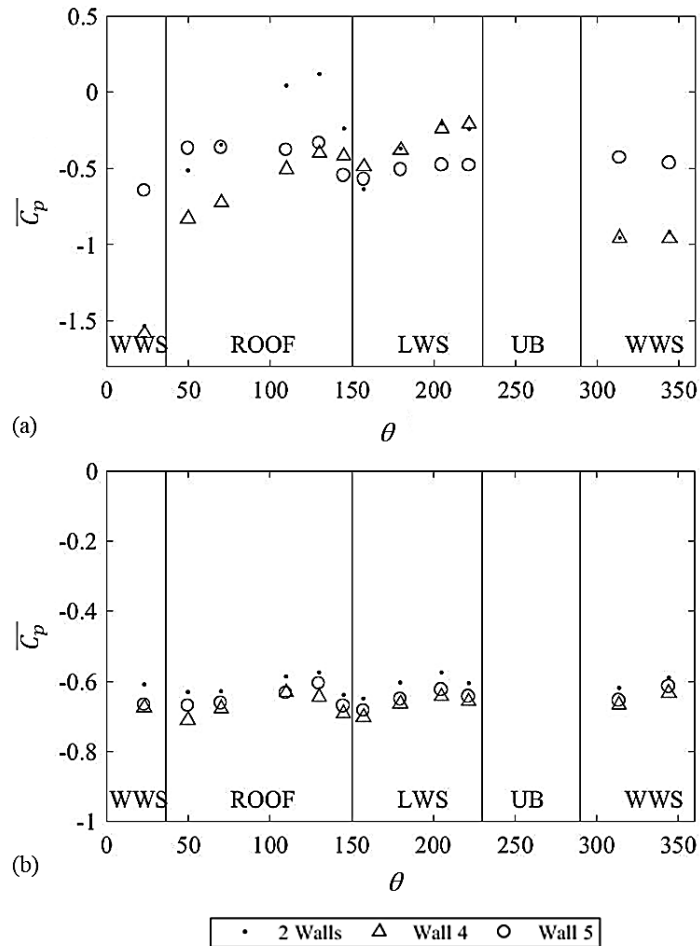
Figure 4.12: Comparison of surface mean pressure coefficient distribution at loop B for wind incidence angles of (a) 30° and (b) 90° for cases (e), (f) and (k).

157

4.5 Conclusions

For the first time, this novel experimental study investigated the influence of windbreak walls with varying angles of transition regions on the flow around a model-scale passenger train. A series of wind tunnel tests were carried out for a number of windbreak walls at varying yaw angles. Windbreak walls were found to cause varying pressure distributions on the train surface. Overall, the windbreak walls used in this study have proved to be capable in reducing the loads on a train surface significantly. The results presented indicate a number of important findings:

- For the 90° yaw angle, in comparison to different windbreak walls, the windbreak wall with a 90° transition angle usually led to the highest $\overline{C_P}$ distribution (i.e. with lowest negative $\overline{C_P}$ values) on the train surface near the nose, while the tallest wall resulted in the lowest $\overline{C_P}$ distribution (i.e. with highest negative $\overline{C_P}$ values), mostly. At transition regions, at a yaw angle of 90°, a slight change in the results was observed where the wall with a 45° transition region showed the lowest negative $\overline{C_P}$ distribution as compared to all other walls.

- For the 30° yaw angle, up to the nose region of the train, the tallest wall was observed to result in the highest negative $\overline{C_P}$ distribution over the circumference of the train; while the shortest wall showed the lowest negative $\overline{C_P}$ distribution. In terms of transition regions at a yaw angle of 30°, near the nose of the train, the wall with a transition angle of 90° provided the lowest negative $\overline{C_P}$ results as compared to the wall with a transition angle of 45°. Beyond the nose region (loop D onwards), the wall with a transition angle of 45° was seen to result in the lowest $\overline{C_P}$ results as compared to all other walls along the longitudinal length of the body.

From loop L onwards, the influence of the tallest wall on the flow resulted in the lowest $\overline{C_P}$ distribution (i.e. with $\overline{C_P}$ values that were most negative).

- Walls with transition regions led to more uniform results where $\overline{C_P}$ was seen to approach zero. These uniform results with lesser variations indicate the smooth pressure distribution around the train possibly signifying the complete detachment of any vortical structures from the train body.

- A comparison between the no wall and with wall cases shows clearly that the overall $\overline{C_Y}$ values for most loops of the train changed from positive to negative with the addition of any wall at both yaw angles. This was as expected and shows the huge impact of windbreak walls. Also, the shielding effect of windbreak walls results in negative and in some cases negligible overall side force coefficient values. Although lift force coefficients remained positive even after the addition of windbreak walls, the intensity of change between the results was clear reflecting on the significant impact of walls. Almost negligible rolling moments were observed with the use of windbreak walls at a yaw angle of 90° and somewhat positive rolling moments were observed with the use of windbreak walls at a yaw angle of 30°.

The motivation of this chapter was to obtain an understanding of the aerodynamic flow, which exists around a train surface due to the presence of different kinds of windbreak walls. This chapter provides some interesting results, which can be used to gain further insight into future works where this chapter would provide analysis on safety and stability of trains. While it is acknowledged that in reality, there is a relative movement between the train and the windbreak walls, the aim of the current chapter was not to calculate the aerodynamic forces and moment for a moving train in the transition region but to provide

159

valuable experimental data for a stationary train in the transition region (with the use of a wind tunnel assessment), instead. The experimental data from the present chapter can help act as a benchmark for future investigations, which can involve performing numerical simulations to better understand the flow structures in order to form an enhanced understanding of the flow behaviour around trains with windbreak walls. Numerical simulations will be able to exhibit numerous flow features, which may not be evident through experimental results while the experimental results will be used to validate the initial numerical simulations. In addition, the flow around a high-speed train consists of several small structures due to the instabilities in the shear layers (Hemida and Krajnovic, 2010). The numerical simulations will help in studying the time-dependent behaviour of the flow structures and the resulting impact on the surface pressure of the train along with the aerodynamic coefficients. Also, numerical simulations will be able to easily assess the relative movement of the train with different windbreak walls along with providing further details of the flow around transition regions in windbreak walls.

CHAPTER 5: Flow around a stationary train subjected to crosswinds with a windbreak wall consisting of a transition region of 45°

5.1 Introduction

This chapter provides the results obtained from the numerical simulation carried out on a stationary Class 390 model-scale train subjected to crosswinds at a yaw angle of 90° with a windbreak wall consisting of a transition region of 45° transition angle. It must be noted that this simulation reproduces the experimental test case (e) provided in section 3.4.1, chapter 3.

The main motivation of this chapter was to perform a numerical investigation to obtain an understanding of the aerodynamic flow, which exists around a train surface due to the presence of a particular kind of windbreak wall with a transition region when subjected to a crosswind. While valuable data is available from the experimental investigation performed on a same case, the experimental results are limited as they only provide insights to the surface pressure and aerodynamic force coefficients of the train. In order to obtain a further understanding on the aerodynamic flow, it is important to perform numerical simulations.

The numerical simulations made use of the widely used Improved Delayed Detached Eddy Simulation (IDDES) method. A 90° yaw angle was chosen because it allows for validation of the numerical model against experimental results, which were presented in chapter 4 and published in Hashmi et al. (2019). In addition, a yaw angle of 90° represents the highest transversal wind case (Cheli et al., 2010) and is recommended in CEN (2018)

standards. Baker (2014) states that higher yaw angles (above 60°) are relevant for stationary trains.

In terms of the windbreak wall, a transition angle of 45° is a mid-way between the no transition region (i.e. 0° transition angle) and maximum transition region (i.e. 90° transition region). While some researchers have attempted to explore the features of different shapes of windbreak walls, no numerical investigation has been carried out on a windbreak wall with a transition angle of 45°.

Section 5.2 provides the verification on the accuracies of the simulations carried out through a mesh sensitivity analysis along with the comparison of the numerical results with the experimental results. The time averaged flow on and around the train body, with the windbreak wall consisting of a transition region of 45°, at a yaw angle of 90° is discussed in detail in this chapter. Section 5.3 provides an analysis on the streamlines' patterns developed from the time averaged velocity field. Section 5.4 elaborates on the time-averaged surface pressure patterns, while section 5.5 analyses the time-averaged velocity patterns and the flow properties. A comparison of the aerodynamic loads between the experimental case and numerical simulation is provided in section 5.6. To understand the transient flow characteristics, section 5.7 presents and discusses the time histories of the aerodynamic load coefficients along with providing a frequency analysis of the forces. In addition, the section looks at the instantaneous flow and pressure fields obtained on the leading car. Section 5.8 assesses the credibility of the experimental method of calculating the aerodynamic loads by a new approach, while section 5.9 presents the general conclusions drawn in this chapter.

5.2 Solution verification and validation

5.2.1 Mesh sensitivity analysis

A mesh sensitivity analysis was carried out in this study for ensuring that the numerical results obtained are based on the boundary conditions and the physics utilised and not on the resolution of the mesh. Hence, it is crucial to observe that the numerical results do not alter with a change in the mesh density. This is the manner in which a mesh independence is achieved. Thus, for the mesh sensitivity analysis, two different meshes (coarse and fine) were investigated. The coarse mesh consisted of 7.94 million cells while the fine mesh consisted of 28.9 million cells. The time-averaged surface mean pressure coefficient distribution around some of the chosen loops on the train is shown in Figure 5.1 for the case with the windbreak wall consisting a transition region of 45° at a yaw angle of 90°. The figure also shows the comparison in results of the two meshes with the experimental results obtained in chapter 4. These loops are chosen due to their geometric position on the train body and thus it is deemed that these loops are able to represent the entire train body, which includes the model's streamlined nose.

On the train nose, it is apparent from Figure 5.1a and Figure 5.1b, the pressure results achieved from the two meshes are consistent with each other with some differences observed around the leeward side (i.e. at $\theta \approx 200°$). Down the length of the train, slight variations are visible in the magnitude of the pressure results achieved from the two meshes but these fall within the bounds of the total experimental uncertainty (±0.17). While this variation between the two meshes is small for loop E, as shown in Figure 5.1c, the variation becomes noticeable at loop G, as shown by Figure 5.1d.
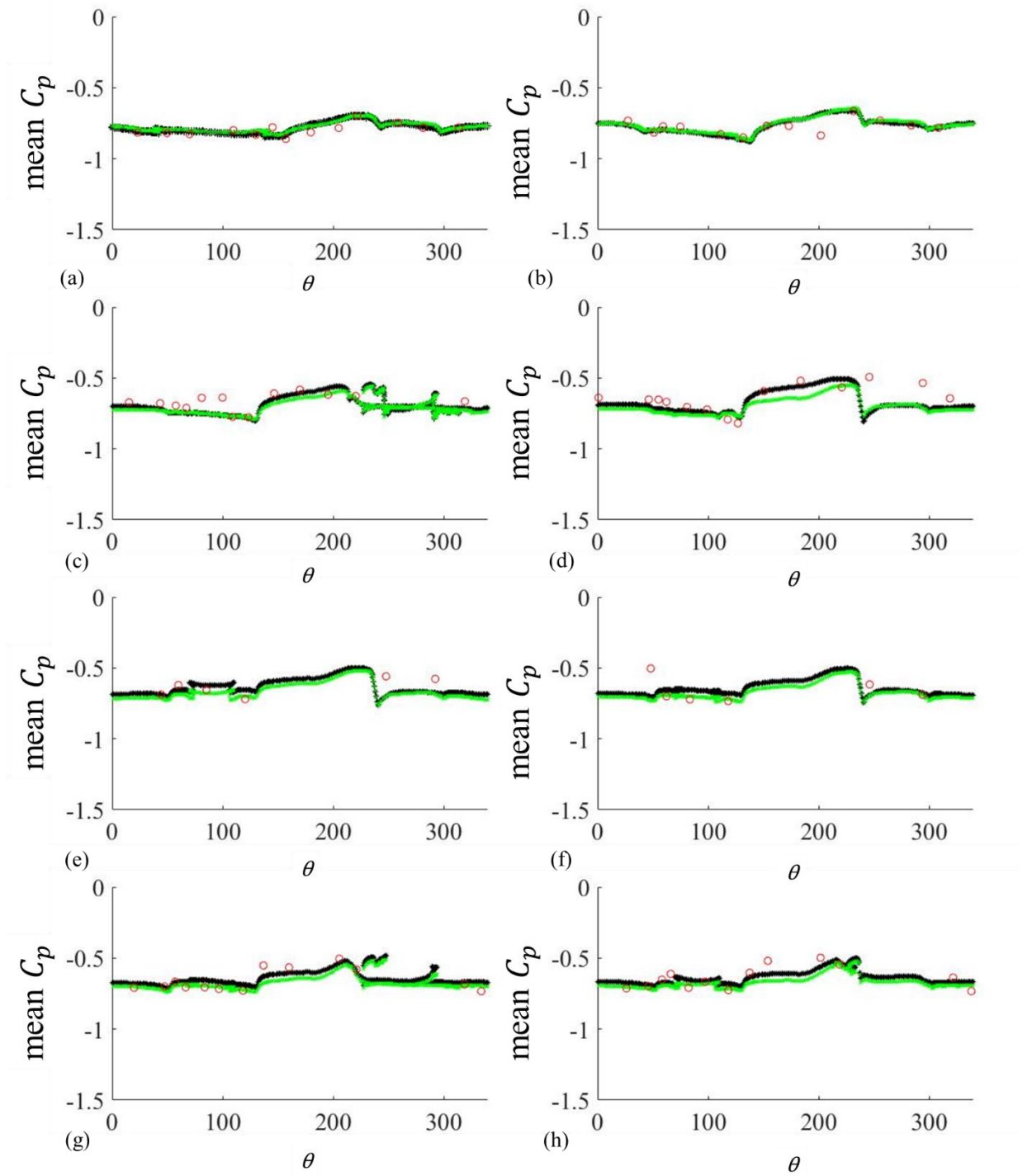
Figure 5.1: Comparison of the surface mean pressure coefficient distribution at (a) Loop B (b) Loop C (c) Loop E (d) Loop G (e) Loop J (f) Loop K (g) Loop L and (h) Loop M for the windbreak wall with 45° transition region at a yaw angle of 90°.

One interesting finding reveals that the variation occurs for both the loops mainly at the leeward side of the train. This trend was also reported by Li et al. (2018) and therefore it can be concluded that mesh size has few effects and that there was not a significant change in the general trend followed by the pressure distribution of the two meshes. The pressure results obtained with the coarse mesh are overall slightly less negative than the pressure results achieved with the fine mesh. The finer mesh preserves more accurate values, which is prevented by the loss of resolution in coarser mesh. Furthermore, at loops much farther from the nose of the train, no significant difference between the results obtained from the two meshes is visible. This can be noted from Figure 5.1 (e-f). The mesh sensitivity analysis shows that while a good agreement is seen, there are some differences in the pressure results that cannot be ignored.

Figure 5.2 demonstrates the streamlines corresponding to the mean velocity field projected onto Loop H with the coarse and fine mesh for the windbreak wall with 45° transition region at a yaw angle of 90°. Detailed similarities are evident in the flow field around the train body and the windbreak wall with the two different meshes used. Two major vortices are noticeable in the flow at this loop; where one develops at the bottom windward side of the train and the other is in the wake of the flow. With an increase in the mesh density, the vortex at the bottom windward side of the train is captured clearly. Also, slight differences are visible in the shape of the vortex but overall, the trend followed by the streamlines is almost similar for both the meshes.
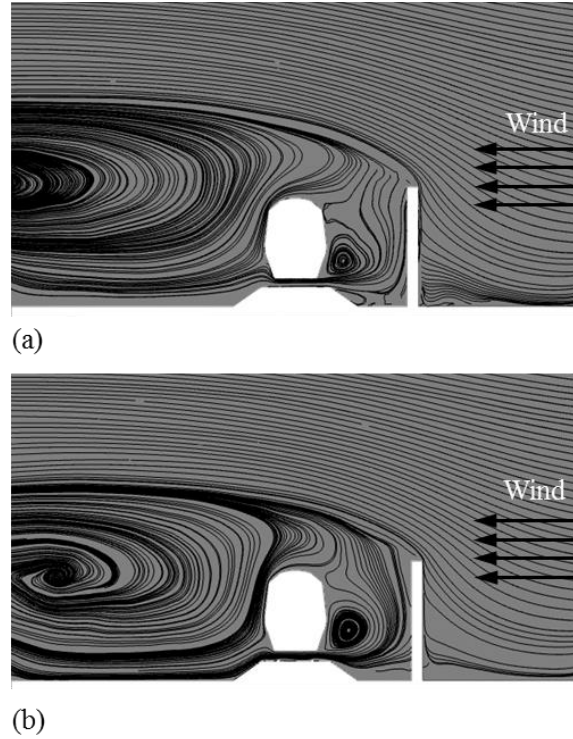
Figure 5.2: Comparison of mean velocity streamlines projected on Loop H obtained using (a) coarse mesh and (b) fine mesh for the windbreak wall with 45° transition region at a yaw angle of 90°.

Generally, the agreement in the pressure results and the flow fields between the two different meshes indicates that the computational domain, boundary conditions, numerical method and computational meshes used in the current work are able to reproduce the flow around the train subjected to crosswinds with the windbreak wall within the bounds of experimental uncertainty. It is understood that the mesh density has some influences on the numerical results. Normally, results with the finer mesh are known to offer slightly better agreement with experimental results (He et al., 2019). Therefore, the results and analysis presented in this chapter will be based on the simulation with the finer mesh as these results were readily available.

Moreover, Figure 5.1 also presents a comparison of the numerical results with the two different meshes to the experimental results. This is done in order to ensure the validity of the numerical results. A good agreement is observed in the surface mean pressure coefficient results. This statement is based on the calculation of error between the numerical and experimental results using the following equation:

$$error(\%) = \left[\frac{C_{\substack{Numerical \\ simulation}} - C_{\substack{Wind \\ tunnel}}}{C_{\substack{Wind \\ tunnel}}} \right] \times 100 \tag{5.1}$$

In Equation (5.1), $C_{Numerical\ simulation}$ refers to the mean C_P obtained from the numerical simulation and $C_{Wind\ tunnel}$ refers to the mean C_P obtained from the wind tunnel experiments.

Based on Equation (5.1), the error for each pressure tap is calculated. This is done by comparing the experimental results for each loop with the numerical results obtained with the finer mesh. Table 5.1 lists the total error of each loop by averaging the individual errors for all the pressure taps in a single loop. It can be determined that the average error between the experimental and numerical results for the entire leading car is less than $6 \pm 1.5\%$. Therefore, the numerical approach utilised in this study has produced similar results to the experimental study to a certain extent. Other studies such as Li et al. (2018) also found similar errors in the comparison of their experimental and numerical results for similar streamlined bodies. Overall, a reasonable agreement is found between the experimental pressure taps and the numerical results obtained at these measuring positions. This agreement is encouraging, particularly when the uncertainty limits outlined in Appendix A for the experimental results are considered. However, on the whole, where slight discrepancies are noticeable between the experimental and numerical results, these usually occur in the leeward side and the underbody region of the model.

167

This is not surprising based on the practical limitations and difficulties noted in the experimental set-up, as discussed in chapter 4. To elaborate, since the pressure measurement system in the experimental work was not on board and was based externally, the pressure tubes were sourced from the bottom of the model. This might have provided a blockage effect on the flow thus creating the variations in the flow in this small region. Also, discrepancies in the underbody region are usually caused due to the variations in the geometry of the train model used in experiments and the numerical work. This was also discussed in Li et al. (2018) who reported results on the same experimental and numerical geometries. These discrepancies mostly arise due to the differences in the model scale real object tested in the wind tunnel and its physical as well as mathematical description in the CFD software. Even though it is aimed to minimise these differences by carefully modelling the computational geometry, it is not possible to completely eliminate any differences and some simplifications have to be made. Additionally, minor differences between the experimental and numerical results could be either due to human error faced during the experiments or due to errors with physical measurements of the geometric positions of the pressure taps. Overall, the experimental results have helped act as a benchmark for the current numerical simulations.

Table 5.1: Estimation of the average total error (%) for each loop of the leading car using Equation (5.1).

Loop	A	B	C	D	E	F	G
Error (%)	5.6	3.1	3.3	5.5	5.6	1.5	10.2
Loop	H	I	J	K	L	M	N
Error (%)	6.9	5.8	8.1	5.1	5.9	8.3	5.9

5.3 Streamlines patterns from the time averaged velocity field

As reported in CEN (2018), numerical simulations are able to predict pressure and velocity fields easily allowing for different configurations to be taken into account. While experimental and numerical surface pressure results of the train agreed well, the current experimental techniques used were unable to provide an insight on the flow fields and flow patterns. In this section, visualisation techniques are utilised to determine the flow fields around the train body, obtained from the numerical simulations.

The time-averaged flow is examined for the solution in order to determine the properties of the flow and the pressure fields. This can assist in exploring the flow structures which develop around the train body in the time-averaged manner. The visualisation package used in this chapter is EnSight. Figure 5.3 illustrates the mean velocity streamlines projected onto contour plots of pressure for all 14 loops on the train. These images are a graphic summary of all the trends followed by the flow around the entire train body. The figure also shows the respective position of the loop on the train with respect to the windbreak wall analysed.
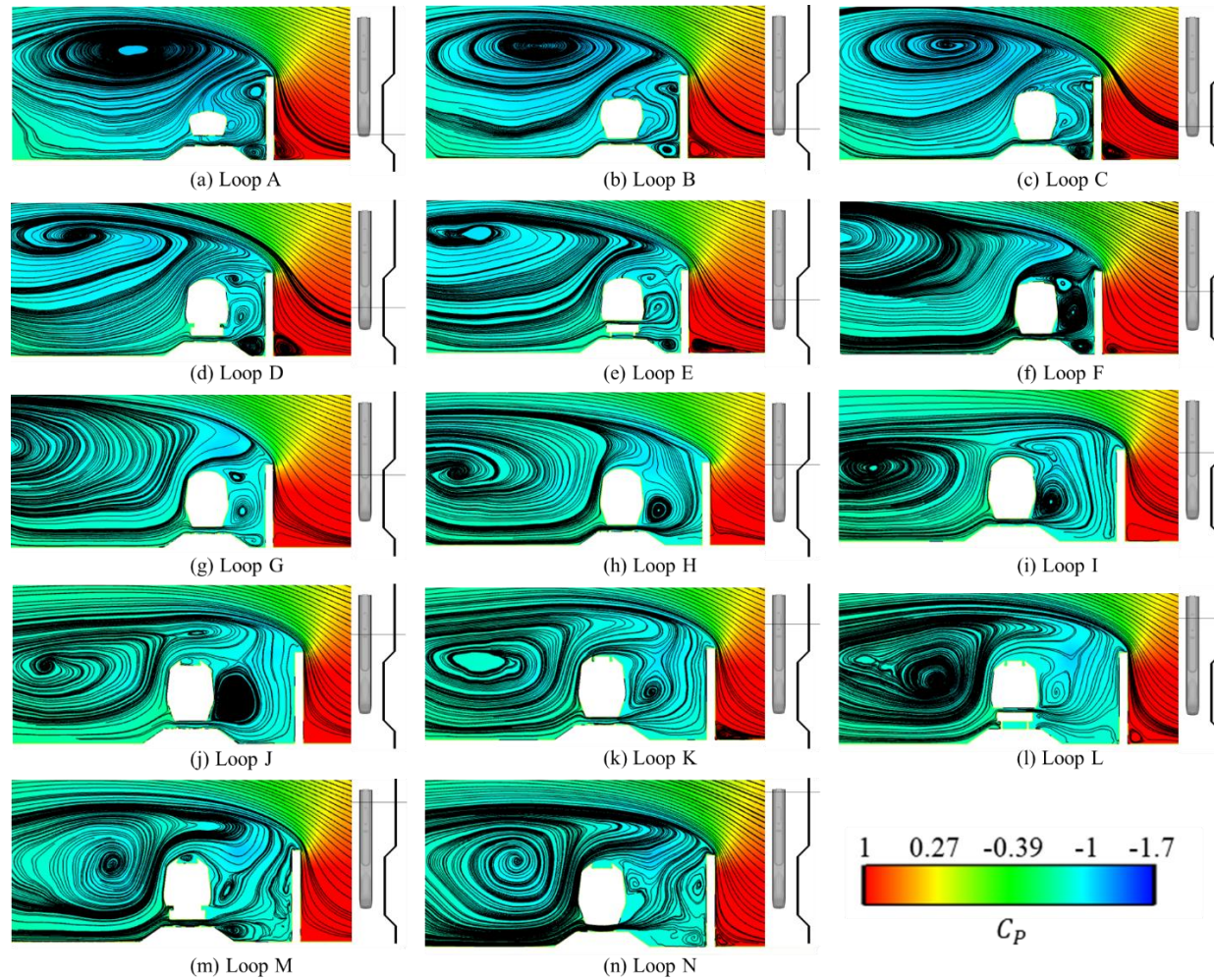
Figure 5.3: Mean velocity streamlines projected onto contour plots of pressure for (a – n) Loop A to Loop N, for the windbreak wall with 45° transition region at a yaw angle of 90°.

The immediate deflection in the incident flow at the tip of the windbreak wall can be easily appreciated. The incident flow streamlines follow the same trend throughout where they attack the windward side of the windbreak wall and then deflect from the top edge of the wall. The streamlines are lifted and the flow above the windbreak wall is accelerated. However, as expected, some significant differences are visible after the flow deflection. To elaborate, for loops A, B and C, which are positioned at the nose of the train and are under the influence of the transition region, a vortex-like structure appears at the leeward top side of the windbreak wall (V1). Also, a small and weak vortex-like structure can be seen to develop near the bottom of the windward side of the train (V2). In the gap between the windbreak wall and the track edge, another small vortex is noticeable (V3). In the wake of the flow, a vortex (V4) exists, much farther from the leeward roof edge of the train. Further down from the nose, at loops D and E, the vortex-like structure, V1, which was found at the leeward top side of the windbreak wall, is seen to drift towards the windward roof edge of the train. In addition, at these loops, the vortex-like structure which was observed near the bottom edge of the windward side of the train, V2, starts to develop into a proper vortex. For illustrative purposes, Figure 5.4 provides a labelled diagram identifying the names of the vortices at loop D. At loop F, V2 becomes a strong vortex. In terms of V3, the vortex continues to exist till loop F while V4 slowly progresses and rolls up and away from the train. V4 exists in the recirculation region behind the train body.
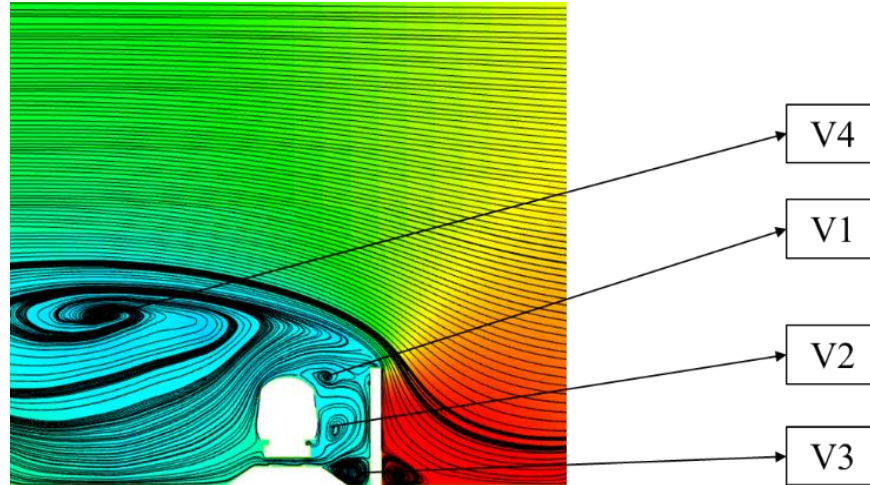
Figure 5.4: Identification of the vortices at Loop D.

It must be acknowledged that the distance between loops A-G and the windbreak wall was constant. However, as Figure 5.3 shows, loop G is under the influence of the sudden change in the geometric shape of the transition region. At loop H, a significant change in the flow pattern is evident. This is due to the sudden change in the distance between the train and the windbreak wall. At this loop H, the vortices V1 and V3 disappears, while V2 becomes stronger. Also, the vortex V4 starts to appear nearer the train. Further down the train length, from loops I to loops N, the distance between the windbreak wall and the train remains the same. The vortex V2 first strengthens till loop J but thereafter, the vortex slowly starts to weaken and finally loses its shape by loop N. The strong vortex V4 continues to come closer to the leeward side of the train while a weak vortex-like structure appears at the leeward side of the wall. Overall, the results show the presence of a fully developed wake, which was dominated by large vortices. Also, the disappearance of vortices V1 and V3 from loop H onwards confirms the suggestion made in the literature review that the random change in the distance between the windbreak wall and the railway track, known as the transition region, can result in the formation of vortices around the

train body, which may hit the train surfaces potentially leading to stability issues for the train. Finally, one interesting finding observed in the incident flow once the transition region ends. To elaborate, from loops A to H, a distinct immediate deflection in the incident flow at the tip of the windbreak wall could be easily appreciated by the upward bending of the streamlines. However, from loop I onwards to the rear of the car, while the immediate deflection in the incident flow is present, this is marked by slightly downward bending of the streamlines as compared to the streamlines seen for earlier loops. This is a clear indication of the effect induced by the transition region.

5.4 Time-averaged surface pressure patterns

The time-averaged pressure distribution is used for calculating the time-averaged surface mean pressure coefficient, $\overline{C_P}$, presented in Figure 5.1. The results indicate that the presence of a windbreak wall causes a more uniform pressure distribution around a single loop with almost constant pressure values. If compared to the no windbreak wall case analysed in chapter 4 at the same yaw angle, it was determined that the latter resulted in a non-uniform pressure distribution on each loop (as shown in Figure 4.2, chapter 4 and Figures A.1-A.4 in Appendix A). Thus, the wall was able to significantly reduce the intensity of the pressures on the windward side of the train while also providing uniformity to the results on the leeward side of the train. This confirms the shielding effects provided by the windbreak wall to the train body from the on-coming crosswind flows. In fact, as noted from the experimental results presented in chapter 4, all cases with windbreak walls were observed to show the reduction in the intensity of surface pressures on the train body, signifying the protective effects of the walls.

173

One interesting finding revealed that for almost all loops, a significant peak in pressure is observed when the flow progresses from the middle of the roof to the leeward side, indicating flow separation, due to the geometry of the train. This can be represented as a weak suction peak. Another of the key findings from the results indicated that at the nose of the train, the magnitude of the $\overline{C_P}$ was lower (i.e. more negative) as compared to the loops farther away from the nose of the train. For example, the weak suction peak, which was found at almost every loop when the flow transited from the middle of the roof to the leeward side, was found at a C_P value of -0.7 at loop B; however, at loop G, this peak was found at a C_P value of -0.5. These results were obtained using both the experimental (case e) and numerical methods, thus showing the accuracy of these findings.

In terms of the pressure contours, an increased positive pressure is noticeable on the windward side of the windbreak wall, as expected. This high pressure remains fairly constant at this region throughout the length of the windbreak wall suggesting stagnation points in these regions. A region of low pressure exists around the train body. This is due to the shielding effect of the windbreak, which leads to the train body being essentially surrounded by a negative pressure area. At the nose of the train, as shown by Figure 5.5, the frontal and leeward sides show a much more negative pressure as compared to the rest of the train body. This results in a stronger suction at this region and is thus explained by the stronger vortices which exist in this region. However, as discussed above, the vortices start to drift away from the train, down the length of the train, and thus the pressure starts to increase slightly at the leeward edge of the train. Overall, the impact of the transition regions in the windbreak wall is apparent on the flow around the train. Also, it can be confirmed that the presence of the wall deviates the flow away from the train.
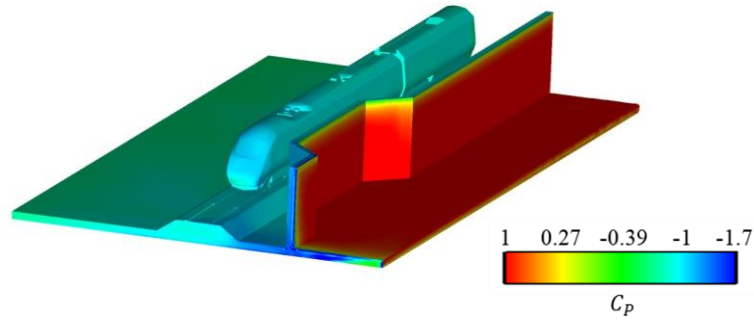
Figure 5.5: Mean surface pressure contours.

5.5 Time-averaged velocity patterns

Figure 5.6 shows time-averaged velocity contours normalised by the relative wind velocity for all 14 loops on the train, for the case with the windbreak wall with 45° transition region at a yaw angle of 90°. Each subfigure shows the position of the loop on the train with respect to the windbreak wall. Overall, the incident wind attacks the windbreak wall, after which the air flow deflects from the tip of the windbreak wall. Air flow with a higher velocity separates from the windward top edge of the windbreak wall. The windbreak wall presence displaces the detachment point of the shear layer to the tip of the windbreak wall. The upper edge of the windbreak wall is the source of a region where the mean velocity variation experiences a sudden increase. Thus, the flow velocity increases in the region near the detachment point. As a result, it can be stated that the windbreak wall implies a solid boundary which deflects the incident flow while slowing down the downstream flow, which exists below the detached shear layer. While a high-velocity region forms above the fence, the momentum of the wind is transported to increased levels. Particularly, the flow separation is initiated from the top of the windbreak wall and extends downstream. This results in largely low velocity regions around the train body, behind the windbreak wall. However, at certain regions, this trend is not consistent and must be discussed.

175
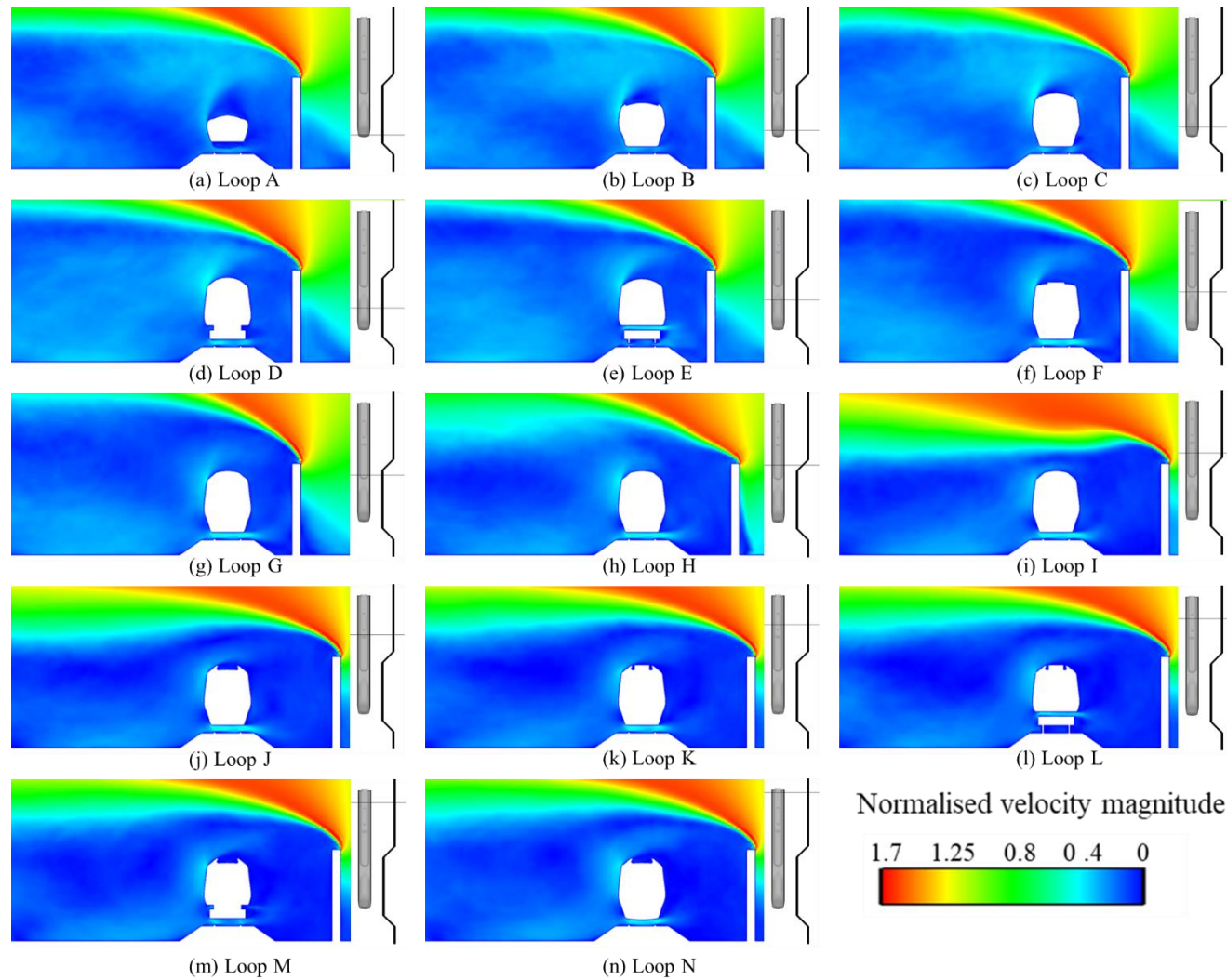
Figure 5.6: Velocity contours at (a – n) Loop A to Loop N for the windbreak wall with 45° transition region at a yaw angle of 90°.

In detail, at loops A to C, the air flow zone appears to be consistent with a slight increase in air velocity observed at the leeward roof edge of the train as the loops progress from A to C. Comparing the wake of the flow, from loop D onwards, an increase in the area occupied by the low velocity zones can be seen. This can be inferred as the interaction between the boundary layer of the train and the separation of the flow from the top of the wall, where, as the geometry (cross-sectional shape) of the leading car changes, the flow is displaced. The changing cross-sectional shape of the leading car affects the flow with a greater influence when the leading car is at its maximum height, comparatively, rather than the wall affecting the flow, as the distance between the wall and the train stays constant at these points.

In terms of the underbody regions, slightly higher velocity regions can be observed as compared to the windward and leeward sides of the train. The effect of the transition region is clear on the flow zones as once the transition region ends, from loop I onwards, the area occupied by the low velocity regions decreases with an evident deviation in the flow. Also, the wake of the flow seems to stabilise in terms of the magnitude of the velocity with much lower velocity occurring behind the train body. However, the wake narrows down resulting in a reduction in the area above the train which experiences the sheltering effects of the windbreak wall. Compared to the leeward side of the train, the windward side of the train shows low velocity regions throughout with slight differences arising from loop I onwards, where the flow shows even much lower velocity regions. This can be supported by the fact that the distance between the windbreak wall and the train stays constant and the distance is higher as compared to earlier loops, which were under the influence of the transition regions.

5.6 Comparison of aerodynamic forces and moments between the experimental and numerical simulations

Table 5.2 provides the time-averaged force coefficients obtained from the experimental and numerical simulations for the case discussed in this chapter.

Table 5.2: Comparison of the overall mean aerodynamic load coefficients for the experimental and numerical cases on the flow around a stationary train subjected to crosswinds with a windbreak wall consisting of a transition region of 45° at a yaw angle of 90°.

	Experiment		IDDES
	Value	Uncertainty	
C_Y	-0.026	±0.001	-0.065
C_Z	0.122	±0.005	0.05
C_{Mx}	0.003	-	0.004

While the side force coefficients obtained using the numerical simulations demonstrate slight deviations from the experimental values, the lift force coefficients obtained using the numerical simulations seem to deviate significantly from the experimental data. This could be due to the simplification of the underbody geometry in the numerical modelling compared to the experimental model or due to blockage effects in the underbody region of the experimental tests. Several earlier works (Diedrichs et al., 2003) have noted that while the side force coefficient shows a somewhat good agreement with the wind tunnel data obtained, the lift force coefficient is seen to deviate significantly. Usually, this can be explained based on the blockage effects of the rails used in the numerical modelling. As a result, results for the lift force coefficient may be over predicted. In addition, the

experimental method of calculating the mean aerodynamic force coefficients involves the discrete integration of the mean pressure coefficient distribution on a limited number of pressure taps, which may have a result on the overall coefficient values. Moreover, as noted in Figure 5.1, there were some differences obtained in the underbody region between the experimental and numerical cases where the numerical case showed a lower pressure. Consequently, this resulted in the lift force coefficient obtained from the numerical simulation to be lower than the one calculated from the experimental method. Furthermore, it is worth mentioning that force and moment coefficients obtained using CFD are calculated by the software based on a sum of the pressure and viscous forces and moments, respectively. Whereas, in the experimental method of calculating the forces and moments coefficients, the impact of viscous shear stress is ignored. This could also have had a direct impact on the results and thus lead to differences in the comparisons. Nevertheless, the rolling moment coefficient obtained using the numerical simulation appears to be close to that obtained from the experiment, indicating the dominance of the side force in this calculation. Overall, a relatively small value of both, the side and lift force coefficients indicates the impact of stability provided by the windbreak wall.

Impact of the windbreak wall discussed in this chapter, in terms of aerodynamic load coefficients, is also reflected by a comparison with a no windbreak wall case. Chapter 4, section 4.3 discusses in detail the effects of a no windbreak wall on the overall aerodynamic load coefficients of the train. A significant decrease is noticed in both the side force and the lift force coefficients as well as the rolling moment coefficient, as seen by the values presented in Table 4.1 and Table 5.2. The side and lift force coefficient values changed from positive to negative with the addition of the wall. This shows the shielding effects due to the wall which are clearly represented by the change in values.

The negligible rolling moment coefficient obtained with the wall case also confirms these findings.

5.7   Transient flow

5.7.1   Time histories of the side and lift force coefficients

The time histories of the side and lift force coefficients obtained from the numerical simulation are shown in Figure 5.7 and Figure 5.8. These are computed at each time step and the values are saved during the averaging process. As shown in Figure 5.7a, the side force coefficient of the leading Class 390 train is unsteady initially and stabilises with the progress of the numerical simulation after a non-dimensional time of 75. Hence, any initial peaks are ignored and the non-dimensional time interval of 75-200 is used for time averaging the pressure and force coefficients. Figure 5.7b and Figure 5.8b show the side and lift force coefficients for the non-dimensional time interval of 75-200, respectively. For the side force coefficient, the peak value obtained is -0.03 while the minimum value is -0.1. The maximum and minimum values of the lift force coefficient are 0.08 and 0, respectively. In both cases, the coefficients can be seen to oscillate around their own mean values with time. The standard deviations of the side and lift force coefficients are 0.013 and 0.017, respectively. This shows that there are greater fluctuations in the lift force coefficient as compared to the side force coefficient, possibly due to the interaction of the aerodynamic flow with the vortex shedding from the wall. Finally, as noted earlier in this chapter, formation and development of vortices close to the top and bottom of the train induce disturbance in the surface pressures, thus leading to fluctuations in the lift force coefficient. Also, pressure fluctuations on the sides of the train due to temporal flow structures contribute to the instantaneous side force coefficient of the leading car.
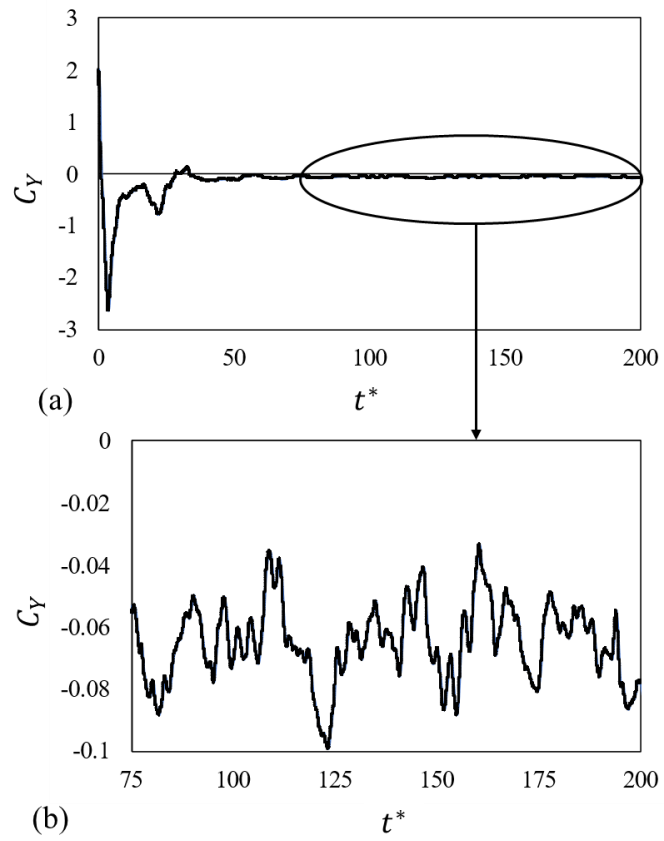
Figure 5.7: Time history of the side force coefficient obtained on the leading car of the Class 390 from the numerical simulation (a) for the entire time interval (b) for the non-dimensional time interval of 75-200.
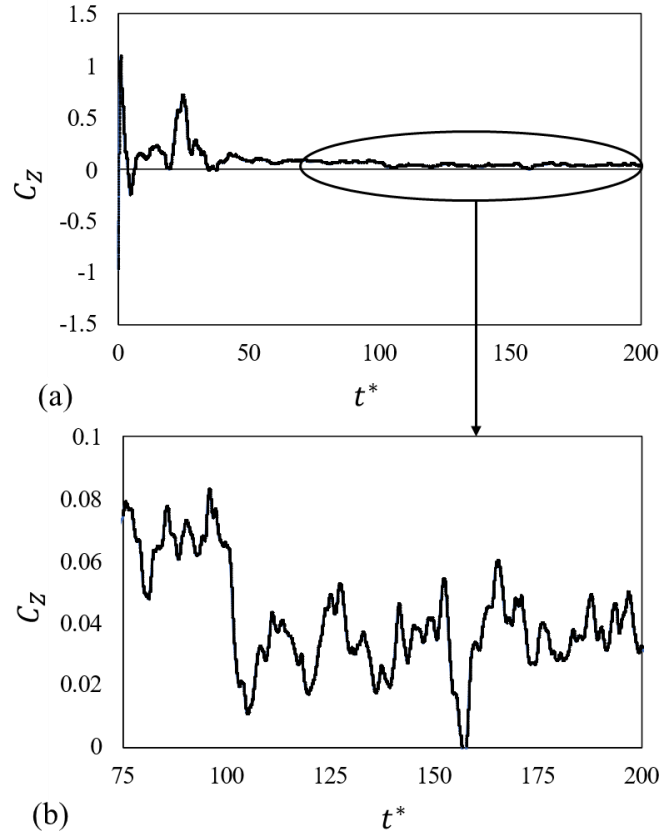
Figure 5.8: Time history of the lift force coefficient obtained on the leading car of the Class 390 from the numerical simulation (a) for the entire time interval (b) for the non-dimensional time interval of 75-200.

5.7.2 Frequency analysis of the forces

In this section, frequency analysis of the side force on the leading car of the Class 390 train is carried out to investigate the transient effects of the flow on the train, with specific reference to the potential instability of the train. The time history data of the side and lift force coefficients of the leading car is converted to the power spectral density (PSD) in order to look for any oscillating components of the side and lift force that may cause lateral instability of the train. This spectral analysis is performed to determine if there are any dominating frequencies of the time-dependent side and lift force coefficients. Fourier

182

transform is used to resolve the dominating frequencies representing the crosswind induced force frequencies.

Figure 5.9 shows the PSD of the side and lift force coefficients, normalised by their variance, against the Strouhal number (St), for the leading car of the Class 390 train analysed in this chapter. Strouhal number (St) refers to a dimensionless frequency and is given as:

$$St = \frac{fW}{V_{rel}}$$

(5.2)

where f is the frequency of the flow, W is the characteristic length, which is the width of the leading car and V_{rel} is the free stream velocity.
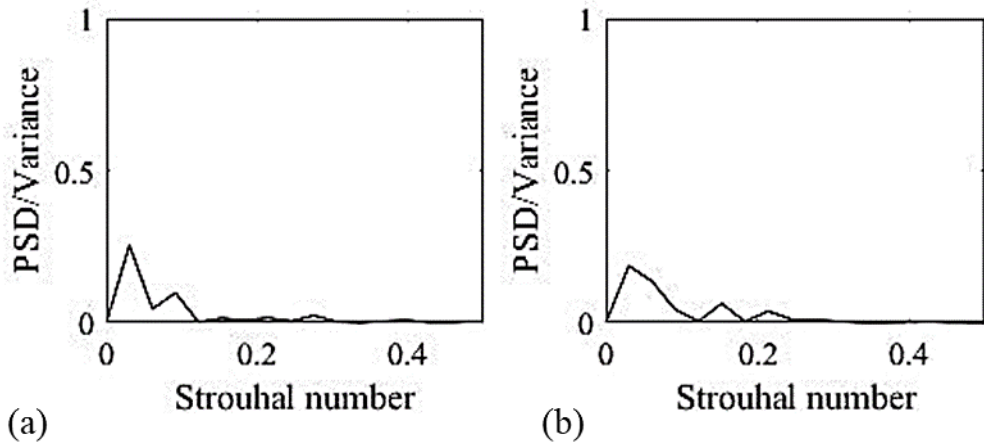
Figure 5.9: Normalised PSD of the (a) side and (b) lift force coefficients against the Strouhal number for the leading car of the Class 390 train.

As seen in Figure 5.9a, there are two distinct peaks of the oscillating components found on the power spectra of the side force coefficient in the range $0 < St < 0.12$. The dominant component of the side force coefficient is observed at $St \approx 0.03$. Another low frequency peak appears on the power spectra at $St \approx 0.09$. These dominant peaks at low frequencies imply a type of vortex shedding that is dominating the lateral forces on the leading car.

183

Some minor fluctuations are observed in the range 0.15 < St < 0.3, which appear to be related to the attachment and detachment of the small flow structures on the surface of the leading car and due to instabilities in the shear layer but these do not seem to be significant as expected due to the presence of the windbreak wall. For the lift force coefficient, as shown in Figure 5.9b, three dominating low frequency peaks representing the shedding frequencies are observed at $St \approx$ 0.03, 0.15 and 0.22, respectively. These can correspond to some type of vortex shedding and the instability of the weak vortices within the separation region above the roof of the leading car. No high frequency peaks are noticed.

5.7.3   Instantaneous flow and pressure fields

To understand the transient simulation, the instantaneous pressure fields obtained using the IDDES scheme are analysed herewith. For illustration purposes, the instantaneous pressure fields on some of the taps of loops A and H are demonstrated along with the location of these taps on the loop, however, the trend noted on all the loops is discussed. Figure 5.10 demonstrates the time-varying signals of the instantaneous pressure obtained on the windward side of the train. These variations were smaller as compared to the taps located on the roof of the train, as illustrated by Figure 5.11. Quantification of these changes is discussed further in detail in this section. In terms of the taps located at the roof, it was observed that pressure variations on the taps at the leeward roof edge of the train were larger as compared to those near the windward roof edge of the train. With regards to the leeward side of the train, as shown by Figure 5.12, there are again significant variations in the pressures obtained, however, it appears that the variations stay similar on the entire leeward side.

For loop A, on the windward side, the mean pressure value was ≈ -29.8 Pa, with minimum pressure value being ≈ -34.5 Pa and maximum pressure value being ≈ -27.5 Pa. This is shown by the graph in Figure 5.10a, while the red pointer locates the discussed tap on loop A, on the right-hand side of the figure. Therefore, the difference in the pressure values on the windward side for this loop was ≈ 7 Pa. For loop H, on the windward side, the mean pressure value was ≈ -28 Pa, with minimum pressure value being ≈ -31 Pa and maximum pressure value being ≈ -26 Pa. Therefore, the difference in the pressure values on the windward side for this loop was ≈ 4.5 Pa. For loop H, on the windward corner of the roof, the mean pressure value was ≈ -28.5 Pa, the minimum pressure value was ≈ -31 Pa and maximum pressure value was ≈ -26 Pa. The resulting difference in the pressure values at the windward roof corner was ≈ 5 Pa. However, as the flow started to move around the roof, there was a larger variation in the pressure values. To elaborate, at the middle of the roof, the mean pressure value was ≈ -29 Pa, the minimum pressure value was ≈ -34 Pa and maximum pressure value was ≈ -24.5 Pa. Therefore, the resulting difference in the pressure values at the middle of the roof was ≈ 9 Pa, higher than that of the windward side. Over the leeward corner of the roof, the mean pressure value was ≈ -30 Pa, the minimum pressure value was ≈ -39 Pa and the maximum pressure value was ≈ -26 Pa. Therefore, the resulting difference in the pressure values was ≈ 13 Pa, which was the highest compared to the windward side and the rest of the roof. At the entire leeward side, for loop A, the mean pressure value was ≈ -29.5 Pa, with minimum pressure value being ≈ -35 Pa and maximum pressure value being ≈ -26 Pa. Therefore, the difference in the pressure values on the leeward side for this loop was ≈ 9 Pa, thus confirming that the pressure variations at the windward side of the train were lesser as compared to the roof and the leeward side of the train. These observations seem to be in line with previous

findings which stated that the windbreak wall was able to provide enhanced shielding effects to the windward side of the train.

In terms of the statistics of the time-varying signals of the instantaneous pressures obtained on loop A, the taps on the windward side have the root mean square (RMS) values in the range of 0.14 to 0.20. Whereas, the taps on the leeward side have the RMS values in the range of 0.08 to 0.15. For loop H, the taps on the windward side have the RMS values in the range of 0.003 to 0.018 while the taps on the roof have the RMS values in the range of 0.047 to 0.28. This trend is observed at latter loops as well, which are located farther from the nose of the train. Also, on the whole, the pressure taps on the windward side have the smallest RMS comparatively.

Overall, variations in pressures are linked to the flow fluctuations, which result due to flow separations and flow accelerations. Therefore, a sharp variation in pressure is related to a higher turbulence in the flow. Also, all pressure taps are noted to provide negative pressure at all times. Finally, it can be concluded that the variations in the side and lift forces discussed in section 5.6 are due to the variations in pressure on the different sides of the train.
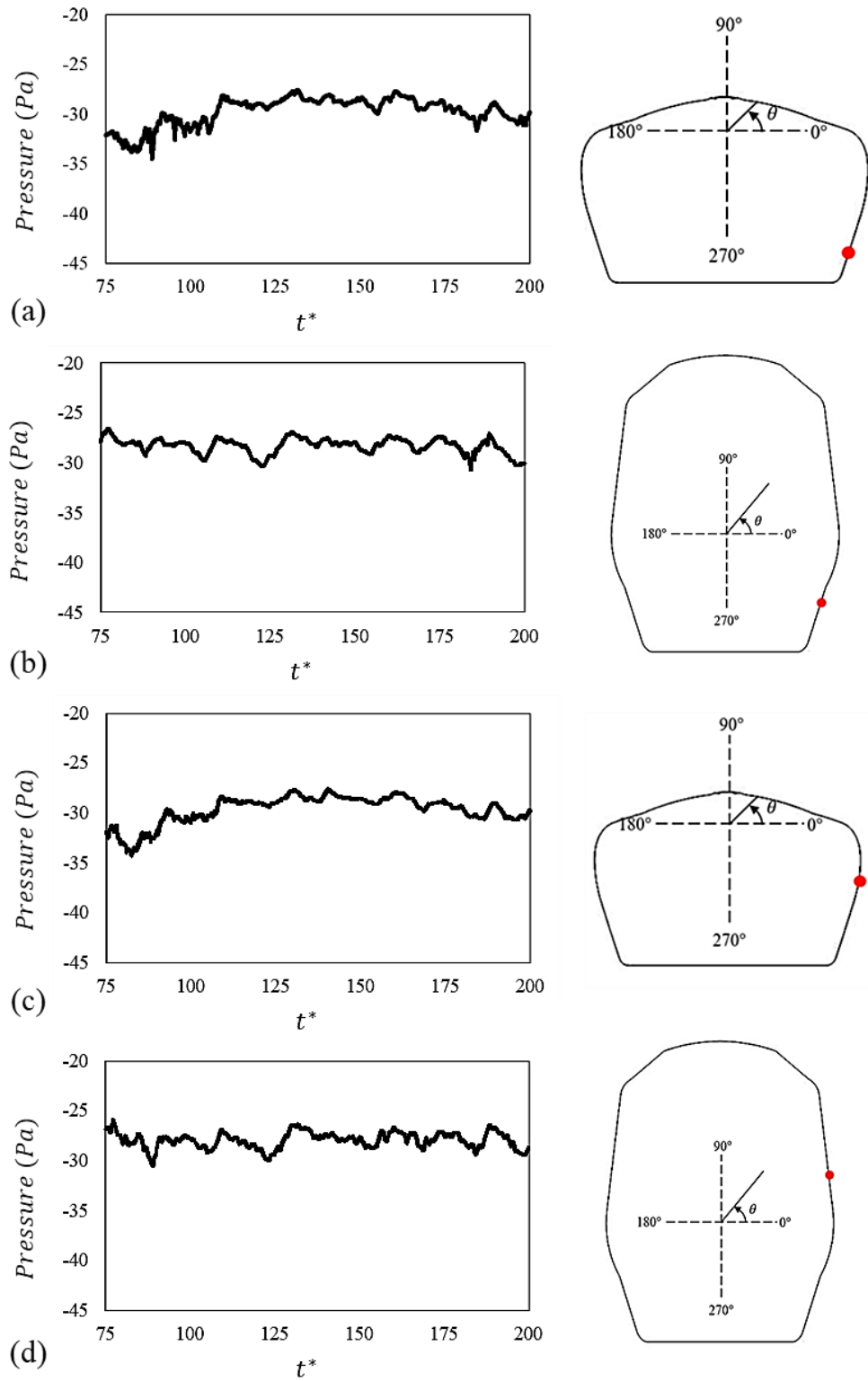
Figure 5.10: Time-varying signals of the pressure on some of the pressure taps located on the windward sides of (a and c) loop A and (b and d) loop H for the non-dimensional time interval of 75-200.

187
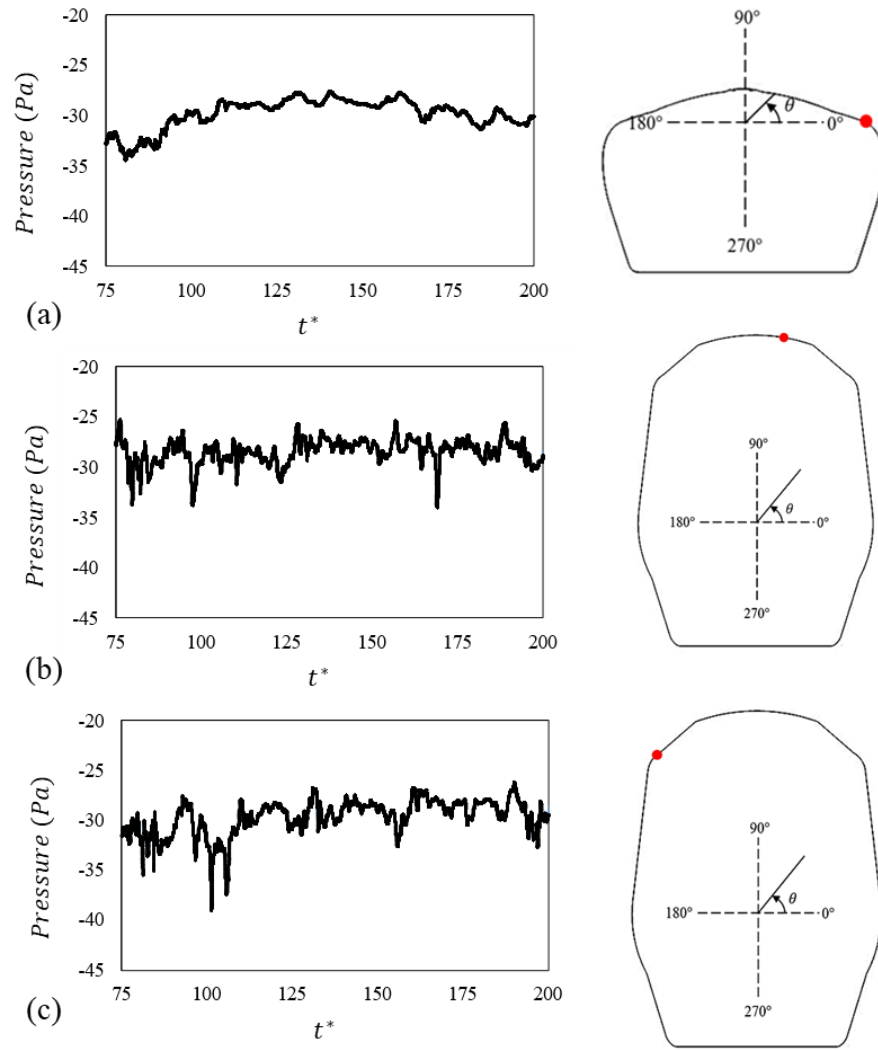
Figure 5.11: Time-varying signals of the pressure on some of the pressure taps located on the roof of (a and c) loop A and (b and d) loop H for the non-dimensional time interval of 75-200.
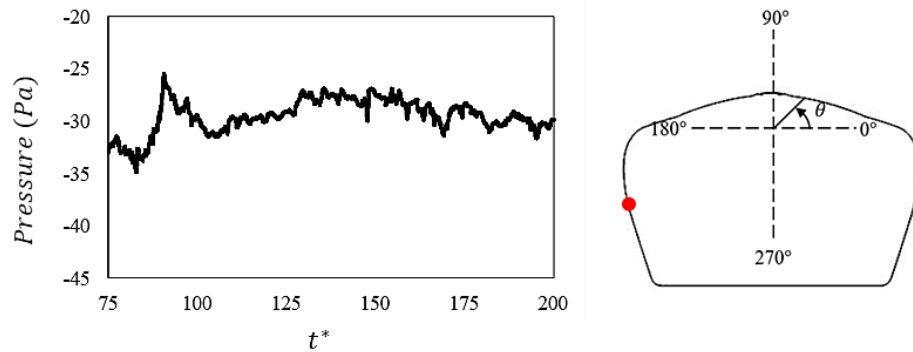
Figure 5.12: Time-varying signals of the pressure on a pressure tap located on the leeward side of loop A for the non-dimensional time interval of 75-200.

5.8 Assessment of the credibility of the experimental method

The experimental processing methodology adopted for calculating the overall mean aerodynamic load coefficients for the side (lateral), $\overline{C_Y}$, and lift (vertical), $\overline{C_z}$, forces along with the rolling moments about the X-axis discussed in chapter 3, section 3.6 is based on the measurement of surface pressure distribution over the train. This methodology has been successfully used in several earlier studies (Sanquer et al.,2004; Dorigatti et al., 2015; Gallagher et al., 2018), and involves the discrete integration of the mean pressure coefficient distribution over the train surface. To do so, the discretisation method of the model surface area into a number of smaller areas around each pressure tap assumes that the pressure measured at each individual pressure tap is constant and uniformly distributed across the corresponding surface. This assumption of pressure staying constant may raise concerns on the adequacy of the method employed and therefore, in this section, the credibility of the discretisation method used in this thesis for the experimental calculations is assessed. This will also allow an assessment of the experimental error, if any, due to only having pressure taps at limited points. To do so, all individual pressure results obtained from the numerical simulations are interpolated onto the same experimental pressure taps for case (e) of the experiments. Numerical simulations provided extensive results on the entire circumference of the train. Therefore, pressure data in terms of mean pressure coefficients corresponding to the same position as the experimental pressure taps for each loop was extracted from the numerical simulations. Thereafter, the mean pressure coefficients obtained from the numerical simulations were used in equations 3.1 and 3.2, provided in chapter 3. Next, the aerodynamic load coefficients were evaluated using the experimental discretisation

technique discussed in section 3.6, chapter 3. The resulting outcomes are shown in Table 5.3.

Table 5.3: Comparison of the overall mean aerodynamic load coefficients obtained using a new method with the experimental and numerical cases.

	Experiment		IDDES	CFD pressure used in the experimental method
	Value	Uncertainty		
C_y	-0.026	±0.001	-0.065	-0.081
C_z	0.122	±0.005	0.05	0.046
C_{Mx}	0.003	-	0.004	0.057

As noted from Table 5.3, a value of -0.08 is obtained for the side force coefficient and a value of 0.05 is obtained for the lift force coefficient. It appears that these values are closer to the values obtained from the numerical simulations (i.e. -0.065 and 0.05 for the side and lift force coefficients, respectively) that were computed by the CFD software used. While these values are close, there are some differences, specially in the rolling moment coefficient values. This is an interesting finding and carrying out this procedure allowed for an assessment of the experimental error due to only having pressure taps at limited points. Fundamentally, it seems that the experimental method of converting the model surface into a simplified geometry composed of discreet rectangular surfaces is in fact, somewhat, a decent approach in calculating the non-dimensional surface pressure coefficients. However, this method has potential limitations in terms of calculating the mean aerodynamic load coefficients where the limited number of pressure taps may have a significant result on the overall coefficient values, as noted in section 5.6. Also, the

uncertainty analysis presented in Appendix A for calculating the total uncertainties for the mean aerodynamic load coefficients could be underpredicted as it does not take into consideration the uncertainty introduced through discretising the geometry of the train model. Since it was assumed that pressure is uniform across each discretised area in the process of pressure integration, there could possibly be some error introduced.

5.9 Conclusions

This chapter provides the results obtained from the numerical simulations carried out on a stationary Class 390 model-scale train subjected to crosswinds at a yaw angle of 90° with a windbreak wall consisting of a transition region of 45° transition angle. This chapter has explained the influence of a windbreak wall and in particular the effect of a typical transition region in a windbreak wall on the flow around a stationary passenger train. The next chapter will build up from this chapter and present the results of a detailed numerical investigation, which will take into account the relative movement of the train and the windbreak wall with the transition region.

Overall, the results demonstrated in this chapter have shown that:

- While a decent agreement is observed in the $\overline{C_P}$ values between the experimental and numerical results overall, slight discrepancies are still noticeable, mainly in the underbody regions. This is not surprising based on the practical limitations and difficulties noted in the experimental set-up. Differences in the mean aerodynamic load coefficients are discussed.

- The immediate deflection in the incident flow at the tip of the windbreak wall can be easily appreciated. The incident flow streamlines follow the same trend throughout where they attack the windward side of the windbreak wall and then

deflect from the top edge of the wall. The streamlines are lifted and the flow above the windbreak wall is accelerated. The presence of a windbreak wall displaces the detachment point of the shear layer to the tip of the windbreak wall. Thus, the flow velocity increases in the region near the detachment point where the flow separates.

- There exists a fully developed wake, which was dominated by large vortices and a recirculation zone. The disappearance of vortices V1 and V3 confirms the suggestion made in the literature review that the random change in the distance between the windbreak wall and the railway track, known as the transition region, can result in the formation of vortices around the train body.

- Comparison of aerodynamic forces and moments between the experimental and numerical simulations demonstrated that while there are slight deviations in the side force coefficients obtained, there are significant deviations in the lift force coefficients. This is most likely due to simplification of the underbody geometry in the numerical modelling or blockage effects in the underbody region of the experimental tests. Also, the effect of using a limited number of pressure taps in the experimental calculation of the mean aerodynamic force coefficients cannot be ignored. Finally, CFD software make use of pressure and viscous forces and moments to determine the relevant coefficients whereas, impacts of viscous shear stress are ignored in experimental calculations. Nevertheless, the rolling moment coefficient obtained match well, indicating the dominance of the side force. Overall, a relatively small value of both, the side and lift force coefficients indicates the impact of stability provided by the windbreak wall.

CHAPTER 6: Flow around a moving train subjected to crosswinds with a windbreak wall consisting of a transition region of 45°

6.1   Introduction

This chapter provides the results obtained from the numerical simulations carried out on a moving Class 390 model-scale passenger train subjected to crosswinds with a windbreak wall consisting of a 45° angled transition region. The numerical simulations made use of the widely used Improved Delayed Detached Eddy Simulation (IDDES) method.

Chapters 4 and 5 presented results on stationary investigations where the train model was not moving. In such static investigations, the relative wind coincides with the onset wind and therefore, the yaw angle is calculated by the onset wind direction to the track. Hence, the effect of a yaw angle can be determined by altering the relative orientation between the oncoming flow and the vehicle. However, in chapter 6, the relative wind and onset wind do not coincide due to the movement of the vehicle. In a moving vehicle investigation, the relative wind is determined using the vector sum of the wind velocity and vehicle speed, as explained in chapter 3. Using the velocity triangle method, the train experiences a relative wind velocity of 57.8 m/s at a yaw angle of 15°.

A 15° yaw angle was chosen as it belongs in the low yaw angle range. Usually, as discussed in chapter 5, higher yaw angles are relevant for stationary or slow-moving trains only (Baker, 2014a). In addition, this yaw angle creates an opportunity to further validate the numerical results obtained in this chapter. Also, in numerical (CFD) simulations, a

specific mesh design has to be created for each specific yaw angle which would mean that multiple meshes need to be recreated for different wind incident angles, thus increasing both the associated processing times and the computational costs.

In terms of the windbreak wall, a transition angle of 45° is a mid-way between the no transition region (i.e. 0° transition angle) and maximum transition region (i.e. 90° transition region), as discussed in chapter 5. Therefore, for the moving model investigation, a similar windbreak wall was used as in chapter 5, with the exception being in the length of the windbreak wall. This was due to scaling up the size of the domain in order to accommodate a three-car train model, as discussed in chapter 3, section 3.6.1.

Thus, this chapter aims to study the influence of crosswinds across the specified transition region on a moving passenger train. To do so, the chapter provides an in-depth analysis on the flow behaviour which exists around the windbreak wall and the subsequent effects of a moving train on the wind flow induced by a change in the windbreak wall geometry. The surface pressure results in this chapter are presented in terms of a non-dimensional pressure coefficient, C_P. It must be noted that in normalising the pressure data for achieving a C_P value for each case, the relative velocity of 57.8 m/s was used. Therefore, for the pressure contour plots demonstrated in this chapter, it must be considered that the C_P results on the windbreak wall are based on the choice of the relative velocity of 57.8 m/s.

Section 6.2 illustrates the position of the moving train with time, explaining where the first car of the train is and the cross-sectional loops are in the domain specifically, respectively to the stationary windbreak wall. Section 6.3 provides and discusses the results of surface pressure distribution at the different cross-sectional loops of the train with time in terms of graphical figures. To better understand the aerodynamics of the

194

high-speed train, section 6.4 studies the surface pressure patterns on the windward, roof, and leeward side of the high-speed moving train. Next, in section 6.5, an analysis of the flow fields that exist around the train body, obtained using different visualization techniques, is provided. Section 6.6 further investigates the performance of the windbreak wall studied in this chapter by presenting and analysing the overall aerodynamic load coefficients obtained for the leading car of the moving Class 390 train under crosswinds. Finally, section 6.7 presents the general conclusions drawn in this chapter and indicates the importance of considering the relative motion of the train and the windbreak wall.

6.2   Position of the moving train with time

Figure 6.1 illustrates the location of the moving train with respect to the windbreak wall at different arbitrary times, which are chosen to assess the results in different regions. On Figure 6.1a, the position of different loops on the head of the train can be observed. It must be noted that these loops are labelled in the same order and are at the same distance from the origin as in chapter 3. The locations of the moving train are presented at various non-dimensional times, $t^* = \frac{tV_{rel}}{H}$, where t is the simulation time, V_{rel} is the free stream velocity and H is the height of the train.

(a) $t^* = 7.4$ (b) $t^* = 11.1$ (c) $t^* = 14.8$ (d) $t^* = 18.5$
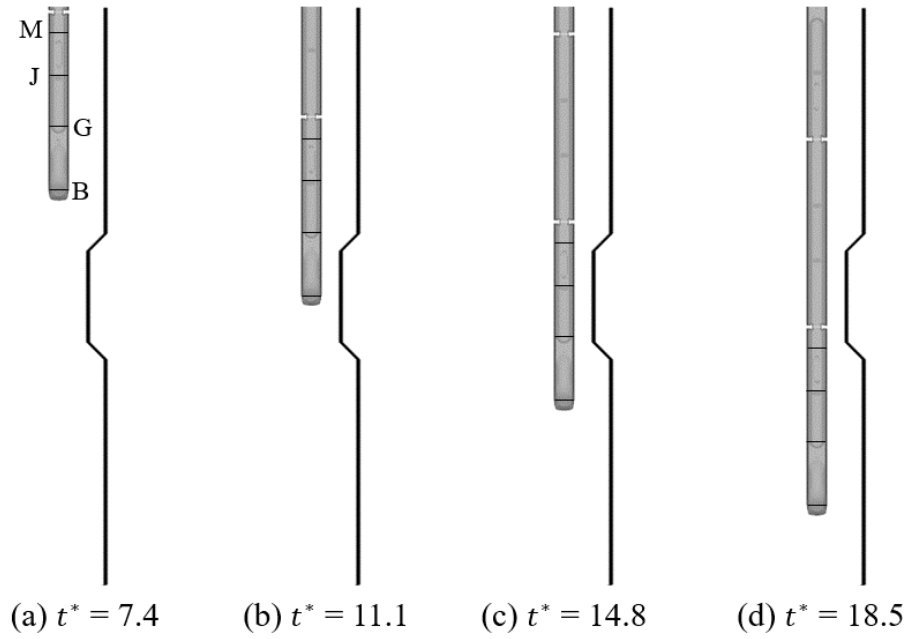
Figure 6.1: Location of the moving train with respect to the windbreak wall at different t^*.

At $t^* = 7.4$, the first car of the train has just started to move against the uniform section of the windbreak wall. At this point, the nose of the train is about to approach the transition region of the windbreak wall. At $t^* = 11.1$, the nose of the train and a part of the first car's body are under the influence of the transition region while the rest of the first car is moving against the uniform section of the windbreak wall. It must also be noted that $t^* = 11.1$ is the closest representation of the stationary case analysed in chapter 5. At $t^* = 14.8$, the nose of the train has passed the area surrounding the transition region, but the rest of the first car is under the influence of the transition region. At $t^* = 18.5$, the nose and most of the first car's body have passed the transition region area and are under the influence of the uniform section in the windbreak wall, with the exception being the tail of the first car which is now under the influence of the transition region.

6.3 Surface pressure distribution at different cross-sectional loops of the first car with time

This section provides and discusses the surface pressure distribution results at different cross-sectional loops of the train with time. Figure 6.2-6.5 present the surface pressure distributions at Loops B, G, J and M of the moving train at different times. In addition, these figures also show the cross-sectional images of each respective loop on the right-hand side of the figure.

Loop B represents a critical part of the nose of the train, which is located on the leading car. Based on Figure 6.2a, it is evident that at the start of the WWS of the moving train, there is a sharp increase in surface pressure ($\theta = 272°$ to $\theta = 306°$), i.e. a decrease in the negative pressure, however, as the flow continues to progress on the WWS, the surface pressure tends to gradually decrease till a weak suction peak appears, representing possible flow separation. At the windward edge of the roof, the surface pressure increases, after which a sudden positive pressure peak is observable ($\theta = 39°$). Such an extreme pressure represents a stagnation point, which appears on the nose of the first car due to the compressible effects of a moving train on the oncoming crosswinds. In addition, to elaborate, the flow around the train is characterised by three-dimensional structures, which arise mainly on the nose of the train due to the impact of crosswinds. Following on, over the windward side of the roof, an increase in surface pressure is noticeable, whereas on the leeward side of the roof, the pressure starts to decrease, due to the shielding effect. Regardless of these changes in the surface pressure, the magnitude of the surface pressure at the roof remains positive. Similar to the windward edge of the roof, a positive pressure peak appears at the leeward edge of the roof ($\theta = 142°$). It is worth mentioning that the shape of the pressure plot at the roof resembles the geometry of the

aerodynamic nose of the train. The circumference of the train at Loop B is not smooth, as demonstrated by the loop B image on the right-hand side of Figure 6.2a, hence the sudden changes in the surface pressure. Achieving such a finding in an experimental campaign will be hard as usually, physical models do not have pressure taps all around the circumference of the train due to practical limitations. This indicates the importance of carrying out a numerical investigation in order to capture such interesting revelations. Numerical simulations can also be quickly reconfigured to study different scenarios. A sudden change is evident in the surface pressures as the flow progresses towards the LWS of the train, where two strong suction peaks occur. However, over the LWS, the pressure starts to gradually increase till the bottom leeward side, at which, the surface pressures start to decrease indicating flow separation due to the geometry of the vehicle. Similarly, the underbody region experiences low velocity regions where the surface pressures continue to decrease, leading to a kind of suction peak.

(a) $t^* = 7.4$

(b) $t^* = 11.1$

(c) $t^* = 14.8$

(d) $t^* = 18.5$
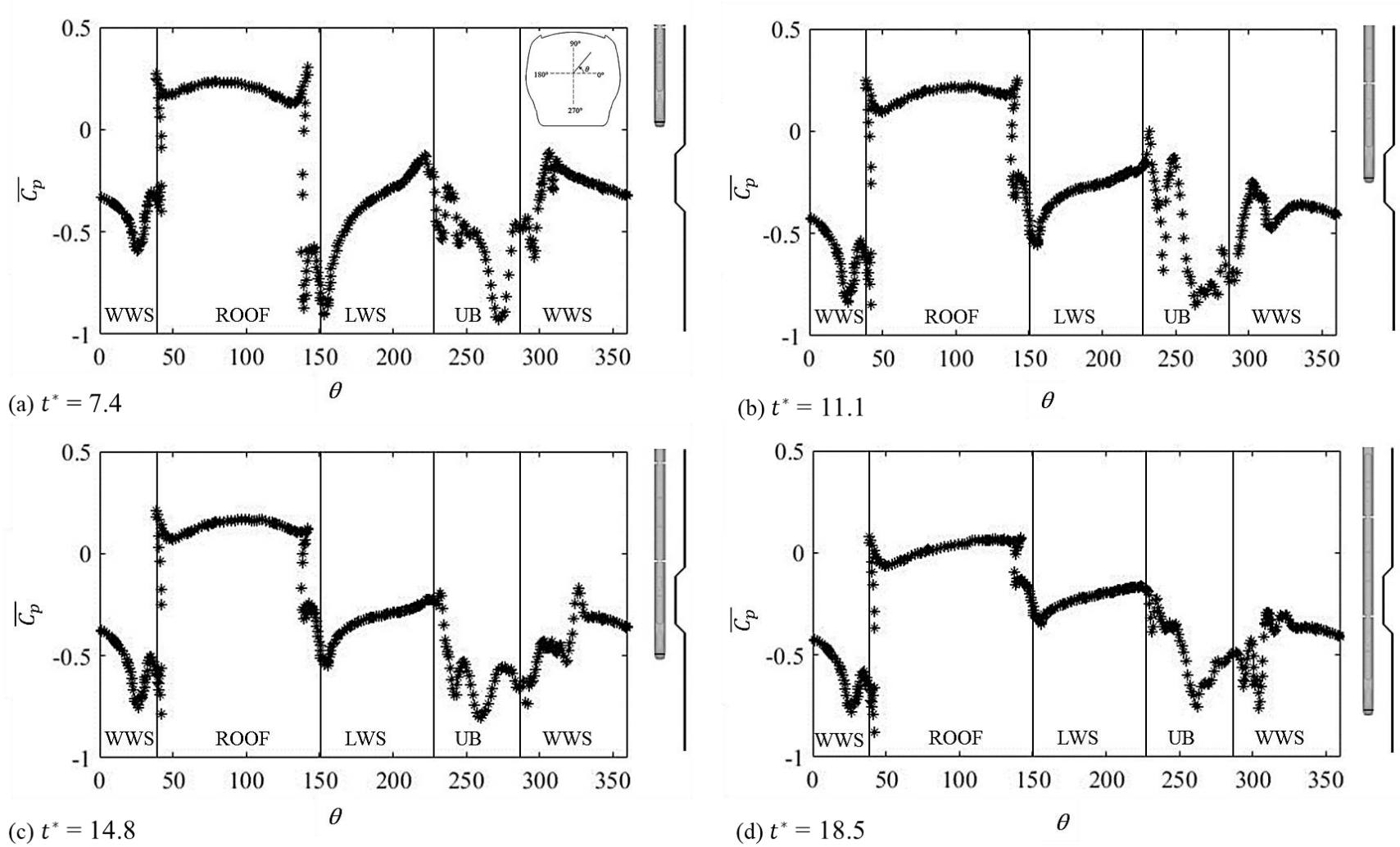
Figure 6.2: Surface pressure distribution at Loop B of the moving train at different t^*.

199

As the train continues to travel, similar pressure trends are observable at Loop B. However, a close look at the results of the surface pressure shows some differences that exist. To elaborate, comparing the windward sides at $t^* = 7.4$ and 11.1, a slight change in the trend adopted by the surface pressures is apparent. While a smooth decrease was observed at $t^* = 7.4$, a fluctuation is evident at $t^* = 11.1$. In addition, towards the upper windward edge at $t^* = 11.1$, a more intense suction peak is visible ($\theta = 27°$), comparatively. The value of the $\overline{C_P}$ at this point is -0.83, which is much lower than the value obtained at $t^* = 7.4$, of -0.58. This sharp decrease in pressure is due to the change in the position of the train. At $t^* = 11.1$, Loop B is under the influence of the transition region, where the distance between Loop B and the windbreak wall is almost half the distance of Loop B and the windbreak wall at $t^* = 7.4$. Therefore, the impact of the transition region on the flow separation is clearly visible, creating a region of low pressure, due to the decrease in the distance between the wall and the moving train, which causes intensification in flow separation. Following on, at these two times discussed, while the roof of the train presents quite similar results, the two strong suction peaks are seen at $\theta=139°$ and $\theta=153°$ fades out at the latter time. A clear difference in the magnitude of the surface pressures is also obvious. At further times as well, some differences are evident in the trends. For instance, the strong positive pressure peak seen at $\theta = 142°$ at former times, weakens at later times. Similarly, the weak suction peak at $\theta = 139°$ continues to fade out with time. While the LWS presents similar trends, one interesting finding can be identified in the underbody region at $t^* = 14.8$ and 18.5, where at the former time, there are some significant fluctuations in the surface pressures. The underbody region might be impacted by the transition region as at $t^* = 14.8$, the nose of

the train has just left the transition region zone whereas at $t^* = 18.5$, the nose is much

farther away from the transition region zone, comparatively.

Overall, while the windbreak wall is present, the fluctuations in the surface pressure at

this loop highlight the interaction of the moving train and oncoming wind, which arise

due to the movement of the high-speed train in the stagnant airflow region (high-pressure

area), where the nose of the train is the first to travel against the oncoming flow. In

addition, the results represent sharp gradients at this loop. Since this loop is based on the

nose of the train, it is not unreasonable to speculate the existence of an unsteady flow

mechanism, whose effects are visible by the movement of the train. The intensified high

pressure regions on the nose appear due to different wind profiles on the moving train

(i.e. an increased local relative wind velocity versus the distance from the ground). At the

front of the nose, compression waves are formed, which causes an increase in pressure

followed by an expansion wave which decreases pressure on the train nose and body. The

compression wave is caused due to the static air on the front of the nose of the train.

Loop G is located away from the nose of the train on the leading car, near the mid-point

of the train in the longitudinal direction. The cross-sectional shape of this loop has some

visible differences as compared to Loop B. For instance, there are no sharp corner edges

at the roof of Loop G. In terms of the numerical results on this loop, with time, based on

Figure 6.3a, to a certain extent, fairly uniform surface pressures exist on the entire WWS

of the moving train, ($\theta = 300°$ to $\theta = 50°$). As a result, the shielding effect of the

windbreak wall is visible at the WWS of this loop. However, as the flow progresses from

the WWS towards the roof, the surface pressures experience a sudden decrease. Over the

roof ($\theta = 50°$ to $\theta = 150°$), considerable fluctuations and variations can be seen in the

surface pressures with overall much lower pressures (i.e. more negative) as compared to

the rest of the loop. It must be noted that Figure 6.3a presents the results at $t^* = 7.4$, where the moving train has just entered the domain. Due to the entrance of the first car of the domain in the computational domain, consisting of crosswinds, an unsteady turbulence phenomenon takes place. This causes the formation of low-pressure vortices around the train. Therefore, certain uncertainties may be possible in the flow that develops around the moving train. In terms of the LWS and the underbody regions, somewhat uniform pressure results are noticeable.

As the train continues to travel behind the wall, at $t^* = 11.1$, Loop G is at the start of the transition region, as depicted by Figure 6.1. As shown by Figure 6.3a, the surface pressures on the WWS, LWS and the underbody region can be seen to become quite stable with subtle steady variations. This clearly indicates that the windbreak wall has been successful in providing its sheltering effects to the train from the oncoming winds. However, the roof of the train shows some significant variation in the surface pressures with overall much lower (i.e. with more negative) values as compared to the rest of this loop. It seems that while the rest of the loop is under the sheltering effects of the windbreak wall, a low pressure region exists at the roof, possibly due to the presence of a vortex, which might be originated due to the effects of the former part of the body, which is now under the influence of the transition region, on the flow. Furthermore, as the train continues to travel with time, compared to $t^* = 11.1$, the surface pressures at t^* = 14.8 on the WWS show slight fluctuations, thus indicating the effect of the transition region, while lesser fluctuations can be noticed on the roof of the train as the flow on the roof of the train is mainly dominated by the wind moving over the top of the wall. Nevertheless, the roof still presents much lower (i.e. negative) surface pressures. Based on these results, it can be stated that the change in the distance between the windbreak

wall and the train has a significant influence on the fluctuations of the surface pressures on the roof, as well as to a certain extent on the other sides of the loop. As the train travels past the transition region, at $t^* = 18.5$, the surface pressures at the roof of this loop starts to show fluctuations again. The rest of the loop at $t^* = 18.5$ presents similar results to earlier times.

Figure 6.3: Surface pressure distribution at Loop G of the moving train at different t^*.

204

Loop J is situated near the mid-point of the first car of the train in the longitudinal direction, hence it was selected for discussion. The cross-sectional shape of this loop is slightly different from Loop G. To elaborate, Loop J has sharp corner edges at the roof, where a part of the roof lies between and below these edges in a hollow straight section, as demonstrated by the loop G image on the right-hand side of Figure 6.3a. At $t^* = 7.4$ and 11.1, Loop J is under the influence of the different uniform sections of the windbreak wall. According to the results presented in Figure 6.4, at $t^* = 7.4$, the surface pressures on the WWS of the train demonstrate a decrease (i.e. they become increasingly negative), until the flow progresses to the roof. At the windward edge of the roof, the surface pressures start to increase, where over the roof, an unsteady trend can be seen in the results. However, the LWS and the underbody region seem to be sheltered by the windbreak wall, thus showing less fluctuations in the surface pressures. As the train travels farther, the sudden changes in the surface pressure decrease on the roof as compared to the earlier time, with somewhat uniform surface pressures over the rest of the loop. At $t^* = 14.8$, Loop J is under the influence of the transition region. The results indicate that when this loop is behind the transition region, the surface pressures at the WWS, LWS and underbody region become uniform. Such a finding was also obtained for earlier loops such as Loop G. In terms of the roof, slight fluctuations still exist but are not very strong. At $t^* = 18.5$, Loop J has just left the transition region and the results indicate that a much more uniformity and stability in the surface pressures on the WWS, LWS and the underbody region. Some instability is still experienced by the roof of this loop where a chaotic pressure distribution takes place over the roof. Also due to the complex geometry, each position probe faces a unique velocity profile. However, these fluctuations are less severe compared to ones experienced by the same loop earlier.

(a) $t^* = 7.4$

(b) $t^* = 11.1$

(c) $t^* = 14.8$

(d) $t^* = 18.5$
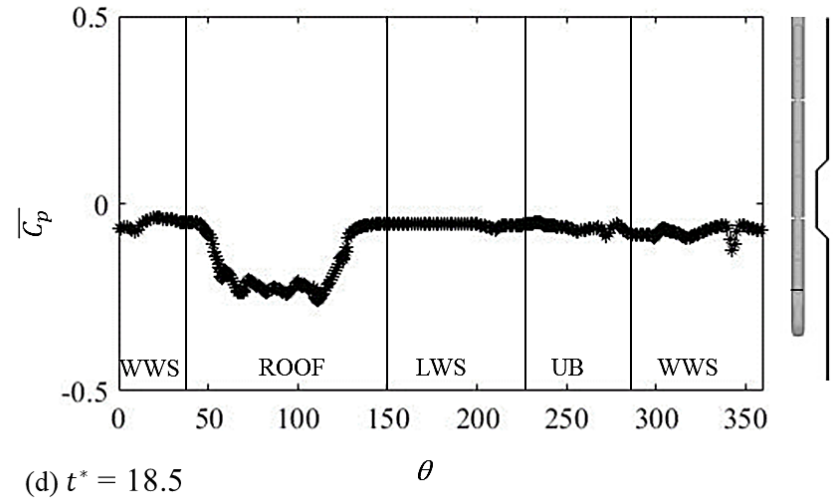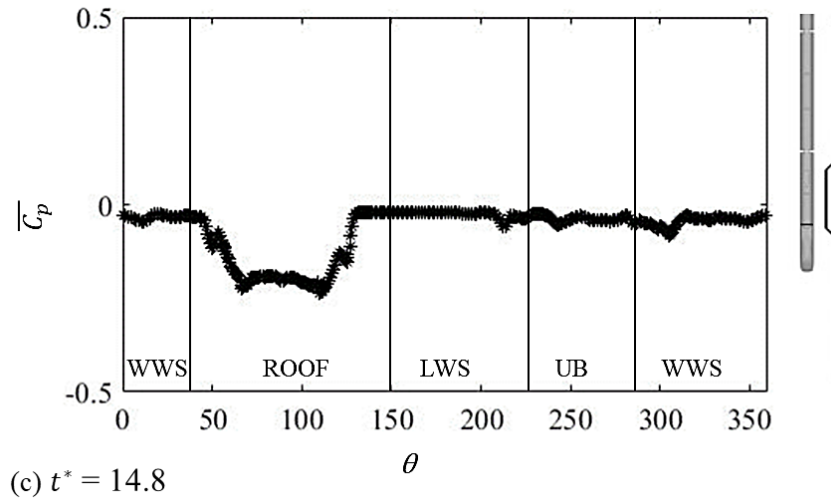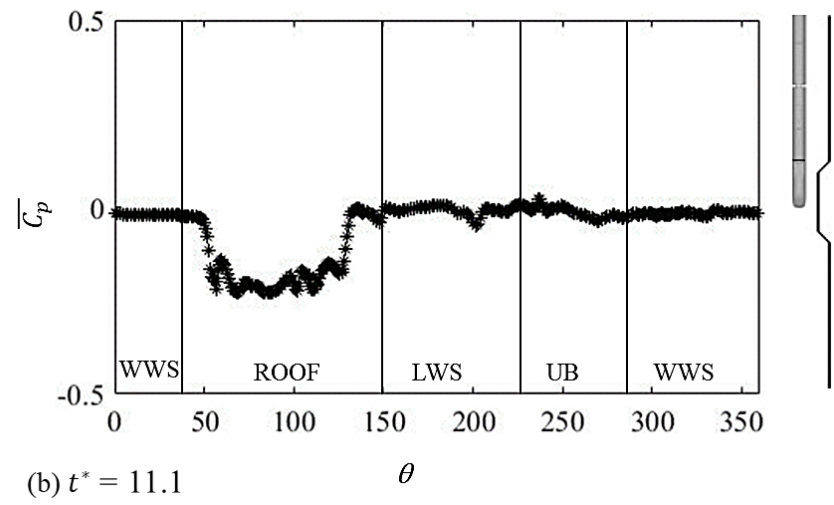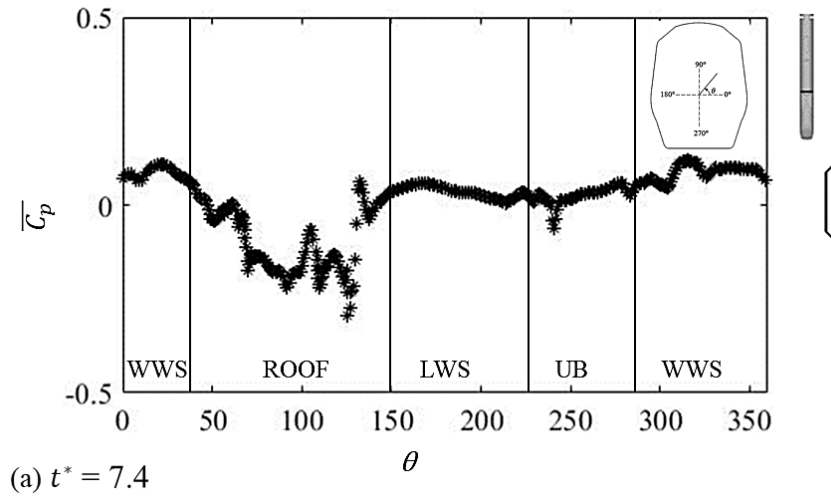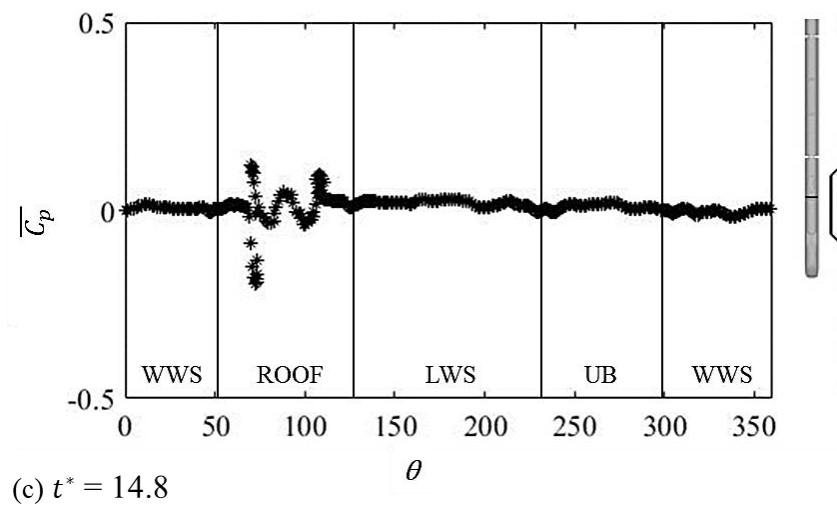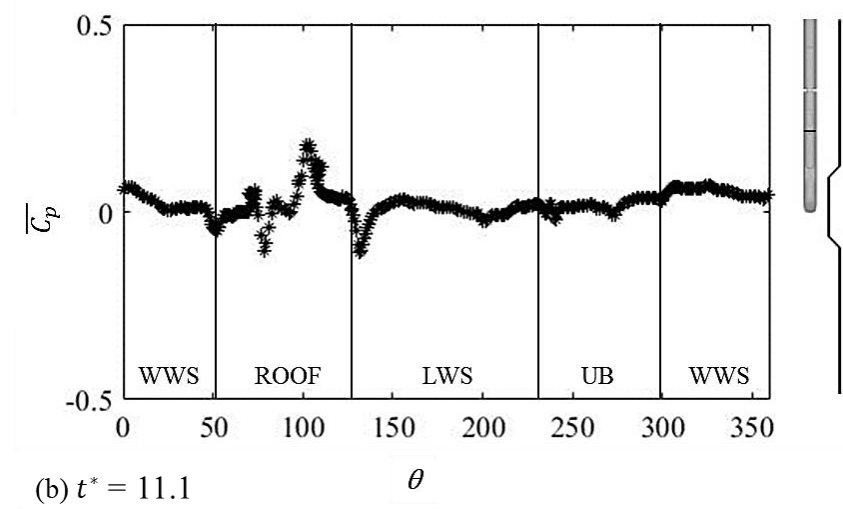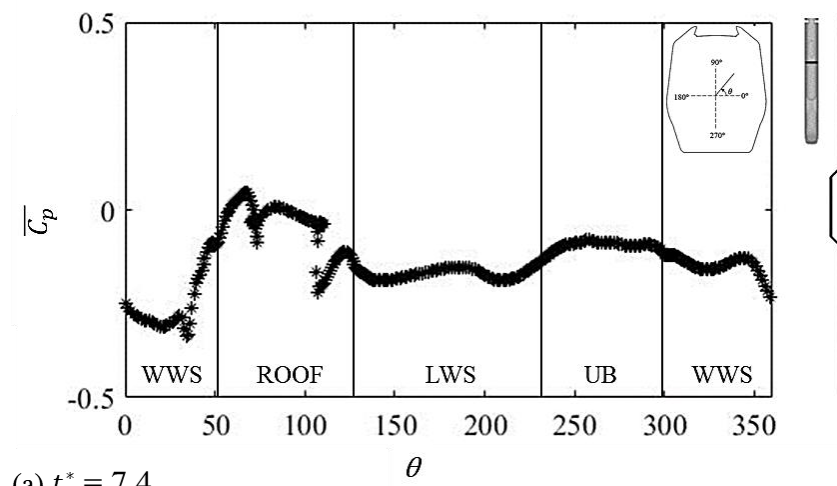
Figure 6.4: Surface pressure distribution at Loop J of the moving train at different t^*.

206

Loop M is situated at the tail of the first car and the cross-sectional shape of this loop is similar to Loop J, specifically for the roof region. Based on the analysis of the results, it appeared that Loop M was able to provide a better overall representation of the tail of the first car as compared to Loop N, where the latter would somewhat be affected by the second car of the train as the entire train was moving and not stationary. As shown in Figure 6.1a, the first car of the train has just completely entered the domain consisting of crosswinds. As a result, the flow is not expected to develop completely on Loop M. This can be seen by Figure 6.5a, where at $t^* = 7.4$, there appears a uniform surface pressure distribution that can be noticed to approach almost a zero value, over the entire circumference of Loop M. At $t^* = 11.1$, Loop M is positioned behind the uniform section in the windbreak wall. The trend followed by the surface pressures on this loop is quite similar to the trend followed by Loop J, at the specified time. Hence, it appears that the tail of the first car and regions closer to the tail present similar trends when positioned against the uniform section of the windbreak wall. At $t^* = 14.8$, Loop M begins to approach the transition region in the windbreak wall. While uniform surface pressures appear on the WWS, the roof, LWS and the underbody regions experience some instability where a haphazard pressure distribution takes place in these regions. In addition, a weak suction peak appears at the start of the WWS. However, these fluctuations are less severe compared to the fluctuations experienced by the same loop at $t^* = 11.1$. At $t^* = 18.5$, Loop M is still under the impact of the transition region in the windbreak wall. A decrease in the surface pressure can be seen as the flow progresses on the WWS. From $\theta = 323°$ to $\theta = 351°$, the $\overline{C_P}$ decreases from 0.1 to -0.04, due to the flow separation as it goes round the bottom windward corner of the train. The surface pressure then increases and stabilises till the flow reaches the hollow section of the roof where

surface pressures increase and become positive in magnitude. At the LWS, a uniform surface pressure distribution can be noticed, where the pressures were seen to approach zero. These uniform results at the LWS with almost negligible variations indicate the complete detachment of any vortical structures from the LWS. Overall, at all times, the surface pressure distribution at Loop M and in fact all other loops except the loops located at the nose of the train, can be expected to be under the influence of the flow that takes place at rest of the train body. Based on the results presented in this section, it can be concluded that the sheltering effects of the windbreak wall are visible on a moving train as well. However, some flow instability is also noticeable, specially at the nose region of the train. While mostly a negative surface pressure distribution is noticed on the train surface, some regions of the first car are observed to show a positive pressure distribution. This indicates that even though the train was travelling behind the windbreak wall, some incident wind was able to attack certain train surfaces directly. This could also be based on the height of the windbreak wall. Finally, with regards to the overall moving case analysed in this chapter, the case was designed in such a manner that the windbreak wall was sufficient in length to ensure that the train experiences a straight uniform section of the wall before running behind the transition region.
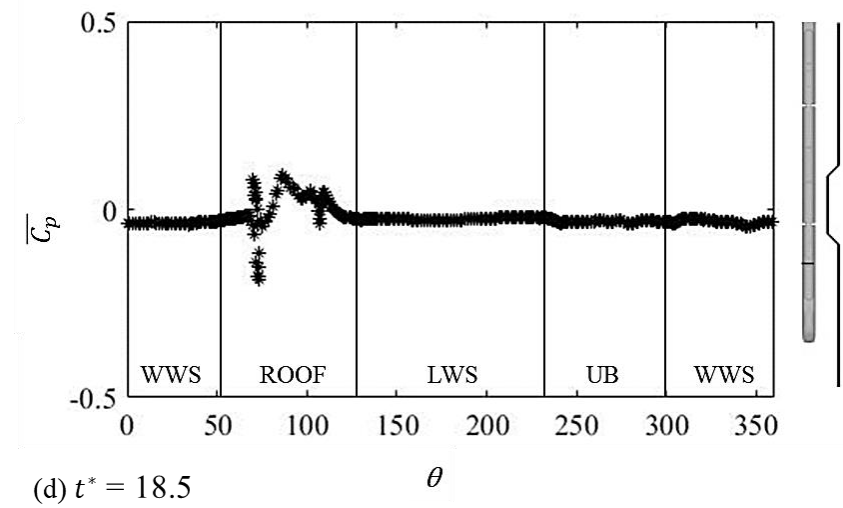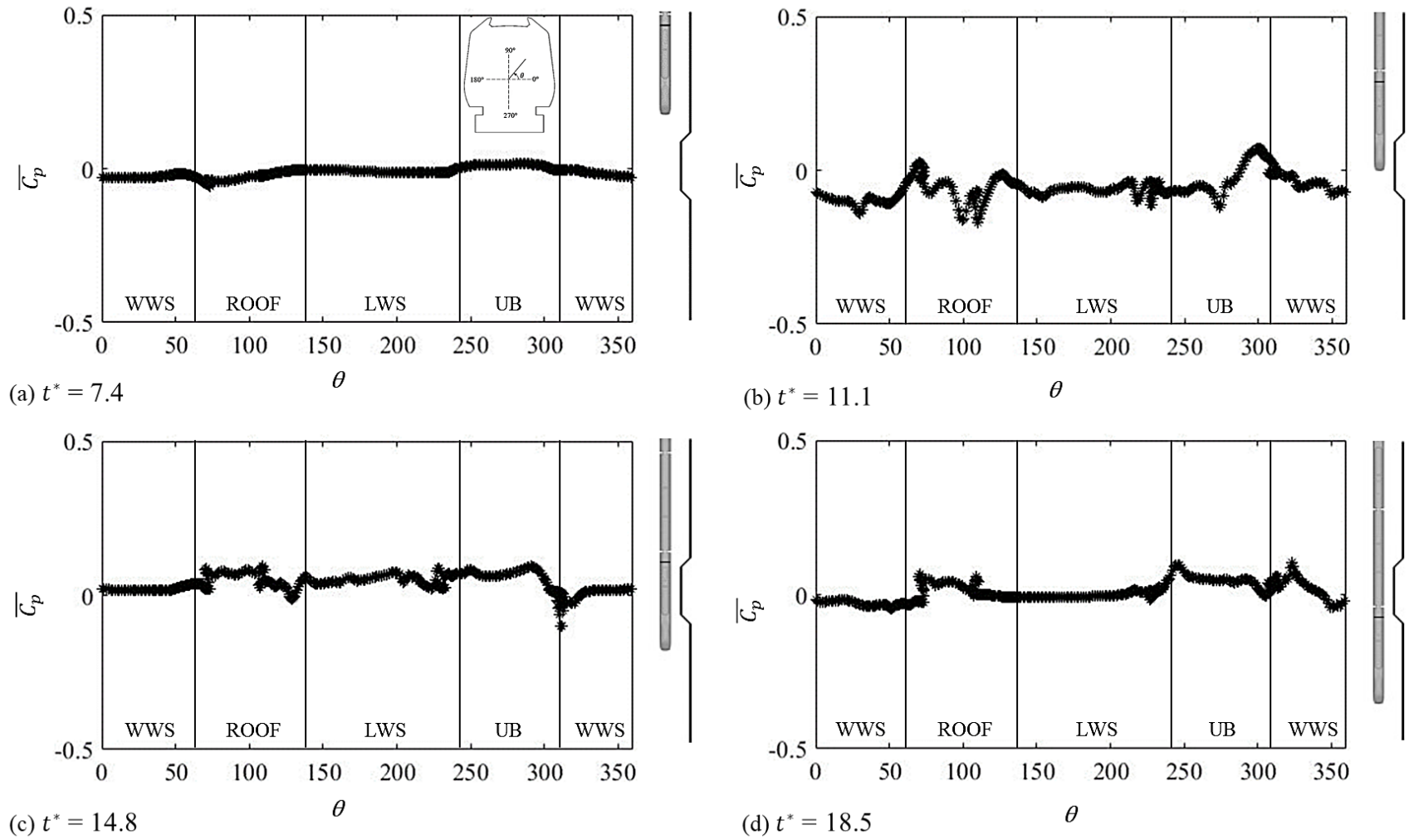
Figure 6.5: Surface pressure distribution at Loop M of the moving train at different t^*.

6.4   Surface pressure contours

Section 6.3 provided insights on the surface pressure distribution on specific loops of the moving train. However, in order to better understand the flow around the train, the surface pressure patterns on the train need to be studied. Figure 6.6 demonstrates the surface pressure patterns on the WWS of the moving train and the stationary windbreak wall at different times. The WWS of the windbreak wall presents highly positive pressures, as expected, due to the stagnation created because of the direct attack of crosswinds on the wall. In terms of the nose of the moving train, at $t^* = 7.4$, a strong positive pressure region can be seen on the frontal region of the nose, whereas a strong negative pressure region can be observed on the rest of the streamlined nose of the first car. This trend which is also apparent at later times is as expected in relation to the stagnation pressure on the train nose; however, slight differences appear. To elaborate, at $t^* = 14.8$, there appears to be a decrease of 0.06 in $\overline{C_P}$ at the front of the nose, as shown by Figure 6.6c. At $t^* = 18.5$, there is a further reduction in the positive surface pressures at the front of the nose. This could be due to the fact that the nose of the train nose is much farther away from the transition region in the windbreak wall and is approaching towards the end of the windbreak wall. Nevertheless, the extreme positive pressures obtained at the frontal region of the nose could be due to the compressible effect of the moving train on the air around. Also, the pressures on the streamlined nose can be affected by the complex curved surface, which results in a diversified distribution at this region. At a slight farther distance from the nose of the train, the region just behind the strong low-pressure region, at $t^* = 7.4$, a uniform low surface pressure distribution can be seen indicating some separated flow in this region.
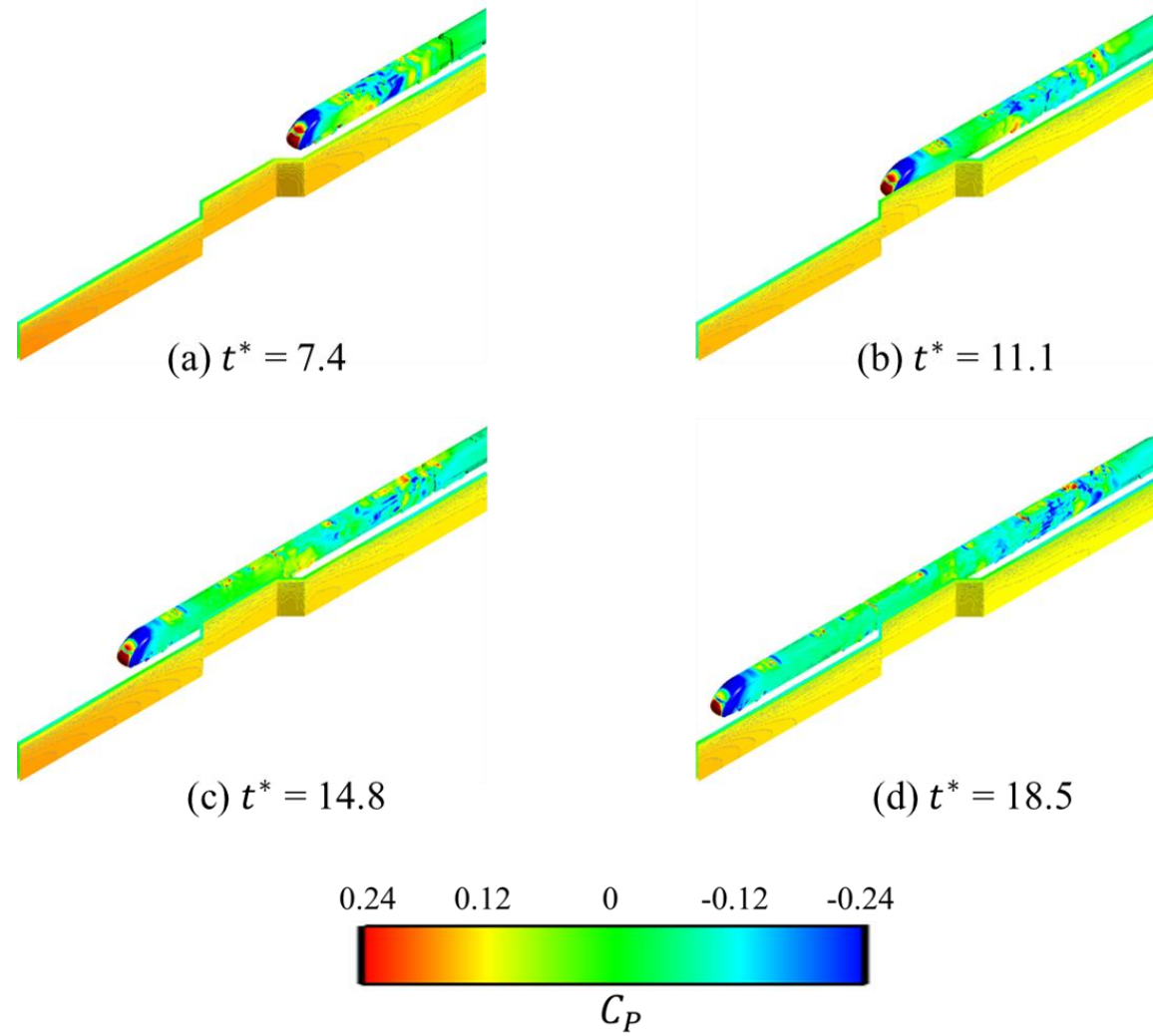
Figure 6.6: Illustration of surface pressure distribution on the WWS of the moving train and the stationary windbreak wall at different t^*.

As explained earlier, at the front of the nose, compression waves are formed, which causes an increase in pressure followed by an expansion wave which decreases pressure on the train nose and body. However, at the same region, at $t^* = 11.1$, there appears to be a decrease in the pressure, specially at the roof of the moving train. This is mainly due to the transition region in the windbreak wall. At $t^* = 14.8$, an increase in the surface pressure can be observed at the same area as it travels away from the transition region in the windbreak wall, followed by a decrease at $t^* = 18.5$. Near the mid-point of the train, at $t^* = 7.4$, a coexistence region of positive and negative pressures exists, behind the uniform section of the windbreak wall. It must be noted that the entrance of the first car of the train in the computational domain, consisting of crosswinds, can lead to the creation of an unsteady turbulence, resulting in low pressure vortices around the train. As time increases, and as the train travels farther, the mid-point of the train shows much uniform surface pressure distributions. This was reported in section 6.3 as well and suggests that the windbreak wall is able to provide excellent sheltering effects to most parts of the moving vehicle.

Figure 6.7 demonstrates the surface pressure patterns on the LWS of the moving train and the stationary windbreak wall at different times. Overall, the LWS of the windbreak wall presents a diverse pressure distribution unlike the WWS. This is mainly due to the moving train, which impacts the flow around it and as a result affects the surface pressure distributions on the LWS of the windbreak wall. The LWS of the moving train is surrounded by varying low pressure (negative) regions where a strong negative pressure region exists on the streamlined nose of the train. Thereafter, regions of low pressure around the rest of the LWS of the moving train indicate that flow separation has taken place much before the LWS.

(a) $t^* = 7.4$

(b) $t^* = 11.1$

(c) $t^* = 14.8$

(d) $t^* = 18.5$

0.24   0.12   0   -0.12   -0.24

C_P
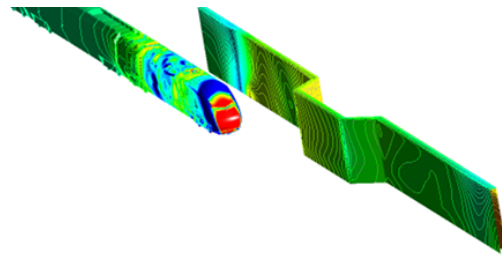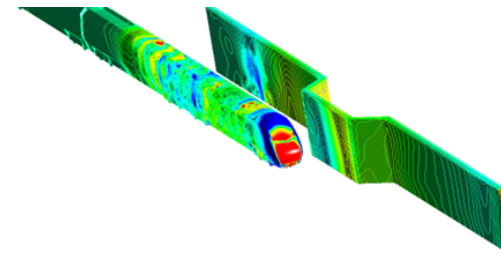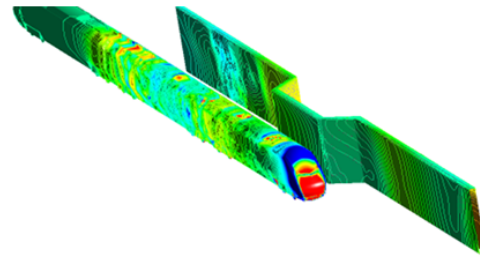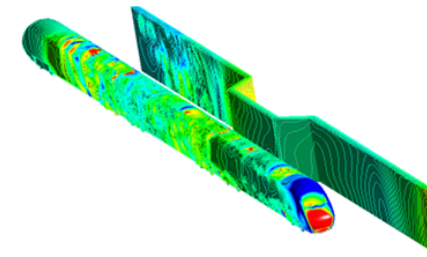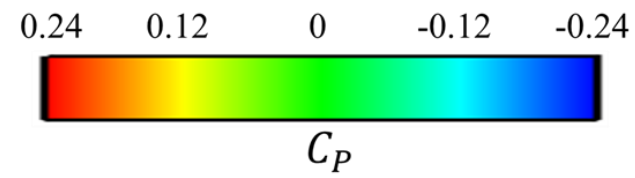
Figure 6.7: Illustration of surface pressure distribution on the LWS of the moving train and the stationary windbreak wall at different t^*.

6.5 Flow fields

In the previous sections, the aerodynamic behaviour of the moving train was studied in terms of the surface pressure distribution on the moving train. This section provides an analysis on the flow fields that exist around the train body, obtained using different visualisation techniques. This can assist in exploring the flow structures which develop around the moving train, when it runs behind the windbreak wall. In order to fully comprehend the flow behaviour, seven planes are cut at different cross-sections of the computational domain, as shown by Figure 6.8.

(a) $t^* = 7.4$ (b) $t^* = 11.1$ (c) $t^* = 14.8$ (d) $t^* = 18.5$
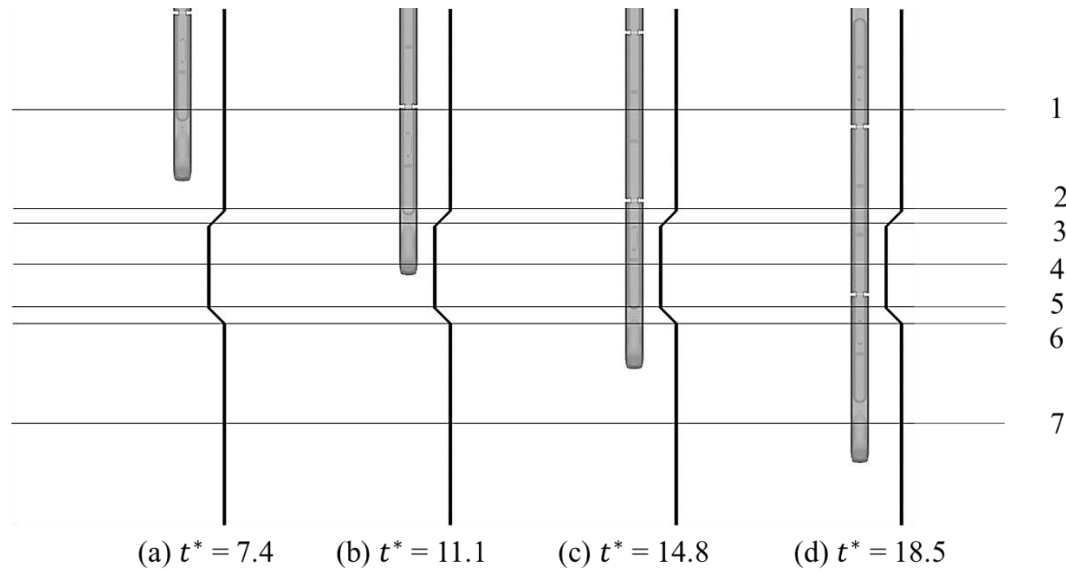
Figure 6.8: Position of planes in the computational domain at different t^* with respect to the moving train.

6.5.1 Results at different cross-sections perpendicular to the tracks

Figure 6.9 - Figure 6.15 demonstrate the velocity streamlines projected onto pressure contour plots at planes 1, 2, 3, 4, 5, 6 and 7, respectively.

Plane 1 is created at the start of the stationary domain and represents the region around the first uniform section of the windbreak wall as this is one of the key zones that need to

be modelled in order to understand the flow mechanisms that take place. Prior to this point, outside the stationary domain, the train is stationary and is only allowed to move once the flow inside the stationary domain develops completely. Therefore, it is deemed irrelevant to model the train outside the stationary domain as this is considered to not affect the results since the train moves a certain distance before entering the stationary domain. At the particular cross-section of plane 1, the distance between the centre of the track and the windbreak wall is 0.24 m. According to Figure 6.9, at $t^* = 7.4$, a stagnation point exists at the WWS of the windbreak wall signified by a high pressure region, mainly due to the direct attack of the crosswind flow, as shown by the velocity streamlines. Once the crosswind flow approaches the windbreak wall, there is an immediate deflection in the flow, at the tip of the windbreak wall. The incident flow deflects from the top edge of the wall, as shown by the lifting of the velocity streamlines. The flow then begins to accelerate while being forced to move away from the train body, thus creating flow separation above the train. While the flow deflection is common throughout the domain, some significant differences are visible after the flow deflection at each respective time period.

At $t^* = 7.4$, the first car of the train has recently entered the stationary domain, consisting of crosswinds. Due to the entrance of the train and its acceleration in the domain behind the windbreak wall, an unsteady flow mechanism takes place, which results in the build-up of some low-pressure vortices around the first car. Obviously, a moving vehicle is accompanied with flow velocities and variations of the static pressure in its proximity. In addition, highest pressure changes are associated with the passing of the train head that results in the head pressure pulse. Soon, at $t^* = 7.4$, as the first car continues to travel, these low pressure unsteady vortices increase in size as turbulence causes them to interact

215

with each other while spreading around the train body, as shown in Figure 6.9b. In addition, there are some changes in the pattern of flow deflection as it transits from the tip of the windbreak wall. This flow separation results in a large reverse flow region, right above the roof of the train. A well-defined vortex at this region confirms this finding. This reverse flow field has a high velocity as well, therefore producing a low-pressure region, surrounding the vortex formation area. In terms of the near wake flow, at $t^* = 11.1$, two low pressure vortices appear, where one is closer to the LWS of the train while the other one is at a slight distance. The latter weakens and shifts farther away with time as the train continues to travel. At $t^* = 18.5$, this vortex can be seen to disappear. With regards to the far wake flow, a large vortex exists, much farther from the LWS of the train. With time, this vortex slowly progresses and drifts farther upwards and away from the train. It must be noted that these strong suctions observed in Figure 6.9 are a result of the moving train which impacts the flow and thus produces instability in the flow. On the train body itself, as demonstrated by Figure 6.6 and Figure 6.7, a diversified distribution of pressures is noticeable. On the first car, the nose and somewhat the middle of the first car show strong low pressure regions as compared to the rest of the car.

Figure 6.9: Velocity streamlines projected onto pressure contour plots on plane 1 at different t^* with respect to the moving train.

Plane 2 is created at the start of the transition region. At $t^* = 7.4$, the train has not yet crossed plane 2. Based on the results presented in Figure 6.10a, at $t^* = 7.4$, a weak vortex can be observed on the area between the windward side of the track and the leeward side of the windbreak wall. This vortex arises most likely due to the gradient in the geometry of the windbreak wall at the transition region. Above the centre of the track, a relatively higher-pressure region can be noticed. This indicates that even though the train has not reached the plane, the effect of the moving train is perceived at this position due to the compression waves created in front of a moving train that lead to regions of high pressure. It is known that a train generates three-dimensional pressure waves upon entry in tunnels. Quite similarly, with a barrier on one side, a moving train is expected to produce some kind of pressure waves. This phenomenon is experienced by objects that are moving at high speeds and have some form of streamlined design to improve speed and efficiency. The nose of the train presents a complex phenomenon of positive pressures due to compression waves followed by negative pressures due to expansion waves.

In the wake of the flow from the windbreak wall, a recirculation region exists. At $t^* = 11.1$, the train's entrance results in a pressure decrease in the region that lies between the windbreak wall and the track. Also, the weak vortex seen in this region at $t^* = 7.4$ disappears but appears at $t^* = 14.8$ and 18.5. At $t^* = 11.1$, a part of the roof of the train is masked by a low-pressure region, however, with time, the roof is no longer masked by such strong low-pressure regions. Also, the vortex observed in the wake of the flow in Figure 6.10a moves away with time. As Figure 6.10d demonstrates, there are some low pressure vortices attached on the LWS of the train, signifying potential suctions in this region. One interesting finding is demonstrated on the WWS of the windbreak wall.

Figure 6.10: Velocity streamlines projected onto pressure contour plots on plane 2 at different t^* with respect to the moving train.

Compared to plane 1, at plane 2, the streamlines are more lifted from the base. This indicates that the gradient in the transition region also has an impact on the oncoming crosswind flow.

Plane 3 is positioned at a part of the transition region and represents the start of the uniform section in the transition region of the windbreak wall. At this particular cross-section, the distance between the centre of the track and the windbreak wall is 0.145m, which is almost half of the distance between the centre of the track and the windbreak wall at the cross-section presented in Plane 1. Based on Figure 6.11a, at $t^* = 7.4$, the trend in the flow deflection is slightly different from the trend observed at earlier planes. At earlier planes, the velocity streamlines at the same time step had a lower velocity. This is mainly due to the change in the distance between the track and the windbreak wall. At $t^* = 11.1$, a portion of the first car of the train has passed plane 3. As a result, some low-pressure regions can be observed on the bottom WWS and LWS along with the underbody region. Over the roof, a positive pressure bubble is apparent, which can be seen at $t^* = 14.8$ as well. Since this positive pressure was not seen at earlier planes, it appears that the sudden change in the geometry of the windbreak wall results in such a stagnation region on the roof of the train. However, as the train travels farther, the flow around the train seems to stabilise and thus at $t^* = 18.5$, this positive pressure region on the roof no longer exists. In addition, at $t^* = 14.8$, a low-pressure vortex starts to develop in the flow which deflects from the tip of the windbreak wall. By $t^* = 18.5$, this vortex grows in size. In the wake of the flow, a vortex can be seen that becomes stronger with time.
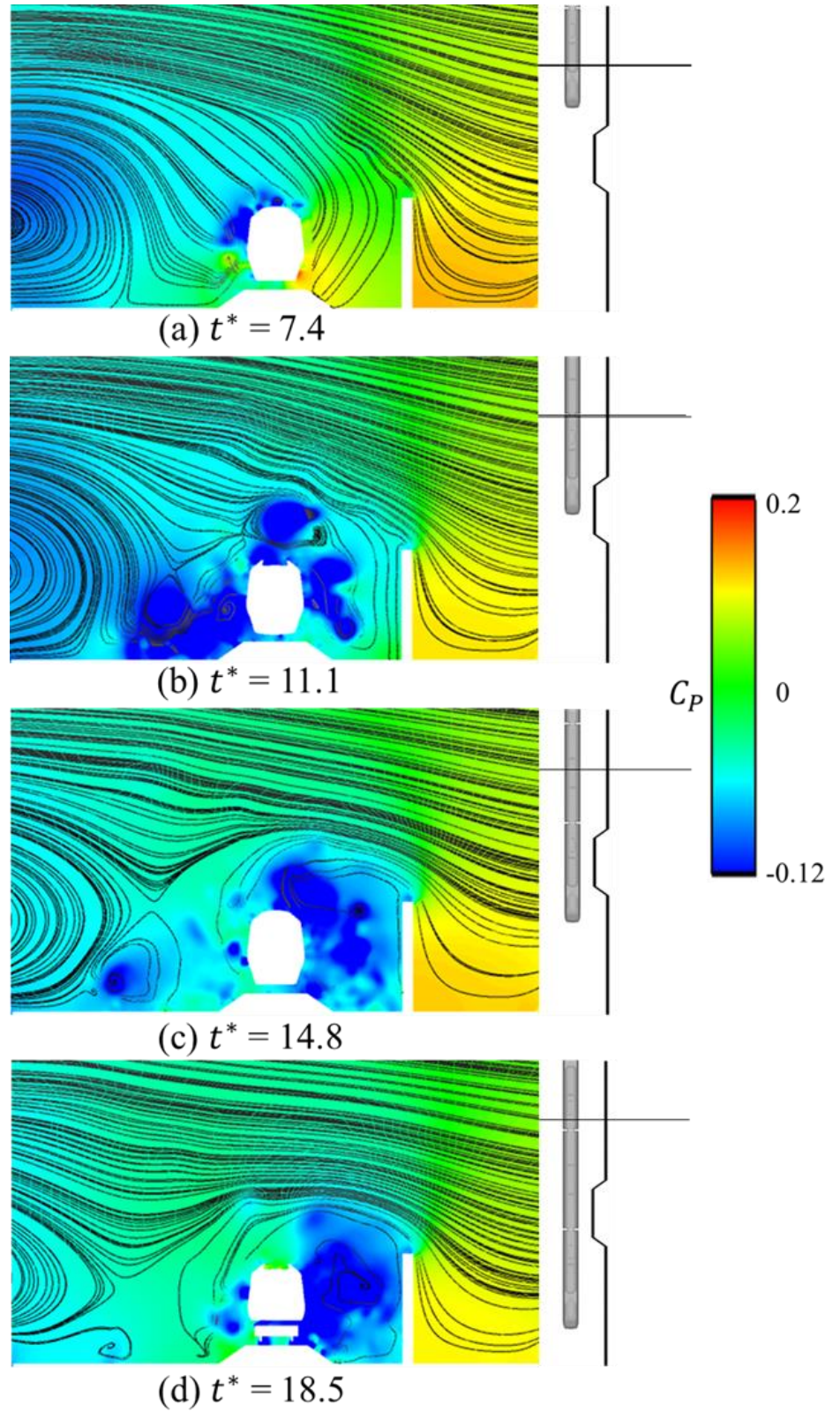
Figure 6.11: Velocity streamlines projected onto pressure contour plots on plane 3 at different t^* with respect to the moving train.

Plane 4 is also positioned at a part of the transition region and represents the middle of the uniform section in the transition region of the windbreak wall. At $t^* = 7.4$, without the presence of the moving train, there seem to be some differences in the way the flow deflects from the top of the windbreak wall, due to differences in the shape and the position of the windbreak wall under assessment. On Figure 6.12a, a weak vortex can be observed on top of the tracks, which was not present at plane 3. As the train approaches, at $t^* = 11.1$, the WWS, LWS and the underbody of the train at plane 4 are masked by strong low pressures while a strong positive region exists on the roof due to the geometry of the nose, where the plane cuts off perpendicular to the train nose. Since plane 4 at $t^* = 11.1$ represents the nose of the train, such an intense pressure distribution can be expected. At $t^* = 14.8$, plane 4 represents the middle of the first car of the moving train. Similar to plane 3 at the same time, a low-pressure vortex can be seen near the leeward roof edge of the wall. This vortex grows in size, becomes stronger and moves slightly away from the wall by $t^* = 18.5$. In terms of the moving train, it can be seen that once the nose and almost half of the first car has travelled behind the windbreak wall, the flow around the train develops and stabilises.

Figure 6.12: Velocity streamlines projected onto pressure contour plots on plane 4 at different t^* with respect to the moving train.

Plane 5 is also positioned at a part of the transition region and represents the end of the uniform section in the transition region of the windbreak wall. The effect of the compression waves generated by a moving train can be once again seen at $t^* = 11.1$, where a higher-pressure region is seen even without the presence of train, as compared to $t^* = 7.4$. As a result, the flow which deflects from the windbreak wall also seems to be impacted by the oncoming train. At a glance, some weak low-pressure bubbles can be seen to originate. This most likely occurs due to the transition region of the windbreak wall, which changes the direction of the airflow. Once the train moves behind the windbreak wall, these low-pressure vortices grow in size and become stronger, as displayed in Figure 6.13d. Another interesting feature is observed in the wake of the flow at plane 5. As compared to earlier planes, generally, the wake of plane 5 shows that there is not much flow in this region. It appears that the reverse flow region, which usually occurs in this region, does not take place at this plane. This might be due to the position of plane 5 where it represents the end of the uniform section in the windbreak wall and the start of the gradient in the geometry of the windbreak wall.
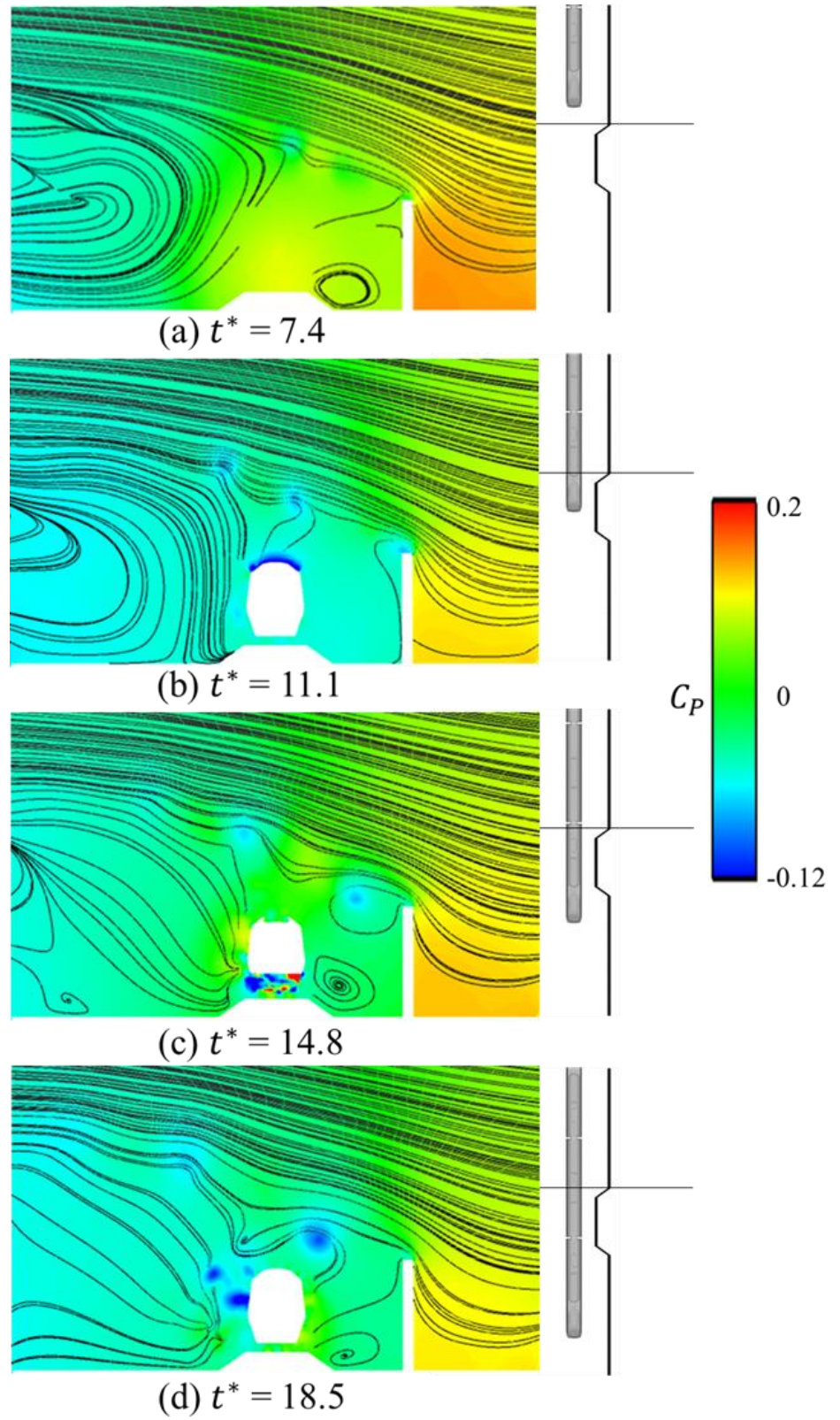
Figure 6.13: Velocity streamlines projected onto pressure contour plots on plane 5 at different t^* with respect to the moving train.

Plane 6 is created at the end of the transition region. At $t^* = 7.4$ and 11.1, the train has not yet crossed plane 6. Since the train is quite far away, at $t^* = 7.4$, a stronger recirculation region can be seen in the wake of the flow, characterized by a vortex. On the tip of the windbreak wall, as the flow separates, a weak longitudinal vortex exists. Also, similar to plane 2, a weak vortex can be observed in the area between the windward side of the track and the leeward side of the windbreak wall in Figure 6.14a. As the train is about to appear, at $t^* = 11.1$, this vortex dies away. In terms of the strong vortex in the wake of the flow, as the train crosses plane 6, this vortex tends to weaken and loses some of its shape. In addition, the vortex can be seen to stick to the base. With regards to the train, at $t^* = 14.8$, while the train body is surrounded by low negative pressures, the underbody of the train presents a diverse mix of pressure distribution with some strong low-pressure regions. Moreover, a low-pressure vortex can also be seen close to the leeward edge of the roof of the windbreak wall.
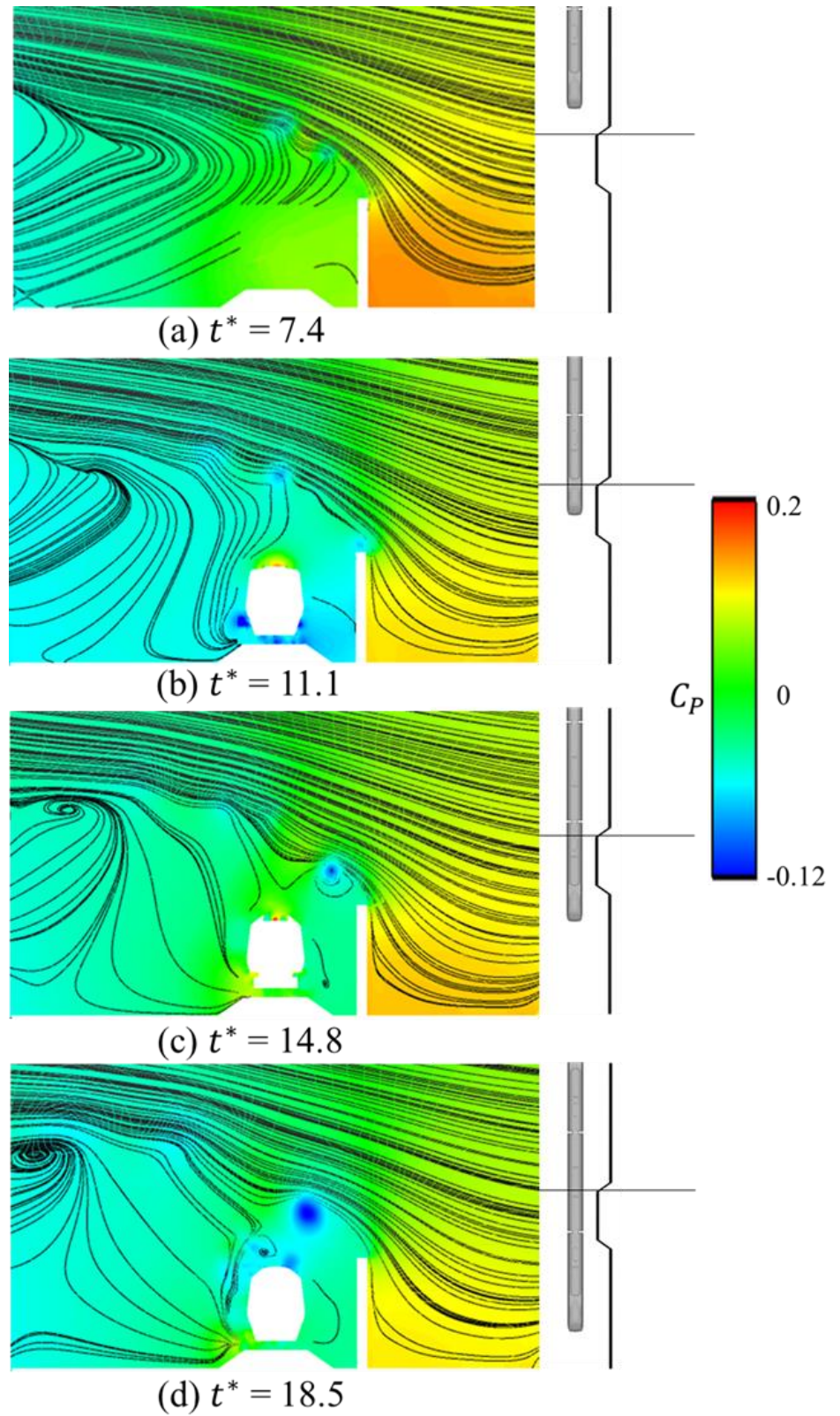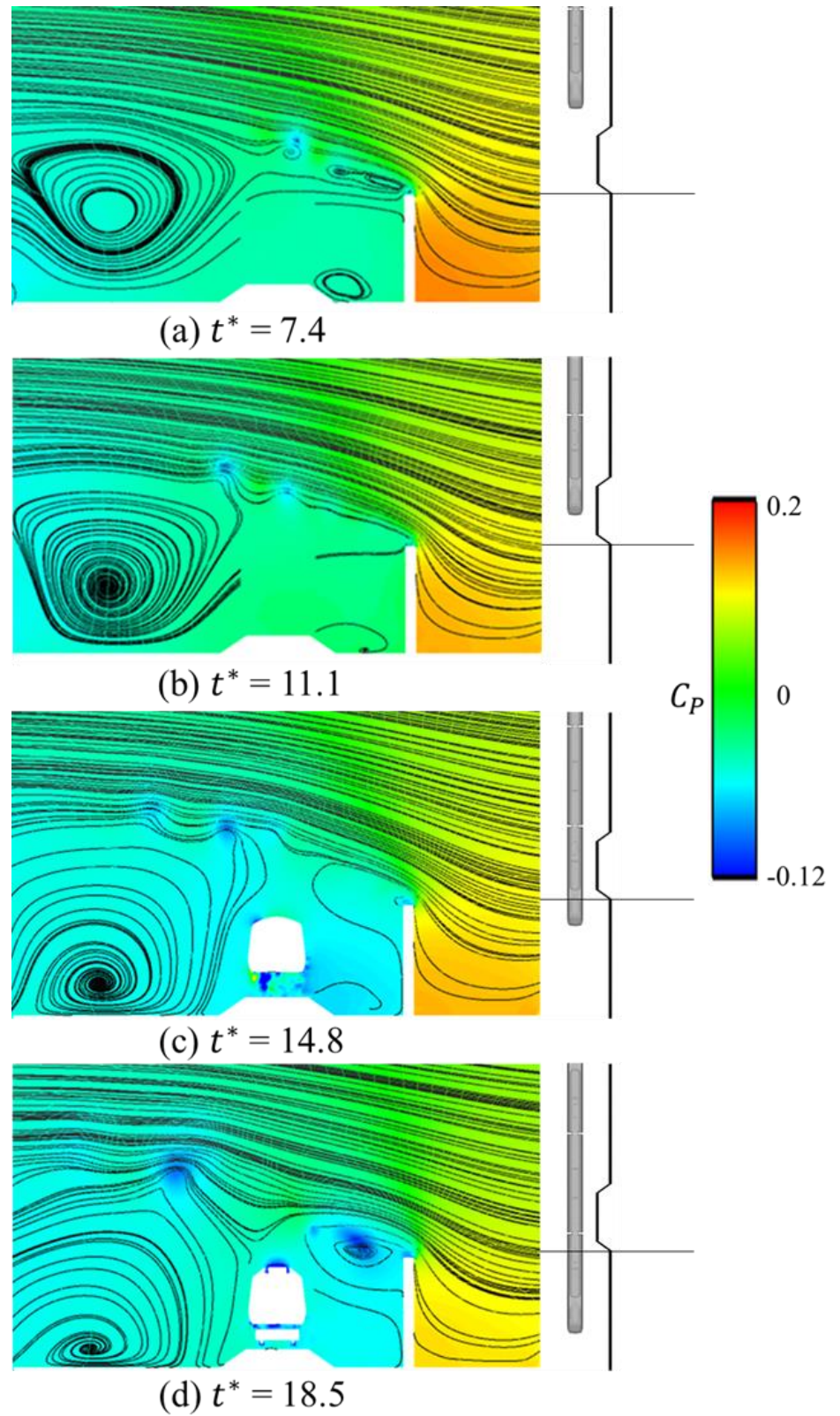
Figure 6.14: Velocity streamlines projected onto pressure contour plots on plane 6 at different t^* with respect to the moving train.

Plane 7 is created at the end of the stationary domain and represents the region around the second uniform section of the windbreak wall. At $t^* = 7.4$, 11.1 and 14.8, the train has not yet passed this plane. Hence, the results at these times can be used to develop an understanding of the flow and its features, behind the windbreak wall, without the presence of the train. At $t^* = 7.4$, while the WWS of the windbreak wall comprises of a stagnation point, the LWS of the windbreak wall is accompanied of low-pressure regions, as expected. Due to the high pressure on the windward side of the windbreak wall, a streamline effect is generated, as some of the flow is forced over the windbreak wall. This results in upward-bending streamlines upwind of the windbreak wall, followed by compression of streamlines above the windbreak wall, and some downward-bending streamlines on the leeward region of the windbreak wall. Above the windbreak wall, the compression of streamlines results in an increase in the crosswind speeds. Thus, the flow deflection from the windbreak wall is not smooth. To further elaborate, at $t^* = 7.4$, as shown by Figure 6.15a, after the flow deflection, there are some weak and unsteady low pressure bubbles that exist in the flow. With time, these bubbles become stronger and grow in size. At $t^* = 14.8$, the effect of the oncoming train is perceived by the flow. At $t^* = 18.5$, the sudden appearance of the train nose behind the windbreak wall leads to the development of some strong and unstable low-pressure vortices in the vicinity of the train. In terms of the wake of the flow, the strong vortex seen at earlier times disappears with the sudden train movement.
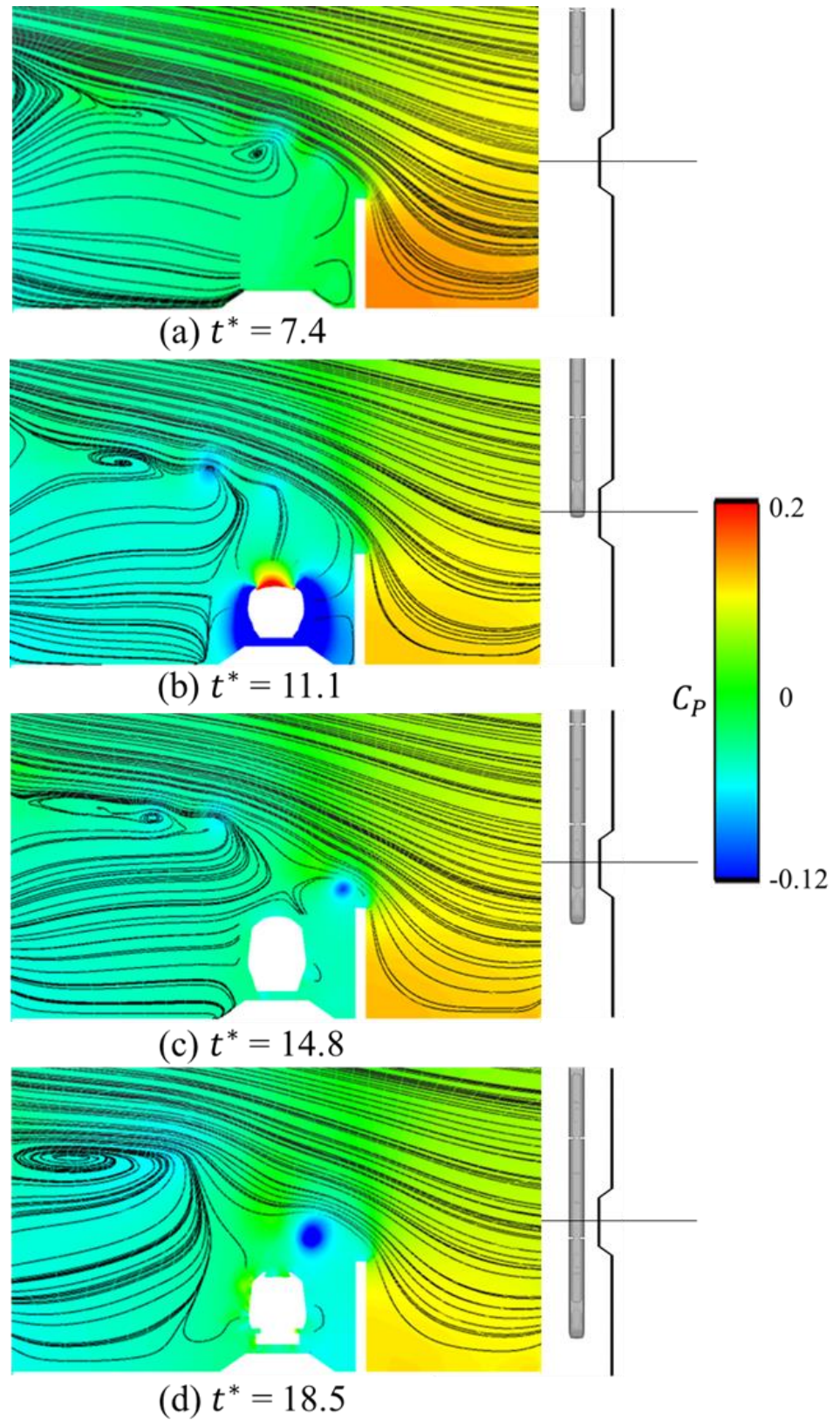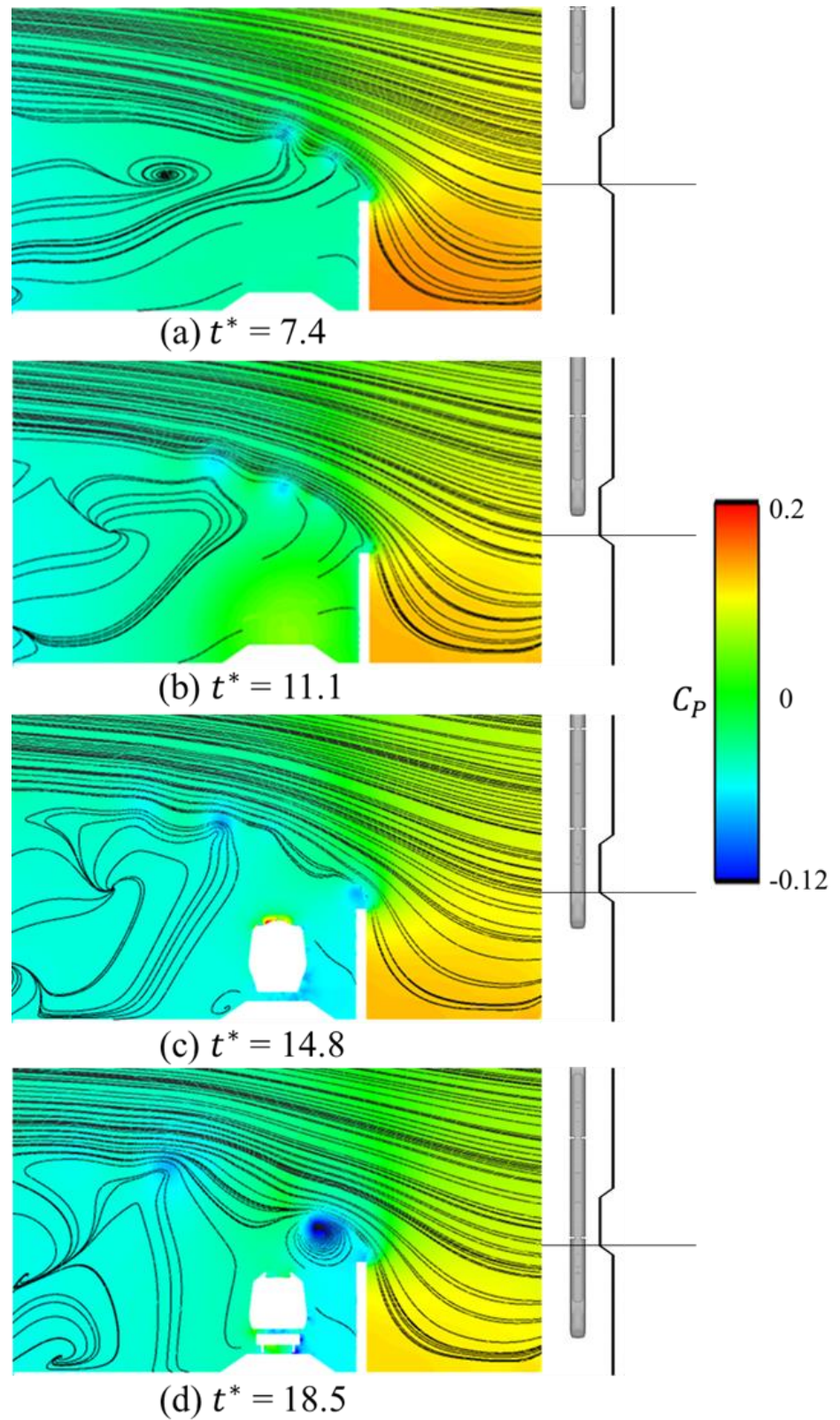
Figure 6.15: Velocity streamlines projected onto pressure contour plots on plane 7 at different t^* with respect to the moving train.

6.5.2 Results at different cross-sections parallel to the tracks

Overall, velocity streamlines and pressure contours on planes 1-7 have been successful in assisting with the interpretation of the effects of the chosen windbreak wall on the flow inside the computational domain. However, for further understanding, it is a good idea to present velocity streamlines and pressure contours on horizontal cross-sectional planes as well, that are parallel to the track at different positions from the track top.

Six planes at different positions from the top of the track are created as shown by Figure 6.16 that demonstrates the position of planes 8 – 13 with respect to the train and the windbreak wall.
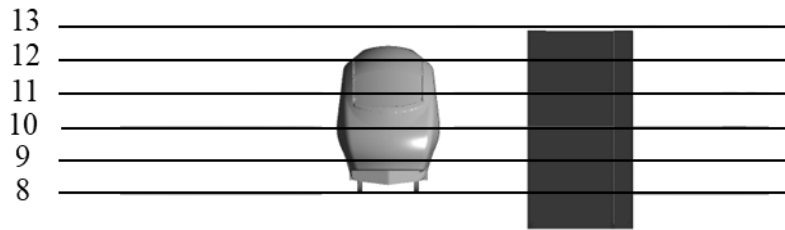
Figure 6.16: Position of planes 8 -13 in the computational domain with respect to the train and the windbreak wall.

Figure 6.17 - Figure 6.22 demonstrate the velocity streamlines projected onto pressure contour plots at planes 8, 9, 10, 11, 12 and 13, respectively.

Plane 8 is created at the base of the train wheels and thus shows the flow features around this region. Based on Figure 6.17a, the two low pressure regions at the right and left side of the moving train can be seen. These are formed due to the entrance of the train and its acceleration in the domain behind the windbreak wall which leads to an unsteady flow mechanism that results in the build-up of some low-pressure vortices, as discussed earlier in section 6.5.1 with reference to Figure 6.9.

230

The low-pressure vortex on the leeward side of the train at $t^* = 7.4$ develops with time as the train continues to travel farther. However, it stays at its original position while growing in size, as seen in Figure 6.17d. On plane 9, which is positioned slightly above the track, slight differences can be seen in the flow, as compared to plane 8. The low pressure vortex seen at plane 8 still exists, however, at $t^* = 18.5$, there is another longitudinal shaped vortex (i.e. generated due to differences in pressure between the upwind and downwind sides) that exists on the leeward side of the train, behind the transition region, as illustrated by Figure 6.18d. This vortex can be seen to originate after the movement of a major portion of the first car of the moving train. At plane 10, which is created somewhat at the middle of the train body, this vortex exists with a much stronger intensity, showing a recirculation region in the wake of the flow, as shown by Figure 6.19d. At plane 11, at $t^* = 14.8$, this vortex can be seen. This is an interesting finding as at this particular time, the previous planes did not show the existence of this vortex. Therefore, it appears that this vortex is mainly associated to the upward leeside of the train. As a result, it is visible at $t^* = 11.1$, 14.8 and 18.5 on planes 12 and 13. It seems that there is a periodic vortex shedding from the top of the wall, as a vortex formation can also be seen in Figure 6.13b and Figure 6.14b. This vortex then appears to be enhanced by the interaction of the aerodynamic flow of the moving train. Analysis of earlier times (without the presence of a moving train) also demonstrated this periodic vortex shedding from the top of the wall, evidently induced by the sharp edge of the transition region. Overall, the results demonstrate that the windbreak and its transition region have an immediate physical effect on the flow that exists around it leading to some complex interrelationships with the moving train. Therefore, it can be stated easily that a windbreak wall with a transition region can have both, positive as well as negative effects on a

moving train. Concisely, the crosswind flow is influenced by the windbreak and its transition region in three ways:

- Modification of streamlines

- Reduction in the mean horizontal windspeeds

- Alteration in the turbulent structures of the crosswind flow

(a) $t^* = 7.4$ (b) $t^* = 11.1$ (c) $t^* = 14.8$ (d) $t^* = 18.5$

C_P

0.24   0.12   0   -0.12   -0.24
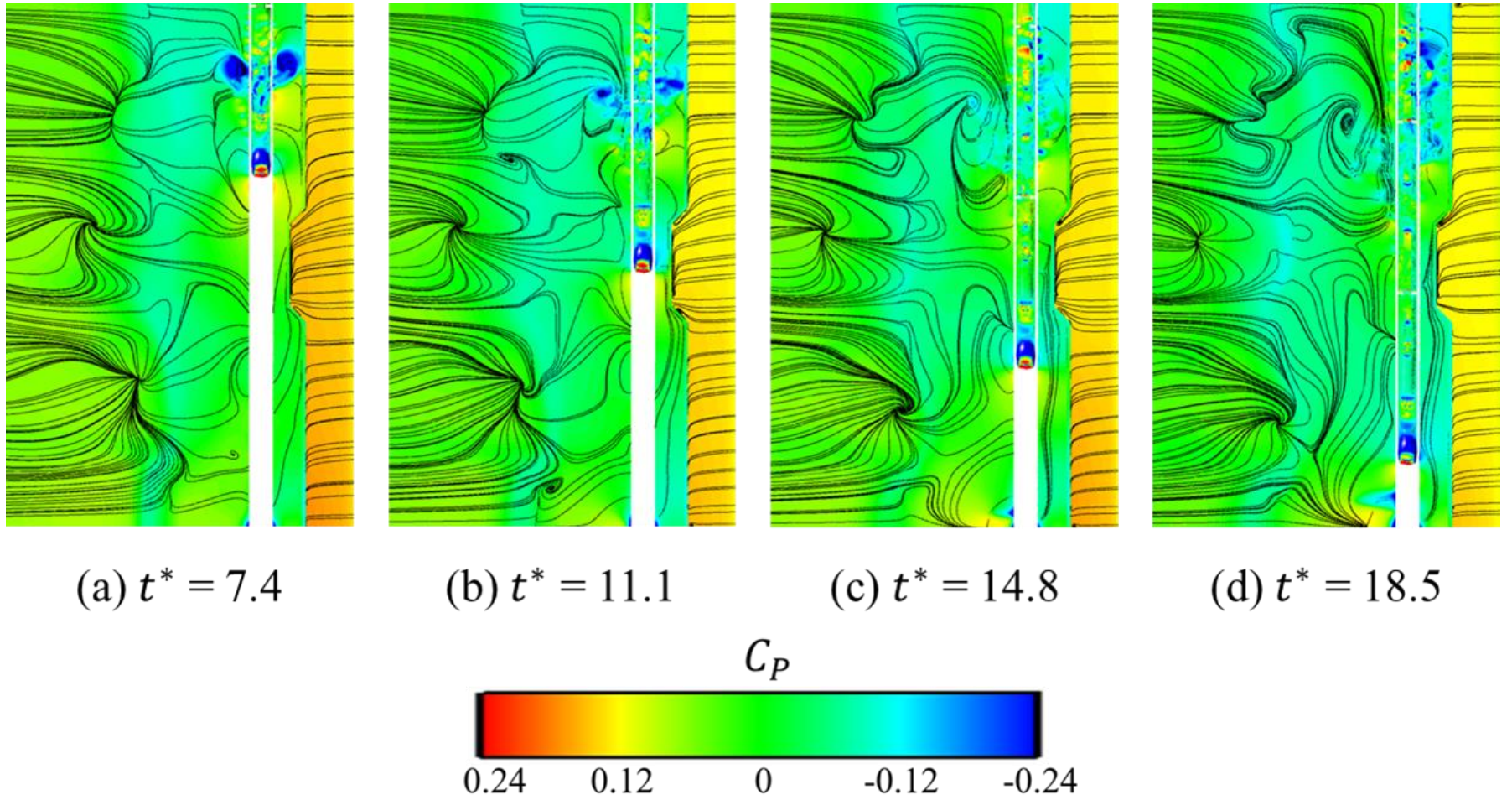
Figure 6.17: Velocity streamlines projected onto pressure contour plots on plane 8 at different t^* with respect to the moving train.

(a) $t^* = 7.4$ (b) $t^* = 11.1$ (c) $t^* = 14.8$ (d) $t^* = 18.5$

C_P

0.24   0.12   0   -0.12   -0.24
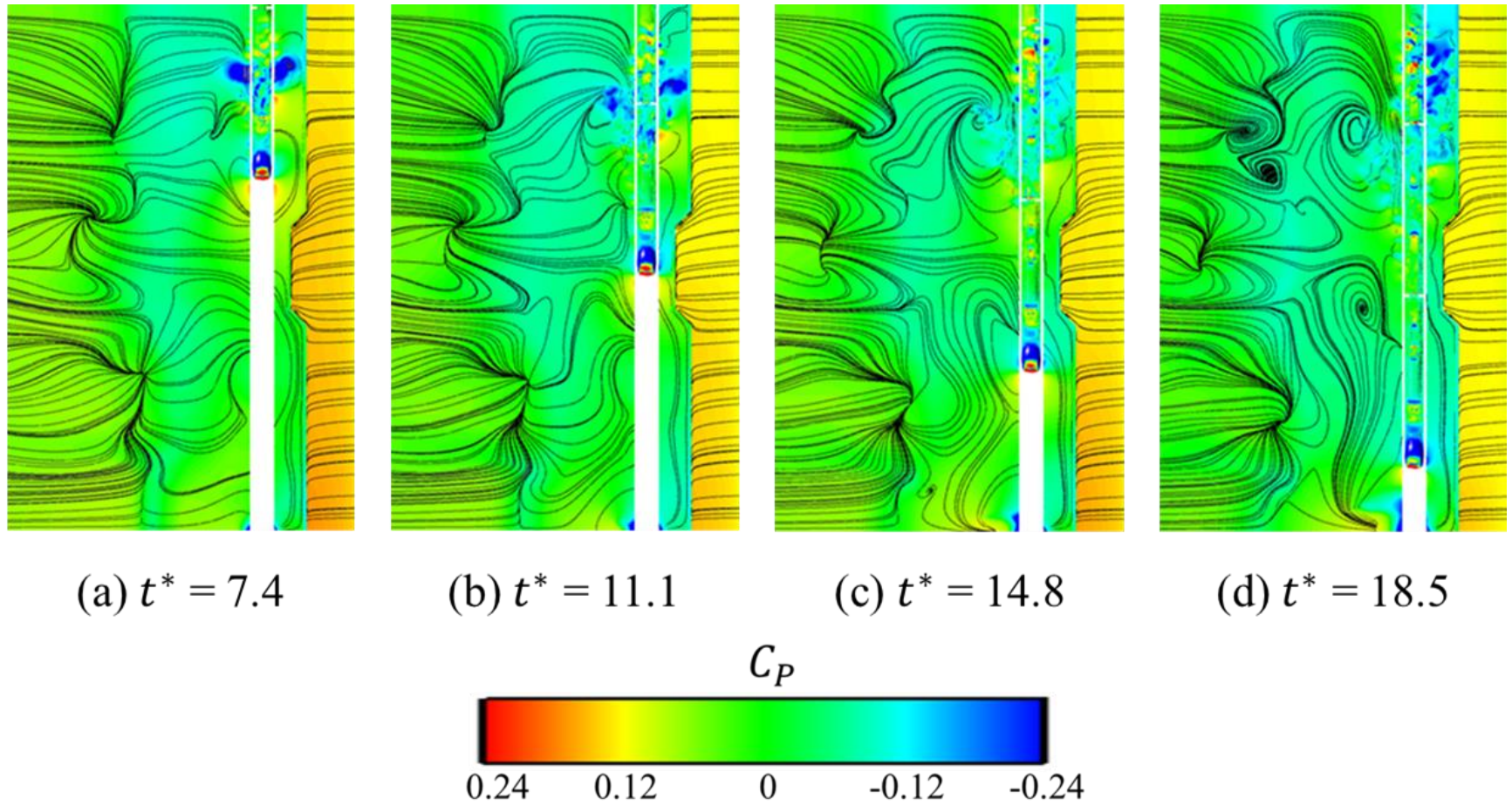
Figure 6.18: Velocity streamlines projected onto pressure contour plots on plane 9 at different t^* with respect to the moving train.

(a) $t^* = 7.4$ (b) $t^* = 11.1$ (c) $t^* = 14.8$ (d) $t^* = 18.5$

C_P

0.24   0.12   0   -0.12   -0.24
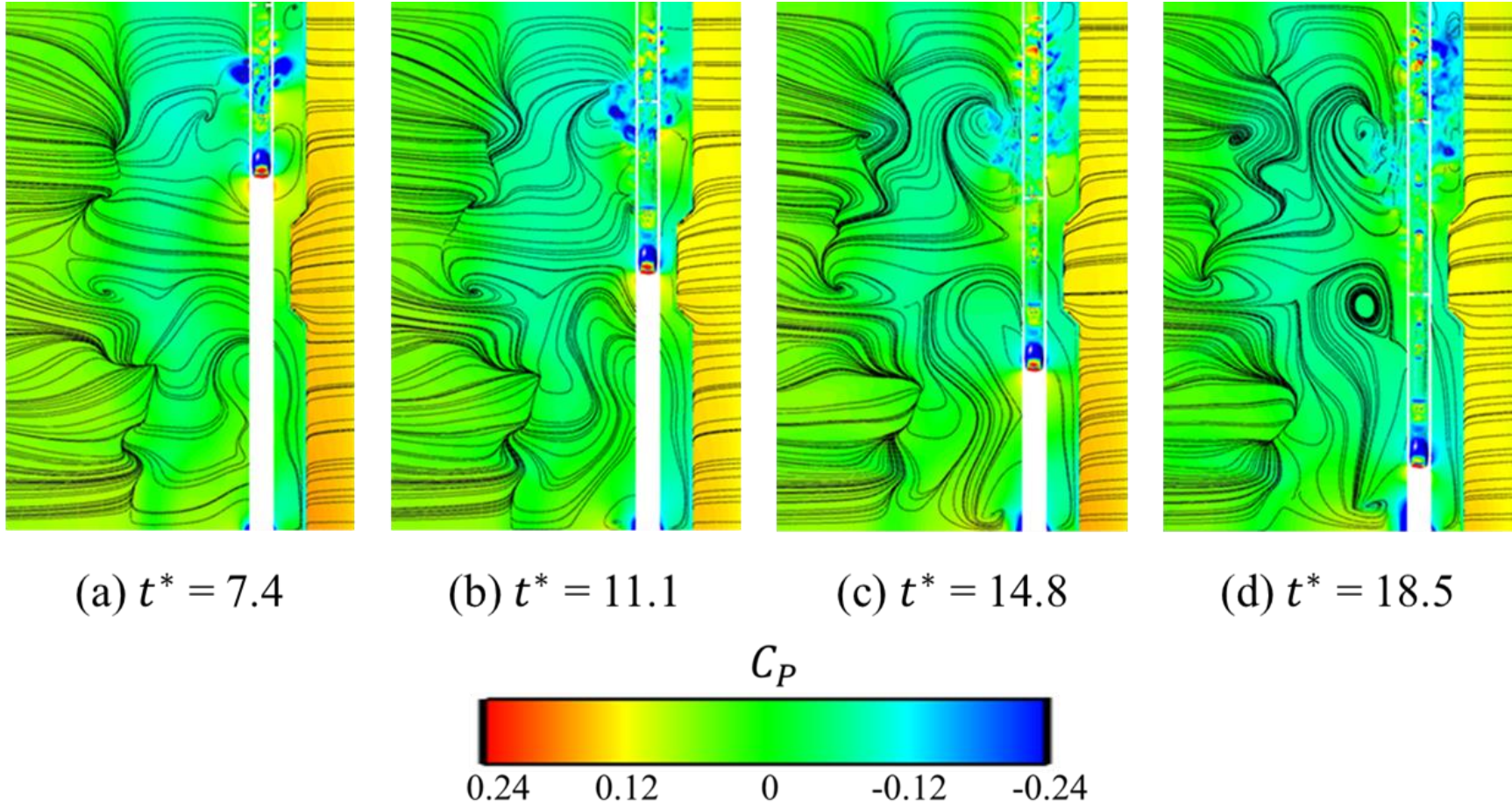
Figure 6.19: Velocity streamlines projected onto pressure contour plots on plane 10 at different t^* with respect to the moving train.

(a) $t^* = 7.4$ (b) $t^* = 11.1$ (c) $t^* = 14.8$ (d) $t^* = 18.5$
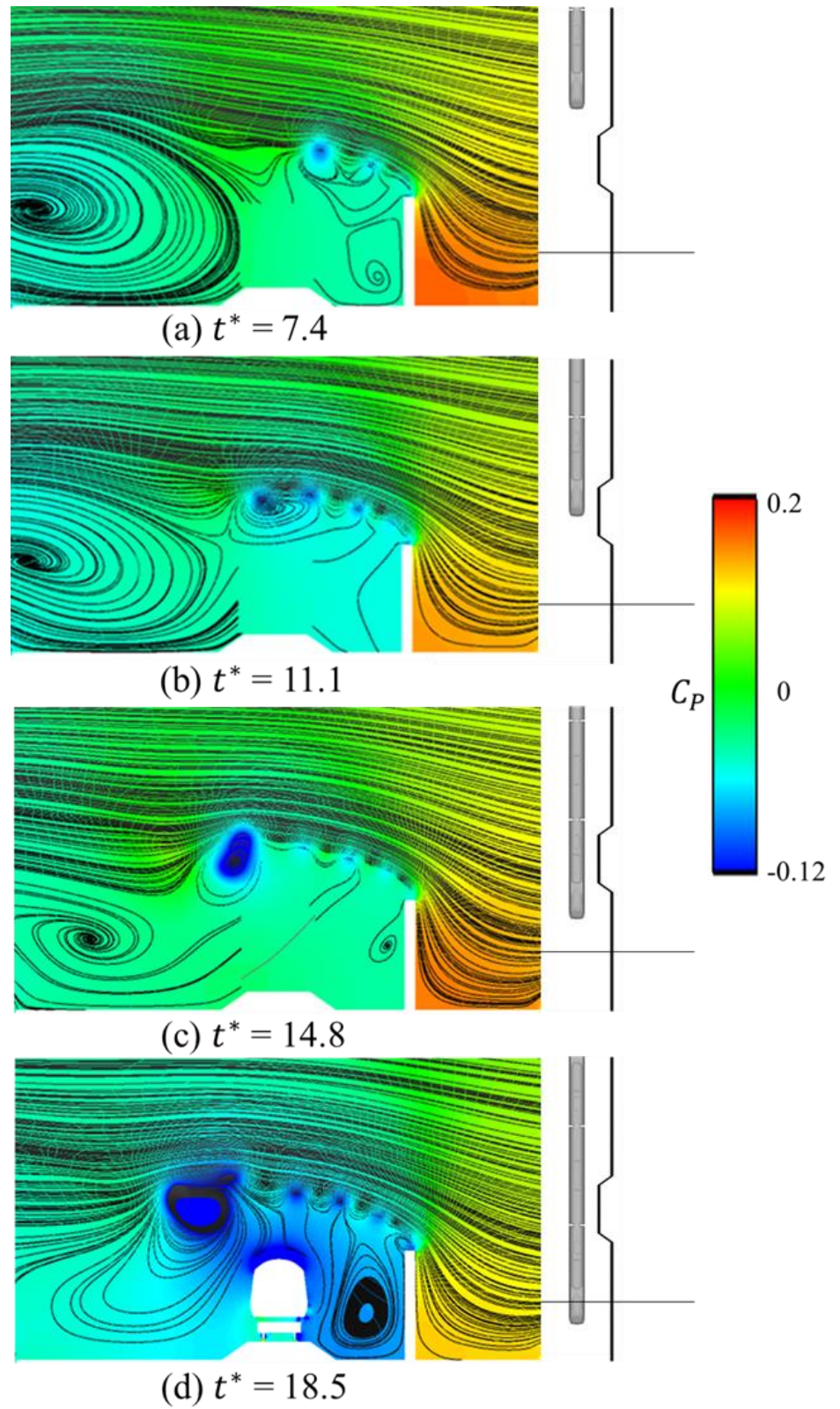
C_P

0.24   0.12   0   -0.12   -0.24
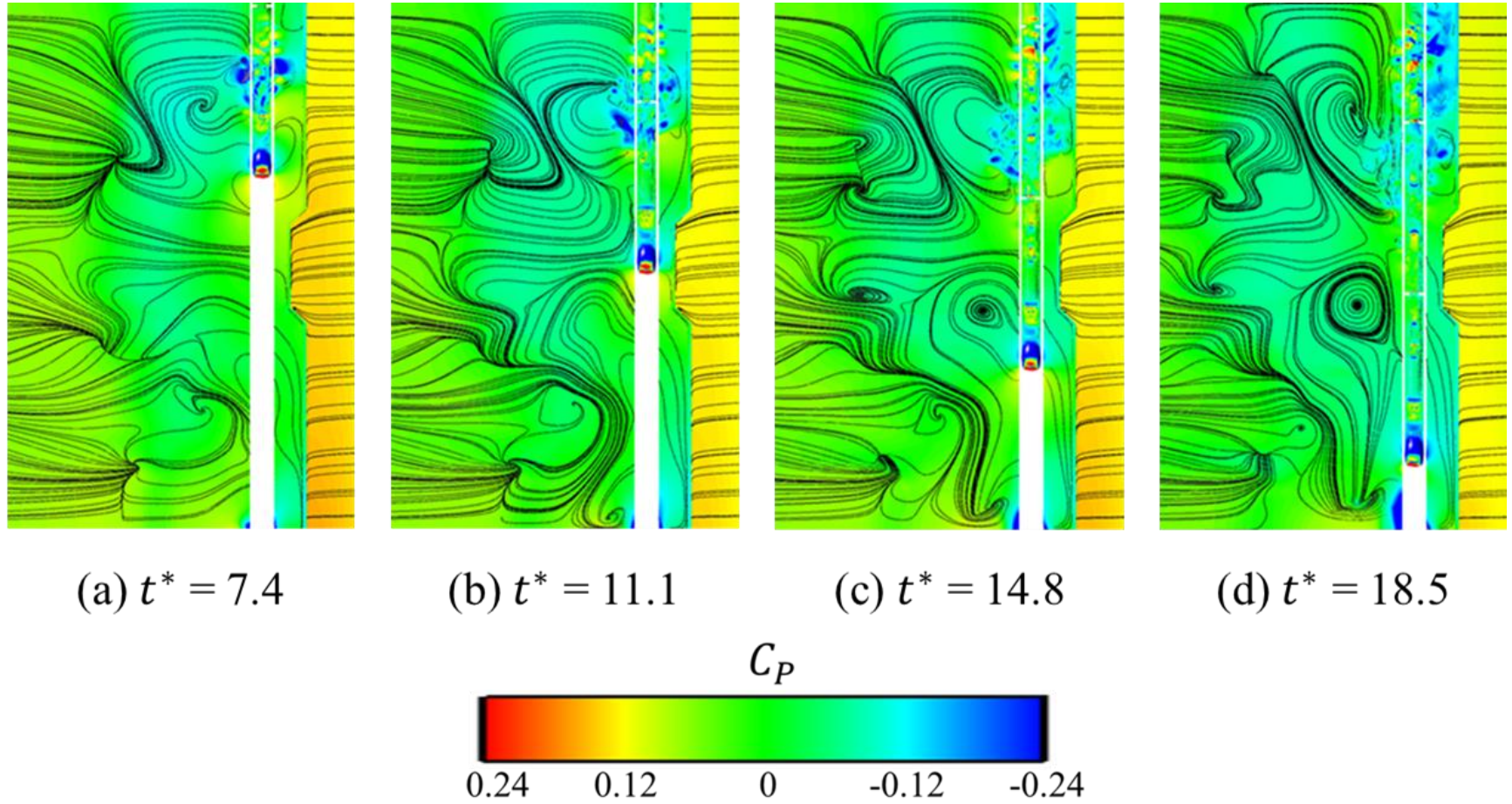
Figure 6.20: Velocity streamlines projected onto pressure contour plots on plane 11 at different t^* with respect to the moving train.

(a) $t^* = 7.4$ (b) $t^* = 11.1$ (c) $t^* = 14.8$ (d) $t^* = 18.5$

C_P

0.24   0.12   0   -0.12   -0.24
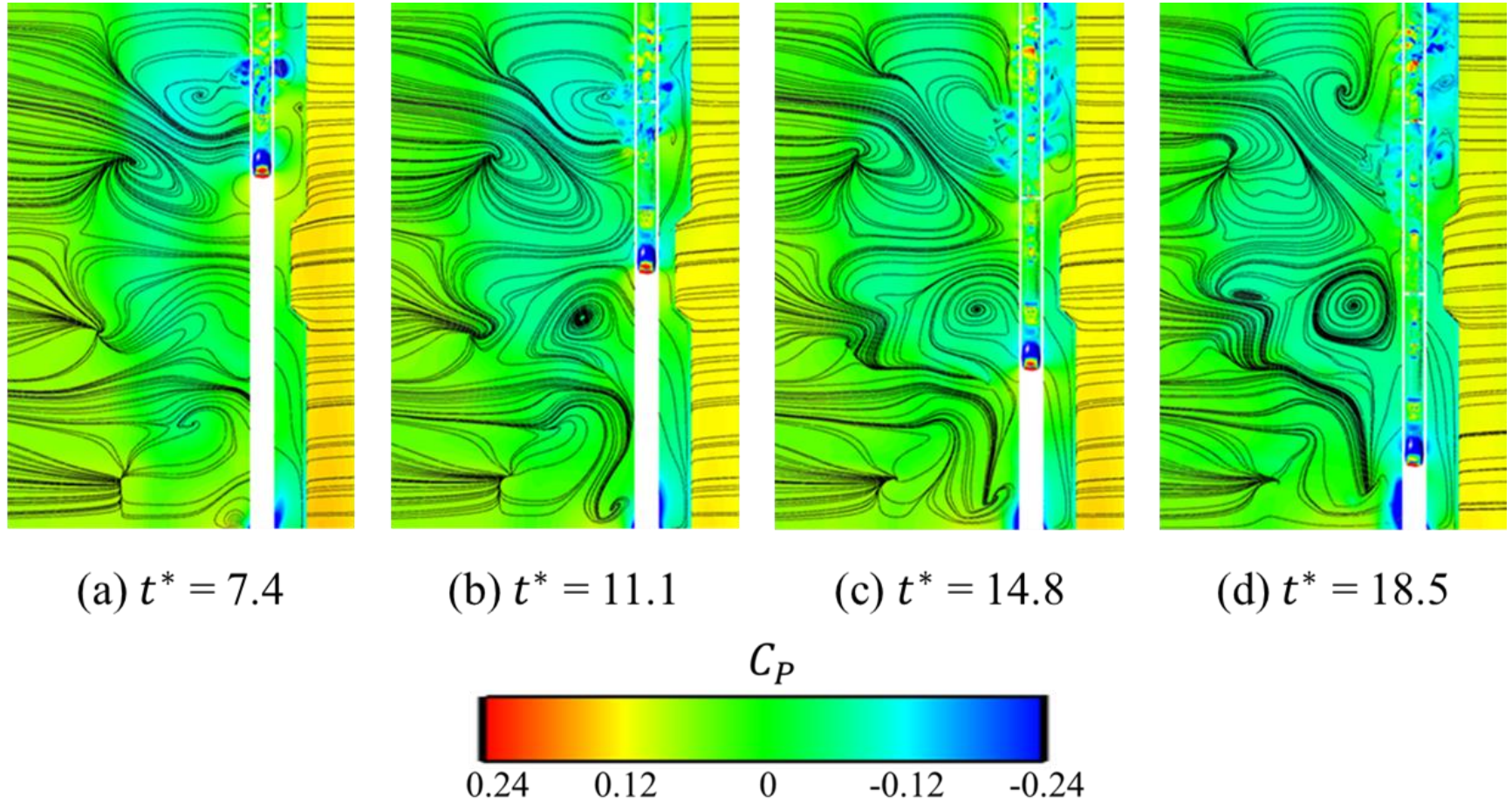
Figure 6.21: Velocity streamlines projected onto pressure contour plots on plane 12 at different t^* with respect to the moving train.

(a) $t^* = 7.4$ (b) $t^* = 11.1$ (c) $t^* = 14.8$ (d) $t^* = 18.5$

C_P

0.24   0.12   0   -0.12   -0.24
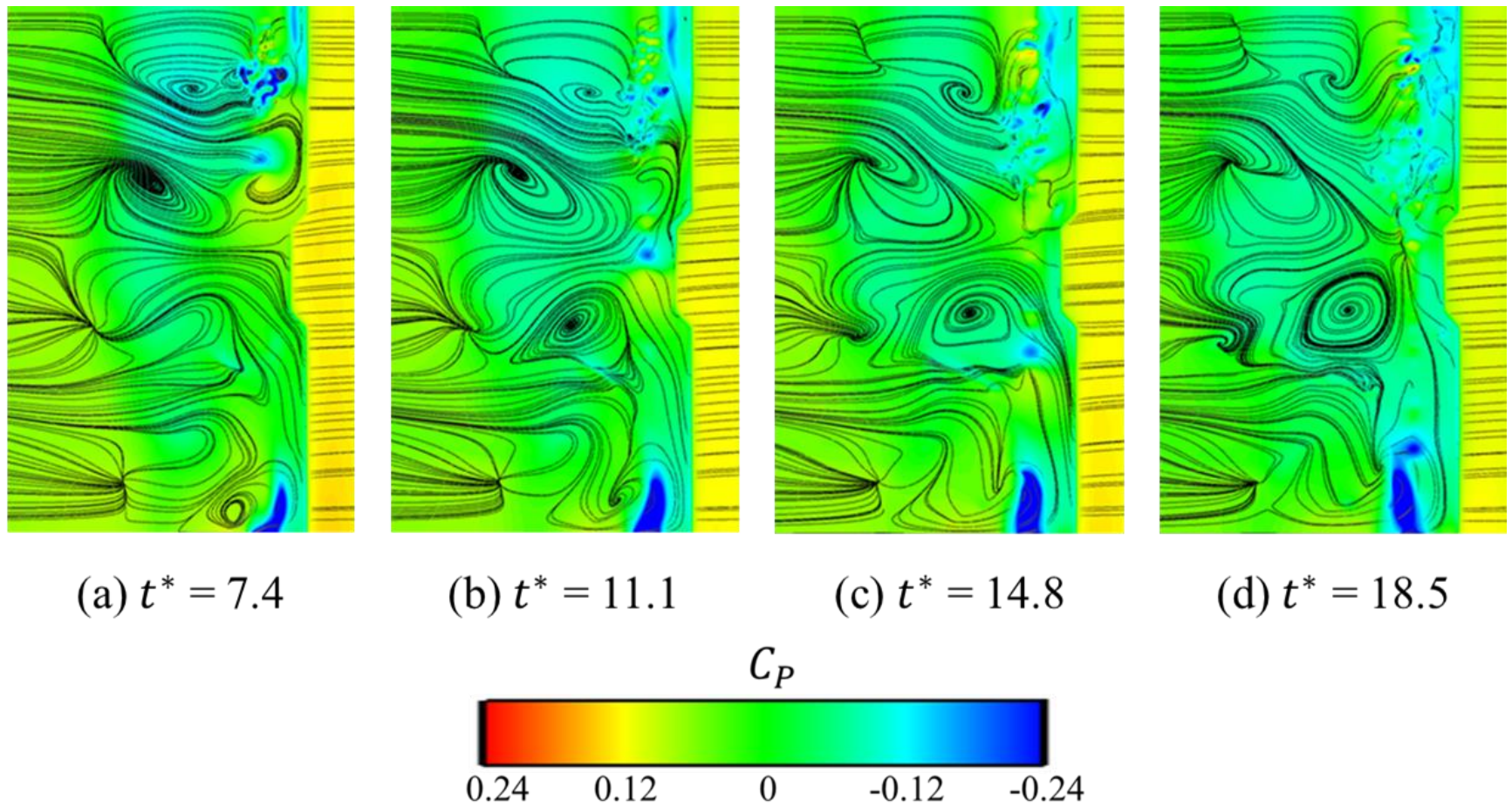
Figure 6.22: Velocity streamlines projected onto pressure contour plots on plane 13 at different t^* with respect to the moving train.

6.6   Aerodynamic loads

This section aims to further investigate the performance of the windbreak wall studied in this chapter by presenting and analysing the overall aerodynamic load coefficients obtained for the leading car of the moving Class 390 train under crosswinds. The results presented in this section are obtained directly from the numerical simulations carried out as part of this study. Therefore, the aerodynamic forces computed originate from the pressure and viscous forces that act on the body. To ensure that results are accurate, the aerodynamic loads are obtained after the first car of the train has moved a certain distance in the domain that has a fully developed flow field.

Figure 6.23 illustrates the time-varying side coefficient of the leading car of the moving Class 390 train, respectively. The results are demonstrated with respect to the non-dimensional time, t^*. As noted earlier, Figure 6.1 demonstrates the position of the train at different t^*. In terms of the side force coefficient of the leading car, it appears that as the car moves behind the uniform section of the windbreak wall ($t^* = 7.4$ onwards), the side force coefficient is positive, which means that it acts in the direction of the crosswinds. This positive side force coefficient starts to decrease as the train runs behind the uniform section of the windbreak wall and reaches a relatively stable value, as seen at $t^* = 9.41$. However, once the first car starts to travel behind the sharp transition region, the positive side force coefficient further decreases, as expected based on the shielding effects of the windbreak wall. It then reaches a stable point around $t^* = 10.7 - 11.4$. This is when the nose of the first car enters behind the uniform section of the transition region in the windbreak wall. The reduction of side force coefficient in this region is in equilibrium with the uniform section of the non-transition region of the windbreak wall.

Following on, there is a slight fluctuation in the side force coefficient, probably due to the sharp edges of the transition region, but thereafter, there is a further continued decrease in the side force coefficient as more of the leading car continues to enter behind the transition region. At $t^* = 14.5$, when most of the leading car is within the transition region of the windbreak wall, the side force coefficient reaches a value of -0.02. However, after $t^* = 14.5$, there is an increase in the side force coefficient as the middle and the rear end of the leading car are both within the sharp edges of the transition region of the windbreak wall. Despite this, the side force coefficient stays below 0, indicating the shielding effects of the windbreak wall. At $t^* = 17$, the side force coefficient starts to decrease rapidly. This is because most of the leading car is now within the other uniform section of the windbreak wall. It appears that the leading car starts to leave the domain at approximately $t^* = 19.5$, as the side force coefficient starts to increase rapidly. Overall, the trend shown by the side force coefficient is expected based on the understanding gained in previous sections focusing on the illustration of the velocity and pressure flow fields. Thus, it can be stated that changes in the side force coefficient are due to the varying flow fields that develop around the train, induced by the irregular changes in the windbreak wall.
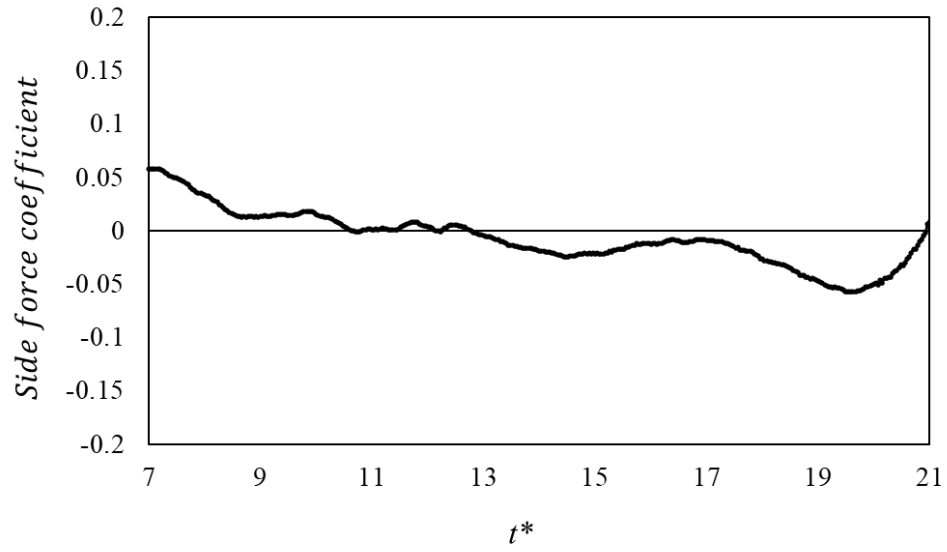
Figure 6.23: Variation of the side force coefficient of the leading car of the moving Class 390 train against t^*.

Figure 6.24 illustrates the time-varying lift force coefficient of the leading car of the moving Class 390 train, respectively. In terms of the lift force coefficient, as the leading car of the train moves behind the uniform section of the windbreak wall, at $t^* = 7.4$ onwards, there are small fluctuations in the magnitude, but the relative average stays the same up until $t^* = 9$. After $t^* = 9$, the lift force coefficient increases till $t^* = 10.7$. This is due to the movement of the train behind the transition region of the windbreak wall, where the sharp edges of the transition region induce an increase in the lift force. Soon, as the nose of the leading car crosses the first sharp edge of the transition region, the lift force coefficient starts to decrease all the way till $t^* = 14.7$, where the positive lift force coefficient becomes negative at $t^* = 13$. This is due to the fact that at this moment, both the front and rear ends of the leading car are behind the transition region and the aerodynamic flow around the train is influenced by the interaction of the flow separating from the top of the closer windbreak wall. Similar to how the lift force coefficient increased from $t^* = 9$ - 10.7, it increases from $t^* = 15.4$, showing that the sharp edges of

241

the transition region of the windbreak wall increase the lift force coefficient. Once the leading car exits the transition region, the lift force coefficient further increases as expected due to a reduction in the shielding effects.
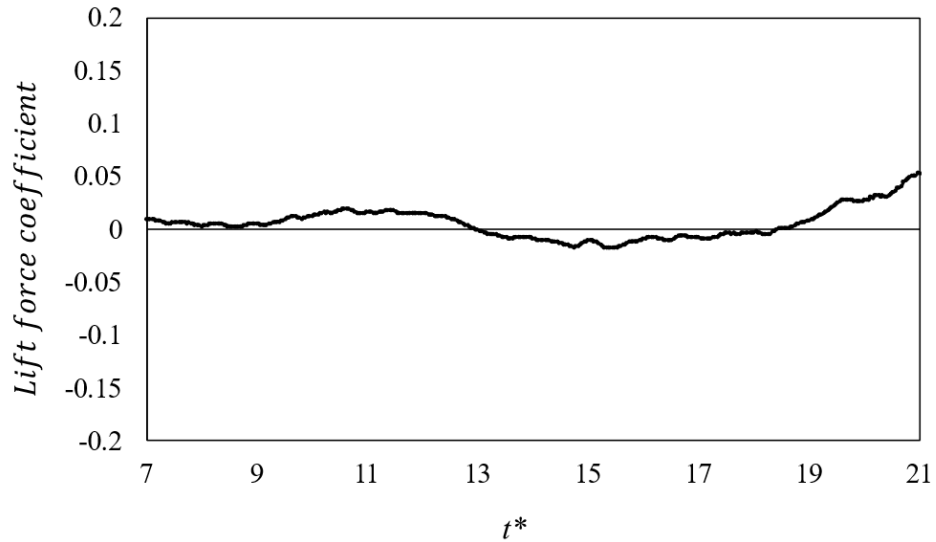
Figure 6.24: Variation of the lift force coefficient of the leading car of the moving Class 390 train against t^*.

Figure 6.25 shows the time-varying rolling moment coefficient of the leading car of the moving Class 390 train. The variation in the rolling moment arises from the collective contribution of the side and lift forces. It must be noted that a positive rolling moment indicates that the train may overturn in the direction of the crosswinds. As the leading car of the train moves behind the uniform section of the windbreak wall, the rolling moment coefficient decreases and thereafter becomes relatively stable with slight fluctuations. At $t^* = 14.5$ onwards, the rolling moment coefficient increases slightly reaching a value of 0 at $t^* = 17$. At this point, it appears that since the rear end of the leading car is behind the transition region and the frontal part of the car is behind the uniform section of the windbreak wall, the resulting forces balance out and thus the rolling moment coefficient

reaches 0. Thereafter, the rolling moment coefficient decreases (i.e. there is an increase in the negative rolling moment coefficient).

Figure 6.25: Variation of the rolling moment coefficient of the leading car of the moving Class 390 train against t^*.

6.7 Conclusions

This chapter provides the results obtained from the numerical simulations carried out on a moving Class 390 model-scale train subjected to crosswinds at a yaw angle of 15° with a windbreak wall consisting of a transition region of 45° transition angle. A series of conclusions can be drawn from the results provided and the analysis presented in this chapter:

- As the high-speed train starts to travel behind the windbreak flow, due to the sudden movement of the train, there is an unsteady flow mechanism which takes place that results in the build-up of some low pressure vortices around the first car. Obviously, a moving vehicle is accompanied with flow velocities and variations of the static pressure in its proximity.

243

- Highest pressure changes are associated with the passing of the train's first car that results in the head pressure pulse.

- Overall, the flow around a high-speed moving train, behind the windbreak wall, is three-dimensional and turbulent in nature. The analysis shows that there are potential flow accelerations and decelerations, existence of curved boundaries, flow separations and recirculation regions throughout the domain. Hence, the use of IDDES method has been successful in showing these results.

- The transition region in the windbreak wall can be observed to influence the flow in a significant manner. In fact, different flow features are visible behind the transition region due to the non-uniformity of the transition region. These flow features are discussed in detail in the chapter.

CHAPTER 7: Comparisons of flow structures around the stationary and moving trains

7.1 Introduction

In the current study, wind tunnel results presented in chapter 4 on a stationary train behind a windbreak wall were found to match the numerical results presented in chapter 5. This is an important finding as it lends credence to the traditional methods adopted in the current codes of practice and also offers scientific evidence to support the continued use of the current method, even for analysis with an external infrastructure such as windbreak wall. However, it is yet to be established whether the method of crosswind analysis on a stationary train, behind a windbreak wall, is sufficient to replace the moving train method. Therefore, this chapter presents a discussion on the comparisons in the results presented in chapter 5 and chapter 6 in order to see the difference between the stationary and moving results. It is acknowledged that the windbreak wall studied in chapter 6 is longer than that utilised in chapter 5, but the transition region and its design is kept the same in both the windbreak walls. Also, the yaw angle faced by the windbreak wall is maintained as 90° in both cases as the wall is stationary. Hence, a comparison can be made between the two cases. This comparison will demonstrate whether the method of crosswind analysis on a stationary train, behind a windbreak wall, is sufficient to replace the moving train method.

7.2 Discussion

There are several publications available in the literature such as the works of Zhang et al. (2013; 2017), which have studied the aerodynamic properties of wind barriers on a train

bridge model to calculate dynamic response. These studies, which are considered notable, were also performed on stationary models to obtain the three-component coefficients for the vehicle. Furthermore, Avila-Sanchez et al. (2014; 2016) also presented an interesting research where the shelter effectiveness of a set of windbreaks placed over a railway twin-track embankment was experimentally analysed. A set of wind tunnel tests were undertaken and results corresponding to pressure tap measurements over a section of a typical high-speed train were presented. All of these studies along with the studies of Cheli et al. (2010), Tomasini et al. (2015), He et al. (2014) and Hashmi et al. (2019) did not take into account the relative movement of the train unit compared to the walls. In terms of Dorigatti et al. (2015) research, the authors explored the results obtained from a physical model study, which investigated the wind induced forces and pressures on a 1:25 scaled model of the Class 390 pendolino train. The results of the study and the analysis provided confirmed that differences between the static and moving model experiments were observed only on the nose region of the train. Over the rest of the train body, it was proved that any difference in the pressure distribution between the static and moving experiments was within the experimental uncertainty. The study further stated that in terms of the overall mean aerodynamic side and lift forces and rolling moment coefficients, the static experiments are sufficient. Quite similarly, chapter 4 in this thesis acted as an initial step towards understanding the impact of windbreak walls with different designs on a typical stationary passenger train. Based on chapter 4, the study was further expanded in chapter 6 to consider the relative movement of the train and to verify the above claims. As discussed earlier in chapter 6, the surface pressure results are presented in terms of a non-dimensional pressure coefficient, C_P to assist in comparison. It must be noted that in normalising the pressure data for achieving a C_P value for the moving case,

the relative velocity of 57.8 m/s was used, whereas a relative velocity of 7.2 m/s was used for the stationary case.

For both cases, stationary and moving train, as demonstrated by Figure 5.3 and Figure 6.9-6.15, respectively, the oncoming crosswind flow is influenced by the windbreak and its transition region through the modification of streamlines and reduction in the mean horizontal windspeeds. However, there are major differences in the presence of vortices around the stationary and moving train analysed. To elaborate, in the stationary case, the windward side of the train had varying sizes of vortices attached. The decrease in the distance between the windbreak wall and the railway track, marked by the transition region, resulted in the formation of vortices around the stationary train body. For the moving train case, the windward side of the train had very few and weak vortices, signifying that the movement of the train reduces the appearance and the impact of the vortices that are produced by the windbreak wall and exist close to the train body. Figure 7.1 shows a comparison between a stationary and moving model at similar positions (Loop B), illustrating the differences in the flow structures developed in the two cases. Based on this figure, it is evident that not only is there a significant difference in the flow field but also in the magnitude of pressures experiences by the two train types. In terms of the leeward side of the train and the wake of the flow in the stationary train case, a large vortex is apparent close to the train, as demonstrated in Figure 7.1a. In the moving train case, this large vortex is much farther away and exists in the far wake of the windbreak wall.

Figure 7.1: An illustration of the velocity streamlines projected onto pressure contour plots showing the differences in flow structures around the (a) stationary and (b) moving train for similar positions (Loop B).

Figure 7.2 shows a comparison between a stationary and moving model at similar positions (Loop D), illustrating the differences in the flow structures developed in the two cases. At this position, both, the stationary and moving train are behind a uniform section of the transition region in the windbreak wall. Although the decrease in the distance between the windbreak wall and the railway track, marked by the transition region, did not result in the formation of vortices around the nose of the moving train, it appears that at farther distances from the nose of the train, at Loop D, there is a large vortex attached to the windward side of the track, between the windbreak wall and the train body. This is demonstrated in Figure 7.2b. Nevertheless, for the moving train case, the very few and weak vortices signify that the movement of the train reduces the appearance and the impact of the vortices that are produced by the windbreak wall and exist close to the train body. However, there are a greater number of smaller vortices which exist in the flow moving across the top of the moving train, mainly induced due to the windbreak wall.

Figure 7.2: An illustration of the velocity streamlines projected onto pressure contour plots showing the differences in flow structures around the (a) stationary and (b) moving train for similar positions (Loop D).

Relative to the windbreak wall, for the stationary case, Loop H is situated behind the midpoint of the gradient in the transition region, whereas for the moving case, Loop F is situated behind this point. Hence, Figure 7.3 shows a comparison between a stationary and moving model at a same position, illustrating the differences in the flow structures developed in the two cases. Regardless of the change in the geometry of the two loops, some clear differences are evident. Once again, there is a strong vortex attached to the bottom windward side of the stationary train, while no such vortices are present in the moving case. The flow characteristics for the two cases at this point are quite similar to Figure 7.1.

Figure 7.3: An illustration of the velocity streamlines projected onto pressure contour plots showing the differences in flow structures around the (a) stationary train (Loop H) and (b) moving train (Loop F) for a similar position.

The above discussion was made on the two trains studied with regards to the transition region. It is also useful to compare the flow fields around the two train types when they are behind the uniform section of the windbreak wall. Figure 7.4 illustrates a comparison between a stationary and moving model at a similar position, that is immediately at the start of the uniform section of the windbreak wall, after the transition region ends.

Figure 7.4: An illustration of the velocity streamlines projected onto pressure contour plots showing the differences in flow structures around the (a) stationary train (Loop I) and (b) moving train (Loop G) for a similar position.

The flow trend for the stationary case in Figure 7.4a is quite similar to Figure 7.3a, while this is not the same for the trend followed by the flow in the moving case. It seems that when the moving train is running behind the uniform section of the windbreak wall, there is a strong vortex attached to the windward side of the track. It is worth mentioning that this was also seen in Figure 7.2b, where the train was running behind the uniform section of the transition region in the windbreak wall.

Figure 7.5 illustrates a comparison between a stationary and moving model at a similar position, that is farther away from the transition region. When the two trains are behind the uniform section of the windbreak wall, the vortex seen in Figure 7.4a on the windward side seems to be stronger and bigger, as shown in Figure 7.5a. Whereas, for the moving train case, the vortex seen in Figure 7.4b is weaker and smaller in size in Figure 7.5b. Also, while the flow fields for the stationary case at Loops I and J stay similar, this is not

the case for the Loops G and I on the moving train. Near the leeward side of the track, there is a strong vortex present.
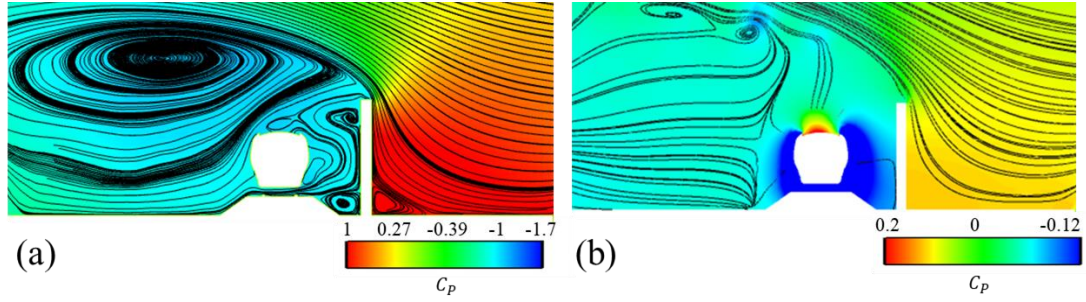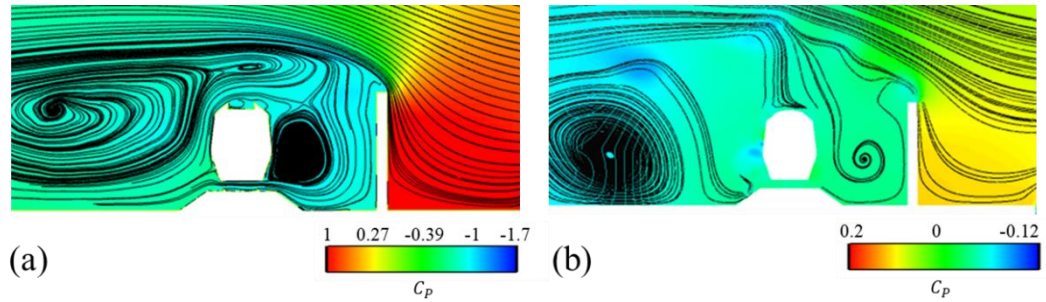

Figure 7.5: An illustration of the velocity streamlines projected onto pressure contour plots showing the differences in flow structures around the (a) stationary train (Loop J) and (b) moving train (Loop I) for a similar position.

Figure 7.6 illustrates a comparison between a stationary and moving model at a similar position, that is much farther away from the transition region. The weak vortex seen on the windward side of the moving train in Figure 7.5b is not present in Figure 7.6b. Also, near the leeward side of the track, the strong vortex present in Figure 7.5b, is much farther away from the moving train, at latter loops of the train, as demonstrated in Figure 7.6b. It must also be noted that for the stationary case as well, the strong vortex on the windward side of the train, seen in Figure 7.3-7.5a, is not very strong in Figure 7.6a.
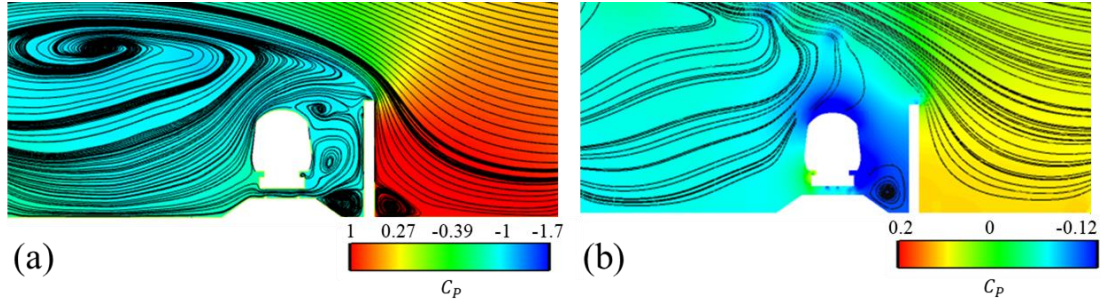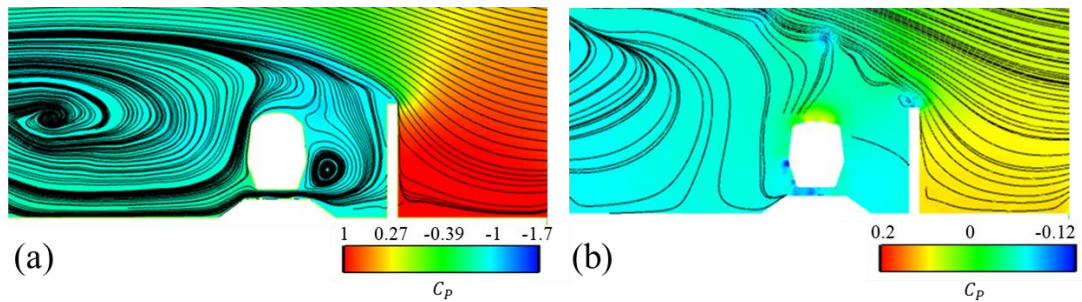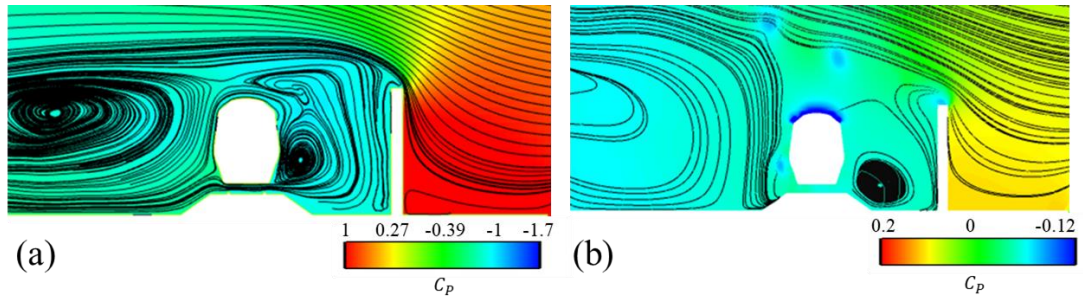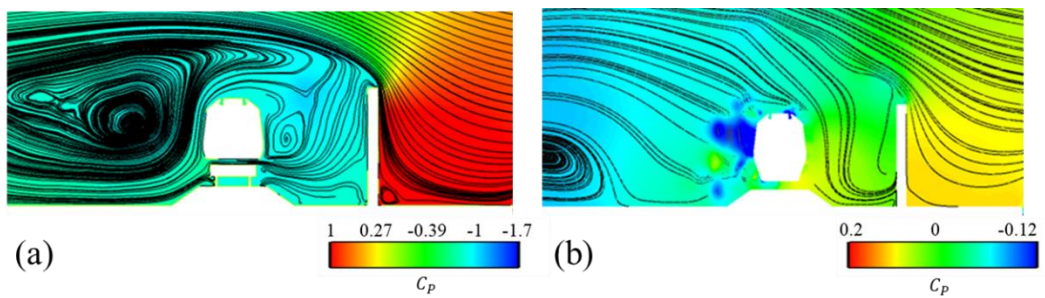

Figure 7.6: An illustration of the velocity streamlines projected onto pressure contour plots showing the differences in flow structures around the (a) stationary train (Loop L) and (b) moving train (Loop K) for a similar position.

Based on these results, it can be concluded that the stationary train and the windbreak wall in a stationary case act as a single body, where the domain has a single wake interaction. Whereas, in the moving train case, there appears the interaction of two wakes: one originating from the windbreak wall and the other from the movement of the train in the wake of the windbreak wall.

With regards to the surface pressure on the train for the stationary and moving cases, there appears to be a significant difference in the surface pressure values, as demonstrated by Figure 7.6b. Therefore, based on the analysis of the flow structures and the pressure distribution on the train surfaces of the two cases studied, it can be concluded that the stationary and moving trains have different influences on the flow fields. As the pressure distribution on the stationary train is significantly different than the pressure distribution on the moving train, this suggests that the presence of the windbreak wall leads to a difference in the flow structures around the moving train. These flow structures cannot be expected to resemble the flow structures obtained around the stationary train. Hence, the methodology adopted for simulating stationary trains is not enough to replace the method for moving trains. Based on this revelation, it seems that the finding presented by Dorigatti et al. (2015), which states that the difference between stationary and moving experiments occurs mainly near the nose of the train and in the underbody, is valid just for a train moving through crosswinds, without the influence of any external infrastructures such as windbreak walls. Therefore, in order to obtain a clear understanding of the aerodynamic flow on the trains with a windbreak walls, it is important that the relative motion of the train and the windbreak wall is taken into consideration. It appears that the aerodynamic interaction of the infrastructure, the transition region in the windbreak wall and the moving train is time dependent. Therefore,

it is crucial that a moving train simulation method is adopted in studies which aim to assess aerodynamics of vehicles in relation to surrounding infrastructures.

7.3 Conclusions

This chapter provides a discussion on the comparisons of flow structures around the stationary and moving train. The main conclusions which can be drawn from the results provided and the analysis presented in this chapter are:

- Between the stationary and moving train cases, there are significant differences in the flow field that develops around the two trains with a windbreak wall. Stronger vortices exist around the stationary train as compared to the moving train, where most of these vortices are concentrated in the transition region between the windward side of the stationary train and the windbreak wall. Also, the pressure distribution on the stationary train and the moving train differs in the trend and as well as in the magnitude thus indicating that the methodology for simulating stationary trains is not enough to replace the methodology for simulating the moving trains.

- In order to obtain a clear understanding of the aerodynamic flow on the trains with windbreak walls, it is important that the relative motion of the train and the windbreak wall is taken into consideration.

CHAPTER 8: Conclusions and recommendations for further work

8.1 Introduction

The main motivation behind this research is the occurrence of wind-related accidents in the railway industry, where passenger safety is put at a risk. Installing windbreak walls along the railway line, beside the tracks, where strong crosswinds are expected, seems to be an effective measure for reducing the effect of crosswinds on the stability of trains while ensuring passenger comfort. However, in reality it is not possible to develop an entirely uniform and continuous windbreak structure due to possible complexities in the surrounding terrain such as cuttings, which cannot be avoided. The windbreak wall would therefore consist of a discontinuous structure with a series of transition regions. Transition regions refer to the specific design implementations on a windbreak wall to tackle different topographies and terrains that exist along the railway lines; essentially deviations in the structure from the generalised continuous form parallel to the railway track. This research was aimed at understanding the aerodynamic flow, which exists around a train surface due to the presence of different kinds of windbreak walls, whilst subjected to crosswinds. Section 8.2 provides the research novelties while section 8.3 presents a series of conclusions drawn in terms of the research aim and objectives stated in chapter 1. Recommendations for further work train aerodynamics with windbreak walls are considered in section 8.4.

8.2 Research Novelties

For the first time, this novel study:

- Experimentally investigated the influence of windbreak walls with varying angles of transition regions on the flow around a model-scale passenger train subjected to crosswinds.

- Numerically investigated the influence of a windbreak wall consisting of a transition region of 45° on a stationary passenger train model subjected to crosswinds.

- Numerically investigated the influence of a windbreak wall consisting of a transition region of 45° on a moving passenger train model subjected to crosswinds.

8.3 Conclusions

Analysis of existing studies on the aerodynamics of windbreak walls has demonstrated that those with continuous geometries are more actively researched compared to discontinuous geometries; even though it is not possible to develop an entirely uniform and continuous windbreak structure due to various unavoidable terrains and cuttings. The literature review carried out in this study indicated the need of a focused study on understanding the aerodynamic flow, which exists around a train surface due to the presence of different kinds of windbreak walls, mainly ones with transition regions.

The experimental research carried out as part of this study indicated a number of important findings:

- For the 90° yaw angle:

- o in comparison to different windbreak walls assessed, the windbreak wall with a 90° transition angle mostly led to the lowest negative pressure distribution on the train surface near the nose, while the tallest wall resulted in the most negative pressure distribution, mostly.

- o At transition regions, a slight change in the results was observed where the wall with a 45° transition region showed the lowest negative pressure distribution as compared to all other walls.

- o Most differences in the results were observed at the windward side as compared to the leeward side thus suggesting the detachment in the wake of the flow.

- For the 30° yaw angle:

  - o Up to the nose region of the train, the tallest wall was observed to result in the highest negative pressure distribution over the circumference of the train, while the shortest wall showed the highest pressure distribution (i.e. with highest positive $\overline{C_P}$ values or lowest negative $\overline{C_P}$ values).

  - o In terms of transition regions, near the nose of the train, the wall with a transition angle of 90° provided the lowest negative pressure results as compared to the wall with a transition angle of 45°. Beyond the nose region (loop D onwards), the wall with a transition angle of 45° was seen to result in the most negative pressure results as compared to all other walls along the longitudinal length of the body. From loop L onwards, the influence of the tallest wall on the flow resulted in the most negative pressure distribution.

- Walls with transition regions led to more uniform results where the mean non-dimensional pressure coefficient was seen to approach zero. These uniform results with lesser variations indicate the smooth pressure distribution around the train possibly signifying the complete detachment of any vortical structures from the train body.

- Generally, it is presumed that a strong vortex can lead to the sharp transition or drop in the pressure.

- Overall, the addition of windbreak walls led to uniform results in the leeward side comparatively, possibly due to the detachment of the flow in the wake region; while the shielding effects of different windbreak walls were clearly evident over the entire train body.

- In terms of the differences in the results obtained for the yaw angles of 30° and 90°, it was observed at 30° yaw angle that due to the orientation of the model, both positive and negative mean non-dimensional pressure coefficient values were revealed, whereas at 90° yaw angle, the windbreak walls resulted in all lower mean non-dimensional pressure coefficient values.

- A comparison between the no wall and with wall cases shows clearly that the values of the overall mean aerodynamic load coefficient for the side (lateral) for most loops of the train changed from positive to negative with the addition of any wall, at both yaw angles assessed. This was as expected and shows the huge impact of windbreak walls. Also, the shielding effect of windbreak walls results in negative and in some cases negligible overall side force coefficient values.

- Although lift force coefficients remained positive even after the addition of windbreak walls, the intensity of change between the results was clear reflecting on the significant impact of walls.

- Almost negligible rolling moments were observed with the use of windbreak walls at a yaw angle of 90° and somewhat positive rolling moments were observed with the use of windbreak walls at a yaw angle of 30°.

- The use of a windbreak wall in the leeward side of the train seems unnecessary, as the flow does not seem to be significantly affected by the presence of this wall. However, the wall does lead to less fluctuations in the rapid transitions in the pressure over the circumference of the train.

- If the two windbreak walls with transition regions (i.e. walls 4 and 5) are compared, it is clearly visible that both tend to provide a uniform surface pressure distribution but there are certainly some differences between the two cases at different wind incidence angles.

- Overall, the windbreak walls used in this experimental study have proved to be capable in reducing the loads on a train surface significantly.

Based on the experimental work, a numerical study was carried out on the windbreak wall consisting of a transition region of 45° transition angle at a yaw angle of 90°. This windbreak wall was chosen as it is a mid-way between the no transition region (i.e. 0° transition angle) and maximum transition region (i.e. 90° transition region). As experimental work performed at the University of Birmingham's wind-tunnel facility was used to validate the intial numerical simulations in this research, exact dimensions of the train model, the STBR and the windbreak walls used in the experiments were maintained for the CAD model to ensure a quality validation of the numerical simulations.

Analysis on the numerical simulations carried out on a stationary model indicated that:

- The use of the improved delayed detached eddy simulation (IDDES) method for performing numerical simulations is successful as the accuracy of the numerical simulations was validated and verified.

- While a good agreement is observed in the pressure distribution between the experimental and numerical results, slight discrepancies are still noticeable, mainly in the underbody regions. This is not surprising based on the practical limitations and difficulties noted in the experimental set-up.

- The use of numerical simulations assisted in predicting the time-averaged pressure and velocity fields easily around the entire configuration with the help of visualisation techniques.

In terms of the numerical results on the stationary model, the following conclusions can be made:

- The immediate deflection in the incident flow at the tip of the windbreak wall can be easily appreciated. The incident flow streamlines follow the same trend throughout where they attack the windward side of the windbreak wall and then deflect from the top edge of the wall. The streamlines are lifted and the flow above the windbreak wall is accelerated.

- The flow pattern on the windward side of the windbreak wall at all positions confirms relatively uniform area of stagnation. Also, the presence of a windbreak wall displaces the detachment point of the shear layer to the tip of the windbreak wall. Thus, the flow velocity increases in the region near the detachment point where the flow separates.

- A series of vortical structures and vortices are evident at different positions inside the computational domain.

- The results show the presence of a fully developed wake, dominated by large vortices and a recirculation zone.

- The disappearance of some vortices confirmed the suggestion made in the literature review that the change in the distance between the windbreak wall and the railway track, known as the transition region, can result in the formation of vortices around the train body, which may hit the train surfaces potentially leading to stability issues for the train.

- Overall, the windbreak wall was able to significantly reduce the intensity of the pressures on the windward side of the train while also providing uniformity to the results on the leeward side of the train. This confirms the shielding effects provided by the windbreak wall to the train body from the oncoming crosswind flows. In addition, largely low velocity regions can be seen around the train body, behind the windbreak wall.

Validation of the initial numerical results on a stationary model assisted with ascertaining the accuracy of the method utilised along with providing additional details on the aerodynamic flow. Based on the initial results, further numerical work was built up, which considered the relative movement between the train and the windbreak wall. To maintain consistency, the same design of the windbreak wall was chosen for the moving analysis case as the stationary analysis case.

Analysis of a numerical investigation on a moving passenger train model subjected to crosswinds with a windbreak wall consisting of a transition region of 45° transition angle revealed that:

- The windward side of the windbreak wall consists of a stagnation region mainly due to the direct impact of the crosswinds. This finding has been achieved in each part of this study.

- There is an immediate deflection in the incident crosswind flow at the tip of the windbreak wall creating a flow separation diverting the flow over the top of the train.

- As the high-speed train starts to travel behind the windbreak flow, due to the sudden movement of the train, there is an unsteady flow mechanism which takes place that results in the build-up of some low pressure vortices around the first car. Obviously, a moving vehicle is accompanied with flow velocities and variations of the static pressure in its proximity.

- Highest pressure changes are associated with the passing of the train's first car that results in the head pressure pulse.

- The flow around the moving train can be categorized by three-dimensional structures which are a result of the combination between the crosswinds and train-induced wind on the zone of train nose.

- Regions of higher suctions and smaller suctions vary from time to time over the train body, depending on the position of the train, behind the windbreak wall.

- The shielding effect of the wall is depicted on the pressure distribution of windward side of the moving train.

- The extreme pressure obtained at stagnation point, appears on the nose of the first car due to the compressible effects of a moving train on the air, while the lower pressures on other parts of the train indicate some separated flow in these regions. In terms of the compressible effects produced by the nose of the car, these are

merely compression waves, which are created in front of a moving train that lead to regions of high pressure. These are amplified as the train travels in somewhat a confined space, i.e. travelling behind a barrier.

- Overall, the results demonstrated that the flow around a high-speed moving train, behind the windbreak wall, is three-dimensional and turbulent in nature. The analysis shows that there are potential flow accelerations and decelerations, existence of curved boundaries, flow separations and recirculation regions throughout the domain. Hence, the use of IDDES method has been successful in showing these results.

- Concisely, the crosswind flow is influenced by the windbreak wall and its transition in three ways:

  o Modification of streamlines

  o Reduction in the mean horizontal windspeeds

  o Alteration in the turbulent structures of the incident flow

- The streamlines produce an effect as an increased pressure on the windward side of the windbreak wall forces some of the flow over it. This results in an upward-bending of the streamlines upwind of the windbreak wall, followed by the compression of the streamlines above the windbreak wall, proceeded by the downward-bending of the streamlines, in the leeward side of the windbreak wall.

- The transition region in the windbreak wall can be observed to influence the flow in a significant manner. In fact, different flow features are visible behind the transition region due to the non-uniformity of the transition region. These flow features are discussed in detail in the thesis.

- Between the stationary and moving train cases, there are significant differences in the flow field that develops around the two trains with a windbreak wall. Stronger vortices exist around the stationary train as compared to the moving train, where most of these vortices are concentrated in the transition region between the windward side of the stationary train and the windbreak wall. Also, the pressure distribution on the stationary train and the moving train differs in the trend and as well as in the magnitude thus indicating that the methodology for simulating stationary trains is not enough to replace the methodology for simulating the moving trains.

- In order to obtain a clear understanding of the aerodynamic flow on the trains with a windbreak walls, it is important that the relative motion of the train and the windbreak wall is taken into consideration.

8.4   Recommendations for further work

- The experimental data gathered in this research can be used for benchmarking future CFD cases. This would allow for an accurate verification and validation of the numerical simulations, thus overcoming the limitations faced in a typical experimental campaign.

- The results from the numerical simulations on the moving train model can be further verified by performing an aerodynamic investigation at the The University of Birmingham's Transient Aerodynamic Investigation (TRAIN) rig. The TRAIN rig is a unique facility built for measuring the aerodynamics of scaled moving models. Also, the scaled models to carry such a campaign are readily available from this research. Thus, the experimental study can be easily carried out.

- The results of this study indicate that vehicle movement has an effect on the aerodynamic flow around a train, behind a windbreak wall. Further work can include numerically simulating different transition region designs in windbreak walls while considering the relative motion of the train and the windbreak wall.

- The research carried out in this study has focused on a passenger train only. Crosswinds are known to have an effect on the stability of both passenger and freight trains. Perhaps, future work can consider the influence of windbreak walls on the stability of freight trains.

- Even though a Single Track and Ballast Rail (STBR) is a reference scenario, in the presence of wind barriers, the Double Track Ballast and Rail (DTBR) might modify the distance between the train and any downwind barriers. This scenario can be tested in a further study.

- The use of symmetrical windbreak walls in both, windward and leeward sides of the train can also be studied for any follow up studies.

- In this work, each windbreak wall with a transition region consisted of one transition region only. In the future, the effect of more than one transition region in a single windbreak wall can be studied to analyse the effect a series of transition regions have on the aerodynamic flow with respect to the train movement.

REFERENCES

Alam, F. and Watkins, S. (2007). Effects of Crosswinds on Double Stacked Container Wagons. In 16th Australasian Fluid Mechanics Conference (AFMC). 758–761. School of Engineering, The University of Queensland.

Andersson, J., Pettersson, V., Thune, E., Viktorsson, H. and Oisjoen, D. (2009). Simulation of the Slipstream and wake of a High-Speed Train in Crosswinds. Bachelor's Thesis. Department of Applied Mechanics. Chalmers University of Technology.

Ansys. (2017). Ansys® Academic Research, Fluent. Release 18.2.

Ariza, C., Casado, C., Wang, R., Adams, E., Marugán, J. (2018). Comparative Evaluation of OpenFOAM® and ANSYS® Fluent for the Modeling of Annular Reactors. Chemical Engineering & Technology. 41(7), 1473-1483.

Avila-Sanchez, S., Pindado, S., Lopez-Garcia, O. and Sanz-Andres, A. (2014). Wind Tunnel Analysis of the Aerodynamic Loads on Rolling Stock over Railway Embankments: The Effect of Shelter Windbreaks. The Scientific World Journal. 1-17.

Avila-Sanchez, S., Lopez-Garcia, O., Cuerva, A., Meseguer, J. (2016). Characterisation of cross-flow above a railway bridge equipped with solid windbreaks. Eng Struct. 126, 133-146.

Baker C. (1991). Ground vehicles in high crosswinds - Part I: Steady aerodynamic forces, J Fluids and Structures. 5, 69 – 90.

Baker, C. (2003). Some complex applications of the wind loading chain. Journal of Wind Engineering and Industrial Aerodynamics. 91:1791-1811.

Baker, C. (2010). The flow around high speed trains. J. Wind Eng. Ind. Aerod. 98, 277-298.

265

Baker, C. (2014a). A review of train aerodynamics Part 1 – Fundamentals. The Aeronautical Journal. 118 (1201), 201-228.

Baker, C. (2014b). A review of train aerodynamics Part 2 – Applications. The Aeronautical Journal. 118 (1202).

Baker, C., Brockie, N. (1991). Wind tunnel tests to obtain train aerodynamic drag coefficients: Reynolds number and ground simulation effects. J. Wind Eng. Ind. Aerod. 38(1), 23-28.

Baker, C., Cheli, F., Orellano, A., Paradot, N., Proppe, C., Rocchi, D. (2009). Cross-wind effects on road and rail vehicles. Vehicle System Dynamics. 47 (8), 983-1022.

Baker, C., Dalley, S., Johnson, T., Quinn, A. and Wright, N. (2001). The slipstream and wake of a high-speed train. Proceedings of the Institution of Mechanical Engineers, Part F: Journal of Rail and Rapid Transit. 215 (2), 83–99.

Baker, C., Gilbert, T., Jordan, S. (2013c). The validation of the use of moving model experiments for the measurement of train aerodynamic parameters in the open air. Proceedings of the World Congress on Rail Research. Sydney, Australia.

Baker, C., Hemida H., Iwnicki, S., Xie, G., Ongaro, D. (2011). Special issue: The integration of crosswind forces into train dynamic modelling. Proceedings of the Institution of Mechanical Engineers. Part F J. Rail Rapid Transit. 225 (2), 154-164.

Baker, C., Johnson, T., Flynn, D., Hemida, H., Quinn, A., Soper, D., Sterling, M. (2019). Train Aerodynamics. Butterworth-Heinemann. ISBN 9780128133101.

Baker, C., Jones, J., Lopez-Calleja, F. (2003). Measurements of the cross wind forces on Mark 3 and Class 390 vehicles. Proceedings World Congress on Railway Research, Edinburgh.

Baker, C., Jones, J., Lopez-Calleja, F., Munday, J. (2004). Measurements of the crosswind forces on trains. J. Wind Eng. Ind. Aerod. 92, 547-563.

Baker, C., Quinn, A., Sima, M., Hoefener, L., Licciardello., R. (2013a). Full-scale measurement and analysis of train slipstreams and wakes: Part 1 Ensemble averages. Proceedings of the Institution of Mechanical Engineers. Part F: Journal of Rail and Rapid Transit, 10.1177/0954409713485944

Baker, C. J., Quinn, A., Sima, M., Hoefener, L., Licciardello, R. (2013b). Full-scale measurement and analysis of train slipstreams and wakes. Part 2 Gust analysis. Proceedings of the Institution of Mechanical Engineers. Part F: Journal of Rail and Rapid Transit.

Baker, C. and Sterling, M. (2009). Aerodynamic Forces on Multiple Unit Trains in Cross Winds. ASME. J. Fluids Eng. 131 (10), 101103.

Barcala, M., Meseguer, J. (2007). An experimental study of the influence of parapets on the aerodynamic loads under cross wind on a two-dimensional model of a railway vehicle on a bridge. Proceedings of the Institution of Mechanical Engineers. Part F J. Rail Rapid Transit. 221 (4), 487-494.

Bearman, P. (1997). Near wake flows behind two and three dimensional bluff bodies. Journal of Wind Engineering and Industrial Aerodynamics. 69-71: 33-54.

Bearman, P. and Obasaju, E. (1982). An experimental study of pressure fluctuations on fixed and oscillating square-section cylinders. Journal of Fluid Mechanics. 119: 297-321.

Bell, J. R., Burton, D., Thompson, M. C., Herbst, A. H., Sheridan, J. (2015). Moving model analysis of the slipstream and wake of a high-speed train. Journal of Wind Engineering and Industrial Aerodynamics. 136, 127-137.

Bi, H., Ma, G., Wang, H. (2011). Aerodynamic characteristics of high-speed trains with wind fence. In: The 3rd international conference on transportation engineering. Chengdu, China. 2521–2526.

Blackadar, A. and Tennekes, H. (1968). Asymptotic similarity in neutral barotropic planetary boundary layers. Journal of Atmospheric Sciences. 25, 1015–1020.

Bocciolone, M., Cheli, F., Corradi, R., Muggiasca, S., Tomasini, G. (2008). Crosswind action on rail vehicles: wind tunnel experimental analyses. J. Wind Eng. Ind. Aerod. 96, 584-610.

Bradshaw, P. (1969). Analogy between streamline curvature and bouyancy in turbulent shear flow. Journal of Fluid Mechanics. 36 (1): 177-191.

Browand, F., Ross, J., McCallen, R. (2009). The Aerodynamics of Heavy Vehicles II: Trucks, Buses, and Trains. Berlin.

Cebeci, T. and Smith, A.M.O. (1974). Analysis of turbulent boundary layers. New York, Academic Press, Inc.

CEN. (2010). Railway Applications – Aerodynamics Requirements and test procedures for aerodynamics in tunnels. BS EN 14067-5: 2006+A1:2010.

CEN. (2013). Railway applications - Aerodynamics - Part 4: Requirements and test procedures for aerodynamics on open track. BS EN 14067-4:2013. CEN/TC 256.

CEN. (2018). Railway applications - Aerodynamics - Part 6: Requirements and test procedure for cross wind assessment. PrEN 14067–6 2009-02. CEN/TC 256.

Cengel, Y.A., Turner, R. H., Cimbala, J, M. (2008). Fundamentals of Thermal-Fluid Sciences. 3rd Edition. McGraw-Hill.

Cheli, F., Corradi, R., Rocchi, D., Tomasini, G., Maestrini, E. (2010). Wind tunnel tests on train scale models to investigate the effect of infrastructure scenario. J. Wind Eng. Ind. Aerod. 98, 353-362.

Cheli, F., Rocchi, D., Tomasini, G. (2011a). Study of the Reynolds effects on aerodynamic coefficients of a railway vehicle through wind tunnel tests. In: The 13th international conference on wind engineering. Amsterdam, Netherlands.

Cheli, F., Rocchi, D., Schito, P., Tomasini, G. (2011b). Steady and moving high-speed train crosswind simulations. Comparison with wind-tunnel tests. In: Proceedings of the Ninth World Congress on Railway Research. WCRR 2011. Lille, France.

Chen, G., Li, X.B., Liu, Z. et al. (2019). Dynamic analysis of the effect of nose length on train aerodynamic performance. J. Wind Eng. Ind. Aerodyn. 184, 198–208.

Chen, Z., Liu, T., Yu, M., Chen, G., Chen, M., Guo, Z. (2020). Experimental and numerical research on wind characteristics affected by actual mountain ridges and windbreaks: a case study of the Lanzhou-Xinjiang high-speed railway. Engineering Applications of Computational Fluid Mechanics. 14(1), 1385-1403.

Chen, Z., Hashmi., S.A., Liu, T., Hemida, H., Sun, Z., Guo, Z. (2021). Impact of windbreak transition on the flow around a railway track with different angles of wind attack. In preparation.

Chiu T. W. (1995). Prediction of the aerodynamic loads on a railway train in a cross-wind at large yaw angles using an integrated two- and three-dimensional source/vortex panel method. Journal of Wind Engineering and Industrial Aerodynamics. 57, 19-39.

Chiu, T. W. (1991). A two-dimensional second-order vortex panel method for the flow in cross-wind over a train and other two-dimensional bluff bodies. Journal of Wind Engineering and Industrial Aerodynamics. 37, 43-64.

Chiu, T.W., Squire, L.C. (1992). An experimental study of the flow over a train in a crosswind at large yaw angles up to 90°. J. Wind Eng. Ind. Aerod. 45, 47-74.

Chu, C., Chang, C., Huang, C., Wu, T., Wang, C., Liu, M. (2013). Windbreak protection for road vehicles against crosswind. J. Wind Eng. Ind. Aerod. 116, 61-69.

Constantinuescu, G. and Squires, K. (2003). LES and DES investigations of turbulent flow over a sphere at Re=10,000. Journal of Flow, Turbulence and Combustion. 70:267-298.

Cooper, K. (1993). Bluff-body aerodynamics as applied to vehicles. Journal of Wind Engineering and Industrial Aerodynamics. 49 (1-3), 1–21.

Cooper, R. (1984). Atmospheric turbulence with respect to moving ground vehicles. Journal of wind engineering and industrial aerodynamics. 17 (2), 215–238.

Cooper, R. (1979). The probability of trains overturning in high winds. In: Proceedings of the 5th International Conference on Wind Engineering. Fort Collins. 2, 1185-1194.

Copley, J. (1987). The three dimensional flow around railway trains. J. Wind Eng. Ind. Aerod. 26, 21-52.

Deeg, P., Jonsson, M., Kaltenbach, H-J., Schober, M., Weise, M. (2008). Cross comparison of measurement techniques for the determination of train induced aerodynamic loads on the track bed. In: Proceedings of the conference on Bluff Bodies Aerodynamics and its Applications. Milano, Italy.

Deng, E., Yang, W., Lei, M., Zhu, Z., Zhang, P. (2019). Aerodynamic loads and traffic safety of high-speed trains when passing through two windproof facilities under crosswind: A comparative study. Engineering Structures. 188, 320-339.

Department for Transport. (2017). Rail factsheet: (2017). National Statistics. Crown copyright.

270

Diedrichs, B. (2006). Studies of Two Aerodynamic Effects on High-Speed Trains: Crosswind Stability and Discomforting Car Body Vibrations Inside Tunnels. PhD Thesis, TRITA-AVE Report 2006:81, ISSN 1651-7660. Dep. of Aeronautical and Vehicle Engineering, Royal Institute of Technology (KTH). Stockholm, Sweden.

Diedrichs, B. (2003). On computational fluid dynamics modelling of crosswind effects for high-speed rolling stock. Proceedings of the Institution of Mechanical Engineers. Part F J. Rail Rapid Transit. 217 (3), 203-226.

Diedrichs B. (2010). Aerodynamic Crosswind Stability of a Regional Train Model. Proc. IMechE Part F: J. Rail and Rapid Transit. 224, 580-591.

Dorigatti, F. (2013). Rail vehicles in crosswinds: analysis of steady and unsteady aerodynamic effects through static and moving model tests. Ph. D. thesis, University of Birmingham, UK.

Dorigatti, F., Sterling, M., Baker, C., Quinn, A. (2015). Crosswind effects on the stability of a model passenger train - A comparison of static and moving experiments. J. Wind Eng. Ind. Aerod. 138, 36-51.

Douglas, J., Gasiorek, J., Swaffield, J. and Jack, L. (2011). Fluid mechanics. 1st ed. Harlow: Pearson/Prentice Hall.

Duncan, W. J., Thom, A. and Young, A. (1970). Mechanics of fluids, 1st ed. London: Edward Arnold.

EC. (2008). TSI—technical specification for Interoperability of the trans-European high-speed rail system, 'rolling stock' sub-system, TSI-HS2008/232/EC. Off. J. Eur. Union.

European Rail Agency. (2008). Technical Specification for Interoperability (TSI) - Rolling stock subsystem, 96/48/EC.

Favre, T., Diedrichs, B., Efraimsson, G. (2010). Detached-eddy simulations applied to unsteady crosswind aerodynamics of ground vehicles. In: Peng, S.-H., Doerffer, P., Haase, W. (Eds.), Progress in Hybrid RANS–LES Modelling. Springer, Berlin Heidelberg.

Figura-Hardy, G. (2005). RSSB Slipstream Safety - Analysis of Existing Experimental Data on Train Slipstreams Including the Effects on Pushchairs.

Flynn, D., Hemida, H., Soper, D., Baker, C. (2014). Detached-eddy simulation of the slipstream of an operational freight train. Journal of Wind Engineering and Industrial Aerodynamics. 132, 1-12.

Flynn, D. (2015). A numerical investigation of the effect of crosswinds on the slipstream of a model-scale freight train and associated effects. PhD thesis, University of Birmingham, UK.

Franke, J., Hellsten, A., Schlunzen, H., Carisimo, B. (2010). The Best Practise Guideline for the CFD simulation of flows in the urban environment: an outcome of COST 732. The Fifth International Symposium on Computational Wind Engineering (CWE2010). Chapel Hill, North Carolina.

Fujii, T., Maeda, T., Ishida, H., Imai, T., Tanemoto, K., Suzuki, M. (1999). Wind induced accidents of train vehicles and their measurements in Japan. Q.J. RTRI Japan. 401, 50-55.

Gallagher, M. (2016). Experimental investigation of the aerodynamics of a Class 43 high speed train. PhD thesis, University of Birmingham, UK.

Gallagher, M., Morden, J., Baker, C., Soper, D., Quinn, A., Hemida, H., Sterling, M. (2018). Trains in crosswinds – comparison of full-scale on-train measurements, physical model tests and CFD calculations. J. Wind Eng. Ind. Aerod. 175, 428-444.

Garcia, J., Munoz-Paniagua, J., Jimenez, A., Migoya, E., Crespo, A. (2015). Numerical study of the influence of synthetic turbulent inflow conditions on the aerodynamics of a train. Journal of Fluids and Structures. 56(9), 134–151.

Gatski, T., Hussaini, M., Lumley, J., John, L. (1996). Simulation and Modelling of turbulent flows. Oxford University Press.

Gawthorpe, R. (1994). Wind effects on ground transportation. Journal of Wind Engineering and Industrial Aerodynamics. 52, 73–92.

Gaylard, A. P. (1993). The application of computational fluid dynamics to railway aerodynamics. Journal of Rail and Rapid Transit, Proc Instn Mech Engrs. 207, 133.

Gil, N., Baker, C., Roberts, C., Quinn, A. (2010). Passenger train slipstream characterization using a rotating rail rig. Journal of Fluids Engineering. 132, 061401.

Gritskevich, M.S., Garbaruk, A.V., Schütze, J., Menter. F.R. (2012). Development of DDES and IDDES Formulations for the k-w Shear Stress Transport Model. Flow, Turbulence and Combustion. 88(3):431–449.

Guo, W., Xia, H., Karoumi, R., Zhang, T., Li, X. (2015). Aerodynamic effect of wind barriers and running safety of trains on high-speed railway bridges under crosswinds. J. Wind Struct. 20 (2), 213-236.

Haque, N. M., Katsuchi, H., Yamada, H., Nishio, M. (2014). Investigation of Flow Fields Around Rectangular Cylinder Under Turbulent Flow by LES. Engineering Applications of Computational Fluid Mechanics. 8(3), 396-406.

Hashmi, S. A., Hemida, H. and Soper, D. (2019). Wind tunnel testing on a train model subjected to crosswinds with different windbreak walls. Journal of Wind Engineering and Industrial Aerodynamics. 195. https://doi.org/10.1016/j.jweia.2019.104013.

He, X., Zou, Y. F., Wang, H. F., Han, Y., Shi, K. (2014). Aerodynamic characteristics of a trailing rail vehicles on viaduct based on still wind tunnel experiments. J. Wind Eng. Ind. Aerod. 135, 22-33.

He, M., Huo, S., Hemida, H., Bourriez, F., Robertson, F., Soper, D., Sterling, M., Baker, C. (2019). Detached eddy simulation of a closely running lorry platoon. Journal of Wind Engineering and Industrial Aerodynamics. 193, 103956.

Hemida, H. (2006). Large-Eddy Simulation of the Flow around Simplified High-Speed Trains under Side Wind Conditions. Goteborg: Chalmers Reproservice.

Hemida, H. and Krajnovic, S. (2009). Exploring Flow Structures Around a Simplified ICE2 Train Subjected to a 30 Degree Side Wind Using large-Eddy Simulation. Journal of Engineering Applications of Computational Fluid Mechanics. 3(1), 28-41.

Hemida, H., Baker, C. and Gao, G. (2012). The calculation of train slipstreams using large-eddy simulation. Proceedings of the Institution of Mechanical Engineers, Part F, Journal of Rail and Rapid Transit. 228 (1), 25-36.

Hemida, H., Baker, C. (2010). Large-eddy simulation of the flow around a freight wagon subjected to a crosswind. Comput. Fluids. 39 (10), 1944–1956.

Hemida, H., Baker, C.J., Gao, G. (2014). The calculation of train slipstreams using large-eddy simulation. Proc. Inst. Mech. Eng., Part F: J. Rail Rapid Transit. 228, 25–36.

Hemida, H., Krajnovic, S., Davidson, L. (2005). Large-eddy simulations of the flow around a simplified high speed train under the influence of a cross-wind. AIAA paper number 5354.

Hemida, H., Krajnović, S. (2010). LES study of the influence of the nose shape and yaw angles on flow structures around trains. J. Wind Eng. Ind. Aerodyn. 98, 34–46.

Hinze, J. O. (1976). Turbulence. New York; London (etc.): McGraw-Hill.

Hoppmann, U., Koenig, S., Tielkes, T., Matschke, G. (2002). A short-term strong wind prediction model for railway application: design and verification. Journal of Wind Engineering and Industrial Aerodynamics. 90:1127.1134.

Huang, S., Hemida, H., Yang, M. (2016). Numerical Calculations of the Slipstream of the CRH2 High-speed Train. Proceedings of the Institution of Mechanical Engineers, Part F: Journal of Rail and Rapid Transit. 230, 1, 103-116.

Humphreys, N. and Baker, C. (1992). Forces on vehicles in cross winds from moving model tests. J Wind Eng Ind Aerodynamics. 44, 2673–2684.

Johnson, T. and Dalley, S. (2002). 1/25 scale moving model tests for the trans-aero project. In: Schulte-Werning B, Gregoire R, Malfatti A, Matschke G, editors. Transaero-a European initiative on transient aerodynamics for railway system optimization. Berlin: Springer. 123–135.

Khier, W., Durst, F., Breuer, M. (2000). Flow structure around trains under side wind conditions: a numerical study. Computers & Fluids. 29:179–195.

Kim, N. and Rhode, D. (2000). Streamwise Curvature Effect on the Incompressible Turbulent Mean Velocity Over curved surfaces. Journal of Fluids Engineering. 122:547-551.

Kiya, M., Arie M., Koshikawa K. (1980), An analysis of uniform shear flow past a porous plate attached to a plane surface. Journal of Fluids Engineering. 102, 160- 165

Krajnovic, S. and Davidson, L. (2004). Large eddy simulation of the flow around an Ahmed body. In 2004 ASME Heat Transfer/Fluids Engineering Summer Conference, Charlotte, North Carolina, USA.

Krajnović, S., Ringqvist, P., Nakade, K., Basara, B. (2012). Large eddy simulation of the flow around a simplified train moving through a crosswind flow. Journal of Wind Engineering and Industrial Aerodynamics. 110, 86-99.

Kravchenko, G. and Moin, P. (2000). Numerical studies of flow over a circular cylinder at Re=3900. Physics of Fluids. 12(2):403-417.

Lakshminarayana, B. (1986). Turbulence Modelling for Complex Shear Flows. AIAA Journal. 24: 1900-1917.

Li, B., Xu, Z., Yang, Q., Feng, S. (2012). Effects of railway wind fence on the aerodynamic forces of train and fence. In: The 12th international symposium on structural engineering. Wuhan, China. 625- 630.

Li, T., Hemida, H., Zhang, J., Rashidi, M., Flynn, D. (2018). Comparisons of Shear Stress Transport and Detached Eddy Simulations of the Flow Around Trains. Journal of Fluids Engineering. 140(11), 111108-12.

Li, X.B., Chen, G., Wang, Z., Xiong, X.H., Liang, X.F., Yin, J. (2019). Dynamic analysis of the flow fields around single-and double-unit trains. J. Wind Eng. Ind. Aerodyn. 188, 136–150.

Liu, T., Chen, Z., Zhou, X., Zhang, J. (2018). A CFD analysis of the aerodynamics of a high-speed train passing through a windbreak transition under crosswind. Engineering Applications of Computational Fluid Mechanics. 12(1), 137-151.

Liu, Y., Hemida, H., Liu, Z. (2014). Large Eddy Simulation of the flow around a train passing a stationary freight' Journal of Rail and Rapid Transit. DOI: 10.1177/0954409713488096, 2013.

Lyn, D., Einav, S., Rodi, W. and Park, J. (1995). A laser-Doppler velocimetry study of ensemble-averaged characteristics of the turbulent near wake of a square cylinder. Journal of Fluid Mechanics. 304: 285.

Mancini, G., Malfatti, A., Violi, A., Matschke, G. (2001). Effects of experimental bogie fairings on the aerodynamic drag of the ETR 500 high-speed train. World Congress on Railway Research. Munich.

Masbernat, F., Wolffhugel, Y.F., Dumas, J.C. (1993). CFD Aerodynamics of the French high-speed train, GEC ALSTHOM Technical Review No. 11.

Matschke, G. and Heine, C. (2002) Full Scale Tests on Side Wind Effects on Trains. Evaluation of Aerodynamic Coefficients and Efficiency of Wind Breaking Devices. In: Schulte-Werning B., Grégoire R., Malfatti A., Matschke G. (eds) TRANSAERO — A European Initiative on Transient Aerodynamics for Railway System Optimisation. Notes on Numerical Fluid Mechanics and Multidisciplinary Design (NNFM), vol 79. Springer, Berlin, Heidelberg.

Matschke, G. and Schulte-Werning, B. (1997). Measures and strategies to minimise the effect of strong crosswinds on high speed trains, Proceedings of the WCRR World Congress of Railway Research, Florence, Italy, Vol. E, 569–575.

Matschke, G., Tielkes, T., Schulte-Werning, B., Locher, P., Fermaud, C., Bohnenblust, H. (2000). in: S. Kondo, K. Furata (Eds.), Influence of Strong Side Winds on HighSpeed Trains of the German Railway (DB)—A Risk Assessment Approach, PSAM5—Probabilistic Safety Assessment and Management, Universal Academy Press, Tokyo. 2039–2045.

Menter, F.R., Kuntz, M., Langtry, R. (2003). Ten years of experience with the SST turbulence model. 4th International Symposium on Turbulence Heat and Mass Transfer. 625–632.

Meroney, R. and Bradshaw, P. (1975). Turbulent Boundary Layer Growth over a Longitudinally Curved Surface. AIAA Journal. 13(11): 1448.

Mittal, R. and Moin, P. (1997). Suitability of upwind-biased finite difference schemes for large-eddy simulation of turbulent flows. AIAA Journal. 35(8):1415-1417.

Morden, J., Hemida, H., Baker, C. J. (2015). Comparison of RANS and detached eddy simulation results to wind-tunnel data for the surface pressures upon a class 43 high-speed train. Journal of Fluids Engineering. 137(4), 041108.

Muck, K., Hoffmann, P., Bradshaw, P. (1985). The effect of convex surface curvature on turbulent boundary layers. Journal of Fluid Mechanics. 161(-1), p.347.

Muld, T.W., Efraimsson, G., Henningson, D.S. (2012). Flow structures around a high-speed train extracted using proper orthogonal decomposition and dynamic mode decomposition. Comput. Fluids. 57, 87–97.

Nishino, T., Roberts, G., Zhang, X. (2008). Unsteady RANS and detached-eddy simulations of the flow around cylinder in ground effect. J Fluid Struct. 24, 18-33.

Niu, J., Zhou, D., Liang,. (2017a). Numerical investigation of the aerodynamic characteristics of high-speed trains of different lengths under crosswind with or without windbreaks. Engineering Applications of Computational Fluid Mechanics. 12(1), 195-215.

Niu, J., Zhou, D., Wang, Y. (2018). Numerical comparison of aerodynamic performance of stationary and moving trains with or without windbreak wall under crosswind. Journal of Wind Engineering and Industrial Aerodynamics. 182, 1-15.

Niu, J.Q., Zhou, D., Liang, X.F. (2017b). Numerical simulation of the effects of obstacle deflectors on the aerodynamic performance of stationary high-speed trains at two yaw angles. Proc. Inst. Mech. Eng. - Part F J. Rail Rapid Transit. 232 (3), 913–927.

Numeca International. (2017). HEXPRESS/Hybrid 6.2 user guide. NUMECA INTERNATIONAL.

OpenFOAM. (2018). The Open Source CFD Toolbox, Paris, France: ESI Group.

Persson, J. (2015). Synthetic Inlet Boundary Conditions for LES Chalmers. Master's thesis. University of Technology. Göteborg, Sweden.

Pope, C. (1991). The simulation of flows in railway tunnel using 1/25th scale moving model facility. 7th International Symposium on the Aerodynamics and Ventilation of Vehicle Tunnels. 48–56.

Pope, C. (2006). Safety of slipstreams effects produced by trains. A report prepared by Mott Macdonald, Ltd., for RSSB.

Pope, S. (2000). Turbulent Flows. Cambridge University Press.

Premoli, A., Rocchi, D., Schito, P., Tomasini, G. I. S. E. L. L. A. (2016). Comparison between steady and moving railway vehicles subjected to crosswind by CFD analysis. Journal of Wind Engineering and Industrial Aerodynamics. 156, 29–40.

Quinn, A., Sterling, M., Robertson, A., Baker, C. (2007). An investigation of the wind-induced rolling moment on a commercial vehicle in the atmospheric boundary layer. Proceedings of the Institution of Mechanical Engineers, Part D: Journal of Automobile Engineering. 221 (11), 1367–1379.

Reynolds, O. (1895). On the dynamical theory of incompressible viscous fluids and the determination of the criterion. Philosophical Transactions of the Royal Society of London. 186, 123–164.

Richardson, G.M., Richards, P.J. (1995). Full-scale measurements of the effect of a porous windbreak on wind spectra. J. Wind Eng. Ind. Aerod. 54-55, 611-619.

Roache, P. J. (1998). Verification and validation in computational science and engineering. Albuquerque, N.M, Hermosa publishers.

RSSB. (2009). Resistance of Railway Vehicles to Roll-Over in Gales, Railway Group Standard GM/RT 2142. Rail Safety and Standards Board Ltd.

RSSB. (2016). Leading Health and Safety on Britain's Railway. Rail Safety and Standards Board Ltd.

Sanquer, S., Barre, C., deVirel, M.D., Cleon, L.M. (2004). Effect of crosswinds on high-speed trains: development of a new experimental methodology. J. Wind Eng. Ind. Aerodyn. 92, 535–545.

Sanz- Andrés, A., Santiago-Prowald, J., Baker, C., Quinn, A. (2003). Vehicle-induced loads on traffic sign panels. Journal of Wind Engineering and Industrial Aerodynamics. 91 (7), 925–942.

Sanz-Andrés, A. and Santiago-Prowald, J. (2002). Train-induced pressure on pedestrians. Journal of Wind Engineering and Industrial Aerodynamics. 90, 1007-1015.

Schulte-Werning, B., Grégoire, R., Malfatti, A., Matschke, G. (2002). TRANSAERO - A European Initiative on Transient Aerodynamics for Railway System Optimisation. Springer. Berlin.

Shur, M.L., Spalart, P.R., Strelets, M.K., Travin, A.K. (2008). A hybrid RANS-LES approach with delayed-DES and wall-modelled LES capabilities. Int. J. Heat Fluid Flow. 29 (6), 1638–1649.

Sima, M., Andersson, E., Häggström, J., Stichel, S. (2004). Assessment of train overturning risk due to strong crosswinds. Proceedings of the Institution of Mechanical Engineers, Part F: Journal of Rail and Rapid Transit Volume 218 (3), 213–223.

Singh, S. and Mittal, S. (2005). Flow past a cylinder: shear layer instability and drag crisis. Int. J. Num. Meth. Fluids. 47:75-98.

So, R. and Mellor, G. (1973). Experiment on convex curvature effects in turbulent boundary layers. Journal of Fluid Mechanics. 60: 43-62.

Sockel, H. (2002). Aerodynamic effects caused by a train entering a tunnel. Proc. Appl. Math. Mech. 1: 268–269

Solution for Research Ltd. (last accessed: 06/05/2018).

Soper, D., Baker, C. and Sterling, M. (2013). The slipstream development of a container freight train. In 6th European and African Conference on Wind Engineering, Cambridge, UK.

Soper, D. (2014). The aerodynamics of a container freight train. PhD thesis, University of Birmingham, UK.

Spalart, P., Jou, W., Strelets, M., Allmaras, S. (1997). Comments of feasibility of LES for wings, and on a hybrid RANS/LES approach. In: Proceedings of the International Conference on DNS/LES. August 4–8, Ruston, Louisiana, USA.

Sterling, M., Baker, C., Jordan, S., Johnson, T. (2008). A study of the slipstreams of high-speed passenger trains and freight trains. Proceedings of the Institution of Mechanical Engineers, Part F: Journal of Rail and Rapid Transit. 222 (2), 177–193.

Sterling, M., Quinn, A.D., Hargreaves, D.M., Cheli, F., Sabbioni, E., Tomasini, G., Delaunay, D., Baker, C.J., Morvan, H. (2010). A comparison of different methods to

evaluate the wind induced forces on a high sided lorry. Journal of Wind Engineering and Industrial Aerodynamics. 98, 10–20.

Suzuki, M. and Hibino, Y. (2016). Field Tests and Wind Tunnel Tests on Aerodynamic Characteristics of Train/Vehicles under Crosswinds. Quarterly Report of RTRI. 57, 55-60.

Suzuki, M., Tanemoto, K., Maeda, T. (2003). Aerodynamic characteristics of train/vehicles under crosswinds. Journal of Wind Engineering and Industrial Aerodynamics. 91:209.218.

Tabor, G. and Baba-Ahmadi, M. (2010). Inlet conditions for large eddy simulation: A review. Computers & Fluids. 39(4), pp.553-567.

Tavoularis, S. (2005). Measurement in fluid mechanics. Cambridge University Press, Cambridge.

Taylor, J. R. (1997). An introduction to error analysis: the study of uncertainties in physical measuements. University science books, CA, USA.

Temple, J. and Johnson, T. (2003). Review of Slipstream Effects on Platforms. AEA Technology Rail report for RSSB.

TFI. (2011). Turbulent Flow Instrumentation - Cobra Probe - Getting started guide. Technical report.

Thomas, D. (2013). On Rail Vehicle Dynamics in Unsteady Crosswind Conditions. Doctoral Thesis in Vehicle and Maritime Engineering. Stockholm, Sweden.

Tomasini, G., Giappino, S., Cheli, F., Schito, P. (2015). Windbreaks for railway lines: Wind tunnel experimental tests. Proceedings of the Institution of Mechanical Engineers. Part F J. Rail Rapid Transit. 230(4), 1270-1282.

TSI. (2008). EU technical specification for interoperability relating to the 'rolling stock' sub-system of the trans-European high-speed rail system. 2008/232/EC.

Wang, B., Xu, Y.-L., Zhu, L.-D., Li, Y.-L. (2014). Crosswind effect studies on road vehicle passing by bridge tower using computational fluid dynamics. Engineering Applications of Computational Fluid Mechanics. 8(3), 330–344.

Wang, J., Minelli, G., Dong, T., Chen, G., Krajnović, S. (2019). The effect of bogie fairings on the slipstream and wake flow of a high-speed train. An IDDES study. Journal of Wind Engineering and Industrial Aerodynamics. 191, 183-202.

Welahettige, P. and Vaagsaether, K. (2016). Comparison of OpenFOAM and ANSYS Fluent. Proceedings of the 9th EUROSIM & the 57th SIMS. September 12th-16th, 2016, Oulu, Finland.

Wingstedt, E., Vartdal, M., Osnes, A., Tutkun, M. (2013). Development of LES inflow conditions for turbulent boundary layers. Norwegian Defence Research Establishment (FFI).

Wu, M., Li, Y., Chen, N. (2015). The impact of artificial discrete simulation of wind field on vehicle running performance. Wind and Structures. 20(2), 169–189.

Wu, M., Li, Y., Zhang, W. (2017). Impacts of wind shielding effects of bridge tower on railway vehicle running performance. Wind and Structures. 25(1), 63–77.

Xia, C., Shan, X.Z., Yang, Z.G. (2017a). Comparison of different ground simulation systems on the flow around a high-speed train. Proc. Inst. Mech. Eng. - Part F J. Rail Rapid Transit. 231 (2), 135–147.

Xia, C., Shan, X.Z., Yang, Z.G. (2017b). Detached-Eddy Simulation of ground effect on the wake of a high-Speed train. J. Fluids Eng. 139 (5), 051101, 2017.

Yang, M., Du, J., Li, Z., Huang, S., Zhou, D. (2017). Moving Model Test of High-Speed Train Aerodynamic Drag Based on Stagnation Pressure Measurements. PLoS ONE 12(1): e0169471.

Yang, W., Deng, E., Lei, M., Zhu, Z., Zhang, P. (2019). Transient aerodynamic performance of high-speed trains when passing through two windproof facilities under crosswinds: A comparative study. Engineering Structures. 188, 729-744.

Zhang, T., Xia, H., Guo, W. (2013). Analysis on running safety of train on bridge with wind barriers subjected to cross wind. J. Wind Struct. 17(2), 203-225.

Zhang, T., Guo, W., Du, F. (2017). Effect of windproof barrier on aerodynamic performance of vehicle-bridge system. Procedia Engineering. 199, 3083-3090.

Zhang, J., He, K., Wang, J., Liu, T., Liang, X., Gao, G. (2019). Numerical simulation of flow around a highspeed train subjected to different windbreak walls and yaw angles. Journal of Applied Fluid Mechanics. 12(4), 1137–1149.

Zhao, H., Zhai, W., and Chen, Z. (2015). Effect of noise barrier on aerodynamic performance of high-speed train in crosswind. Wind and Structures. 20(4), 509-525.

Zhu, C., Hemida, H., Flynn, D., Baker, C. (2016). Numerical simulation of the slipstream and aeroacoustic field around a High-Speed Train. Proceedings of the Institution of Mechanical Engineers, Part F: Journal of Rail and Rapid Transit.

Appendix A: Data reduction and uncertainty analysis

A.1   Introduction

This appendix presents the full set of surface mean pressure coefficient distribution for the leading car of the Class 390 model-scale train analysed in this study for the configuration without any windbreak walls at a yaw angle of 90° (section A.2). This appendix also describes the methodology adopted in analysing the uncertainties in the experimental work carried out as part of this research study. The following analysis was carried out to evaluate the uncertainty associated with the experimental data obtained from the wind tunnel experiments in this study. This method has also been used successfully by Dorigatti (2013), Soper (2014) and Gallagher (2016) for studies relating to train aerodynamics. Section A.3 describes the two components of total uncertainty – bias limit and random uncertainty. Section A.4 presents the uncertainty calculations and analysis on the wind tunnel tests performed as part of this study. This includes presenting the total uncertainty estimates for both, the mean pressure coefficients and the aerodynamic load coefficients.

A.2   Surface mean pressure coefficient distribution

Figures A.1 – A.4 show the full set of surface mean pressure coefficient distribution for the leading car of the Class 390 model-scale train for the configuration without any windbreak walls at a yaw angle of 90°. In chapter 4, only pressure tap loops B, G and N were presented for analysis of the different test cases, whereas this section illustrates the data from all loops examined. As is clear, loops located closely together indicated similar trendlines, hence the reason as to why only three loops were presented in the thesis.

Figure A.1: Surface mean pressure coefficient distribution at (a) loop A, (b) loop B, (c) loop C and (d) loop D for the case without any windbreak walls at a yaw angle of 90°.

286

Figure A.2: Surface mean pressure coefficient distribution at (e) loop E, (f) loop F, (g) loop G and (h) loop H for the case without any windbreak walls at a yaw angle of 90°.

Figure A.3: Surface mean pressure coefficient distribution at (i) loop I, (j) loop J and (k) loop K for the case without any windbreak walls at a yaw angle of 90°.
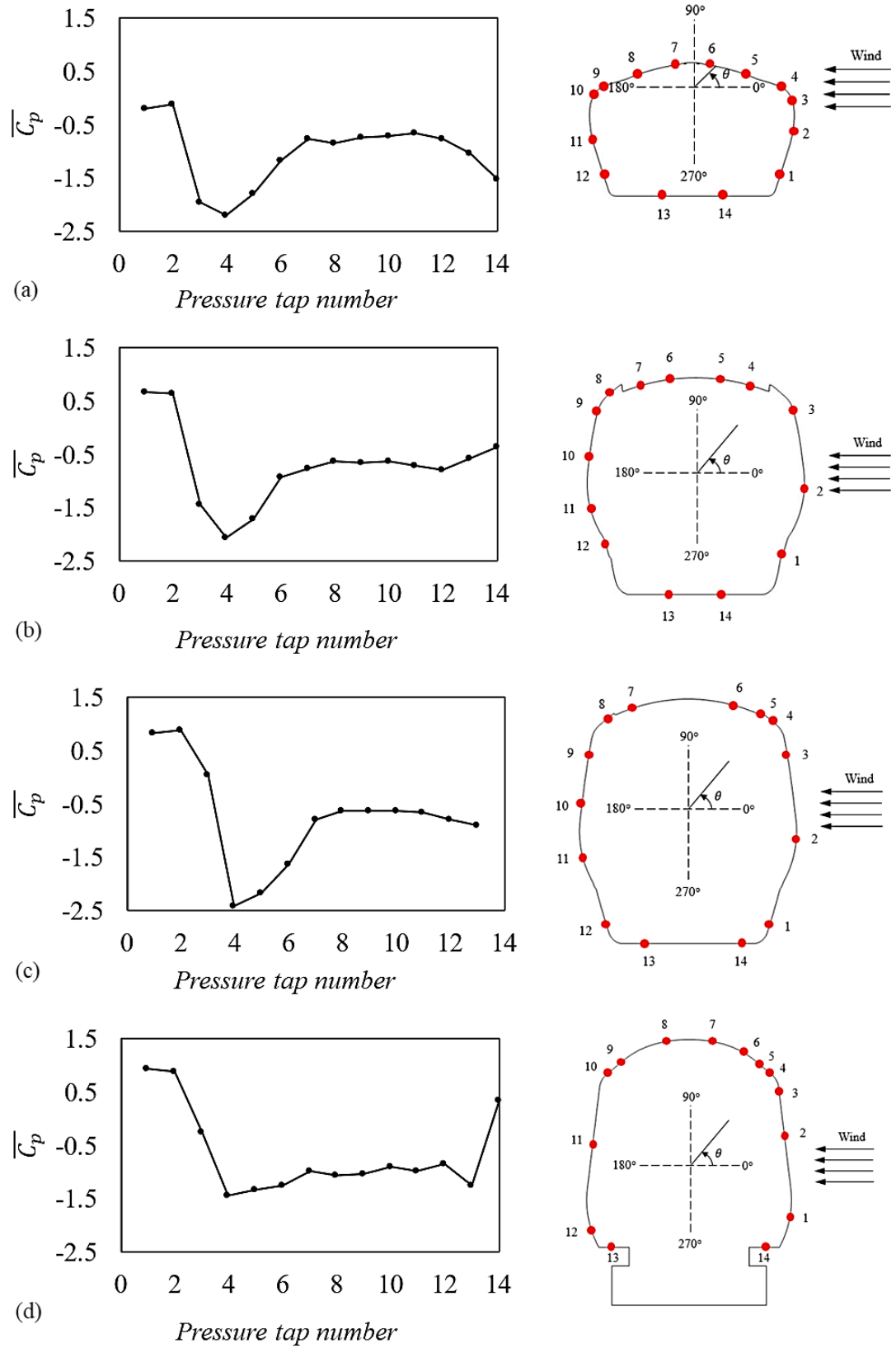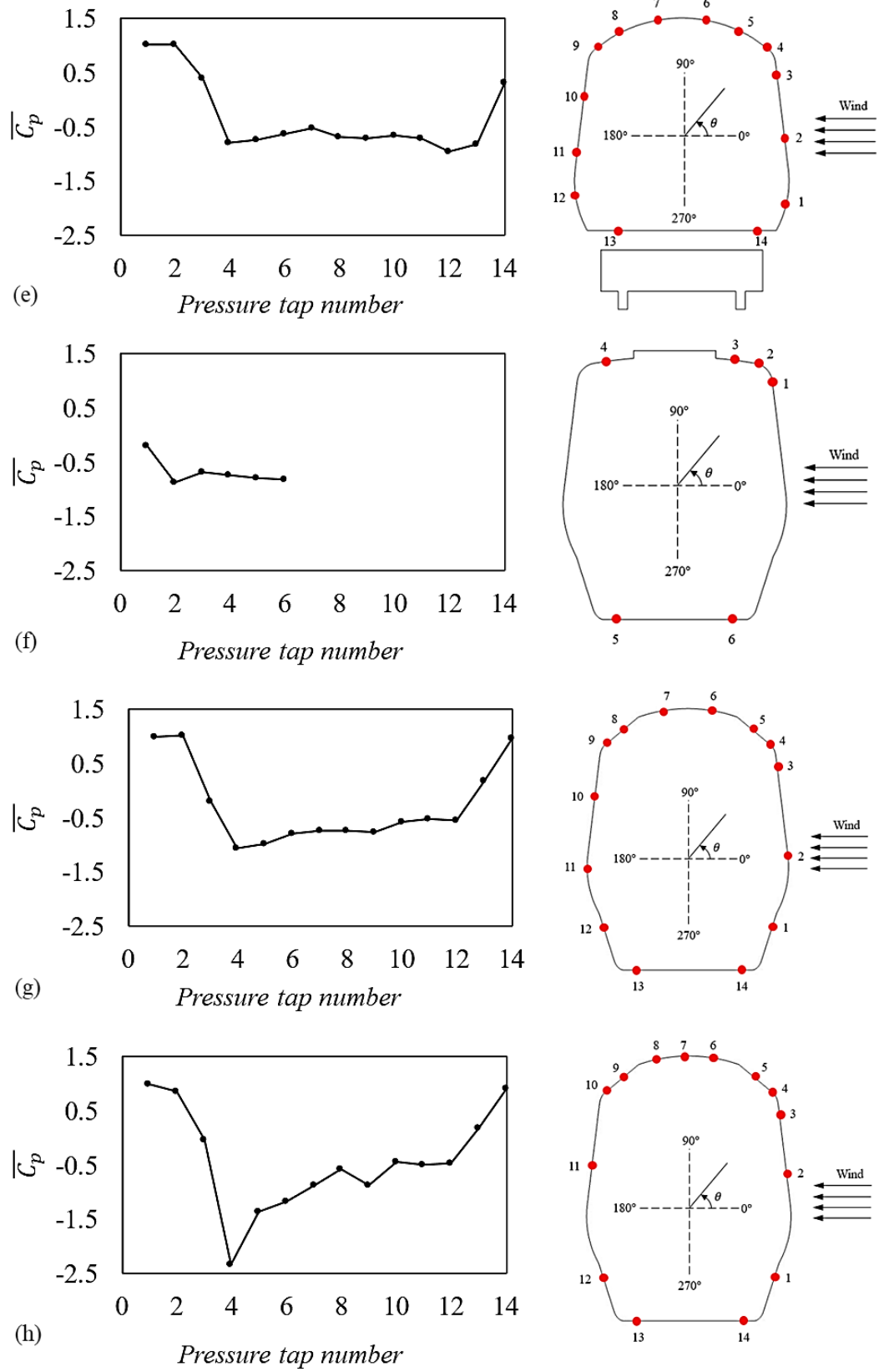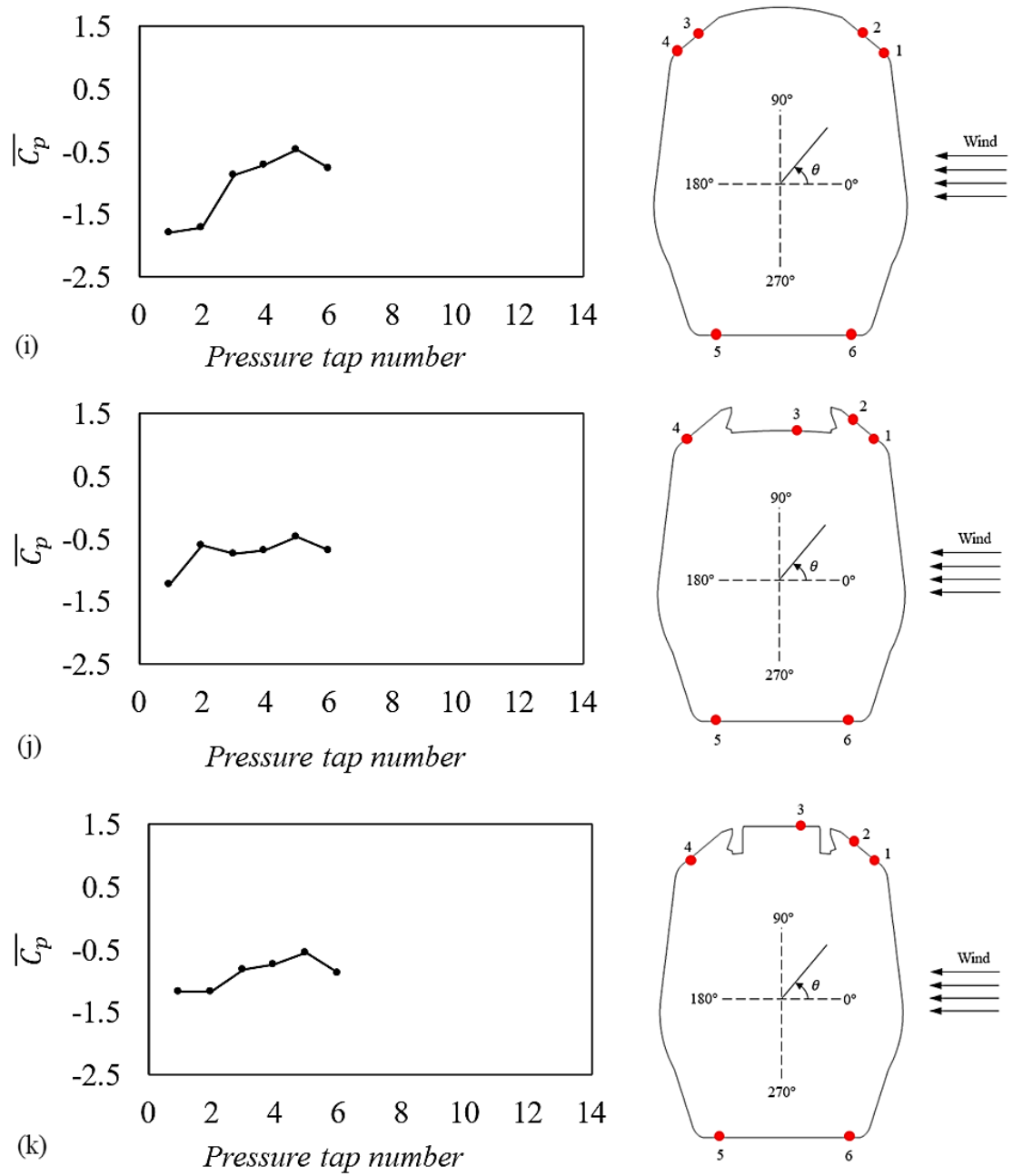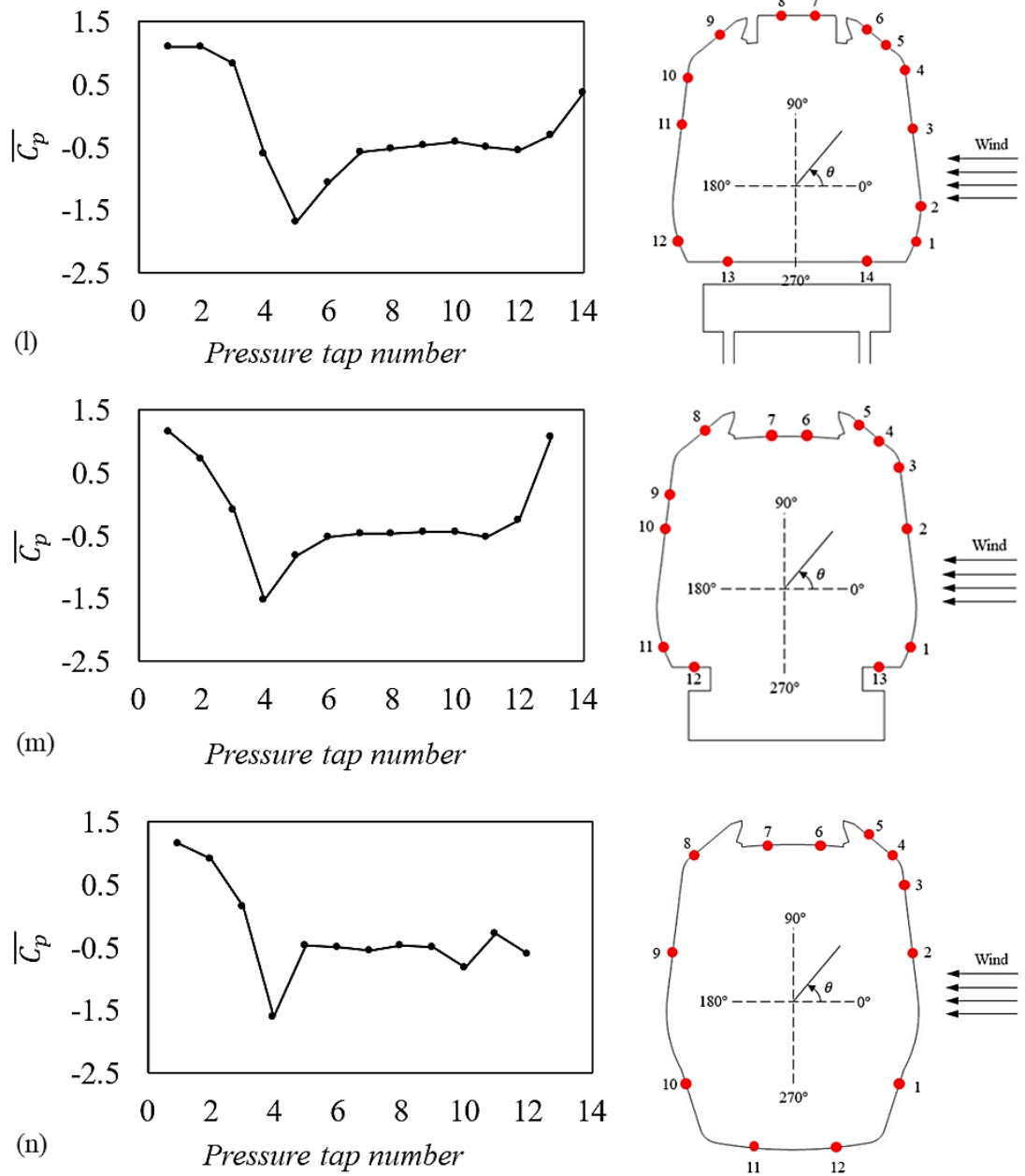
Figure A.4: Surface mean pressure coefficient distribution at (l) loop L, (m) loop M and (n) loop N for the case without any windbreak walls at a yaw angle of 90°.

A.3 Types of uncertainty

As Taylor (1997) and Tavoularis (2005) discussed, a measurement error refers to the difference between measured and true values of a physical quantity or a derived property. Quantification of such a difference is known as the measurement uncertainty. To assess the level of uncertainty, propagation theory is used to estimate the margin of error linked with the mean aerodynamic coefficients obtained (Taylor, 1997).

Experimental uncertainty (errors) in this study is considered to have two main components:

1) Bias limit (E_{BIAS})

2) Random uncertainty (E_{RND})

The bias limit arises from the uncertainty associated with the equipment used to take the measurements and the random uncertainty accounts for the variability relating to the testing process and the unsteadiness of the physical phenomenon being measured.

A.3.1 Bias limit

As discussed throughout in the thesis, the conventional procedure to present aerodynamic results is in the form of non-dimensional coefficients. To obtain these coefficients, a set of physical variables are needed that are measured with different instrumentation. Therefore, each instrument used would have an associated error. It is thus important to consider the combined effect of the individual errors. This can be done using the propagation of error theory, which can assist in determining the uncertainty of the non-dimensional coefficients obtained (Taylor, 1997).

The bias limit arises from the uncertainty associated with the instrumentation employed to take the measurements. It calculates the uncertainty of a measured variable, fundamentally by evaluating the performance limits and characteristics of the used instrumentation. Taylor (1997) defined the bias limit, E_{BIAS} , as:

$$E_{BIAS} = \sqrt{\sum_k \left(\frac{\partial C_\xi}{\partial b_k} \delta b_k\right)^2}$$

(A.1)

where C_ξ is any non-dimensional aerodynamic coefficient, b_k is any generic individual quantity that was directly measured for calculating C_ξ and δb_k is the associated instrumentation uncertainty. It must be noted that hysteresis and non-linearity result in the uncertainty of an instrument and manufacturers usually provide this information in the instrumentation specifications supplied.

A.3.2 Random uncertainty

Aerodynamic coefficients in this study are presented as ensemble averaged values. In order to take into consideration the run-to-run variability of the physical quantity measured, Dorigatti (2013) defined the random uncertainty, E_{RND}, by assuming a normal statistical distribution of each measurement along with a confidence level of 95% as:

$$E_{RND} = \pm 2 \frac{\sigma C_\xi}{\sqrt{N}}$$

(A.2)

where σC_ξ is the standard deviation of any non-dimensional aerodynamic coefficient with respect to the ensemble and N is the ensemble size (number of runs).

A.3.3 Total uncertainty

The bias limit and the random uncertainty measure different quantities and thus can be considered independent. As a result, the total uncertainty is defined as the algebraic sum of the bias limit and the random uncertainty (Dorigatti, 2013):

$$E_{TOTAL} = E_{BIAS} + E_{RND} \tag{A.3}$$

In this study, the errors are presented as absolute values and it is assumed that the error is of equal magnitude in both the positive and negative components.

A.4 Wind tunnel experimental uncertainty

Chapter 4 presents the outcomes of the experimental campaign carried out on the steady train aerodynamics with and without different windbreak walls in terms of mean pressure coefficients and mean load aerodynamic coefficients. Therefore, to calculate the associated uncertainties, the uncertainty of mean pressure coefficients is initially calculated, followed by the uncertainty of aerodynamic load coefficients by applying the propagation theory.

A.4.1 Mean pressure coefficients

A.4.1.1 Bias limit

Table A.1 presents the uncertainties of each measuring instrument used for the wind tunnel tests. The accuracy of each measuring instrument is considered for estimating the bias limit relative to the stationary wind tunnel tests through the propagation of error.

Table A.1: Accuracies of the measuring instrumentation

Measurement type	Accuracy	Instrument
Pressure	±5Pa	Pressure transducers
Wind velocity	0.3 m/s	Cobra probe
Density (derived from ambient conditions)	0.005 kg/m^3	Digital barometer and weather station

The bias limit for the air density was calculated through the propagation of error theory in relation to the ideal gas law. The individual accuracies for the ambient temperature and barometric pressure equipment were ±2 °C and ±200 Pa, respectively. The resulting uncertainty associated to the air density was determined as 0.005 kg/m^3.

Table A.2 and A.3 present the mean and maximum bias limits for the mean pressure coefficients of different test cases examined at wind incidence angles of 90° and 30°, respectively.

A large consistent bias limit is obtained for all the test cases. This was essentially due to the low reference wind speed (of about 7.2 m/s) in the wind tunnel. Based on the theory of propagation of error expressed in equation A.1, all the associated instrumentation uncertainties, δb_k, are weighted on the derivative of $\overline{C_P}$ with respect to any of them. Based on equation 4.1 in chapter 4, the higher the reference wind velocity is, the smaller the derivative of $\overline{C_P}$ is with respect to any generic individual quantity, b_k. Hence, a higher reference wind speed in any wind tunnel test campaign could lead to a reduced impact on the resulting E_{BIAS}. This has also been discussed in detail in Dorigatti (2013), where it

was also noted that total errors linked to a stationary analysis are higher as compared to a moving case due to the increased relative velocity in the latter.

A.4.1.2 Random uncertainty

The random uncertainty associated with the mean surface pressure coefficients is calculated in terms of a normal distribution with a confidence level of 95%. The standard deviation is determined in relation to the individual mean pressure coefficient for each run with respect to the ensemble.

Table A.2 and A.3 present the mean and maximum random uncertainty values for the mean pressure coefficients of different test cases examined at wind incidence angles of 90° and 30°, respectively. It is worth mentioning that since the sampling duration was long and the flow could be deemed to have a stable mean for this duration, the associated random uncertainties were very low.

A.4.1.3 Total uncertainty

The total uncertainty for each pressure tap is the sum of the bias limit and the random uncertainty. Figures A.5 and A.6 show the total uncertainties for the different test cases (a-f) examined in this study at wind incidence angles of 90° and 30°, respectively.
As the figures illustrate, it can be noted that the estimated total uncertainty is relatively constant for all the cases. Also, it is observed from the estimations that the random uncertainty input is much less than the bias limit. Generally, as expected, the bias limits for all the test cases examined remain relatively constant since all the input variables are similar in equation A.1. Nevertheless, the bias limits arise due to the potential effects of

crosswinds on the surface pressures, which cannot be ignored even for the cases consisting of windbreak walls.

Table A.2: Mean and maximum bias, random and total uncertainties for the mean pressure coefficients of different test cases examined at a wind incidence angle of 90°.

Case	Bias limit		Random uncertainty		Total uncertainty	
	Mean	Maximum	Mean	Maximum	Mean	Maximum
(a)	0.162	0.187	0.005	0.042	0.167	0.229
(b)	0.161	0.169	0.009	0.038	0.170	0.207
(c)	0.161	0.170	0.005	0.030	0.166	0.199
(d)	0.161	0.170	0.010	0.067	0.171	0.237
(e)	0.160	0.168	0.013	0.037	0.173	0.206
(f)	0.160	0.167	0.009	0.072	0.169	0.240

Table A.3: Mean and maximum bias, random and total uncertainties for the mean pressure coefficients of different test cases examined at a wind incidence angle of 30°.

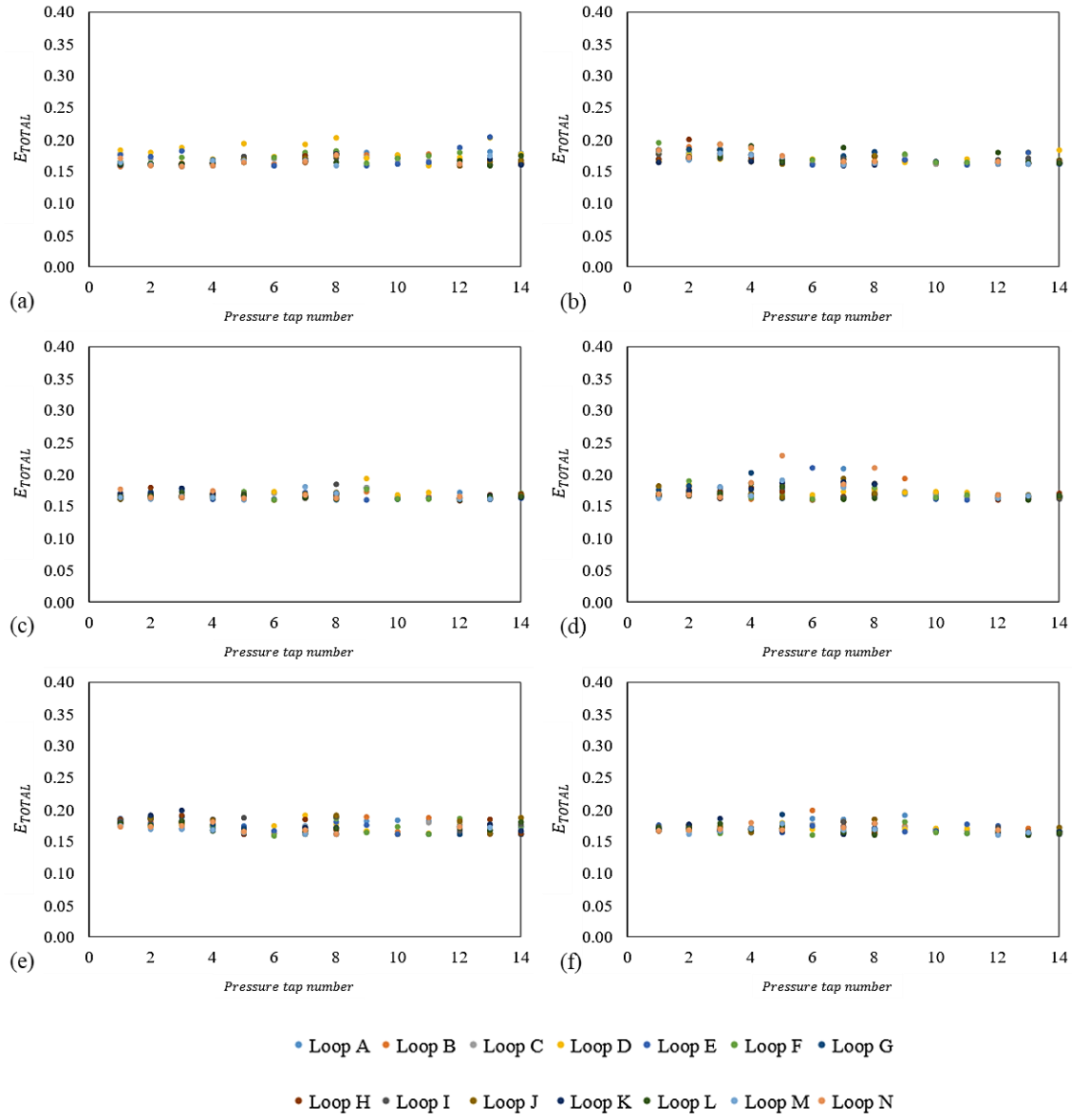| Case	Bias limit		Random uncertainty		Total uncertainty	
	Mean	Maximum	Mean	Maximum	Mean	Maximum
(a)	0.160	0.172	0.012	0.044	0.172	0.216
(b)	0.159	0.164	0.008	0.042	0.167	0.206
(c)	0.159	0.170	0.007	0.027	0.166	0.198
(d)	0.160	0.179	0.006	0.031	0.166	0.210
(e)	0.160	0.172	0.007	0.034	0.166	0.206
(f)	0.159	0.173	0.005	0.023	0.165	0.197

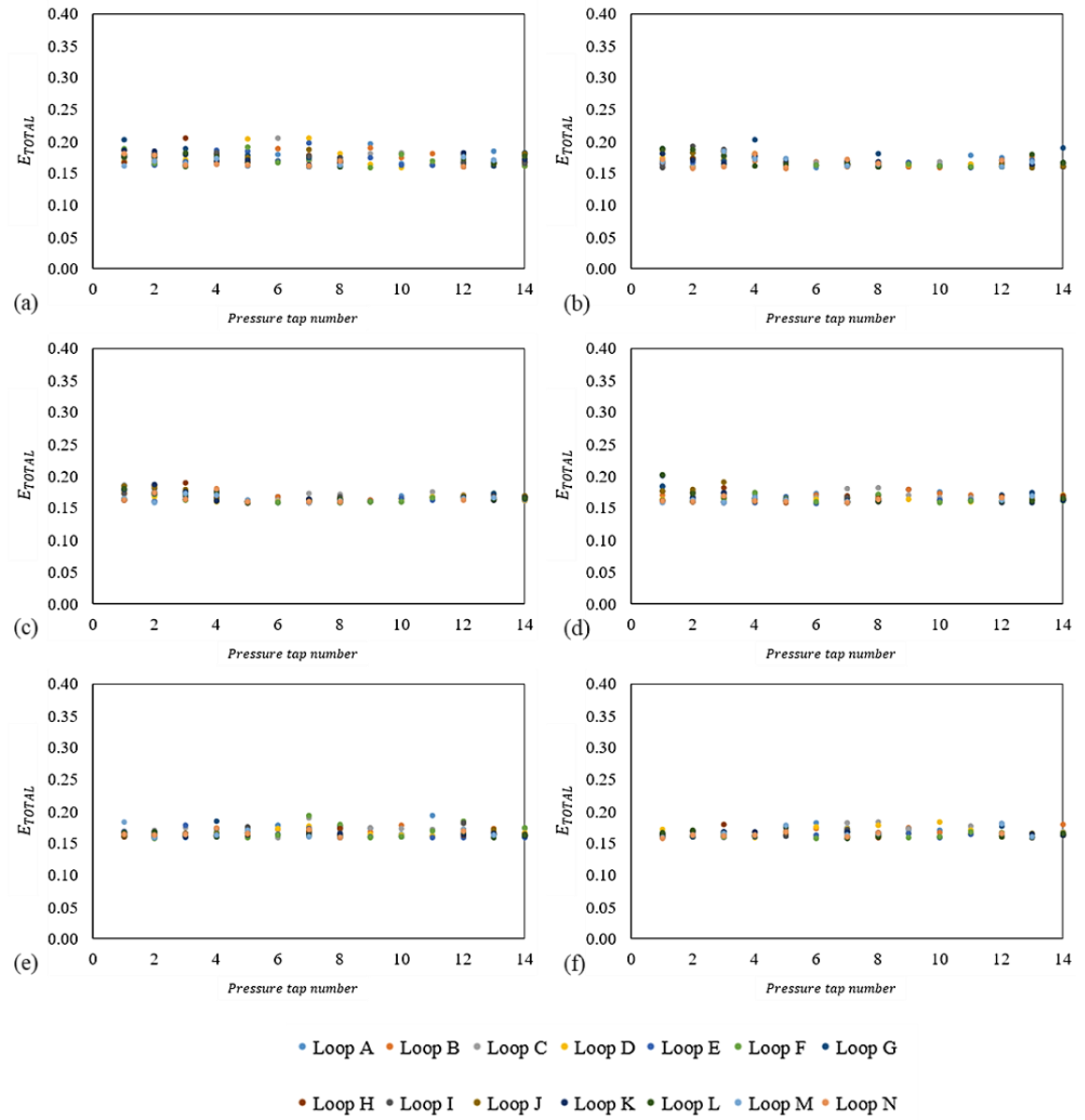Figure A.5: Total uncertainties for test cases (a-f) examined at a wind incidence angle of 90° in this study.

Figure A.6: Total uncertainties for test cases (a-f) examined at a wind incidence angle of 30° in this study.

A.4.2 Aerodynamic load coefficients

The mean aerodynamic load coefficients presented in chapter 4 are side, $\overline{C_Y}$, and lift, $\overline{C_z}$, forces along with the rolling moments about the X-axis and leeward rail, $\overline{C_{M_X}}$ and $\overline{C_{M_{X,lee}}}$, respectively, for different test cases. Uncertainties associated with these coefficients are estimated relative to the uncertainties calculated for the mean pressure coefficients. To do so, the propagation error theory is applied to the equations for the aerodynamic load coefficients presented in chapter 3. In addition, it was assumed that the load contribution for the discretised areas linked to pressure taps was independent. The uncertainty of the mean aerodynamic load coefficients can be given as (Dorigatti, 2013):

$$E_{LOAD} = \sqrt{\sum_i \left(\sum_j \left(\frac{\partial C_\xi}{\partial C_{p_{i,j}}} E_{TOTAL_{ij}} \right) \right)^2} \qquad (A.4)$$

Table A.4 and A.5 present the total uncertainty values for the different mean aerodynamic load coefficients of different test cases examined at wind incidence angles of 90° and 30°, respectively. As noted from the tables, the resulting uncertainties are very low. However, it must be noted that these uncertainties are considered to be less than the true error. This is because the calculation method for the load does not take into consideration the uncertainty introduced through discretising the geometry of the train model. Also, since it was assumed that pressure is uniform across each discretised area in the process of pressure integration, there could possibly be some error introduced in real life (Dorigatti, 2013). Using a force balance could assist in assessing the influence of discretising the train geometry. However, adopting this technique would mean that an additional instrument is used and thus the value for E_{TOTAL} utilised for aerodynamic load uncertainty calculations would change.

Table A.4: Total uncertainties for the mean aerodynamic load coefficients of different test cases examined at a wind incidence angle of 90°.

Case	Total uncertainty			
	C_Y	C_z	C_{M_x}	$C_{M_{X,lee}}$
(a)	0.060	0.056	0.039	0.049
(b)	0.005	0.003	0.003	0.003
(c)	0.002	0.005	0.000	0.000
(d)	0.001	0.005	0.000	0.000
(e)	0.001	0.005	0.000	0.000
(f)	0.001	0.004	0.000	0.000

Table A.5: Total uncertainties for the mean aerodynamic load coefficients of different test cases examined at a wind incidence angle of 30°.

Case	Total uncertainty			
	C_Y	C_z	C_{M_x}	$C_{M_{X,lee}}$
(a)	0.025	0.022	0.017	0.021
(b)	0.014	0.011	0.004	0.004
(c)	0.017	0.002	0.012	0.013
(d)	0.015	0.015	0.010	0.009
(e)	0.015	0.015	0.010	0.009
(f)	0.012	0.015	0.008	0.007